THE STRUCTURE OF JETS IN e^+e^- COLLISIONS

P. MÄTTIG

IPP Canada, and Carleton University Ottawa, Ontario, Canada

NORTH-HOLLAND – AMSTERDAM

PHYSICS REPORTS (Review Section of Physics Letters) 177, Nos. 3 & 4 (1989) 141–317. North-Holland, Amsterdam

THE STRUCTURE OF JETS IN e^+e^- COLLISIONS

P. MÄTTIG

IPP Canada, and Carleton University Ottawa, Ontario, Canada

Received October 1988

Contents:

Single orders for this issue

PHYSICS REPORTS (Review Section of Physics Letters) 177, Nos. 3 & 4 (1989) 141–317.

Copies of this issue may be obtained at the price given below. All orders should be sent directly to the Publisher. Orders must be accompanied by check.

Single issue price Dfl. 133.00, postage included.

Abstract:

Over the last ten years a wealth of information on the structure of jets has been collected in e^+e^- annihilation at c.m. energies between 10 and 45 GeV. It provided us with a rather detailed picture on both the jet properties at a fixed energy and their Q^2 dependence. Measurements exist for single particle distributions and yields, compensation of quantum numbers, properties of jets from quarks of different flavour, and the properties of gluon jets. The data can be accommodated by models based on QCD. The high statistics and long lever arm available at future colliders, particularly at the Z^0 mass will provide a lot of new measures for exploring the hadronization mechanism. Some of them will be discussed. The knowledge of the jet structure plays a crucial role at future colliders that are to explore the interactions of asymptotically free quarks and gluons in the space and time regions probed at the forthcoming generations of new colliders. The perspectives of finding the underlying parton dynamics in jets are summarized.

1. Introduction

It is a universal property of multi-hadron production in all kinds of reactions that the final particles are not distributed uniformly in phase space. Rather they are collimated along some distinct axis and are bundled into rather small regions, into jets. Evidence for such behaviour has been seen in hadronic reactions as well as in deep inelastic lepton nucleon scattering. Jets in e^+e^- annihilations were first observed by the MARKI collaboration about ten years ago [1]. Whereas their data at c.m. energies $W = \sqrt{s} \sim 3$–7 GeV required a thorough statistical comparison to phase space models to establish the existence of jets, these are beautifully displayed at the higher energies around $W \sim 30$ GeV accessible at the e^+e^- storage rings PETRA and PEP. The exploration of the structure of jets became one of the main activities at these machines.

According to today's understanding of elementary processes the first steps in hadron production in terms of fundamental partons are very simple: the initial e^+e^- pair annihilates into a gauge boson (either a photon or at higher energies a Z^0) which in turn decays into a quasi free quark and antiquark (fig. 1.1). In particular four experimental results provide evidence for this picture:

(i) The total hadronic QED cross section in terms of

$$R = \frac{\sigma(e^+e^- \to \text{hadrons})}{\sigma(e^+e^- \to \mu^+\mu^-)}$$

grows stepwise, each step taken when the threshold for the production of new quarks has been passed (for a compilation see ref. [2]). At energies above the bottom threshold it has a value of 4 close to what is expected from the quark charges:

$$3 \cdot \sum e_q^2 = 3.66\,,$$

where the sum goes over all quark species that can be produced at these energies: u, d, s, c, and b-quarks. The factor 3 takes into account their colour charges.

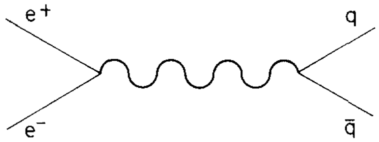

Fig. 1.1. Sketch of the production of a quark-antiquark pair in e^+e^- annihilations.

(ii) The angular distribution of the jets is (e.g. refs. [3, 4])

$$\frac{d\sigma}{d\cos\theta} \propto 1 + \cos^2\theta ,$$

as expected for spin-$\frac{1}{2}$ particles with $M^2/s \ll 1$.
(iii) The charges of the hadrons are not distributed stochastically over the whole event, but each hemisphere has a rather small average total charge of $|Q_{\text{jet}}| = 0.55 \pm 0.25$ [5] in agreement with the average quark charge.
(iv) Even more the charge of a jet tends to be determined by that of particles of high momentum. This can naturally be explained as being the footprints of charged primary partons [6].

At energies of $W \geq 30$ GeV a fraction of the events exhibit a more complicated structure involving a distinct third jet [7]. These events carry all the features expected from QCD bremsstrahlung. Their fraction is in agreement with a value of $\alpha_s(Q^2 = 1000\,\text{GeV}^2) \sim 0.14$ [8], consistent with what has been determined in other measurements. Their event topology indicates an initial three parton state [9, 10] and the angular distribution of the jets suggests the third jet as being due to a spin 1 parton [11–13].

Thus the global structure of hadronic events in e^+e^- collisions around $W \sim 30$ GeV is very well understood in terms of hard partons and QCD. How these partons convert into hadrons is less obvious and cannot be calculated from the first principles. Rather, it is an active field of experimental research aimed at collecting information about the structure of jets, finding regularities and thus allowing one to penetrate deeper into the understanding of hadronisation.

Hadron–hadron, lepton–hadron scattering as well as e^+e^- annihilation have each contributed to today's understanding. In this article the focus is on what is known from the latter reaction. The pros and cons of the various types of reactions relevant to extract information about jets are listed in table 1.1*). The data obtained in e^+e^- collisions display a certain simplicity and transparency to study this part of hadron production. As can be seen from the table, the hadrons produced in e^+e^- annihilations offer a complete and background free picture of jets. Here the c.m. energy of the whole reaction is identical to the invariant mass W_{jj} of the hard process. This is not true for pp and lepton–proton collisions where only a fraction of the initial particles contribute to the hard scattering. Also, in e^+e^- collisions the types of partons are unique. Even more the various quark species occur in a well-known ratio. The jets are well separated and (except for those events with a hard gluon emitted) stem only from quarks, no mixture between jets originating from other types of partons exists. All particles can be unambigously associated to quark jets. There exists no ambiguity as to what is the correct energy scale to use. This all makes e^+e^- collisions a very effective probe for jet properties. In fact its results are frequently used as reference points for understanding special features of jets in other types of collisions.

To summarize the global geography of jet development (see fig. 1.2): outside a space–time region larger than at least $\sim 10^{-17}$–10^{-18} cm quarks behave as point-like particles [14]. These hard partons

---

*) I am grateful to J. Gayler for consultations on the parameters of eq-scattering.

Table 1.1
Relevant parameters for jet physics for the three types of parton scattering

parameter	e^+e^-	ℓq	$q\bar{q}$, qq
primary partons	u, d, s, c, b	u, d, (s, c); diquarks	u, d, s, c, b, g
max. W_{jj}	44 GeV	~20 GeV	~200 GeV
can the complete jet be reconstructed?	yes	yes (fixed target)	no particles of low energy
how to determine the event axis?	from final state (all part.)	from outgoing lepton (NC react.)	from final state (single jets)
$\Delta(W_{jj})/(W_{jj})$	$\sim 10^{-3}$	$\sim 2\times 10^{-3}$	$\sim 10^{-1}$
do additional hadrons disturb jets?	no	no	yes
what energy scale of hadron prod.?	$Q^2 = W_{\text{had}}$	Q^2, W_{had}	E_T, Q^2, W_{had}

travel about half a fermi and form the crystalisation points for distinct jets. They hadronise within a distance of a few fm. The final particles emanate from the interaction point in several bundles of particles. Whereas the first region cannot be probed with today's experimental facilities and it is subject to theoretical speculation and in the focus of the future generation of accelerators, the second region seems to be quite well understood in terms of perturbative QCD. As was pointed out before, it is the third region which is experimentally accessible but not very well understood. This hadronisation region will be the main issue of this article.

The interest in the properties of jets is at least twofold. Firstly, the theoretical penetration into jet evolution and hadronisation has not progressed beyond some general ideas. As will be dicussed in this article, QCD inspired models supply an amazingly good description of jet properties. To achieve this they require a substantial number of free parameters for which no well founded theoretical calculation exists. Beyond the evaluation of parton dynamics jets are a quite virgin field of theoretical research. It is the general belief that the basic theory for calculating jet properties is QCD. However, since hadronisation extends down to low Q^2, it requires non-perturbative methods which makes its properties as yet uncalculable. The special flavour of jet development is that the Q^2 range involved extends from very high Q^2 to low Q^2 and therefore sheds light on the transition between the regions where a perturbative treatment and those where a non-perturbative treatment is applicable.

The second point of interest addresses much higher Q^2. Jets are the measurable traces of quarks and gluons. Any experimental evaluation involving these constituents, be it to determine how quarks couple to the Z^0, or to reconstruct a heavy object decaying into quarks, requires the use of jets as entities representing the fundamental partons. To extract the most precise and extensive information about the quarks and gluons of interest one has to know how they leave their marks in a hadronic event: how the

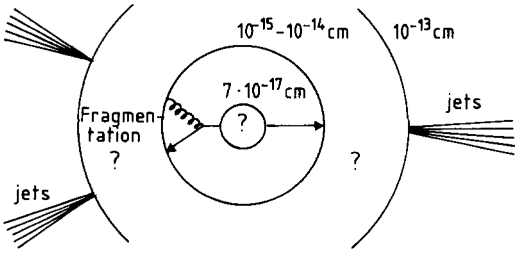

Fig. 1.2. Schematic view of the space–time distribution for the various stages of jet development.

energy, momentum, and flavour of the primary parton is related to the particle structure measured in the detector. Already at the c.m. energies accessible at PETRA and PEP, jets have been used as entities e.g. to determine the gluon spin and the weak couplings of the charmed quark. This aspect of jet physics will become increasingly relevant for the next generation of high energy colliders.

This article will proceed from a summary of measurements of jet properties in e^+e^- reactions to a discussion about future jet physics.

After a survey of the most frequently used models of fragmentation, single particle inclusive distributions will be discussed in the first part. These supply a general overview of what jets look like. It starts with the jet properties as revealed by the sum of all final particles, continues with a discussion of the distributions of identified particles and finishes with a comparison of jets originating from the various kinds of partons.

The second part focusses on the experimental evidence on the space–time structure of jet development. In section 6 the information about the shape and the size of the emitting source will be discussed followed by a discussion of how particles in a single event are related with one another. These measurements outline a picture of the sequence of hadron production and can be divided into two classes: measurements on correlations between groups of particles, i.e. larger parts of an event, and two particle correlations. The first one provides insight into how hadron production at a certain stage depends on the prehistory of jet development (section 7). Two particle correlations, the second class, in particular how and where specific quantum numbers are compensated, have turned out to be one of the most powerful tools for studying the detailed sequence of particle production. They will be discussed in section 8. The second part closes by summarizing the indications about the mass scale at which non-perturbative effects become relevant.

In the third and last part of this article, an extrapolation to jet physics of the future is attempted. It will relate to both interests mentioned before. In section 10 some new measurements about the hadronisation will be discussed that will become possible at the new generation of e^+e^- colliders. The last section is devoted to the reverse problem: how to extract the energy, direction and flavour of the original parton from the properties of jets.

2. General ideas about hadron production

There exists solid evidence that hadron production in e^+e^- annihilations originates from a quasi free $q\bar{q}$ pair. The main experimental evidence for this has been summarized in the introduction. Theories and models which attempt to describe jet development therefore must start from these primary partons and then apply prescriptions to convert them into bundles of hadrons.

However, alternative approaches exist. One class of models applies thermodynamical methods. For example, Ochs [15] assumes hadron production to proceed via a branching process in which heavy objects decay into lighter ones and each of the branchings leads to an equipartition of states in phase space. This model is able to describe features such as the energy dependence of the multiplicity, the momentum distribution as well as general topological quantities such as the rate of three-jet events. However, fundamental properties constituting the evidence for primary quark production such as the $(1+\cos^2\theta)$-distribution of the jet axis or the charge distribution in jets are not accounted for. Although these kinds of statistical models may be helpful in separating kinematic and dynamical aspects of hadronisation they will not be discussed further in this article.

In a similar manner we will not consider in detail models describing the structure of hadronic events at $W_{e^+e^-} \sim 30\,\mathrm{GeV}$ without gluon emission as that of Fredrikson et al. [16]. They suggested that the three-jet events detected at these energies are caused by diquark emission together with an unbound qq($\bar{q}\bar{q}$) system. Another of these models has been proposed by Preparata and Valenti [17]. They imagine a "fire string" of mass W to be produced according to a simple parton model. This firestring then decays into either a low mass meson ($m_M \sim 1$ GeV) plus a firestring or two firestrings of masses m_1 and m_2. Whereas the first process is just how the more popular models to be discussed below treat hadronisation, the second process aims at replacing the gluon bremsstrahlung. The firestring model turns out to be quite flexible and many measurements can be reproduced. However, since the event structure in $e^+e^- \rightarrow$ hadrons can be described so naturally by gluon emission and also other kinds of interaction beautifully exhibit the features expected from QCD, it seems somehow artificial to replace gluon bremsstrahlung by other mechanisms without deep theoretical justification. In addition it does not predict any feature that the QCD models are not able to account for.

Within the quark–parton picture the lowest order QED differential cross section for the hadron production by unpolarized e^+e^- beams is given by

$$\frac{d\sigma_0}{d\Omega\, ds} = 3\,\frac{\alpha^2\beta}{4s}\, e_q^2(1 + \cos^2\theta + (1 - \beta^2)\sin^2\theta)\,. \tag{2.1}$$

Here α is the QED coupling constant, $s = W^2$ the total c.m. energy squared, θ the polar angle and β the velocity $\beta = p/E$, e_q is the charge of the primary parton.

The validity of the quark–parton picture is limited and it has to be supplemented by effects stemming from the strong interaction. These are necessary to account for hadronisation as well as to describe the third jet observed in e^+e^- interactions above $W = 30$ GeV. Quantum Chromodynamics is considered as the underlying theory for describing these properties. The basic success of QCD is its ability to account both for the existence of quasi-free quarks at high Q^2, first observed in deep inelastic scattering, and for the non-observability of free quarks.

There exist excellent textbooks (e.g. refs. [18, 19]) and reviews (e.g. ref. [20]) of QCD. For detailed considerations we refer the reader to those. Here we just want to summarize the most relevant features of QCD with respect to jet physics.

QCD, the theory of strong interactions, is a local gauge theory on the basis of an SU(3) symmetry group. It implies a new quantum number "colour" which occurs in three shades generally denoted by red, green and blue. In the standard theory colour is carried solely by quarks and eight considered massless vector bosons, called gluons. Colour is conserved, therefore the lines of colour flow in parton–parton couplings can be drawn as in fig. 2.1. Gluons are assumed to have neither electric charge nor flavour and as a result the strong interaction is flavour independent.

In contrast to QED, the best known local gauge theory, the vector bosons of QCD carry colour charge themselves and therefore are subject to self-interactions, such that the field strength tensor is

$$F^a_{\mu\nu} = \partial_\mu A^a_\nu - \partial_\nu A^a_\mu + g f^{abc} A^b_\mu A^c_\nu \tag{2.2}$$

with $A^a_\mu(x)$ being the gluon fields, $a = 1, \ldots, 8$, f^{abc} being the structure constant of SU(3). It is this self-interaction that leads to a qualitatively different Q^2-dependence of the strong coupling constant α_s compared to the electromagnetic α. In leading logarithmic order

$$\alpha_s(Q^2) = \frac{4\pi}{(11 - \frac{2}{3}N_f)\ln(Q^2/\Lambda^2)}\,. \tag{2.3}$$

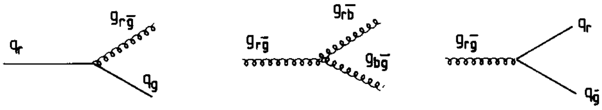

Fig. 2.1. Examples for the colour flow for various parton branchings: $q \to qg$, $g \to gg$, $g \to q\bar q$.

Here Λ is a QCD scale parameter which is experimentally determined as being 100–400 MeV. This Q^2-dependence leads to a vanishing coupling for $Q^2 \to \infty$, i.e. in small regions of space–time quarks and gluons act asymptotically free. For decreasing Q^2, $\alpha(Q^2)$ grows such that partons of compensating colour strongly attract each other. This is the basis of colour confinement perceiving that no free coloured objects exist outside a small space–time volume. Though not proven yet in a strict sense, it is a commonly accepted conjecture.

As a consequence the well-developed machinery of perturbative calculations is restricted to QCD processes at large Q^2 and cannot be applied to processes of the hadronic mass scale. This, in particular, limits the power of theoretical predictions of the properties of jets. New methods for a non-perturbative treatment are being developed, however, they are still far away from an application to jet physics.

This implies that jet models have to combine theoretically well-founded parton distributions with phenomenological models for converting those into hadrons. There exist two theoretical approaches to the calculation of parton distributions. At least historically related to this partition are the mass scales down to which QCD matrix elements are explicitly applied. The parton multiplicity is in both approaches determined by a cut-off mass below which two partons cannot be individually produced. This is schematically displayed in fig. 2.1.1. For a high invariant mass of the gluon–quark system two distinct jets emerge. If its mass is low, the gluon and the quark are not treated as two separate entities but are rather merged into one parton giving rise to a single jet.

The QCD matrix element for on-shell partons has been exactly calculated up to order α_s^2 [21–23]. It has been implemented into the first class of models. These up to four partons with momenta and directions given by the QCD calculations then have to be fragmented into the final hadrons. Most models realize this by a stepwise application of phenomenological probability functions determining the momenta and types of hadrons.

In the second class of models the QCD calculations are applied down to much lower Q^2. Instead of using the explicit second order QCD calculations, the matrix element is regularized by giving a mass to the gluon and summing up the leading logarithmic contributions. Within these models the partons are considered to be off-shell and a higher parton multiplicity is obtained by letting them cascade downwards in off-shellness to a minimum parton mass Q_0. Its value cannot be inferred from theory, however, going beyond

$$\alpha_s(Q_0^2)/\pi = 1$$

or a Q_0 of several hundred MeV seems rather dangerous. As a result the number of partons generated within these shower models is considerably larger than in the first class. Also in these models the generated partons have to be converted into hadrons requiring certain phenomenological models. The ratio of final hadrons to partons is much smaller than in the high cut-off models.

Theoretically the explicit calculation of QCD matrix elements up to nth order gives a more accurate description of the non-collinear kinematics. However, for higher orders these calculations are very tedious, the shower formalism is easier to iterate to higher orders (see discussion in ref. [24]).

In all of these models[*)] a substantial number of statistical distributions are convoluted such that the final jet properties cannot be expressed analytically for most cases. Instead the basic concepts have been transformed into computer programs that allow one to generate single events according to the probability distributions.

In the following we will discuss in section 2.1 the two approaches to the determination of parton distributions, based on the exact QCD matrix element (section 2.1.1) and the Leading Log Approximation (LLA) (section 2.1.2). The various models of how to hadronise these partons will be addressed in section 2.2. They are the Independent Jet Model, the String Model, and the Cluster Model. In principle each way to determine the parton distribution can be combined with each of the models of hadronisation.

2.1. The parton distributions

The first step towards describing jet development is the determination of the parton distributions. This can be achieved on the well-founded basis of QCD. There exist essentially two approaches. The first one determines the exact matrix element for on-shell partons, the second one is based on the Leading Logarithmic Approximation.

2.1.1. The exact QCD matrix element

In the quark–parton model the two collinear quarks are produced according to the electroweak theory. Effects from the strong interaction lead to the emission of gluons with a matrix element that is in principle determined by QCD. Due to reasons discussed below the QCD matrix element can in practice only be calculated if the gluon is hard[**)]. For massless quarks the first order QCD correction is [26]

$$\frac{d\sigma_{q\bar{q}g}}{dx_1\,dx_2} = \sigma_0 \frac{\alpha_s(Q^2)}{\pi} \frac{2}{3} \frac{x_1^2 + x_2^2}{(1-x_1)(1-x_2)}\,, \tag{2.1.1}$$

where σ_0 is the integrated quark–parton model cross section (2.1), $\alpha_s(Q^2)$ the strong coupling constant and x_i the scaled parton energy $x_i = 2E_i/W$ such that

$$x_1 + x_2 + x_3 = 2\,. \tag{2.1.2}$$

Note that due to this constraint only x_1 and x_2 appear in eq. (2.1.1). The extension to massive quarks can be found in refs. [27, 28]. The cross section exhibits singularities when the three parton final state approaches a configuration that is indistinguishable from a two-parton state, equivalent to where the combination of two partons have zero mass. From inspecting eq. (2.1.1) it follows that those cases correspond to $x_i \to 1$ or $x_i \to 0$ (which leads to $x_j \to 1$ due to momentum conservation). These singuarities can be divided into the infrared and collinear singularities known from QED: for x_i and $x_j \to 1$ if follows $x_k \to 0$ leading to an infrared singularity, for $x_i \to 1$ but $x_j \neq 0$, 1, partons j and k are collinear.

[*)] Throughout the article we will use the following notation: primary partons (quarks) are those which couple directly to the photon or Z^0. In a somewhat sloppy way we will refer to primary hadrons as those containing the primary parton. Prompt hadrons are those directly produced in the fragmentation, i.e. before their possible decay. Final particles are the particles after resonance decays.

[**)] A detailed review of the methods applied for the theoretical evaluation of hard QCD effects in jets, their results, and their agreement with experimental measurements can be found in ref. [25].

Since a final state with a collinear or soft gluon emission leads anyhow to a topology that is indistinguishable from that of the zeroth order process $e^+e^- \to q\bar{q}$, and to avoid these singularities, a cut-off is introduced. A gluon is only explicitly generated if it is hard enough such that all masses M_{p_1,p_2} that can be formed from two partons are larger than the cut-off mass M_c (see fig. 2.1.1)

$$M^{\min}_{p_1,p_2} > M_c\,.$$

The cut-off is often expressed in terms of

$$y_c = M_c^2/s\,. \tag{2.1.3}$$

M_c is a free parameter within limits to be discussed below. Only very weak constraints for its value are given by theory. It is normally chosen such as to give a smooth transition between events originating from two and three-parton states after hadronisation. In addition the value of M_c is usually matched to the experimental resolution of discriminating between one and two distinct jets. This suggests M_c to be typically ~5 GeV.

The relation between the cut-off and the $x_i^{\max}$, the maximum scaled energy of the parton is given through massless parton kinematics as

$$x_i^{\max} = 1 - M_c^2/s = 1 - y_c \tag{2.1.4}$$

which is often referred to as "parton-thrust".

This cut-off mass is on the one hand a technical prescription to separate the different topologies that are visible in the data and to avoid the singularities in the matrix element. It was on the other hand suggested that this mass has a deeper relation to the physics of strong interaction. At one stage in the jet development the confining forces become that strong that an emitted gluon will be rescattered in the gluon cloud combining the two colour sources (see refs. [29, 30]).

The value of this cut-off mass and its energy dependence are theoretically uncertain. The most simple assumption is that M_c is independent of the energy. In that case it follows from eq. (2.1.4) that $x_i^{\max}$ increases rapidly towards one with increasing energy. This larger phase space for $\sigma_{q\bar{q}g}$ will obviously lead to violations of unitarity for $\sigma_{q\bar{q}g}$ in eq. (2.1.1) at some s. This deficiency can only be cured by including higher order QCD corrections.

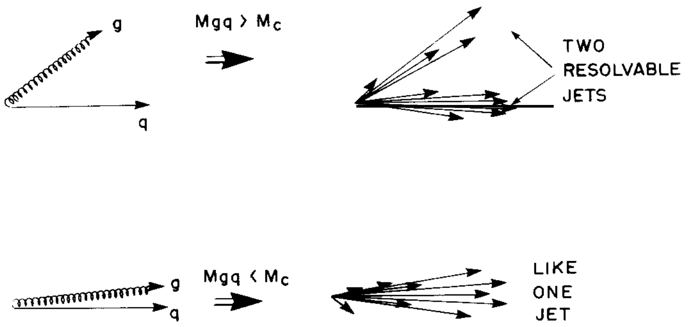

Fig. 2.1.1. Sketch of the concept of cut-off mass applied in QCD calculations. Hard gluons emitted under a large angle leading to a quark–gluon mass M_{gq} larger than M_c give rise to distinct jets. Soft or collinear gluons leading to a mass M_{gq} smaller than M_c are merged into one jet.

The introduction of the cut-off divides the hadronic events into two classes: into events originating from two partons, and those from three partons. The ratio of their particle yields is given by normalizing the event rate to the total cross section in first order QCD

$$\sigma_1 = \sigma_0(1 + \alpha_s(Q^2)/\pi) . \tag{2.1.5}$$

This cross section is finite due to the negative contribution from the interference of the 0th order quark–parton diagram with the vertex corrections (see fig. 2.1.2) which cancels the singular behaviour from the real gluon emission. This cross section is well behaved as required by the Kinoshita–Lee–Nauenberg theorem [31, 32] stating that mass singularities disappear if all degenerate initial and final states are added up.

For the implementation of the QCD bremsstrahlung into the fragmentation models, this cross section is written as an incoherent sum of the two groups of events

$$\sigma_1 = \sigma_{2\mathrm{jet}} + \sigma_{3\mathrm{jet}} . \tag{2.1.6}$$

The three-jet cross section $\sigma_{3\mathrm{jet}}$ is given by eq. (2.1.1) with bounds set by the value of y_c. The two-jet cross section $\sigma_{2\mathrm{jet}}$ is then defined by the difference

$$\sigma_{2\mathrm{jet}} = \sigma_1 - \sigma_{3\mathrm{jet}} . \tag{2.1.7}$$

Since the Monte Carlo procedures can only treat probabilities, $\sigma_{2\mathrm{jet}}$ has to be positive. Therefore $\sigma_{3\mathrm{jet}}$ is limited by σ_1 which in turn limits M_c. In particular, it follows that an energy independent M_c, although suggestive, can only be defined within a certain energy range, but not for all energies. Here again fixed order QCD corrections have been assumed.

The same rules can be applied in an extension of this formalism to higher order QCD calculations. However, the complete calculation of these corrections is a lengthy and complicated procedure. The Feynman diagrams to be considered for the complete second-order calculation are displayed in fig. 2.1.2. Until now only second order QCD corrections have been determined [21–23] and incorporated in the simulation programs. The resulting fractions of jet multiplicities depending on the c.m. energy for various cut-off parameters y_c are displayed in fig. 2.1.3a and for various values of M_c in fig. 2.1.3b. These curves were taken from the simulation program of the Lund group (see below).

Figure 2.1.3a indicates that the fraction of three-parton states decreases logarithmically with W for a cut at a constant y. This is what is expected since the three-jet cross section is proportional to α_s. The energy behaviour looks very different for a constant M_c. As discussed the fraction of multi-jet events increases with energy since the phase space is increasing. This effect can be seen for energies $W \leq 30$ GeV in fig. 2.1.3b. According to the formula for second order corrections this increase should continue. However, to keep the ratio between three- and four-jet events reasonable and to stay within the unitary limit, additional cut-offs have been implemented into the Monte Carlo, slowing down the increase and eventually letting it come to a halt. This indicates a basic deficiency of the models based on the exact QCD matrix element at energies beyond $W \sim 40$ GeV, which can only be cured by introducing higher order QCD corrections.

The various classes of events are often referred to as two-, three-, and four-jet events or $q\bar{q}$, $q\bar{q}g$, etc. events.

After the energies and directions of the on-shell partons are generated they have to be converted

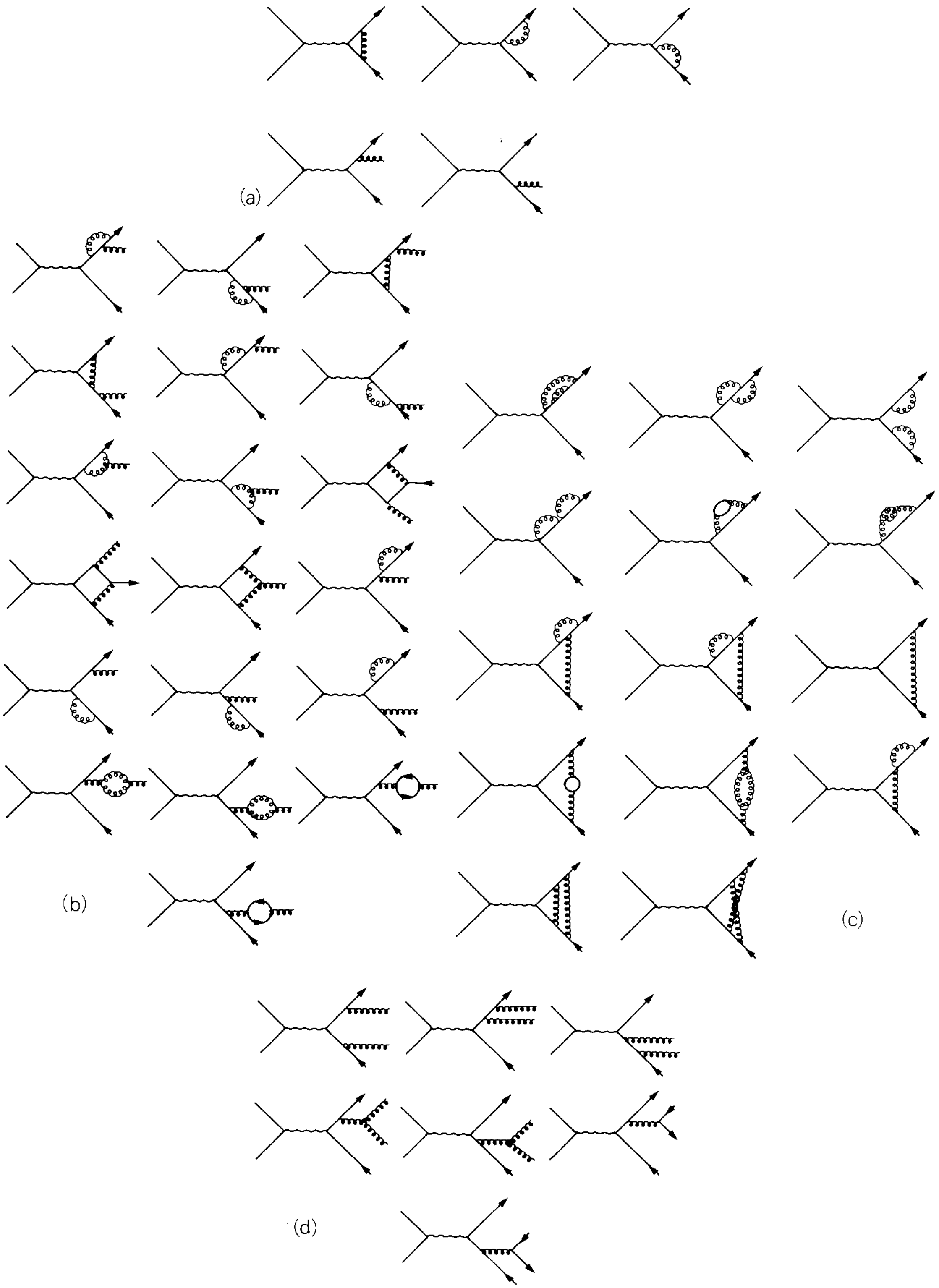

Fig. 2.1.2. (a–d) Feynman diagrams contributing up to $O(\alpha_s^2)$ corrections (from ref. [25]).

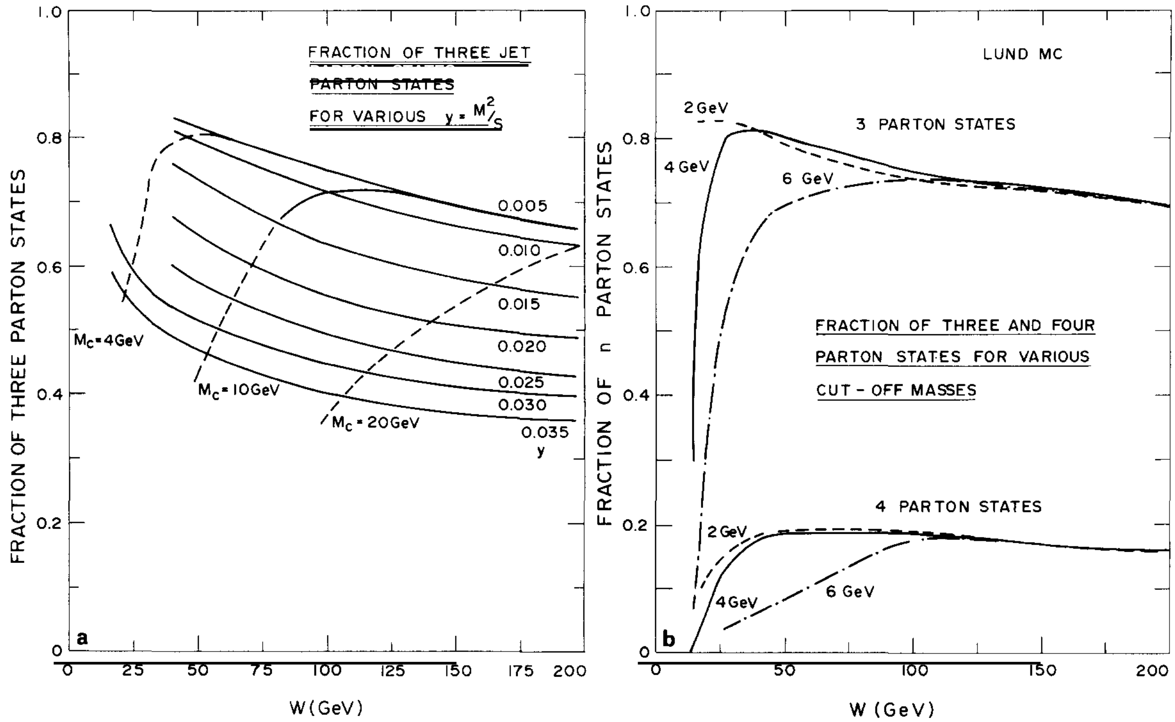

Fig. 2.1.3. Fraction of multiparton states as a function of W (calculated using the LUND–Monte Carlo). (a) Fraction of three-parton states for different values of $y_c = M_c^2/s$ and various values of M_c. (b) Fraction of three and four-parton states for various cut-off masses M_c.

into hadrons. At this stage jet development is treated within models which are more or less motivated by QCD but are by no means derived from first principles. The most frequently used models will be discussed in section 2.2.

2.1.2. *Parton distributions from the leading log approximation*

In the second important approach to the calculation of parton distributions jet development is perceived as a shower process. The primary quarks are produced off-shell and decay into virtual partons (mostly gluons) which in turn decay. With progressive branchings the partons lose virtuality until they reach a certain cut-off mass Q_0. This cut-off mass is usually chosen as being substantially below that applied to the models discussed in section 2.1.1.

Once the partons have been generated they have to be converted into hadrons. At this stage the formulae derived from the well-founded theory of QCD have to be replaced by phenomenological models. Since the ratio of prompt hadrons to partons is small, it is hoped that this hadronistion will retain the basic features of the parton distributions.

The interpretation of the jet development as a QCD shower process has been pursued by Fox and Wolfram [33], Konishi et al. [34] and Odorico and Mazzanti [35, 36]. Important contributions, in particular to the hadronisation scheme, are due to Field and Fox [37] and Gottschalk [38].

For a long time these models had substantial deficiencies and received only little consideration by experimentalists. A major break-through followed the development of the shower model by Webber and Marchesini [39, 40] which included the coherent emission of gluons predicted by [41–44] in the QCD matrix element. This modification leads to a correct description of the energy and particle flow within an event, which had turned out before to be a discrimative test of fragmentation models (see section 6.2).

The shower models are based on an only approximate treatment of QCD contributions. The matrix element is regularized by introducing off-shell partons with a limiting virtuality Q_0 and by developing the result into a sum of logarithms (see ref. [45]). In particular, the inclusive particle distribution $D(Q^2, Q_0^2, x)$ produced at Q^2 with the energy fraction x carried by each parton can be expressed*) by

$$xD(Q^2, Q_0^2, x) = \sum_{n=1}^{\infty} \left(\frac{\alpha_s}{\pi}\right)^n \sum_{p=0}^{n} \left(\log \frac{Q^2}{Q_0^2}\right)^{n-p} c_{n,p}(x) . \tag{2.1.8}$$

By summation of the leading collinear logarithms ($p = 0$) one obtains an equation that forms the basis of a recursive description of jet evolution in terms of elementary branchings q→qg, g→gg, g→q$\bar{\text{q}}$:

$$D(Q^2, Q_0^2, x) = \int_{Q_0^2}^{Q^2} \frac{dk^2}{k^2} \int_{x}^{1-\varepsilon} \left\{dz\, P(z) \frac{\alpha_s}{2\pi} \frac{F(Q^2, Q_0^2)}{F(k^2, Q_0^2)} \frac{1}{z} D\left(k^2, Q_0^2, \frac{x}{z}\right) + \delta(1-x)\right\} . \tag{2.1.9}$$

Here $\varepsilon = Q_0/Q$ and

$$F(Q^2, Q_0^2) = \exp\left\{-\int_{Q_0^2}^{Q^2} \frac{dk^2}{k^2} \int_{\varepsilon}^{1-\varepsilon} dz\, P(z) \frac{\alpha_s}{2\pi}\right\} \tag{2.1.10}$$

is the square root of the Sudakov form factor, determining the virtuality of the decay product. $P(z)$ are the splitting functions [47] for the parton branchings

$$P(z) = \frac{4}{3} \frac{1+z^2}{1-z} , \qquad \text{q}\to\text{qg} , \tag{2.1.11a}$$

$$P(z) = 2N_c\left(\frac{1}{z(1-z)} - 2 + z(1-z)\right) , \qquad \text{g}\to\text{gg} , \tag{2.1.11b}$$

$$P(z) = \frac{N_f}{2} (z^2 + (1-z)^2) , \qquad \text{g}\to\text{q}\bar{\text{q}} . \tag{2.1.11c}$$

z is the energy fraction of one of the decay products, N_c and N_f are the numbers of colours and flavours.

Formula (2.1.9) can be interpreted as giving the probability for an elementary branching process $p_1 \to p_2\, p_3$ (fig. 2.1.4). It thus forms the basis for a Monte Carlo approach to fragmentation. A parton with $Q^2 = W^2 - \boldsymbol{p}^2$ splits into two partons with $q_1^2 = W_1^2 - \boldsymbol{p}_1^2$ and $q_2^2 = W_2^2 - \boldsymbol{p}_2^2$ and energy fractions z_1 and z_2. The probability distribution for this branching is given by the kernel of eq. (2.1.9)

$$dP = \frac{dk^2}{k^2} dz \cdot P(z) \frac{\alpha_s}{2\pi} \cdot \frac{F(Q^2, Q_0^2)}{F(k^2, Q_0^2)} . \tag{2.1.10}$$

---

*) The following discussion is based on a talk of G. Marchesini [46].

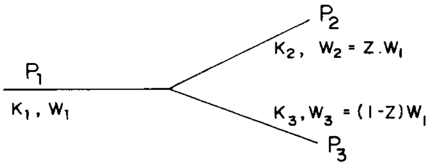

Fig. 2.1.4. Elementary branching of partons considered in shower models.

As mentioned before, interference effects modify the branching kernel. This had been realized once the infrared divergences were correctly treated in leading order. In particular, this is reflected in the emission angles of subsequent branchings: the angles decrease with a later occurrence of the branching (cf. section 3.2.3). The emission angles Θ_1, Θ_2 and Θ_3 of fig. 2.1.5 are ordered according to their sequence of production

$$\Theta_1 > \Theta_2 > \Theta_3 ,$$

where g_1 is the gluon which is radiated first, g_2 the second one, etc.

There exist several ambiguities as to how to implement the QCD shower formalism into a computer program. They refer to the definition of variables like z or Q^2 as well as to the treatment of the kinematics [48, 49].

For example, to implement the angular ordering into the Monte Carlo scheme, Marchesini and Webber express the virtuality in terms of the emission angle ξ

$$Q^2 = q_1^2 + q_2^2 + 2W_1W_2\xi , \tag{2.1.11}$$

where

$$\xi = \frac{q_1q_2}{W_1W_2} \sim (1 - \cos\theta) \tag{2.1.12}$$

if q_1^2 and q_2^2 are small. Bengtsson and Sjöstrand, however, prefer

$$Q^2 = z(1 - z)m^2 . \tag{2.1.13}$$

The latter circumvents some drawbacks of eq. (2.1.11) which for example implies that parton virtualities are not known during evolution. Some effects of different choices of variables are discussed in ref. [48].

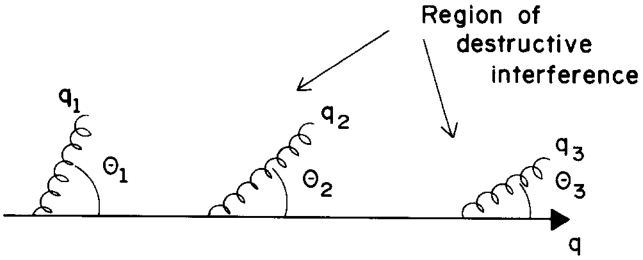

Fig. 2.1.5. Angular ordering of gluon emission.

As was pointed out in ref. [50] (see also ref. [51]), the coherence of gluon emission is only included in a correct way for azimuthally integrated distributions. There exist in addition azimuthal correlations which are not accounted for. This reflects that branchings can only be included in terms of classical probabilities and therefore do not fully account for the quantum mechanical interference effects.

QCD shower programs had some deficiencies which deprived them of a high popularity. One of them, the inconsistency between the particle flow in the data and the QCD shower algorithms, has been cured in the Webber–Marchesini scheme. More fundamental was their failure of describing topology and frequency of events with a hard gluon bremsstrahlung in a natural way. Meanwhile phenomenological ways for implementing hard QCD effects have been proposed. Klima [52] suggested to distribute the energies of the primary quarks originating from $\gamma \to q\bar{q}$ in analogy to the Altarelli–Parisi splitting function for $g \to q\bar{q}$. In another approach Bengtsson and Sjöstrand [48, 53] force the branchings to reproduce the exact first order QCD matrix element (2.1.1).

2.2. Models of hadronisation

The discussion above referred to the evaluation of the parton distribution. The jets finally consist of hadrons and recipes have to be formulated to metamorphose the partons into hadrons. Whereas the parton distribution is evaluated on the firm theoretical basis of QCD, their conversion cannot (yet) be derived from first principles since it involves a non-perturbative treatment. Its realization requires a phenomenological model.

There are essentially three hadronization models which are frequently used: the Independent Jet Model, the String Model and the Cluster Decay. Traditionally the first two are combined with the exact QCD calculations discussed in section 2.1.1, since those determine only few partons and leave much of the final hadron distribution to the fragmentation models. The cluster decays have been developed in the framework of the shower programs that lead to a small ratio of the number of hadrons over partons. These assignments are not necessary and in fact a combination of the distributions obtained from the QCD shower algorithm and the string fragmentation has turned out to be a very promising candidate for the best approach towards jets.

2.2.1. General features of the recursive hadronisation scheme

The Independent Jet Model and the String Model are both used on a recursive scheme. Some of the first recursive algorithms for jet development are those of refs. [54, 55]. Field and Feynman developed a program that became the basis for one of the main approaches to fragmentation [56]. Hadronisation proceeds in repeated steps within these schemes.

A quark q_1 with an energy E_{q_1} picks a $q_2\bar{q}_2$ pair out of the sea and melts into a meson M_1 $(q_1\bar{q}_2)$ leaving the quark q_2. The momentum of M_1 is distributed along the jet axis ("z") according to a "primordial" fragmentation function $f(\eta)$ for the longitudinal component, where η is the ratio of the light-cone variables[*)] $(E + p_z)$:

$$\eta = \frac{(E + p_z)_{M_1}}{(E + p_z)_{q_1}} . \qquad (2.2.1)$$

This leaves q_2 with the energy $E_{q2} \sim E_{q_1}(1 - \eta)$.

[*)] This variable was chosen to describe properties found in jets, especially the rapidity plateau. For large E, $\eta \to z = E_h/E_q$.

The quark q_2 is then treated as a source of a new jet independent of the previous step. The prescription applied for the first step is repeated in the subsequent one: q_2 picks a $q_3\bar{q}_3$-pair out of the vacuum to form a meson $M_2 = q_2\bar{q}_3$ leaving q_3. Its energy is given by the same probability distribution $f(\eta)$, η is now scaled with the light cone momentum of q_2: $\eta = (E+p_z)_{M_2}/(E+p_z)_{q_2}$.

Each single step in the chain is called rank; M_i is the ith rank hadron. The chain continues until all the energy is used up. The probability of finding the final particles with a fractional longitudinal momentum $z = 2E_H/W$ is then given by

$$D(z) = f(1-z) + \int_z^1 f(\eta) D\left(\frac{z}{\eta}\right) \frac{d\eta}{\eta} \tag{2.2.2}$$

and thus completely determined by the primordial function.

There exists no prediction from first principles for the shape of $D(z)$, instead it is guessed from some phenomenological ideas and constraints given by the measurements. We will list the most frequently used parametrisations.

(i) Assuming $f(\eta) = (a_1+1)\eta^{a_1}$ eq. (2.2.2) can be solved leading to

$$D(z) = \frac{a_1+1}{z}(1-z)^{a_1}\,. \tag{2.2.3}$$

This shape was for a long time used as default in the Lund program (see below). Since, the rapidity y equals dz/z, it follows that (a_1+1) particles per unit of rapidity can be found in the plateau region. For large energy fractions this fragmentation function vanishes: $D(z) \to 0$ for $z \to 1$.

(ii) Requiring $D(z)$ to approach a finite value for $z \to 1$, Field and Feynman [56] proposed $f(\eta) = 1 - a_2 + 3a_2\eta^2$ leading to a rather lengthy expression for $D(z)$ of the form

$$D(z) = (1/z)[c_1 + c_2 z^2 + c_3 z^{3-2a_2}]\,. \tag{2.2.4}$$

The constants c_i are completely determined by a_2.

(iii) The fragmentation functions (2.2.3, 2.2.4) have the conceptual disadvantage that they lead to different results depending on where the chain starts. This unattractive feature has been avoided in the formalism suggested in ref. [57]. They propose a primordial fragmentation function

$$f(\eta) \propto \frac{(1-\eta)^{a_3}}{\eta} \exp[-bm^2/\eta]\,. \tag{2.2.5}$$

If transverse momenta are also considered $m^2 \to m^2 + p_T^2$. Another free parameter b is introduced in addition to a_3. Both affect the particle distribution like the multiplicity and the rapidity ordering. An essential feature of this formula is its prediction of a mass dependence of the fragmentation function. No such dependence is conceived in the framework of the other formulas. The difference is small for the light quarks, but renders a harder fragmentation function for heavy quarks.

Additional parameters have to enter the simulation of hadron production. Each quark acquires a transverse momentum being assigned at each step according to a probability function, normally assumed to be a Gaussian

$$g(p_T) \propto \exp(-p_T^2/2\sigma_q^2)\,. \tag{2.2.6}$$

The p_T component is taken to be independent of the c.m. energy or the longitudinal momentum of the particles. As a consequence the transverse component of the prompt hadrons is given by the sum of the transverse momenta of its quark and antiquark. Assuming that the transverse momenta of subsequently produced quarks are uncorrelated, and $\boldsymbol{p}_{T,q_i} = -\boldsymbol{p}_{T,\bar{q}_i}$ it follows that

$$\langle p_T \rangle_{\text{meson}} = \sqrt{\pi}\sigma_q\,. \tag{2.2.7}$$

These assumptions about the dynamical properties of jets have to be supplemented with those about the flavour and spin of the hadrons produced.

In the chain approach outlined above, the flavour of a hadron is naturally given by the flavour of the quark/antiquark pair picked out of the sea. In a linear potential the probability for a $q\bar{q}$ pair to fluctuate out of the vacuum is given by

$$|M^2| \propto \exp(-\pi m_q^2/F)\,, \tag{2.2.8}$$

where m_q is the mass of the quark and F describes the strength of the potential. In the string model it is identified with the string constant $\kappa = 0.2\,(\mathrm{GeV}/c)^2$. Thus the probability of producing a $q\bar{q}$ pair in the sea is rapidly decreasing with the quark mass. In particular, it follows that charm and bottom quark pairs in the sea should be completely negligible and only u, d and s-quarks have to be considered.

The agreement between the data and the model is considerably improved by taking into account resonance production. This requires a parametrisation of the fraction of the various spin states produced in the primordial fragmentation. In general only pseudoscalar and vector particles are considered. The relative abundance of vector particles is parametrized by the $V/(P+V)$ ratio.

Thus four essential free parameters are implemented in the most simple models to describe hadron production. Experimental progress led to the introduction of additional parameters, e.g. to describe baryon production. They are summarized in table 2.2.1. Only vague phenomenological ideas exist for the values of these parameters. In general they have to be determined from the data. Since they frequently affect the same kind of distribution (e.g. the p_T distribution of the final hadrons is related to

Table 2.2.1
Frequently used parameters in chain models of fragmentation

Distribution	shape	typical value
longitudinal fragmentation	$f(\eta) = (a_1 + 1)\eta^{a_1}$	$a_1 = 0.5$
	$f(\eta) = 1 - a_2 + 3a_2\eta^2$	$a_2 = 0.77$
	$f(\eta) \propto \frac{(1-\eta)^{a_3}}{\eta} \exp\left(\frac{-bm^2}{\eta}\right)$	$a_3 = 1, \quad b = 0.7$
transverse momentum	$g(p_T^q) \propto \exp[-p_T^2/(2\sigma_q^2)]$	$\sigma_q = 0.3\ \mathrm{GeV}$
flavour content	$p_u : p_a : p_s : p_c$	$1 : 1 : 0.3 : 10^{-11}$
vector particles	$V/(P+V)$	0.5
baryons	p_{qq}	0.07

both σ_q and $V/(P+V)$) they are difficult to disentangle and their uncertainties are substantial. The values given are only approximate, the consistency between data and the models will be discussed below (in particular in section 4). As will be shown throughout the following discussion, these models work remarkably well and form an important guideline for the interpretation of jet development.

There exist two frequently applied approaches to recursive models. In the (historically) first one each parton fragments independently of the other partons until all its energy is used up. This type of model is named the "Independent Jet Models".

In the second approach colour neutral strings between the partons are formed which then break up to produce a hadron. Thus the partons are glued together at all times and do not fragment independently. These models are called "String Models".

2.2.2. *The Independent Jet Model*

The model of Field and Feynman [56] is the prototype of an Independent Jet Model and has been one of the most successful and frequent approaches to jets. It is based on the iterative scheme outlined above, assuming that each individual parton fragments independently (fig. 2.2.1a). The chain continues until all the energy of the parton is used up such that no hadron can be formed any more. Although the model accommodates the data in a wide range, it has some inherent problems:

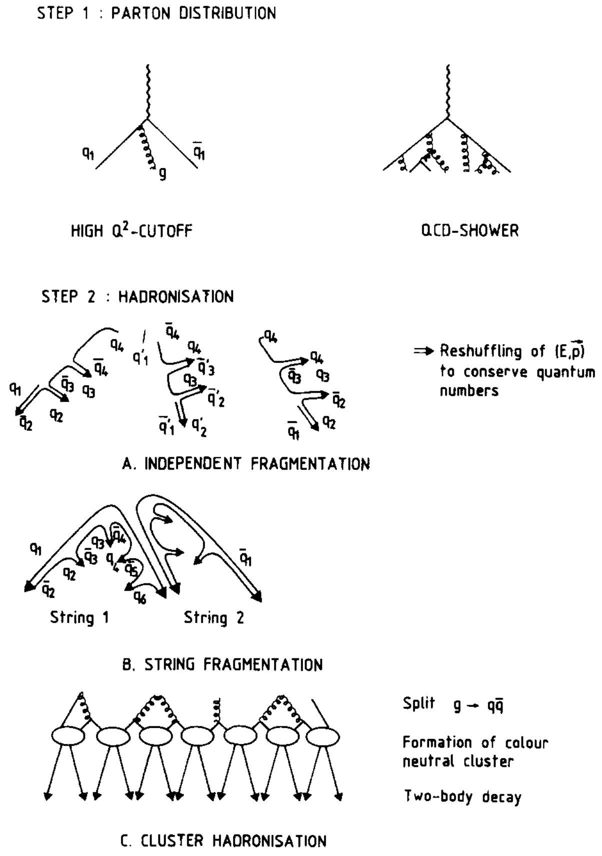

Fig. 2.2.1. Schematic view of the various models for jet development. Step 1 refers to the parton distribution, step 2 to the hadronisation. (a) Independent Jet Model. (b) String model. (c) Cluster model.

(i) The basic property of colour confinement is not even conceptually included in the model. The single parton, although being coloured, has no relation to its colour compensating partner.
(ii) The energy and momentum are not conserved. The primary partons with typical masses of 300 MeV evolve into jets with masses of 4–5 GeV.
(iii) The result is not Lorentz invariant since the fragmentation depends on the energy of the quark.

Some of these flaws can be overcome in a separate step by joining the individual jets and reshuffling energy, momentum and quantum numbers. Technically this imposes no problem. Several prescriptions exist how to redistribute energy and momentum among the particles produced, e.g., affecting only the low energy ones and thus changing the overall topology of an event only marginally. However, it seems unnatural to proceed in these two discrete steps.

Hard QCD corrections are straightforward to implement: instead of the two quarks now each of the quarks and the gluon hadronises independently. In general the gluon jet requires an additional set of free parameters: whereas the probability functions for the momentum and flavour content of the quark and the antiquark jets are the same, the gluon may fragment differently. For example, in the scheme developed by Hoyer et al. [58] the gluon is converted into a $q\bar{q}$ pair, and one of them obtains all the energy. Thus effectively the gluon fragmentation is set equal to the quark fragmentation. In the simulation program of Ali et al. [59] the quark energies are distributed according to the Altarelli–Parisi function [47]

$$f(z) \propto z^2 + (1 - z)^2 \tag{2.2.9}$$

with $z = E_q/E_g$.

2.2.3. The String Model

The string model has turned out to be the most successful and popular description of jet properties at c.m. energies around $W = 30$ GeV in recent years. After being developed for e^+e^--interactions it has been applied to jets in various types of processes like leptoproduction or hadron–hadron collisions. The string concept evolved into a large system of computer programs mainly due to the work of the Lund group [60].

In contrast to the Independent Jet Model not the individual partons fragment but a colour neutral system stretching between the partons. Hadronisation is viewed as the break up of a string built up by the colour fields of two quarks flying apart. The linearity of the Regge trajectories, the potentials of quarkonia and other measurements suggest a linear rise of the colour potential with increasing distance between the colour sources

$$\Phi = \kappa x . \tag{2.2.10}$$

κ is the string constant, $\kappa = 0.2\ \mathrm{GeV}^2$.

In e^+e^--annihilations the string is built up by the primary quarks q_1 and $\bar{q}_1$ flying apart. Classically the potential (2.2.10) would lead to an oscillation of the quark and antiquark, however, within a relativistic quantum mechanical system the potential energy can condense into the production of a flavour neutral parton pair. The string breaks up into a $q_2\bar{q}_2$-pair at the space–time $(\boldsymbol{r}_2, t_2)$ (fig. 2.2.1b). Subsequently other pairs $q_i\bar{q}_i$ at $(\boldsymbol{r}_i, t_i)$ will be produced. These quarks q_i, $\bar{q}_{i+1}$ combine to form hadrons followed by a chain of steps like those discussed before. In a two-dimensional model with space and time coordinates (x, t) the energy and momentum of the $q\bar{q}$ system are given by

$$E(q_1, \bar{q}_2) = \kappa(x_2 - x_1) , \tag{2.2.11a}$$

$$p(q_1, \bar{q}_2) = \kappa(t_2 - t_1) . \tag{2.2.11b}$$

Imposing the constraint that the quark and antiquark form a system with mass m, the points of hadronisation must lie on a hyperbola in space–time

$$(x_2 - x_1)^2 - (t_2 - t_1)^2 = m^2/\kappa^2 . \tag{2.2.12}$$

Compared to the Independent Jet Model the string approach has some attractive features.

(i) Although not calculable from the fundamental theory its basic assumptions agree better with the general ideas of QCD and quark and gluon couplings.

(ii) Energy, momentum and flavour are conserved at each step of the fragmentation process. This conservation is more easily included in the string scheme since at each step the whole massive system is considered whereas in the Independent Jet Model only part of it is treated. Only the last step requires a special procedure for conserving energy and momentum to ensure that the particles acquire the correct mass.

(iii) Related to this is the smooth joining of the two jets. Whereas in the Independent Jet Model energy, momentum and flavour of each jet do not conspire to fulfill the conservation laws at the end of the fragmentation, they are naturally conserved in the Lund scheme. Thus no artificial procedure has to be applied to join these last partons to form a hadron.

In spite of the conceptual differences of the two approaches they lead to very similar results for events of the type $e^+e^- \to q\bar{q}$, since the parameters can be properly adjusted in both algorithms.

The two approaches exhibit a fundamental difference in treating hard gluon emission and predict different properties in three-jet events. Within the string model the gluon is interpreted as a transverse excitation of the colour field between the quark and the antiquark. Basically the gluon is split up into two parts inducing two strings being formed by the quark and a part of the gluon and by the antiquark and the other part of the gluon, respectively. These strings fragment in the usual way. This procedure avoids the introduction of new parameters, since the gluon jet is in the first approximation interpreted as the overlap of two $q\bar{q}$-strings. This different treatment of the gluon is reflected in different predictions for the particle and energy flow by the two approaches and allows one to make a discriminative test with the data (see section 6.2).

To apply string fragmentation in the case of higher parton multiplicities one has to develop prescriptions as to which partons form a common string. These problems become especially relevant when strings supplement the shower algorithm. Procedures have been developed in ref. [61].

2.2.4. *The Cluster Model*

The Cluster Model has been proposed by Wolfram [62] as the hadronisation mechanism for the shower approach. Since only two primary hadrons are produced in a cluster decay, no recursive scheme is needed (fig. 2.2.1c). The hadronisation of the generated quarks and gluons proceeds in three steps. At first each of the final gluons is split into a quark–antiquark pair. These are then combined into colour singlet clusters formed by "colour connected" $q\bar{q}$ pairs. As a result they come out to have a low, Q^2 independent mass such that their distributions resemble those of the partons very closely. A typical distribution of the cluster mass as generated in the Webber–Monte Carlo is shown in fig. 2.2.2. These prescriptions are in agreement with the idea of preconfinement [63] or the local parton–hadron duality [64].

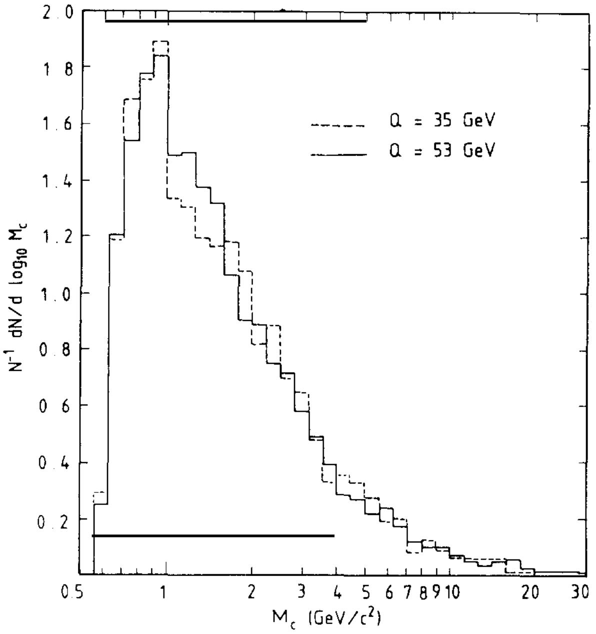

Fig. 2.2.2. Distribution of cluster masses formed in a QCD shower model at two different energies [39].

In a third step these clusters decay. In the most simple approach they decay according to two-body phase space and spin degeneracy into two known resonances. Since the clusters are assumed unpolarized, they decay isotropically. Due to their low mass O(1 GeV) their descendents are found relatively closely together in momentum space.

This scheme of hadronisation leaves the distribution of final particles rather unchanged from that of partons. It attempts to minimize the number of ad hoc assumptions by avoiding parameters like the fraction of $s\bar{s}$ pairs in the sea, the probability for diquark pairs or the ratio of pseudoscalar to vector particles which are necessary in the String and the Independent Jet Model.

As will be discussed later, this model is too simple to describe the hadron distribution in full detail. Its deficiencies are for example the high-x region of the fragmentation function (section 3.2.2) and the angular distribution of $p\bar{p}$ pairs (section 8.3) indicating that the most simple phase space decay has to be modified.

To this end string fragmentation replaces the cluster decays in more recent approaches. This complicates the fragmentation pattern and deprives the shower approach of some of its simplicity since now again one has to worry about the various uncalculable parameters listed in table 2.2.1. It allows an increased flexibility and a comparison to the data indicates that it accommodates the measurements very well [65]. The deficiencies of the pure phase space decay are overcome in such an approach.

2.3. General remarks

The models discussed and their materialization in computer algorithms have turned out to be essential tools for disentangling the properties of jets. Since the jets measured in e^+e^- annihilations are a complicated mixture of different kinds of configurations of hard partons, different flavours, probabilistic distributions of hadrons, kinematical effects like decays and finally interactions in the detector, they are ideal for a simulation with the Monte Carlo technique. Such an approach helps in discriminating between the various stages of jet development and is unique for addressing specific questions.

These models require several free parameters in the hadronisation stage for steering the type and kinematic properties of the hadrons produced. The number is especially large for the models which use a high Q^2 cut-off since phenomenology has to replace explicit QCD matrix elements at an early stage. When the theoretical calculations are applied to low Q^2 as in some shower algorithms, the parton distribution approaches the final hadron distribution rather closely. In such a case one hopes to get along with a smaller number of parameters. Still, how partons turn into hadrons is a completely unsettled question in both approaches.

The uncertainties about hadronisation limit what can be learned from the simulations. In the course of their application, conclusions have been drawn, which turned out to be of only limited validity. The most prominent example is the determination of the strong coupling constant α_s from event topologies which differs by $\sim 50\%$ depending on whether the data are compared to the Independent Jet Model or to the String Model [66]. This indicates potential pitfalls which have to be carefully avoided when trying to derive absolute conclusions about the hadronisation process.

With increasing availability of experimental data one can hope that the shapes of the probability functions used in the Monte Carlo and the values of the corresponding parameters will be known more and more precisely, placing the interpretations on firmer grounds.

Two approaches based on QCD algorithms have been discussed in the previous sections. In their extreme versions these approaches differ conceptually as to how the parton distribution is calculated. In the first one high cut-off masses are applied to the exact QCD matrix element. Corrections have only been determined up to order α_s^2 seeming to be just enough for c.m. energies around $W \sim 30$ GeV (see section 3.2 and section 9). There are indications that higher orders have to be included at higher energies. Their exact calculation, however, is an enormous task and little hope exists for a solution in the near future. The other QCD approach works in a logarithmic approximation of the QCD formulas and assumes non-perturbative effects only to be relevant at very low masses ~ 1 GeV. It therefore presumes that a large number of partons can be determined. Although the QCD matrix elements used there are only approximations, it seems to be the only possible way to accommodate the higher jet multiplicities expected at higher energies.

As will be shown at various places in this article, according to today's insight into the Q^2 dependence of the structure of hadronic events, the merging of the perturbative QCD shower approach with a non-perturbative fragmentation scheme as supplied by the string algorithm is the most promising way to proceed further.

PART I. INCLUSIVE PARTICLE SPECTRA AND EVENT TOPOLOGIES

In this part we present a general overview of the appearance of jets. The inclusive single particle and event shape distributions will be discussed both for a fixed energy and as a function of energy. We will start from a most inclusive picture summing over all particle species, proceed with the measurements of identified particles and finish this part by summarizing the features of jets of identified flavour.

The distributions discussed put rigid constraints on any model of fragmentation. They form the basis for extracting properties like energy and direction of partons from the jets. Insight into the processes inside the hadronisation region is provided both by the production yields of hadrons as well as the Q^2 dependence of jet properties.

3. Inclusive particle spectra in jets

The most easily accessible information on jets is obtained by considering all final particles and events. The outcome is a mixture of various types of particles, decay products and promptly produced hadrons, events originating from quarks of different flavour and events of various parton multiplicities. In total the resulting distributions have a complicated pattern of kinematical and dynamical effects that has to be taken into account before drawing conclusions on jet dynamics. Still, they provide a basic and, as will be seen later, a representative picture of global jet properties.

In this section the overall jet properties as reflected in the distributions of stable charged particles[*] will be discussed. They are easy to measure and since the spectra of charged and neutral particles coincide they provide a representative view of the jet properties.

3.1. *Multiplicity*

3.1.1. *Average charged multiplicity*

A compilation of the average charged multiplicities measured at different energies and by different detectors is shown in fig. 3.1.1. The data show that the pure logarithmic rise

$$\langle n_{\mathrm{CH}} \rangle = a + b \ln s \,, \tag{3.1.1}$$

which provides a very good description for energies $W \leq 9$ GeV [67, 68], underestimates the multiplicity

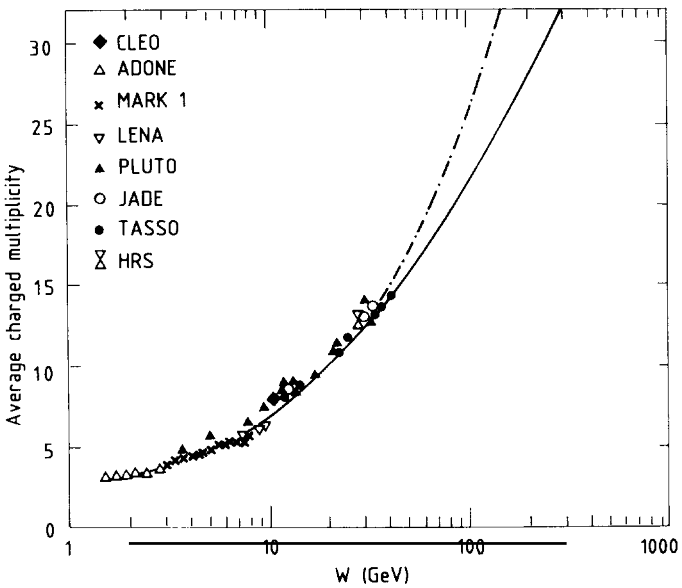

Fig. 3.1.1. Average charged multiplicity as a function of the c.m. energies. The compilation is taken from ref. [3] and supplemented by results from ref. [96]. The curves are results from a fit to the measurements using parametrisations discussed in the text.

---

[*] In most experiments the following convention is applied: particles with a lifetime of $\tau > 3 \times 10^{-10}$ s are considered as stable. That is, the K_S^0 and Λ are assumed to have decayed, and their decay products contribute to the particle spectrum whereas charged particles from K_L^0-decays are not included.

observed at higher energies $W \sim 30\,\mathrm{GeV}$. With the values of $a = 2.1$ and $b = 0.84$ derived from the MARKI data, eq. (3.1.1) gives $\langle n_{\mathrm{CH}} \rangle = 8$ at $W = 34\,\mathrm{GeV}$, a value almost only half of the average multiplicity observed at this energy.

Such a simple logarithmic dependence as given in eq. (3.1.1) is expected e.g. from longitudinal phase space (e.g. ref. [69]) and in fragmentation models without hard QCD effects. Its failure can therefore be taken as evidence that jets do not develop along these simple terms. Although such a dependence is not appropriate for the whole energy range displayed, it gives a fair local description of the data in the intervals $W \leq 10\,\mathrm{GeV}$ and $W \geq 10\,\mathrm{GeV}$ separately. To divide the total range in these two intervals, however, is bare of any physics motivation*⁾.

Instead the energy dependence of the average multiplicity in the total range can be described by various other parametrisations (the fit results are taken from ref. [3]):

(a) A parametrisation successfully applied to the multiplicities measured in pp-collisions [70] is

$$\langle n_{\mathrm{CH}} \rangle = a + b \ln s + c \ln^2 s \,. \tag{3.1.2}$$

A fit to the e^+e^--data yields $a = 3.33 \pm 0.11$, $b = -0.40 \pm 0.08$, $c = 0.26 \pm 0.01$. Its result is indicated by the solid line in fig. 3.1.1.

(b) A power law is predicted from phase space:

$$\langle n_{\mathrm{CH}} \rangle = a\, s^{1/4} \,. \tag{3.1.3}$$

The measurements can be described with $a = 2.18 \pm 0.01$. However, it should be noted that a phase space model in general does not reproduce the jet properties at higher c.m. energies.

(c) QCD calculations interpreting jet evolution as a branching process predict a rapid exponential increase [71–74]

$$\langle n_{\mathrm{CH}} \rangle = a + b \exp\{c \cdot (\ln[s/Q_0^2])^{1/2}\} \,. \tag{3.1.4}$$

With $Q_0 = 1\,\mathrm{GeV}$ this function accommodates the measurements for $a = 2.71 \pm 0.08$, $b = 0.058 \pm 0.010$, $c = 1.97 \pm 0.06$. The result is displayed by the dashed–dotted line in fig. 3.1.1.

All these parametrisations describe the measurements reasonably well**⁾. None of them can be ruled out from the energy dependence of the average multiplicity.

3.1.2. Multiplicity distributions

The multiplicity distributions at a fixed energy as well as their energy dependence has provoked a substantial amount of discussion (see e.g. the review of Carruthers and Shih [75]). The most popular parametrisations and predictions are the Poisson distribution, KNO scaling and negative binomials.

Poisson distribution. The Poisson distribution is one of the most straightforward distributions considered. It follows from a completely incoherent emission of particles and can only be valid if no

---

*⁾ Note that the passing of the b-threshold cannot significantly affect the multiplicity since the bottom pair production $e^+e^- \to b\bar{b}$ contributes only ~9% to the whole event rate.

**⁾ We refrain from giving the χ^2 of the fits. They are only meaningful if the complete errors and their correlations would be well known. This is not the case, in particular for the data at low energies <7 GeV.

constraints like conservation laws affect the particle production considerably. A Poisson distribution is e.g. expected in longitudinal phase space models (e.g. [69]).

In fig. 3.1.2, the charged multiplicity distributions for the three different energies $W = 14$, 22 and 34 GeV are compared to two types of Poisson distributions. The dashed curves represent

$$N(n) = 2 \cdot (\lambda^n/n!)\, e^{-\lambda} \tag{3.1.5}$$

with $n = n_{\mathrm{CH}}$ and $\lambda = \langle n_{\mathrm{CH}} \rangle$, the average charged multiplicity. This distribution is narrower than the data. This discrepancy becomes more pronounced with energy. Deviations from this shape are expected since charge conservation implies an equal number of positive and negative particles thereby introducing some coherence. A more meaningful parametrisation is

$$N(n) = \frac{(\lambda/2)^{n/2}\, e^{-\lambda/2}}{(n/2)!} \,. \tag{3.1.6}$$

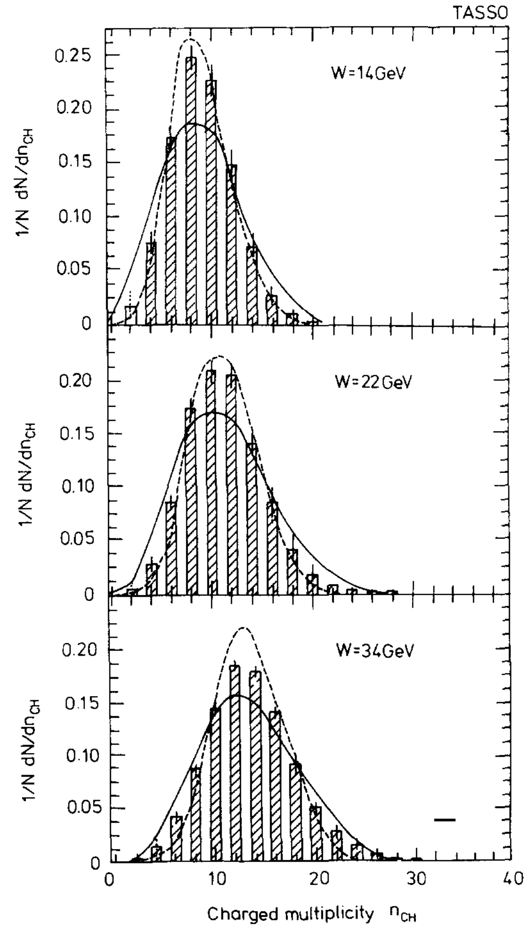

Fig. 3.1.2. Charged multiplicity distributions at $W = 14$, 22 and 34 GeV. The lines drawn correspond to Poisson distributions. The dashed line was calculated for all particles, the full line for particles of only one charge [3].

This distribution is shown by the full line. It is seen to be broader than the data, better agreement can be found with increasing energy. The deviation from a Poisson distribution indicates that the particle production in a jet is not uncorrelated. As was pointed out in ref. [76] a possible reason for this is that energy and momentum conservation still influence the shape of the multiplicity distribution.

The energy variation of the multiplicity distribution can be studied by considering its moments. Frequently used is the dispersion

$$D = (\langle n^2 \rangle - \lambda^2)^{1/2} . \tag{3.1.7}$$

As can be seen in fig. 3.1.3 the measured ratio λ/D is about 3 and almost independent of energy. An exception is the measurement of the HRS collaboration who find a ratio of 3.51 ± 0.18 [70] which is $\sim 3\sigma$ above the values determined by the other experiments. For a Poisson distribution D is given by

$$D = \sqrt{\lambda} \rightarrow \lambda/D = \sqrt{\lambda} . \tag{3.1.8}$$

Since the average multiplicity increases with energy, the ratio λ/D should do the same for a Poisson distribution. Again the two alternative schemes can be analysed. If all particles are considered (dashed line) the observed ratio at $W = 34$ GeV is substantially larger than the expectation. If only a particular sign of the charge is considered*) the prediction approaches the measured value from below. Again the result obtained by the HRS collaboration digresses from this trend. They find $\lambda/D = 3.51$ and $\sqrt{\lambda} = 3.59$ in perfect agreement with the expectation from a Poisson distribution. Since their measurement is restricted to one energy, nothing can be inferred on the energy variation of the dispersion from their data.

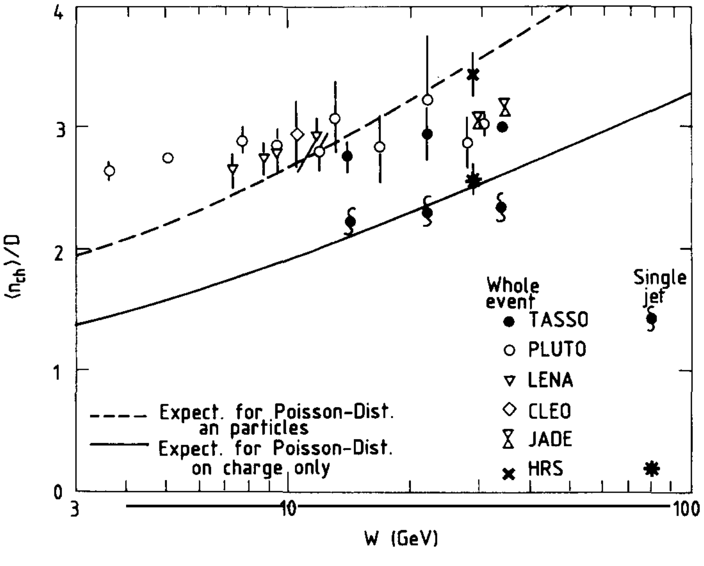

Fig. 3.1.3. Ratio of λ/D of the multiplicity distributions in e^+e^- annihilations. Compilation taken from ref. [3] and supplemented by ref. [77]. The dashed (solid) line indicates the expectation from a Poisson distribution taking into account all (only particles of one charge). Also shown are the measurements for a single event hemisphere.

---

*) Note that $D_{\text{all}} = 2D_{\pm}$; $\lambda_{\text{all}} = 2\lambda_{\pm}$, implies $(D/\lambda)_{\text{all}} = (D/\lambda)_{\pm}$. Here "all" denotes all particles, "±" only particles of one charge sign.

KNO scaling. A non-Poissonian behaviour was anticipated by Koba et al. [78]. Assuming Feynman scaling, i.e. perceiving that the momentum distribution of the particles follows a function $f(x_\parallel)$, $x_\parallel = 2p_\parallel/W$, which is independent of W,

$$f(x_\parallel, W) \rightarrow f(x_i)\,, \tag{3.1.9}$$

they derived for $s \rightarrow \infty$ that the multiplicity distribution can also be parametrised in an energy independent way

$$\lambda P_n = F(n/\lambda)\,. \tag{3.1.10}$$

Here $P_n = (1/N)(\mathrm{d}N/\mathrm{d}n)$ is the probability that an event has a multiplicity n. The data obtained in pp and p$\bar{\mathrm{p}}$ collisions are found to approximately follow KNO scaling for $\sqrt{s}$ between 23 and 63 GeV [70]. The data from the Sp$\bar{\mathrm{p}}$S collider between $\sqrt{s} = 540$ and 900 GeV, however, show deviations from a scaling behaviour [79].

Figure 3.1.4 shows the multiplicity distribution measured in $\mathrm{e}^+\mathrm{e}^-$ annihilations in terms of the KNO variables $z = n/\lambda$ and $P_n\lambda$ for energies between 5 and 34 GeV from PLUTO [80], LENA [81] and TASSO [3]. The data indicate KNO scaling to hold within ~20%. Data by the JADE collaboration [82] are in good agreement with these results (not shown). The measurement by the HRS collaboration at $W = 29$ GeV [83] shows a somewhat narrower distribution, which, as the authors state, is consistent with the data of fig. 3.1.4 within statistical and systematic errors. With the exception of low values of z the HRS collaboration can describe their data well with

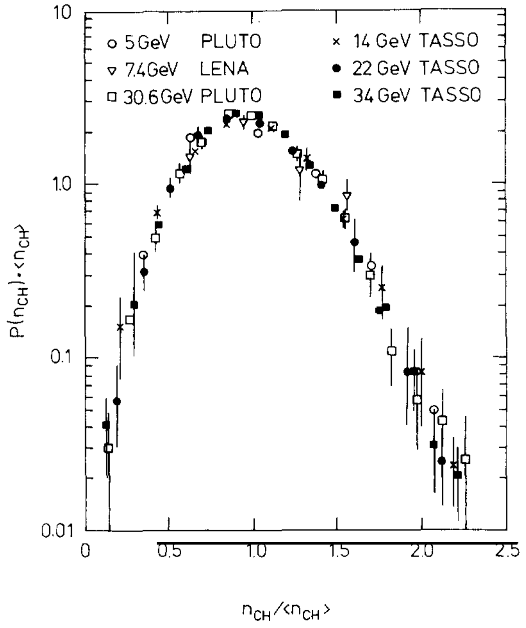

Fig. 3.1.4. Multiplicity distribution measured in $\mathrm{e}^+\mathrm{e}^-$ annihilations in terms of the KNO variables $P(n_{\mathrm{CH}}) \cdot \langle n_{\mathrm{CH}} \rangle$ versus $n_{\mathrm{CH}}/\langle n_{\mathrm{CH}} \rangle$ (compilation from ref. [3]).

$$F(z) = \frac{k^k}{(k-1)!} z^{k-1} \exp(-kz) \tag{3.1.11}$$

with k obtained by a fit as $k = 12.3$.

In contrast to the Poisson distribution KNO scaling implies that λ/D is independent of the energy. Taken at face value the data indicate a gentle rise of ~10% between $W = 5$ GeV and $W = 34$ GeV. However, since the statistical and systematic errors are of the order 7–10% this rise is not significant. The data show no evidence for a violation of KNO scaling.

As will be discussed in section 3.2, Feynman scaling is broken in the energy range considered invalidating the original basic assumption for KNO scaling. In this light the rather small (if any) energy dependence of the KNO distribution is surprising. Bowler and Burrows [84] simulated the multiplicity distributions using the Lund Monte Carlo distribution and found that within this scheme they are quite well described. Within their studies the apparent KNO scaling is due to the conspiracy of several effects like energy conservation, passing of the b-threshold and scale breaking due to gluon emission. KNO scaling in e^+e^- collisions therefore seems more an accidental property than to be related to the fundamental dynamics. We note in addition that KNO scaling can also be reproduced by the QCD shower Monte Carlo of Webber.

Both the TASSO and the HRS collaborations have also studied the multiplicity distribution within a single hemisphere. To this end the hadronic events were divided into two hemispheres with respect to the sphericity axis and the multiplicity distribution determined for the two hemispheres separately. As for the total event KNO scaling holds approximately also for the single jet. The ratio λ/D for single jets is shown in fig. 3.1.3. The data are consistent with a constant of ~2.3. The ratio $(\lambda/D)_{\text{event}}/(\lambda/D)_{\text{jet}}$ is measured as about 1.3 and 1.41 by the TASSO and HRS collaboration respectively. Both values are very close to $\sqrt{2}$, indicating that the multiplicities of the two jets are uncorrelated. Further and more direct evidence for this property will be discussed in more detail in section 7.1.

Negative binomial distribution. After the discovery of the violation of KNO scaling in $p\bar{p}$-collisions much attention has been paid to the negative binomial distribution. It was originally developed assuming that the particles originate from k independent cells. The particles are emitted according to Bose–Einstein statistics with an equal a priori probability in each cell. The multiplicity distribution is [85, 86]

$$P_n^{\text{BE}} = \frac{(n+k-1)!}{n!(k-1)!} \left(\frac{\lambda/k}{1+\lambda/k}\right)^n \frac{1}{(1+\lambda/k)^k} . \tag{3.1.12}$$

This function approaches the Poisson distribution for $k \to \infty$. Its width is given by

$$\frac{D^2}{\lambda^2} = \frac{1}{\lambda} + \frac{1}{k} . \tag{3.1.13}$$

Note that for $k \to \infty$, eq. (3.1.13) is identical to (3.1.8) for the Poisson distribution. For $\lambda/k \gg 1$ the function P_n^{BE} depends only on $z = n/\lambda$ and approaches eq. (3.1.11).

Several interpretations of negative binomial distributions for multiparticle production exist. In ref. [87] it was pointed out that it can be interpreted as being either due to a stimulated emission (like a laser) or to a cascading process. In the former approach the stimulation occurs in k cells, in the latter approach k^{-1} is the ratio of the probability for two particles originating from common cells to the probability that they originate from two different cells. For both interpretations the emissions are assumed to occur independently in each cell.

The negative binomial has been successfully applied to multiplicity distributions in $p\bar{p}$ collisions [88] and later π^+p [89]. It has been used by the HRS collaboration to describe their data obtained in e^+e^- collisions. Keeping in mind that their multiplicity distribution at $W = 29$ GeV is very Poisson-like (see above), it is not surprising that they find a very good agreement between data and the negative binomial. Their data gives a high value of $k = 259$ [90]. Fits to the data published by the TASSO collaboration give $k = 62$, 44 and 35 for $W = 14$, 22 and 34 GeV [91]. These values of k are substantially larger than the total multiplicity, thus it is difficult to interpret these values as the number of emitting cells. Plotting the energy dependence of $1/k$ as a function of the c.m. energy, one finds it to grow with $\ln s$. It starts with a negative value and crosses zero (i.e. $k \to \infty$, as expected for a Poisson distribution) around $W \sim 25$ GeV [92].

Whereas in general the emission is assumed to occur incoherently in the cells, Carruthers and Shih [93] propose an additional coherent contribution to the emission from k cells expressed by a "signal to noise" ratio m. This model describes the data with a small number of cells $k = 2$ and m rising from ~0.1 to ~0.2 for an increase of W from 12 to 34 GeV. The additional contribution broadens the distributions and its increase leads to an approximate scaling behaviour in the KNO variables. It is suggestive to identify this value of k with the number of jets and the more prominent coherent contribution at higher energies as being due to the emission of a third hard parton. No prediction for m, however, is possible within this formalism.

From hadronic interactions ([89], see also ref. [87]) the interpretation of a cascading process is preferred. The stimulated emission according to the Bose–Einstein statistics would imply that the number of cells k_- for the multiplicity distributions of the particles of only one charge would be $k_- \sim \frac{1}{2}k$, k being the equivalent number for all charged particles. This is in contradiction to the measurements*).

Multiplicity distributions in rapidity intervals. The various models for the multiplicity distribution have also been analysed by considering only particles in restricted intervals of the rapidity

$$y = 0.5 \ln\left(\frac{E + p_\parallel}{E - p_\parallel}\right).$$

As was pointed out (e.g. ref. [76]), the shape of the multiplicity in the central region should be less distorted by energy and momentum conservation. Therefore a broader distribution for smaller intervals of rapidity is expected.

The HRS group studied the multiplicity distributions in intervals $-y_0 < y < y_0$, where y_0 varied from 0.1 to 2.5 [94] and indeed found the distribution to broaden with decreasing y_0. KNO scaling does not hold for the different y_0-intervals. The distributions are well described with a negative binomial. The parameter k increases strongly with y_0 from $k \sim 5$ for $y_0 = 0.1$ to $k \sim 25$ for $y_0 = 4$.

The multiplicity in rapidity intervals of $\Delta y = 1$ has been analysed in ref. [95]. The data from the TASSO collaboration have been compared to the prediction from the LUND simulation in the rapidity plateau for $0 < y < 1$, $1 < y < 2$ and $2 < y < 3$. Without hard gluon bremsstrahlung the Monte Carlo

---

*) I am grateful to W. Kittel for pointing this out to me.

calculations exhibit the same shape of the multiplicity for all intervals and energies of $W = 14$, 22 and 34 GeV. Gluon emission leads to a significant tail at large multiplicities $n \gg \lambda$ for $W = 34$ GeV in the interval $0 < y < 1$. Such a tail is also visible in the data.

3.2. Momentum distribution

3.2.1. Energy dependence of the average momentum

The average momenta of the final charged particles are displayed in fig. 3.2.1 [3, 96, 65] as a function of W together with the prediction from a QCD model. In the energy range considered, the increase of the average momentum is approximately linear and can be parametrised by

$$\langle p \rangle (W) = 0.51 + 0.028 \cdot W . \tag{3.2.1}$$

Since the average multiplicity is known to rise with energy this equation can only be correct in a limited W-range. The average momentum should increase slower than perceived from eq. (3.2.1).

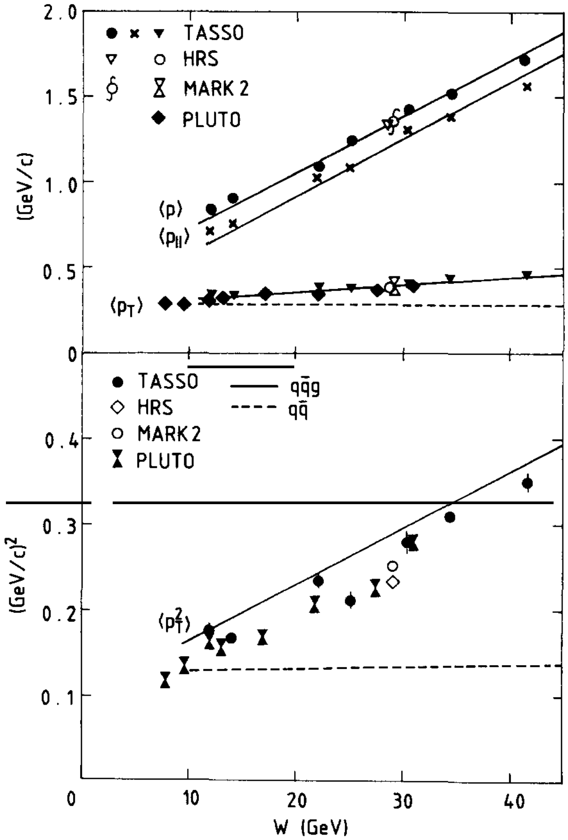

Fig. 3.2.1. Average momentum components as a function of the c.m. energy W [3, 65, 96, 105]. (top:) Total momentum and parallel and transverse component with respect to the jet axis. (bottom:) Squared transverse momentum. The measurements are compared to model calculations: full line including QCD effects, dashed line just for $q\bar{q}$ pair production.

3.2.2. x-Distribution

A simple pattern of the energy variation of the momentum distribution evolves in particular when the particle energies are scaled with the total c.m. energy $x = 2E_h/W$. The use of this variable was suggested by Feynman [97]. It obeys the normalisation

$$\int D(x)x \, dx = 2 , \quad \text{and} \quad \int D(x)x^0 \, dx = n .$$

Here n is the multiplicity. In the quark–parton model the inclusive cross section $e^+e^- \to h + X$ is described by

$$\frac{1}{\sigma_{\text{tot}}} \frac{d\sigma}{dx} = \frac{1}{\sum e_q^2} \cdot \sum e_q^2 \cdot [D_q^h(x, s) + D_{\bar{q}}^h(x, s)] . \tag{3.2.2}$$

Here the sum refers to all types of quarks that can be produced at a c.m. energy $\sqrt{s}$ and e_q is the charge of the quark q. $D_q^h(x, s)$ describes the way the quark breaks up ("fragments") into the final hadrons and is called fragmentation function. It is the probability of a hadron h acquires the scaled energy x from a primary quark q. In general D depends on the kind of primary quark, the type of hadron and s.

Hadron production in e^+e^- annihilation can be expressed in analogy to spacelike lepton–nucleon scattering in terms of the structure functions F_1 and F_2. The differential cross section as calculated by Drell et al. [98] is

$$\frac{d^2\sigma}{dx \, d\cos\theta} = \tfrac{3}{4}\sigma_0 x\beta\left[2F_1(x, s) + \frac{x \cdot \beta}{2} F_2(x, s) \sin^2\theta\right] . \tag{3.2.3}$$

σ_0 is the zeroth order QED cross section. F_1 and F_2 can be expressed in terms of the longitudinal and transverse structure function

$$F_T(x, s) = 2F_1(x, s) , \tag{3.2.4a}$$

$$F_L(x, s) = 2F_1(x, s) + xF_2(x, s) . \tag{3.2.4b}$$

such that in the relativistic limit

$$\frac{d^2\sigma}{dx \, d\cos\theta} = \tfrac{3}{4}\sigma_0 x[F_T(1 + \cos^2\theta) + \tfrac{1}{2}F_L \sin^2\theta] . \tag{3.2.5}$$

In analogy to the scaling behaviour observed in spacelike scattering, which is considered as some of the most convincing evidence for the existence of partons, Drell et al. assumed F_1 and F_2 and therefore F_L and F_T to scale:

$$F(x, s) = F(x) \quad \text{for } s \to \infty .$$

Within the quark–parton model the photon couples to a spin-$\frac{1}{2}$ parton and thus

$$F_L(x) = 0 , \tag{3.2.6a}$$

$$xF_T(x) = 3 \cdot \sum e_q^2 \cdot [D_q(x) + D_{\bar{q}}(x)] \tag{3.2.6b}$$

Therefore the scaling hypothesis implies the fragmentation functions D are independent of the c.m. energy W.

These formulas do not hold within the framework of QCD. Gluon radiation causes a violation of the scaling property and contributes to the longitudinal structure function. Again both these modifications are in analogy to deep inelastic spacelike scattering. Qualitatively they are easy to understand. The emission of a gluon reduces the energy of the quark from E_q to $E_{q'}$. Its hadronic descendents are distributed according to a function scaling in $x' = E_h/E_{q'}$ instead of $x = E_h/E_q$ and thus acquire a momentum which is reduced compared to the quark–parton prediction (see fig. 3.2.2). Therefore QCD scale breaking should lead to an increase of the particle yield at small x but a decrease at high x for increasing c.m. energy. In addition, gluon effects modify the angular momentum properties of the parton configuration giving rise to a longitudinal component F_L.

The change of the quark fragmentation function with Q^2 is given in leading logarithmic expansion by [99, 100]

$$D_q^h(x_h, Q^2) = D_q^h(x_h, Q_0^2) + \frac{\alpha_s(Q^2)}{2\pi} \left\{ \int_{x_h}^{1} \frac{dx}{x} \left[P_{qq}\left(\frac{x_h}{x}\right) \cdot \ln \frac{Q^2}{Q_0^2} \cdot D_q^h(x_h, Q_0^2) \right. \right.$$
$$\left. \left. + P_{gq}\left(\frac{x_h}{x}\right) \cdot \ln \frac{Q^2}{Q_0^2} \cdot D_g^h(x_h, Q_0^2) \right] \right\} . \tag{3.2.7}$$

Here P_{qq} and P_{gq} are the Altarelli–Parisi splitting functions determining the energy spectrum of a quark and a gluon from a quark decay (see eq. 2.1.11). $D_q^h(x_h, Q_0^2)$ and $D_g^h(x_h, Q_0^2)$ are the fragmentation functions of the quark and gluon at Q_0^2. These functions cannot be calculated from the basic theory but instead have to be determined from the data. Equation (3.2.7) then predicts their evolution with Q^2.

In the formulas given above, x is considered the scaled energy. A precise test of scaling or the predicted QCD behaviour therefore requires particle identification. Data exist and will be discussed in section 4. Their accuracy is limited due to additional experimental requirements. However, for large enough c.m. energies and momenta the following relations hold:

$$x_E = \frac{2E}{\sqrt{s}} \sim x_p = \frac{2p}{\sqrt{s}} \sim x_\parallel = \frac{2p_\parallel}{\sqrt{s}} . \tag{3.2.8}$$

Thus the scaling property of the fragmentation function should reveal itself in data without particle identification.

Figure 3.2.3 shows the results from two different experiments. The data are in very good agreement

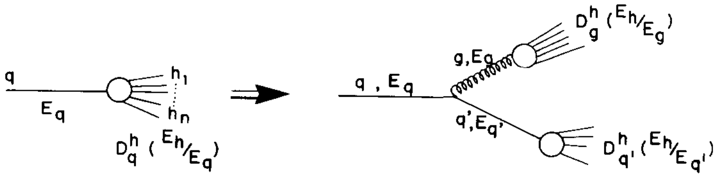

Fig. 3.2.2. Schematic view of scaling violations of the fragmentation function due to gluon emission.

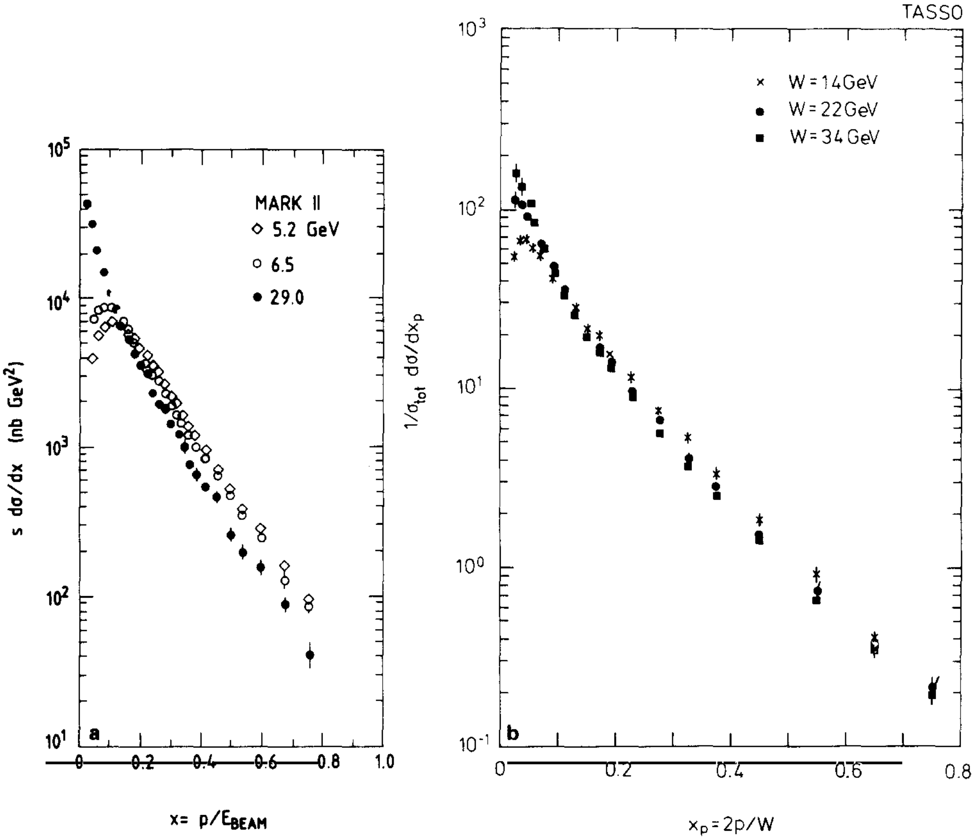

Fig. 3.2.3. Measured fragmentation functions at various energies in terms of $x_p = 2p/W$. (a) From MARK2 [101]. (b) From TASSO [3].

with one another. The data from the MARK2 collaboration [101] cover a large energy range ($5 < \sqrt{s} < 29$ GeV, fig. 3.2.3a). However, since mass and p_T effects are important for their low energy data, the assumption of eq. (3.2.8) is not valid. Additional distortions are due to the crossing of the *b*-threshold. The data from the TASSO group [102, 3] are above the *b*-threshold, however, cover a smaller range in energy (fig. 3.2.3b). Similar results have been obtained by the JADE collaboration [82].

The measurements show a steeply falling fragmentation function decreasing by three orders of magnitude between $x_p \sim 0$ and 0.8. With respect to the energy dependence of the fragmentation function the data exhibit some general features:

(i) For low $x_p < 0.1$ the particle yield rises strongly with energy. In particular in this region mass effects become important and scaling cannot be expected. Obviously the strong increase of the multiplicity discussed in section 3.1 is happening here.

(ii) For $x > 0.2$ the particle spectra are rather similar for different energies. Even though for the data of fig. 3.2.3b the total c.m. energy is changed by a factor 2.5, the particle yield drops only by about 20–30% indicating that scaling holds approximately.

(iii) All data show a systematic decrease with increasing energy in the region of $x > 0.2$. This is just what is expected from QCD scaling violations.

In the following sections we will discuss the properties of the x-distribution in different intervals.

The high x-region. The shape of the particle spectrum in the region $x \rightarrow 1$, i.e. near the kinematic limit is undisturbed by decays. Predictions for the behaviour of the fragmentation function in this region are due to dimensional counting rules and the standard fragmentation models. Using their very good momentum resolution the HRS collaboration studied $f(x_p)$*) up to values very close to $x_p = 1$ (fig. 3.2.4 [103]). A fit of the fragmentation function for $x_p > 0.5$ to the form

$$f(x_p) \propto (1 - x_p)^n / x_p \,, \tag{3.2.9}$$

yields $n = 2.08 \pm 0.21$. A similar result has been obtained by the TASSO collaboration [3]. The results agree with predictions from dimensional counting rules [104–106]. Higher twist effects would distort the fragmentation function as

$$f(x_p) = (1 - x_p)^2 + C/Q^2 \tag{3.2.10}$$

[107]. The parameter C is found to be smaller than $C = 2\,\mathrm{GeV}^2$ at 90% C.L.

The LUND–Monte Carlo can describe the high x-distribution equally well. The simplest cluster decay as included in the Webber–Monte Carlo predicts too steep a fall-off for $x \rightarrow 1$. With some adjustments in its hadronisation part, however, the data can be reproduced.

The medium x-region. The measurements are most sensitive to QCD scaling violations in the region $0.2 < x_p < 0.7$. Both data of high accuracy are available for various energies $W > 10$ GeV and mass and p_T-effects should only play a minor role for these momenta and c.m. energies, though they are not negligible.

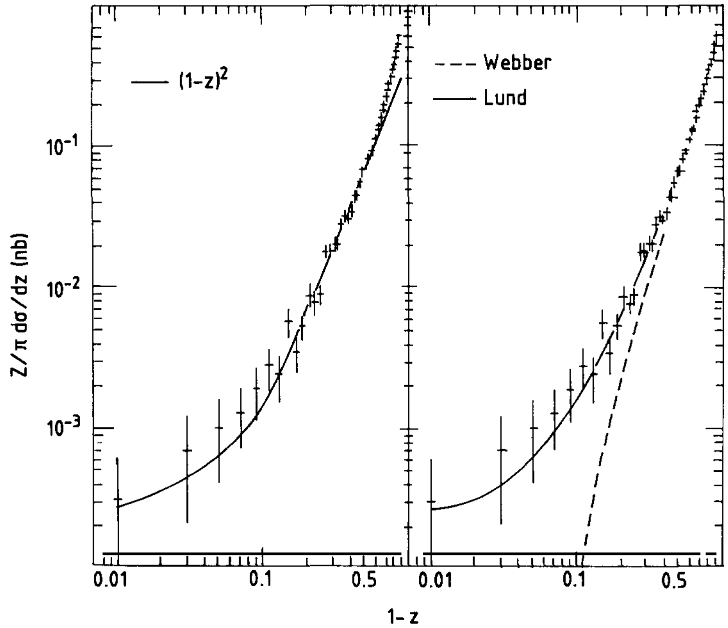

Fig. 3.2.4. Fragmentation function measured close to the kinematical limit $x \rightarrow 1$ [103] together with predictions from an early version of the Webber and from the LUND model. Also shown is the result of a fit to $(1 - z)^2$. Here z denotes the scaled momentum x_p.

---

*) The function $f(x_p)$ should be very close to $D_q^h(x)$. There are two differences: firstly the argument x_p only approximates the scaling variable x. Secondly f is a summation over all kinds of primary quarks, D_q^h not. Therefore we use a different notation.

Figure 3.2.5 displays the particle yield in various x-intervals as a function of s. Results are shown from the TASSO [3], the MARK2 [101, 65], the JADE [82], and the HRS collaboration [96] in an energy range $25 < s < 2000\,\mathrm{GeV}^2$ extending nearly over two orders of magnitude. The results from the various experiments are in good agreement with one another. Whereas for small x_p the particle yield is rapidly rising with energy, it levels off at $x_p \sim 0.2$ and decreases for $x_p > 0.2$.

Motivated by the QCD equation (3.2.7), one can parametrise the s-dependence by

$$\frac{1}{\sigma_{\mathrm{tot}}}\,\frac{\mathrm{d}\sigma}{\mathrm{d}x_p} = c_1[1 + c_2\ln(s/s_0)]\,. \tag{3.2.11}$$

The results from a fit of this equation with $s_0 = 1\,\mathrm{GeV}^2$ to the data from TASSO[*] are indicated by the full lines. The resulting coefficients are listed in table 3.2.1. The slope c_2 is negative for $x_p > 0.2$ with a high statistical significance of $\sim 10\sigma$. Within this region the particle yield decreases by ~25% for an increase of W from 14 to 41.5 GeV. For $x > 0.2$ the slope does not depend strongly on the x-interval considered.

As discussed above, such a decrease is expected from QCD. However, it was pointed out [108] that kinematical effects have also to be taken into account in interpreting the scale breaking observed.

The kinematical effects to be considered are (a) mass and p_{T} effects and (b) the fragmentation properties of heavy quarks.

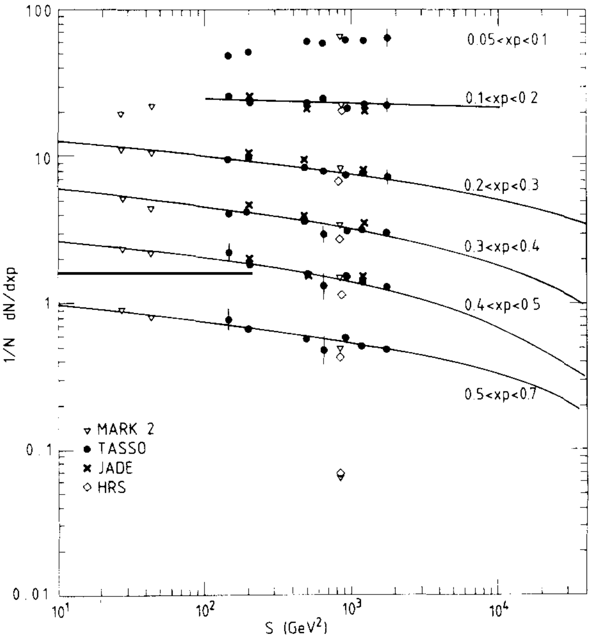

Fig. 3.2.5. Fragmentation function in various intervals of x_p as a function of s, the square of the c.m. energy W [3, 96, 65, 101, 82]. The solid lines are results of a fit according to eq. (3.2.11).

---

[*] Here only one experiment was used to properly take into account the correlations of the relative systematic errors between the various measurements.

Table 3.2.1
Coefficients obtained from a fit of eq. (3.2.11) to the s-dependence of the fragmentation function

x_p	c_1	c_2
0.02–0.05	0.50 ± 0.05	25.3 ± 2.49
0.05–0.10	1.97 ± 0.87	0.32 ± 0.08
0.10–0.20	26.80 ± 1.40	−0.022 ± 0.008
0.20–0.30	14.99 ± 0.81	−0.071 ± 0.005
0.30–0.40	7.27 ± 0.54	−0.081 ± 0.006
0.40–0.50	3.29 ± 0.37	−0.084 ± 0.008
0.50–0.70	1.09 ± 0.16	−0.075 ± 0.012

(a) The scaling of the fragmentation function has been perceived in the Bjorken limit $Q^2 \rightarrow \infty$ assuming the transverse momentum with respect to the event axis $p_T \ll s$ and the particle masses $m \ll s$ to be negligible. At the energies experimentally accessible, the transverse momentum and the mass still influence the distribution. Particles of different mass and the same momentum p have quite different values of x_E for moderate values of x_p and lower c.m. energies (for $x_p = 0.2 : x_E^{\pi} = 0.201$, $x_E^{K} = 0.212$ and $x_E^{p} = 0.244$ at $W = 14\,\text{GeV}$). Because of its steep fall-off the fragmentation function is affected more strongly. On the other hand most of the particles with momenta around $x_p = 0.2$ or $p = 1.5\,\text{GeV}$ are pions (see section 4.1). Thus the fragmentation function in terms of x_E does not differ considerably from that in terms of x_p. Its overall contribution to the scale breaking can be estimated by simulating the fragmentation of light quarks u and d neglecting QCD bremsstrahlung. The result of such a Monte Carlo study using the LUND program is shown in fig. 3.2.6. Plotted (from ref. [109]) is the ratio of particle yield at $W = 14\,\text{GeV}$ over that at $W = 34\,\text{GeV}$. For curve (a) only prompt, i.e. not decayed particles with an intrinsic $p_T = 0$ have been considered. For curve (b) σ_{p_T} was chosen as 440 MeV, a value for which the measurements can be reproduced. For curve (c) the simulation was extended to include resonances. As can be seen both masses and the transverse momenta modify the ratio of the

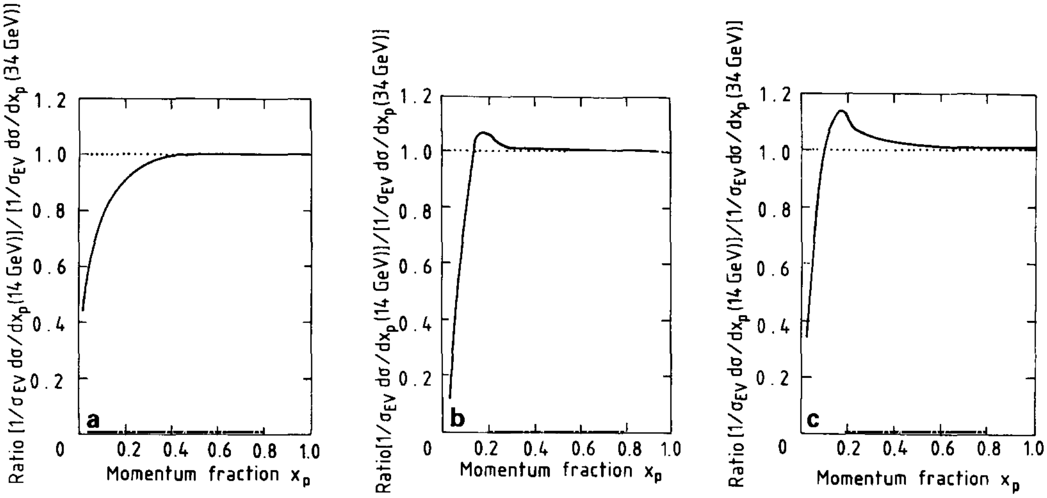

Fig. 3.2.6. Monte Carlo study (LUND V4.3) of kinematical contributions to the scale breaking of the fragmentation function. Displayed is the ratio of the particle yield at $W = 14\,\text{GeV}$ over that at $W = 34\,\text{GeV}$ (from ref. [109]). (a) Only prompt particles are considered, $\sigma_{p_T} = 0\,\text{MeV}$. (b) Only prompt particles are considered, $\sigma_{p_T} = 440\,\text{MeV}$. (c) Resonance decays included.

particle yield leading to a decrease by 10% for $x_p \sim 0.2$. Their impact dies out with increasing x_p. The ratio approaches unity, only 2–3% less particles are produced with $x_p > 0.6$ as W increases from 14 to 34 GeV.

(b) Since heavy quarks inside jets can only be produced as primary particles (see sections 2.2 and 4.4), their yield is completely defined by their photon coupling and thus (almost) independent of the c.m. energy W. On the other hand they can populate a region in x_E that increases with energy leading to a depletion of charmed and bottom hadrons at high x-values. The potential effect for the scale breaking is visualised in fig. 3.2.7 for a constant fragmentation function for D^*'s. Since for this fragmentation function the D^*'s are spread out considerably more towards low x_E for $W = 34$ GeV, the net effect is a higher D^* yield at $x > 0.2$ for $W = 14$ GeV. These distributions suggest that the D^* alone can cause substantial scale breaking in the energy range considered. How this is reflected in the yield of final particles depends on (i) the fraction of heavy quark events (~36% for charm, ~9% for bottom) in the energy range between $W = 14$ to 34 GeV; (ii) the decay multiplicity of heavy hadrons (~3.5 for charmed hadrons, ~8 for bottom particles); (iii) the hardness of the fragmentation function. An estimate of the combined effect is rather involved and can be pursued most reliably with a simulation program.

To this end the parametrisation of ref. [108] with a value of $\varepsilon = 0.04$ has been applied which reproduces the measurements very well (see section 4.5 and in particular eq. (4.5.4)). For the results presented in fig. 3.2.8 QCD effects have again been switched off. Displayed is the scale breaking in charm events between $W = 14$ and 34 GeV in terms of the ratio of the fragmentation functions at $W = 14$ and 34 GeV. The x_p distribution of the D^* (full line) exhibits substantial scale breaking in the relevant region $0.2 < x_p < 0.7$. The high ratio at $x_p < 0.2$ is due to the $1/\beta$ term in the derivative $\mathrm{d}\sigma/\mathrm{d}x_p = (1/\beta)(\mathrm{d}\sigma/\mathrm{d}x_E)$ affecting the distribution at $W = 14$ GeV more strongly. The rapid decrease of the ratio at high values of x is due to the kinematical constraint $p_{\max} = (E_{\text{beam}}^2 - m^2)^{1/2}$. It should be noted that according to the measured fragmentation of D^*'s only very few of them are produced at $W = 34$ GeV

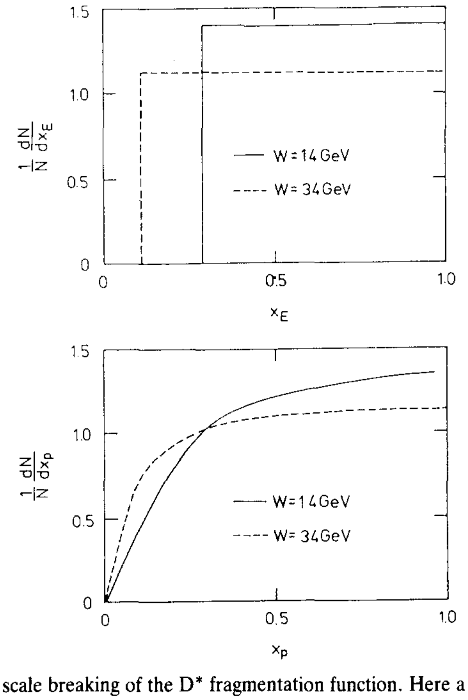

Fig. 3.2.7. Schematic display of the possible scale breaking of the D* fragmentation function. Here a flat fragmentation function has been assumed.

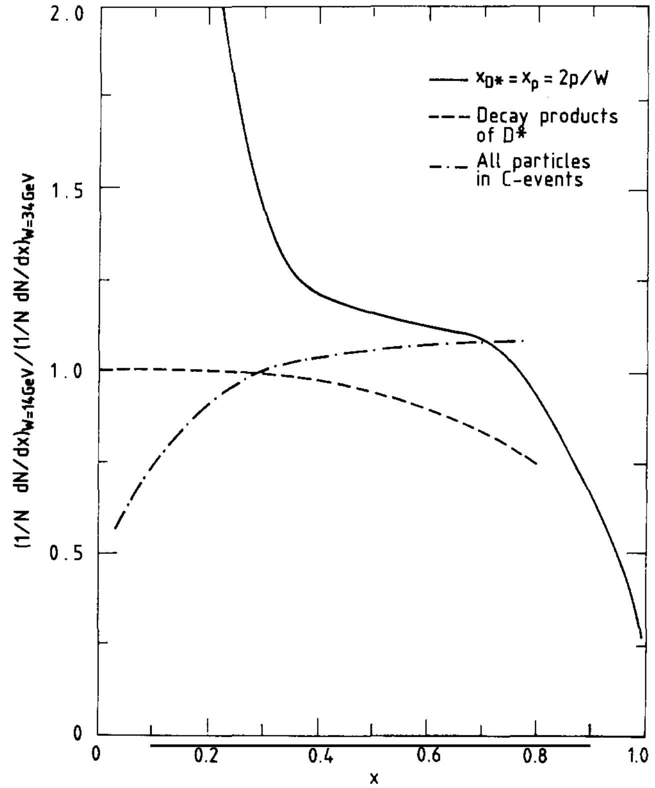

Fig. 3.2.8. Effects of the scale breaking due to D*'s for a fragmentation function as proposed in ref. [108]. Displayed is the ratio of the production yield between $W = 14$ and 34 GeV for the D* itself (solid line), its decay products (dashed) and all particles in charmed events (dashed–dotted line).

with an x_E less than the kinematical threshold for $W = 14$ GeV (see fig. 4.5.2). This is a basic difference to the model of a constant fragmentation function used for fig. 3.2.7. As a result the scale breaking is less prominent in the data. Further one has to note that in the measurements on the scale breaking of (table 3.2.1) the final state particles are considered.

A further step is to consider the scaling property of the D^* decay products. The x_p distribution of those is concentrated at smaller values of x_p even showing a behaviour opposite to QCD scale breaking: there is less production yield at $W = 14$ than at $W = 34$ GeV for $x_p > 0.2$.

This picture changes again once the residual fragmentation is considered. Since more phase space is available for the non-leading system at $W = 34$ GeV, the overall particle distribution is affected more strongly. The particles from the subsequent fragmentation in a charm event induce a scale breaking of ~5–10% between $0.5 < x_p < 0.8$.

To relate this to the scale breaking of the overall event yield, i.e. summing over all quark flavours one has to take into account that the particle yield in charm events is considerably lower than in u, d, s events for high x_p *). As a result the final particles from charm events contribute somewhat to the scale breaking observed, however, it is only a small fraction of what has been measured.

To summarize, both kinematical effects discussed above affect the s-dependence of the particle spectrum leading to some scale breaking with increasing W at high x. This depletion, however, is much

---

*) As will be discussed in section 5.1.3 this fact served to tag light quark jets.

smaller than what has been measured. The data can only be explained by additional contributions due to QCD bremsstrahlung.

In fig. 3.2.9 the prediction of the second order QCD Monte Carlo of the LUND group with a value of the cutoff mass $M_c = 4$ GeV (see section 2.1) and $\Lambda_{QCD} = 0.5$ GeV, of the QCD-shower Monte Carlo of Webber, and of the LUND shower program combining shower evolution up to a cut-off mass of $M_c = 2$ GeV with string fragmentation are compared to the data. The scale breaking is analysed in terms of the ratio of the normalized cross sections for $W = 14$ to that at $W = 34$ GeV as well as that for $W = 22$ to $W = 44$ GeV.

Whereas the general trend of the data can be reproduced by the various QCD models, they tend to underestimate the scale breaking between $0.2 < x_p < 0.5$. This is in particular true for the LUND second-order model, its deficiency is more pronounced for the ratio between $W = 22$ and 44 GeV. The QCD shower models reproduce the data fairly well, the shower model combined with string fragmentaion exhibits an even closer agreement. These results may point towards the need for including higher than second orders of QCD corrections in the simulation.

It was the hope expressed in ref. [108] to determine the mass at which non-perturbative effects become relevant (cut-off mass). This will be studied more closely in section 9.2.

Effects in the low x-region. The exact treatment of infrared divergencies in leading order in the calculation of the fragmentation function led to the prediction of coherent gluon emission. As shown by Mueller [41], Bassetto et al. [42], and Ermolaev et al. [43, 44] this coherence has a striking effect on the

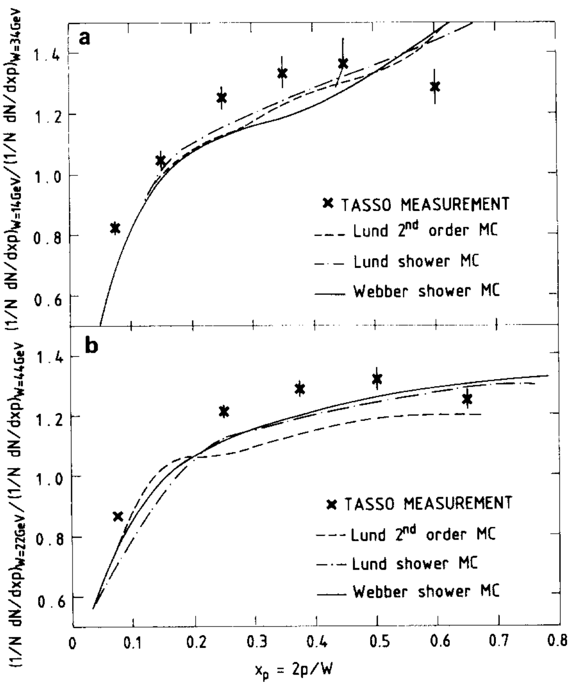

Fig. 3.2.9. Comparison of the measured scale breaking to model predictions. Displayed is the ratio of the fragmentation functions as a function of x_p between (a) $W = 14$ and 34 GeV, (b) $W = 22$ and 44 GeV. The models used are the LUND Monte Carlo including the exact second order QCD corrections (solid line), the Webber Monte Carlo (dashed line) and the combination of shower development and string fragmentation (dashed-dotted line).

shape of the fragmentation function. The distribution $x(\mathrm{d}\sigma/\mathrm{d}x)$ is changed from a plateau as perceived by showering processes without this coherence to a Gaussian

$$\frac{\mathrm{d}\sigma}{\mathrm{d}\ln(1/x)} \propto \left\{\exp\left[\sqrt{\frac{2c_{\mathrm{A}}}{\pi b}}\ln\left(\frac{Q^2}{Q_0^2}\right)\right]\right\}\frac{1}{\sqrt{\ln^{3/2}(Q^2/Q_0^2)}}$$

$$\times\exp\left[-3\sqrt{\frac{8c_{\mathrm{A}}}{\pi b}}\frac{(0.25\ln(Q^2/Q_0^2)-\ln(1/x))^2}{\ln^{3/2}(Q^2/Q_0^2)}\right]. \qquad (3.2.12)$$

Here $c_{\mathrm{A}} = 3$, $b = (33 - 2n_{\mathrm{f}})/12\pi$ and n_{f} is the number of flavours, Q_0 is the energy scale of the QCD calculations. The first exponential describes the increase in the total multiplicity as already discussed in section 3.1.1, the second represents the x-dependence of the particle yield. The distribution is predicted to have a maximum at

$$\ln(1/x) = \tfrac{1}{2}\ln(E/Q_0) \qquad (3.2.13)$$

and to decrease for small x.

This depletion is due to a destructive interference of diagrams contributing to gluon emission. Consider the decay of a quark $\mathrm{q}\rightarrow\mathrm{q}' + \mathrm{g}_1$ (cf. fig. 3.2.10). A second gluon can be emitted from each of the three partons. The diagrams for the emission from q and those from the g and q′ cancel each other outside an angular region given by the emission angle of g_1 (see e.g. ref. [110]). As a result not only the energy but also the emission angle of low energetic gluons is ordered: low energetic gluons have smaller emission angles (fig. 3.2.11). This dynamical suppression in phase space leads to a decrease of the gluon yield at low energies and thus to the dip in the ln x distribution.

The effect is closely related to the Chudakov effect in electromagnetic processes in cosmic rays [111] and can be qualitatively understood in terms of the resolving power of an emitted gluon. A gluon with high Q^2 and/or an emission under a small angle can resolve the colour content of a gluon cloud. It thus has a high probability of interaction. However, for a gluon of low Q^2 emitted under a large angle the gluon cloud acts as an entity and the probability of interaction is diminished (see e.g. the discussion in ref. [112]).

Since only hadrons and not gluons can be measured, a meaningful experimental test of this

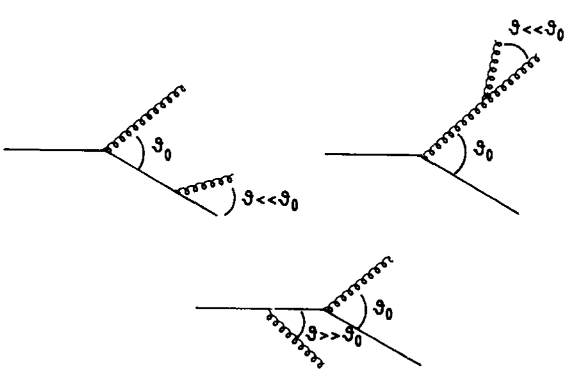

Fig. 3.2.10. Interfering diagrams contributing to the coherence phenomenon [110].

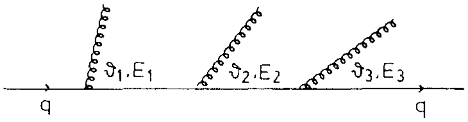

Fig. 3.2.11. Sketch of the angular ordering.

prediction can only be done if the spectra of hadrons and gluons are similar. This is the essence of the local parton–hadron duality conceived by the Soviet group [63] or of preconfinement [64].

In fig. 3.2.12 the x-distribution in terms of

$$\frac{1}{\sigma_{\text{tot}}} x_p \frac{d\sigma}{dx_p} = \frac{1}{\sigma_{\text{tot}}} \frac{d\sigma}{d\ln(1/x_p)}$$

measured by the HRS collaboration [96] is plotted. The particle yield decreases for $x < 0.03$ as expected from coherent gluon emission. The interpretation of the dip, however, is not obvious. Since the partons are assumed to be ultrarelativistic in the calculations, these cannot distinguish x_p and x_E*), leaving some ambiguity in the choice of the appropiate variable. If x_E instead of x_p is considered, the data points of fig. 3.2.12 have to be transformed as

$$\frac{1}{\beta^2} x_p \frac{d\sigma}{dx_p} = x_E \frac{d\sigma}{dx_E} \,. \tag{3.2.14}$$

Since in the region of the dip $\beta_\pi \sim 0.89$, $\beta_K \sim 0.51$, and $\beta_p \sim 0.3$ (at $x_p = 0.02$) this mass effect is not

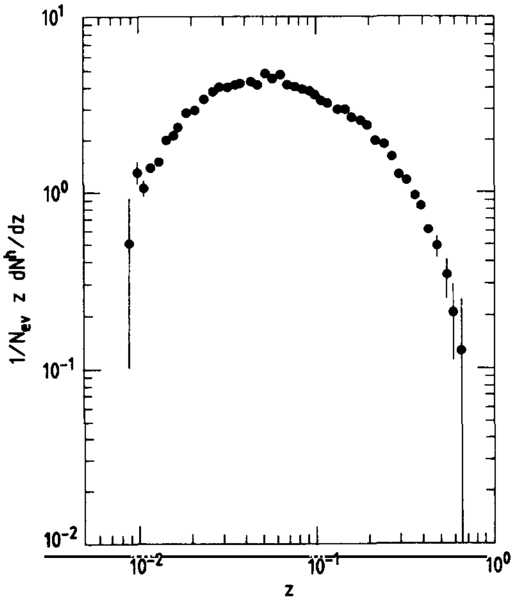

Fig. 3.2.12. $(1/N)x_p(dN/dx_p)$ distribution as a function of x_p (here x_p is denoted by z) [96].

---

*) I am grateful to Yu.L. Dokshitzer and V.A. Khoze for communications on this problem.

negligible. In addition phase space effects are important in the momentum region considered. The distributions in x_E using identified particles will be discussed in section 4.

Another experimental distortion is due to decays. Their effect is visualized in fig. 3.2.13 for which the distribution $x_p(\mathrm{d}\sigma/\mathrm{d}x_p)$ for prompt particles as well as for final (stable) particles was generated using the LUND Monte Carlo. As can be seen the maximum of the distribution of final particles is shifted by about one unit of $\ln(1/x)$ to the lower x-values compared to that of the primary ones. Thus the measured distribution is a mixture of two apparently unrelated contributions: the fragmentation function determined by QCD and the decay properties. A somewhat different view is taken by Azimov et al. [50] who conjecture a duality of fragmentation and hadronic decay. In addition the figure indicates that the dip at low x-values is not unique to the QCD-leading log approach but instead arises also in the classical LUND approach.

These kinematical distortions cancel out in part when the energy variation of the maximum is analysed. Phase space leads to a variation of the maximum like $x_{\max} \propto 0.5 \ln s$ whereas from eq. (3.2.13) it follows that $x_{\max} \propto 0.25 \ln s$. The measurements [3] are compared to this prediction in fig. 3.2.14. The data are in agreement with what is conceived from coherent gluon emission as is indicated by the straight lines which have a slope of $\frac{1}{4} \ln s$. It should be noted that the 2nd order LUND Monte Carlo predicts a similar slope, whereas the simulation of just $q\bar{q}$ hadronisation gives a higher slope. Thus again the LUND QCD simulation coincides with the prediction from coherent gluon emission.

At this stage of the analysis it can be concluded that the QCD prediction of coherent gluon emission is consistent with the data. But the implications of coherent gluon emission can also be described by other approaches, in particular the LUND model. A careful experimental test of the validity of the theoretical prediction has to include kinematical constraints. We return to the status of the experimental evaluation of coherent gluon emission in sections 4.4 and 6.2.

3.3. *The momentum distributions with respect to the jet axis*

Since jets are characterized by a distinct reference axis, it is natural to analyse the particle yield with respect to this axis. Experimental methods to find the jet axis from the measured particles are discussed

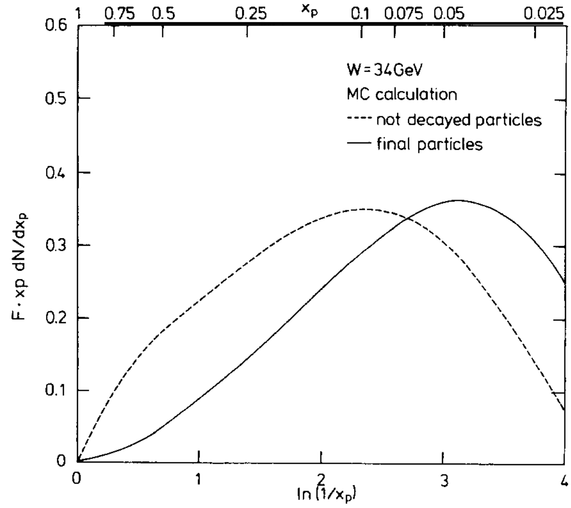

Fig. 3.2.13. Monte Carlo comparison of the particle spectrum before (dashed line) and after (solid line) decays.

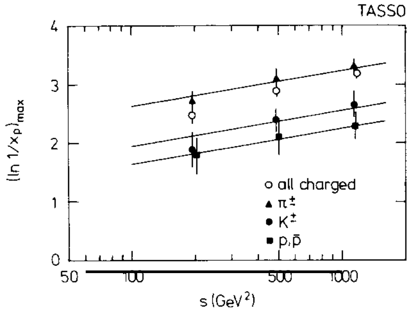

Fig. 3.2.14. Energy dependence of the maximum of the ln $1/x_p$ distribution for various types of particles [3]. The lines indicate the slope expected from coherent gluon emisssion.

in the appendix A.2. Although, in particular, for events of low multiplicities, the reconstructed axis may be biased, it reproduces the direction of the original parton in general quite well and allows one to obtain a representative picture of the longitudinal and transverse properties of jets in e^+e^- annihilations.

3.3.1. The average longitudinal and transverse components

Whereas the average longitudinal momentum increases roughly proportional to the c.m. energy, the transverse component increases only marginally. The measurements of the average transverse momentum from TASSO [3], PLUTO [113], HRS [96], and MARK2 [65] are shown in fig. 3.2.1a. The $\langle p_T \rangle$ grows by ~30%, the average longitudinal momentum by ~130% for an increase of W from 14 to 41.5 GeV. This indicates that on the average the particles within a jet are more collimated with increasing energy. On the other hand the growth of $\langle p_T^2 \rangle$ is much more prominent: it is doubling (fig. 3.2.1b) in the same energy range, suggesting the change in p_T is due to particles with large momentum. Such a high p_T-component arises naturally from a third jet and constitutes one of the prime indications of hard gluon emission.

The transverse component can be analysed in more detail by separating the contributions in and out of the event plane (their definition and the method for their determination are discussed in the appendix A.2). The measurements are displayed in fig. 3.3.1 and show that the high transverse

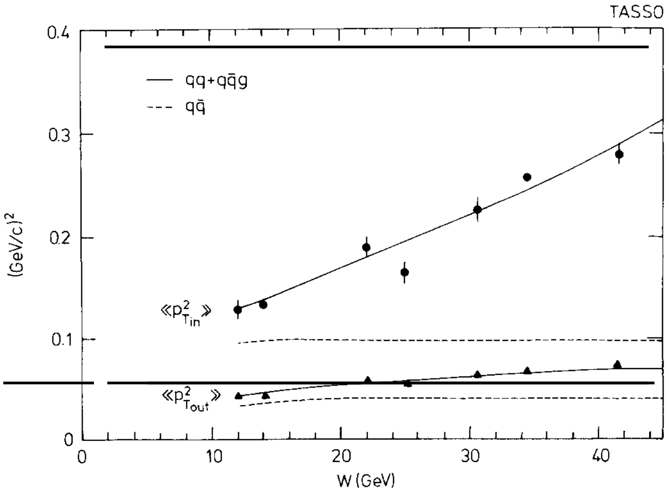

Fig. 3.3.1. The average squared transverse components of the events in and out of the event plane as a function of the c.m. energy W [3].

component is concentrated in a plane: $\langle\langle p_{T,in}^2 \rangle\rangle$ increases much stronger than $\langle\langle p_{T,out}^2 \rangle\rangle$. In interpreting these results one has to be aware of biases due to the calculation procedure of the event plane. These tend to reduce the reconstructed component out of the event plane in particular for events of low multiplicity. Also shown are the predictions from simulation studies with and without QCD bremsstrahlung (which are also subject to these biases). Whereas the model without hard gluons falls short of describing the rise of $\langle\langle p_{T,in}^2 \rangle\rangle$, the results can very well be reproduced by models including hard gluon bremsstrahlung. It should be added that models without the emission of a hard gluon but an increase of the (azimuthally symmetric) transverse momentum of the hadrons (σ_{p_T}, see section 2.2.6) do not reproduce the trend of the data.

3.3.2. The inclusive distribution of longitudinal and transverse components

For completeness the longitudinal scaled momentum of the final particles $(1/\sigma)(d\sigma/dx_{\parallel})$ is displayed in fig. 3.3.2*). Qualitatively it is very similar to $(1/\sigma)(d\sigma/dx_p)$ discussed above. Again the scaling violation is seen for $x_{\parallel} > 0.2$.

The hard component of the transverse momentum can be directly studied in fig. 3.3.3, where the particle yield depending on p_T and p_T^2 with respect to the sphericity axis**) is displayed for various energies between $W = 14$ GeV and 41.5 GeV. The picture exhibits a core of particles of low transverse momenta as well as a tail extending to very high transverse momenta with increasing energy. For the low transverse momentum $p_T < 0.5$ GeV, the particle yield at the various energies has a rather similar

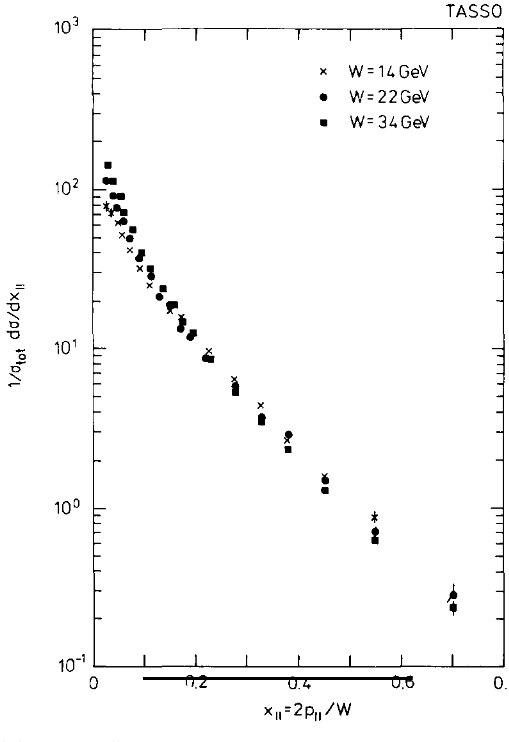

Fig. 3.3.2. Longitudinal fragmentation function for various energies [3].

---

*) Nearly all of the figures shown in the rest of this section are taken from ref. [3].

**) The absolute values of the differential cross section depend significantly on how the event axis was reconstructed. In particular this is true for the high transverse momenta. However, the general trend of the data, especially its energy dependence, is not biased.

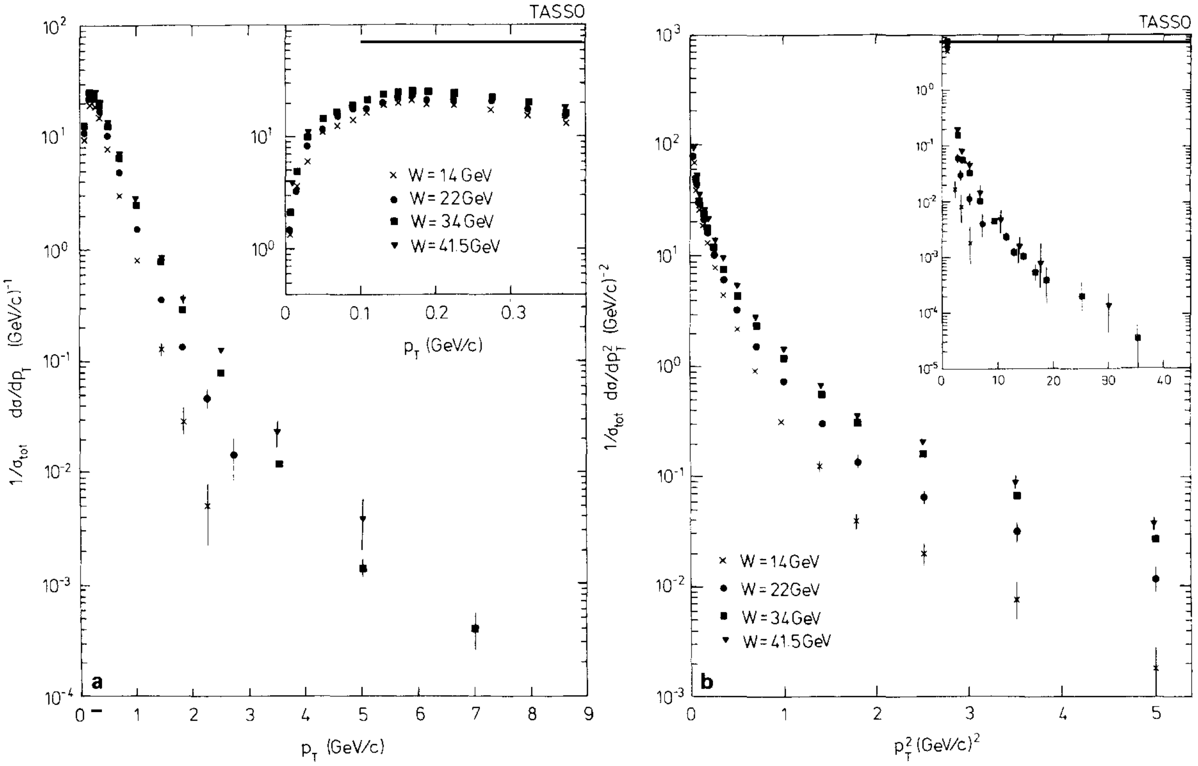

Fig. 3.3.3. Transverse component of the particle spectrum [3]. (a) $(1/N)(dN/dp_T)$. (b) $(1/N)(dN/dp_T^2)$.

shape, its increase reflects the higher multiplicities at higher W. For larger transverse momenta the particle yield falls off differently for the various energies, exhibiting a tail which becomes more pronounced with increasing W.

The p_T-distribution or equivalently the angular distribution around the jet axis as a function of the longitudinal momentum follows a pattern that is nearly independent of W. The particle yield for $W = 14$, 22 and 34 GeV and different $p_{\parallel}$ is displayed in fig. 3.3.4 as a function of the angle α with respect to the jet axis. The data reveal two features:

(a) As expected, the particles get more and more collimated around the jet axis with increasing parallel momentum. The particles at low parallel momentum are nearly isotropically distributed.

(b) Although the $p_{\parallel}$-distribution for the various c.m. energies is quite different, the angular spectrum of particles with a certain $p_{\parallel}$ is remarkably independent of W. This "fan invariance" holds only approximately as can be seen by analysing the dependence of $\langle p_T \rangle$ on $p_{\parallel}$ (see fig. 3.3.5). The angle α and p_T are related by

$$p_T = p_{\parallel}\, \mathrm{tg}(\alpha)\,. \qquad (3.3.1)$$

For parallel momenta of $p_{\parallel} \sim 3$–4 GeV, the average transverse momentum at $W = 34$ GeV is only about 10% higher than that at $W = 14$ GeV, considerably less than the increase in the total $\langle p_T \rangle$. The transverse component becomes more prominent only for larger $p_{\parallel}$ at higher c.m. energies, when the kinematical limit is reached.

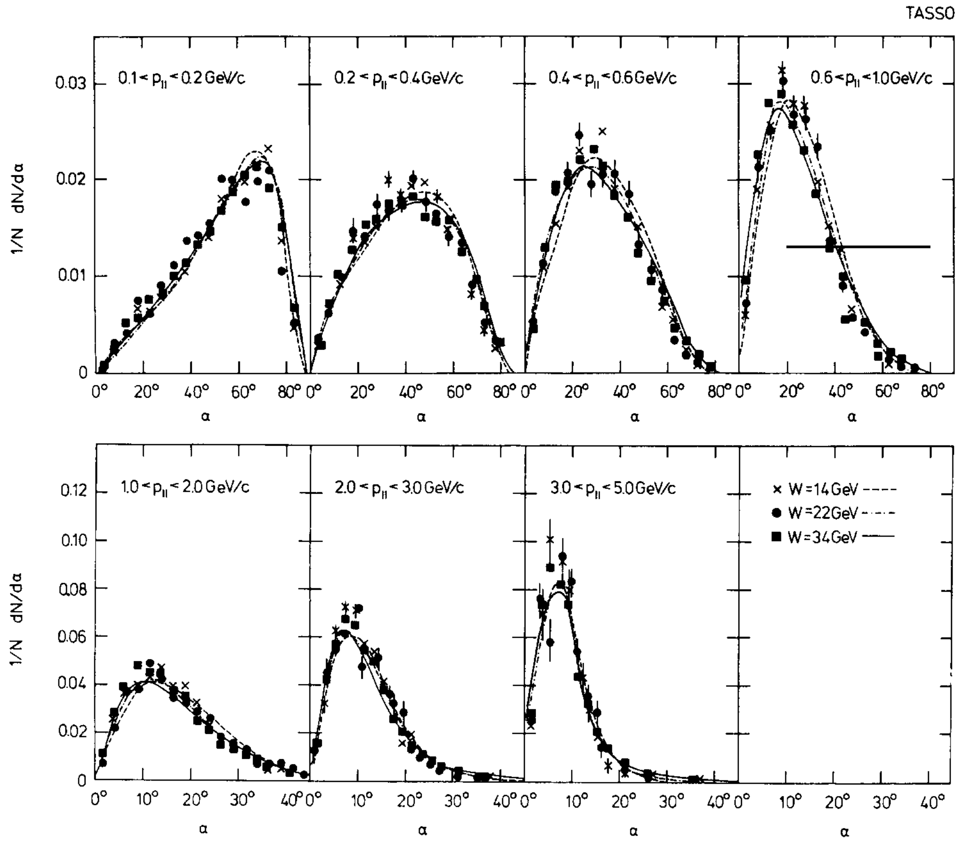

Fig. 3.3.4. The angular spectrum of particles at various energies for different intervals in $p_\parallel$ [3]. The data are compared to the predictions of a QCD simulation.

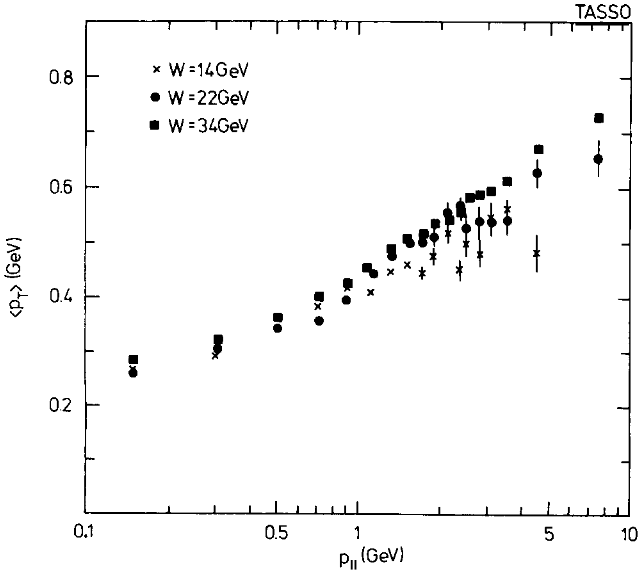

Fig. 3.3.5. $\langle p_T \rangle$ as a function of $p_\parallel$ for various c.m. energies [3].

A pattern like the fan invariance can arise from a p_T-distribution that is independent of $p_\parallel$ and W. For simple two-jet events this is a straightforward assumption, it is, however, not trivial that the effect should persist in events with gluon bremsstrahlung. The fan invariance is closely related to the transverse pattern of QCD effects, and can be reproduced by the standard QCD Monte Carlo (see lines in fig. 3.3.4).

The longitudinal and transverse components of the momentum are treated in a fundamentally different way in the quark parton picture of jet development. Independence of W is obtained by scaling the longitudinal component but considering the absolute transverse momentum. However, with increasing energy the hard transverse component is more and more determined by QCD bremsstrahlung and thus induces approximate scaling in $x_T = p_T/E_{\text{beam}}$.

As can be seen from the first order QCD formula for a parton of transverse momentum x_T

$$\frac{1}{\sigma_0}\frac{d\sigma_1}{dx_T^2} = \frac{2}{\pi}\frac{4}{3}\alpha_s\frac{1}{x_T^2}\left[\left(1-\frac{x_T^2}{4}+\frac{x_T^4}{4}\right)\ln\left[\frac{1+\sqrt{1-x_T^2}}{x_T}\right]-\frac{1}{4}\sqrt{1-x_T^2}(3-x_T^2)\right] \tag{3.3.2}$$

(e.g. ref. [114]) the transverse component is independent of the c.m. energy up to logarithmic variations. Neglecting scaling violations in the fragmentation function, such a behaviour can also be anticipated for the transverse distribution of the particles, once their transverse momenta exceed that of single parton fragmentation. In fig. 3.3.6 the scaled transverse momentum spectrum is displayed for energies between $W = 14$ GeV and 41.5 GeV. As expected the yield at low x_T increases strongly with W.

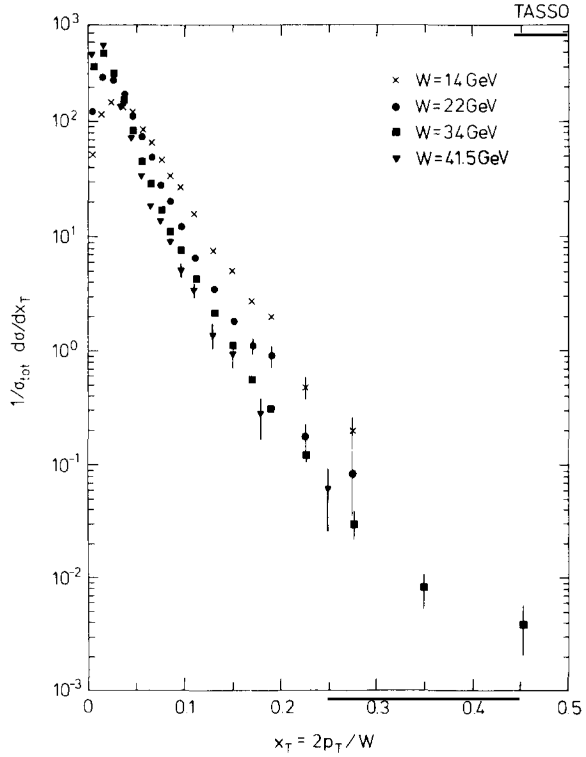

Fig. 3.3.6. Distribution of the scaled transverse momentum $(1/N)(dN/dx_T)$ for various c.m. energies [3].

In this region the transverse component is dominated by fragmentation effects (2.2.6). As discussed above in the context of the $(1/N)(dN/dp_T)$ distribution, the shape of the transverse component is rather similar in terms of p_T in this region. However, for large x_T and increasing energies the distributions at the various energies become more and more similar and the high x_T distribution tends to scale as expected from hard QCD effects.

These results suggest that two contributions determine the transverse spectrum, which can be separated according to their variation with energy. In the standard simulation approaches the part which exhibits an invariant distribution in p_T is considered being due to non-perturbative effects, the high p_T part, which scales approximately in x_T, is due to hard QCD effects.

The broad transverse distribution of jets makes them experimentally rather inconvenient objects. The energy of a single parton is spread considerably in space. In particular, the hard gluon bremsstrahlung complicates the assignment of particles to partons. This problem will be addressed again in section 11.

3.3.3. *The rapidity distribution*

The rapidity

$$y = 0.5 \ln\left(\frac{E + p_\parallel}{E - p_\parallel}\right)$$

combines the transverse and longitudinal momentum components. The distribution of particles in terms of this variable is particularly nice and simple. As can be seen from fig. 3.3.7 [3] the rapidity spectrum*) exhibits a plateau stretching out with W and a rather steep fall-off towards the maximum rapidity value

$$y_{\max} \sim \ln(W/m_\pi) .$$

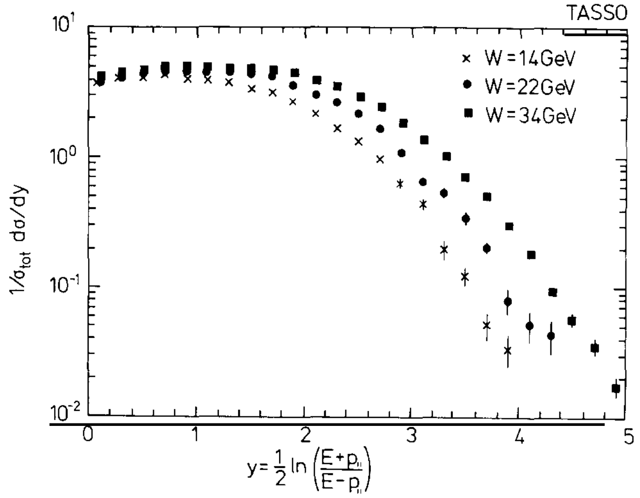

Fig. 3.3.7. Rapidity distribution at various energies. Particles from both jets are folded around $y = 0$ [3].

---

*) For the inclusive spectra pion masses have been assumed. The data are folded around $y = 0$ since neither of the hemispheres with respect to the jet axis is distinct.

This fall-off is very similar for the different energies. Figure 3.3.8 displays the height of the plateau as a function of W. The rise of the plateau is another indication of the scale breaking of the fragmentation function.

A closer look at the plateau reveals that it is not exactly flat. Rather the particle yield decreases by 10–20% for $y \to 0$. This dip in the rapidity has also been observed in refs. [96, 65]. Several checks have been made to establish that it is not due to experimental biases. Its magnitude depends on how the jet axis is determined, e.g. the sphericity axis leads to a more flat behaviour. Simulation studies indicate that the thrust axis is more appropriate for the rapidity distribution. The dip is also not due to the assignment of wrong particle masses and/or the special properties of heavy quark fragmentation and decays (see section 5). Both affect higher rapidity values and lead to smaller deviations from a flat distribution than observed in the data.

The increase at low values of rapidity is more clearly shown in fig. 3.3.9, where the ratio of the particle yield at $y = y'$ to the particle yield for $0.1 < y < 0.2$*) is displayed both for the data and the simulation using the string approach supplementing a 2nd order QCD matrix element. This ratio seems to increase with energy. The existence of the dip can be well described by the LUND model, if and only if gluon emission is included, whereas the Independent Jet Model fails to reproduce it. It therefore seems to be due to a conspiracy of hard QCD effects and fragmentation properties.

It is very suggestive to relate this dip to the prediction of coherent gluon emission discussed in section 3.2.2 and indeed the QCD shower model by Webber does reproduce the effect. Azimov et al. [50], however, argue that coherent (as well as incoherent) gluon emission should induce a maximum around $y = 0$. Bengtsson and Sjöstrand [48] analysed this dip in the rapidity with different Monte Carlo approaches at a futuristic energy of $W = 1$ TeV. Comparing the outcome of the calculations on the parton level using shower algorithms with and without the coherence, they find that the dip at $y \sim 0$ only occurs with coherent branchings. After hadronisation they find the dip for showering without coherence which they attribute to the string fragmentation applied.

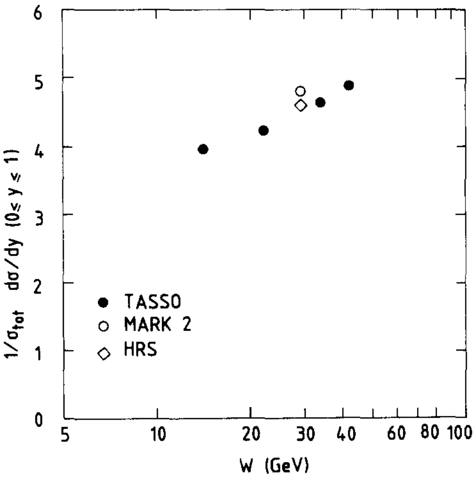

Fig. 3.3.8. Height of the rapidity plateau $0 < y < 1$ as a function of W [3, 96, 65].

---

*) This rapidity interval is relatively free of systematic uncertainties. For $y < 0.1$, however, there exist considerable uncertainties which are due to a limited acceptance and the ambiguities in the reconstruction of the event axis.

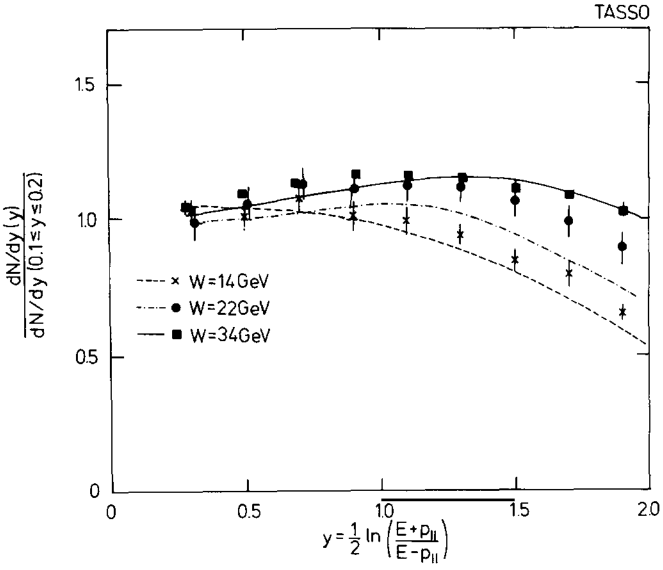

Fig. 3.3.9. Particle yield at rapidities $0.2 < y < 2$ normalized to that at $0.1 < y < 0.2$ for various energies [3].

The shape of the fall-off at high rapidity values in terms of

$$y' = y - y_{\max}$$

is similar for the different c.m. energies (fig. 3.3.10) but discloses a systematic trend with energy: the data at high W are below the measurements at lower W. This reflects the scaling violation property discussed before (see section 3.2). Its interpretation is complicated due to the particle masses involved in the definition of y (note, for fig. 3.3.10 pion masses have been assumed). For example, a proton of $y_p = 2.1$ for a correctly assigned mass, will yield a value $y_\pi = 4.0$ if it is considered a pion (assuming $p_T = 0$). For a correct mass assignment the rapidity spectrum should therefore drop faster. Since the heavy particle content is increasing with rapidity and does not change very much with W for a certain momentum (see section 4), the y_π-distribution is expected to underestimate possible effects from scale breaking.

3.4. Event shapes

Condensing the kinematical properties of all its particles into one variable, one can obtain measures of the topology of an event. The most important ones refer to the jettiness and the flatness of an event and are defined in the appendix.

The sphericity and thrust are the variables most generally used for characterizing how jetlike an event is. Perfect two-jet events have $S = 0$ ($T = 1$), isotropic events have a large value of S (small value of T).

The energy dependence of the average sphericity (and $1 - T$) values are shown in fig. 3.4.1. Both distributions fall off quite rapidly between $W = 14$ GeV and ~25 GeV, but decrease rather little above $W \sim 30$ GeV. The thrust $(1 - T)$ distribution is displayed in fig. 3.4.2 for different energies. The distributions exhibit a core of events becoming more narrow at larger thrust values with increasing

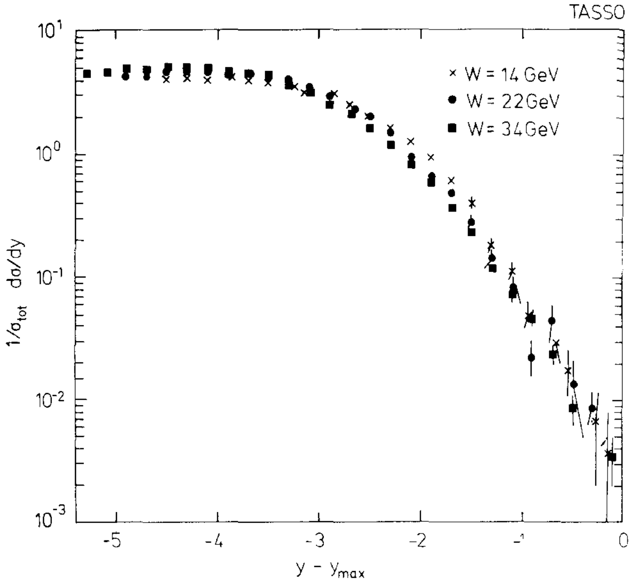

Fig. 3.3.10. Rapidity distribution as a function of $y - y_{\max}$ [3].

energy. In these events the bulk of particles have an almost energy independent distribution in p_T discussed before. For higher energies a tail emerges at low values of T, marking the considerable fraction of broad events expected from hard gluon emission.

We can understand the general features of the energy dependence in these variables by schematically dividing the events into two classes. The first one consists of only two-jet events with a p_T-distribution that is independent of the energy. The other component is made out of three-jet events. Scale breaking effects in the single jets are neglected.

For the first class $\langle p_T^2 \rangle = c$ is energy independent and $\langle p^2 \rangle \propto c'W^2$. Thus

$$\langle S_{\text{frag}} \rangle \sim \frac{3}{2} \left(\frac{\Sigma\, p_T^2}{\Sigma\, p^2} \right)_{\text{frag}} \sim \frac{3}{2}\, \frac{nc}{nc'W^2} \propto \frac{1}{W^2}\,, \tag{3.4.1}$$

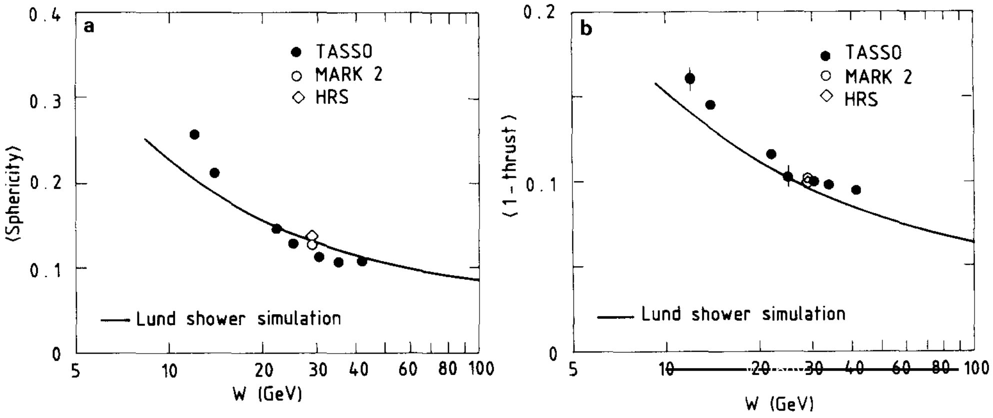

Fig. 3.4.1. Energy variation [3, 96, 65] of (a) the average sphericity S, (b) the average thrust $1 - T$. The lines represent results of the simulation studies using the LUND-shower-Monte Carlo.

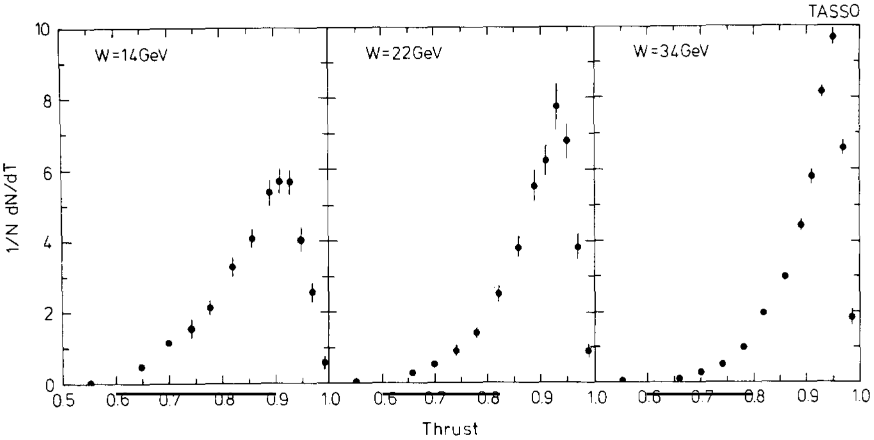

Fig. 3.4.2. Thrust distribution at $W = 14$, 22 and 34 GeV [3].

Here n denotes the multiplicity. As discussed before, the most prominent contribution to the transverse component in the second class is due to hard gluon emission and $\langle x_T \rangle$ is approximately energy independent.

$$\langle S_{\rm QCD} \rangle \sim \frac{3}{2} \left(\frac{\Sigma p_T^2}{\Sigma p^2} \right)_{\rm QCD} \sim \frac{3}{2} \frac{n(\langle x_T \rangle W)^2}{nc' W^2} \sim \text{const.} \tag{3.4.2}$$

The total average sphericity is the sum of the two contributions according to

$$\langle S \rangle_{\rm tot} \sim (1 - r) \langle S_{\rm frag} \rangle + r \langle S_{\rm QCD} \rangle\,, \tag{3.4.3}$$

where r is the fraction of events with a hard bremsstrahlung changing with energy as

$$r \propto \alpha_s(W) \propto 1/\ln(W^2)\,. \tag{3.4.4}$$

Since r is only slightly decreasing with W and $\langle S_{\rm QCD} \rangle$ is constant, the energy dependence of the average sphericity changes from $1/W^2$ to $1/\ln(W^2)$. This considerable slowing down of $\langle S \rangle$ is visible in the data for $W \geq 25$ GeV. The data are reasonably reproduced by the LUND shower Monte Carlo as displayed in fig. 3.4.1a and b.

Whereas thrust and sphericity parametrise the overall broadness of an event, the aplanarity and, in a similar way, the acoplanarity characterizes its flatness (see appendix A.2). Only the components out of the event plane contribute to A, perfectly flat events have $A = 0$. As for the sphericity and thrust their shape is determined both by non-perturbative effects and hard bremsstrahlung. The latter one only contributes through second or higher order QCD effects, whereas the first order hard bremsstrahlung lies within the plane. The acoplanarity distribution measured by the JADE group at $W = 22$, 34 and 44 GeV [115] is displayed in fig. 3.4.3 together with model predictions (see discussion in section 9.4). The bulk of the events is increasingly flat with energy. However, in addition to these planar events a wide tail of acoplanar events emerges at high energies. The sensitivity of the aplanarity distribution to second-order corrections can be seen from fig. 3.4.4 [116]. Here the aplanarity is compared to the outcome of simulations including first and second order QCD corrections. In both cases the fragmenta-

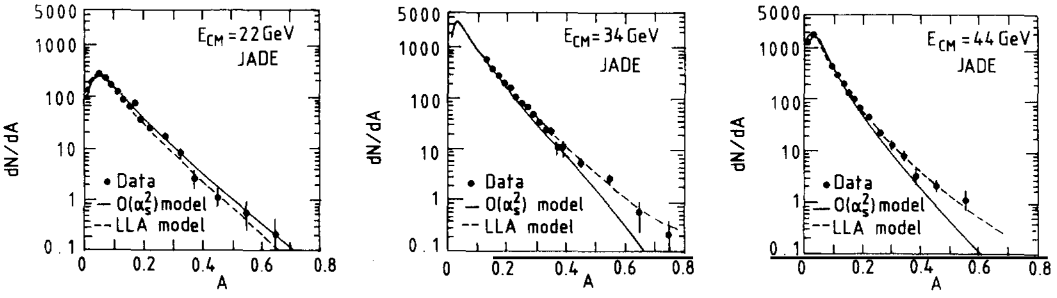

Fig. 3.4.3. Distribution of the acoplanarity $(1/N)(\mathrm{d}N/\mathrm{d}A)$ at various energies together with model calculations using the second order LUND program and the shower algorithm of Webber [115].

tion parameters (see section 2.1) have been optimised to describe this aplanarity and other distributions being sensitive to the fragmentation parameters. It is evident that at least second order corrections are needed to reproduce the data. As will be discussed in more detail in section 9.4, the JADE analysis even indicates the need for higher than second order contributions.

A more detailed view of the topological properties of the events is given by correlating the aplanarity and the sphericity. The measurement by TASSO [3] is shown in fig. 3.4.5 for $W = 14$, 34 and 41.5 GeV together with a general characterization of the events and Monte Carlo simulations. The events show a relatively broad distribution in the sphericity but even those of high sphericity have only very small values of aplanarity. Such structure is expected from two-jet events (low sphericity, low aplanarity) and three-jet events (high sphericity, low aplanarity). Only very few events are found in the region of high sphericity and high aplanarity at least for $W > 30$ GeV. This region is expected to be populated by events containing more than three jets and also by potential heavy quark production. The relatively high population at $W = 14$ GeV can be partly explained by the vicinity of the bottom threshold. The absence of spherical events at $W > 40$ GeV indicates that no open top is produced at these energies.

The definition of aplanarity is based on the sphericity tensor or more generally on contributions being quadratic in momentum. The equivalent concept can be applied to variables being linear in momentum leading to the definition of "major" and "minor" (in analogy to p_T^{in} and p_T^{out}). The oblateness $O = F_{\mathrm{major}} - F_{\mathrm{minor}}$ as measured by the MARKJ group [117] is shown in fig. 3.4.6 and compared to the two-jet and QCD prediction. As for the other distributions discussed, the oblateness

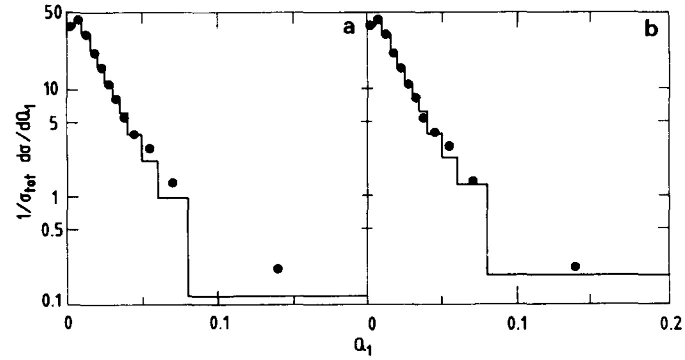

Fig. 3.4.4. Measured aplanarity distribution (open cirles) compared to Monte Carlo calculations including first (a) and second (b) order QCD corrections (histograms) [116].

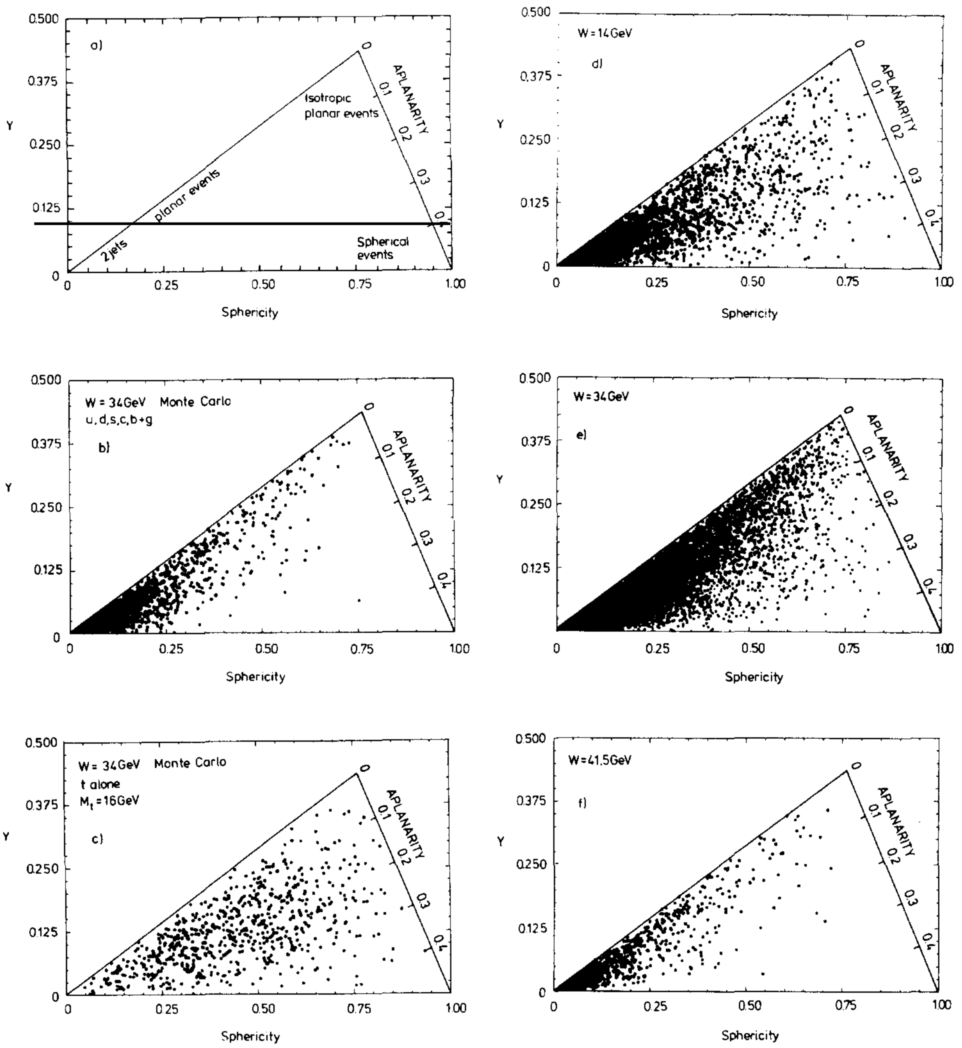

Fig. 3.4.5. Scatter plot of the sphericity versus the aplanarity of events. The left column displays what kinds of events contribute to which region (a) and the expectation for events coming from u, d, s, c and b quarks supplemented by QCD effects (b) and from top production (c). The right column displays the measurements at various energies [3].

reveals the need for QCD bremsstrahlung in the simulation in order to reproduce the data. A two-jet Monte Carlo with an exponential p_T-distribution and $\langle p_T \rangle = 650\,\mathrm{MeV}$ is not excluded from this plot (but from others).

3.5. Conclusions

The hadronic events at high energies $W \geq 30\,\mathrm{GeV}$ exhibit jet structures in a clear and convincing way. The first evidence for jets at SPEAR was based on statistical arguments, since at these energies the momenta of particles parallel to the event axis did not exceed their transverse component considerably. At the higher energies of PETRA and PEP $\langle p \rangle \gg \langle p_T \rangle$ and jets reveal themselves beautifully in events. These data allow one to study the basic properties of jets both at a fixed c.m.

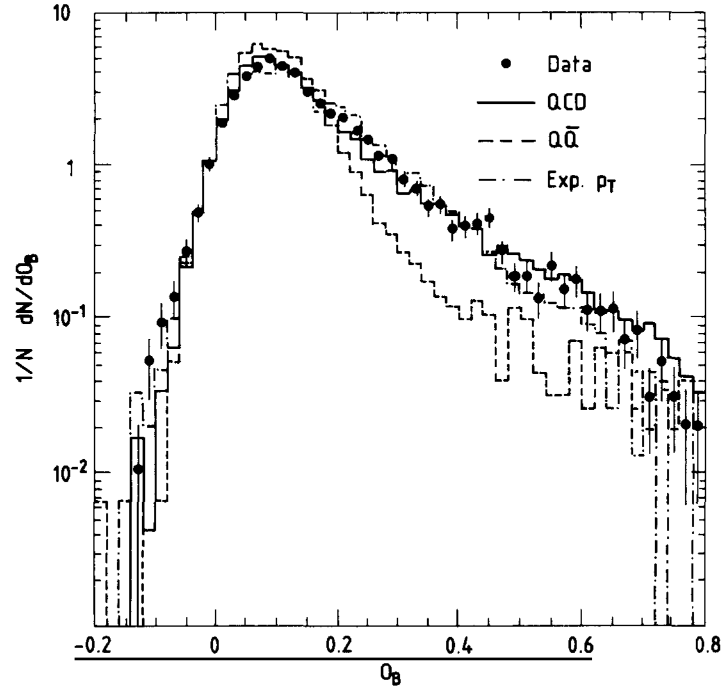

Fig. 3.4.6. Oblateness distribution at $W = 35$ GeV [117]. The measurement is compared to results from simulation studies based on the approach of ref. [59]. The dashed line is the prediction of the $q\bar{q}$ Monte Carlo assuming a Gaussian p_T distribution with $\langle p_T \rangle = 300$ MeV. The dashed-dotted line is due to a $q\bar{q}$ Monte Carlo assuming an exponential a transverse momentum distribution $\exp(-p_T/\sigma)$ with $\sigma = 650$ MeV/c.

energy and as a function of W. One of the most prominent features at these energies is the occurrence of a third jet. All the event properties indicate that it is due to a gluon.

The average multiplicity increases sharply, much stronger than expected from an extrapolation of the low energy behaviour or from longitudinal phase space. It is in agreement with QCD predictions. The multiplicity distributions can be described quite well by a negative binomial, with a large value of k, however, also KNO scaling holds within ~20%.

The increase in the particle yield is due to particles at low x. The particle yield at $x_p > 0.2$ shows a slight but significant decrease with energy. The scale breaking is of the order 25% for $x > 0.2$ between $W = 14$ and 41.5 GeV and cannot be explained by mass and p_T effects alone. Rather one needs a substantial QCD component to accommodate the measurement.

In contrast to the longitudinal component, the transverse one rises only weakly. Jets become more and more collimated. On the other hand there exists clear evidence for a hard component in the transverse spectrum growing with energy and giving rise to very broad events. All their features indicate that they originate from hard QCD bremsstrahlung. As a result the energy dependence of the general event shapes is slowing down. QCD effects are also observable in other parameters like the rapidity. The acoplanarity distribution indicates the need for corrections higher than first order at energies above $W = 30$ GeV.

4. Identified particles in jets

The overall distributions of stable particles discussed in section 3 revealed the global structure of jets. A more precise picture is provided through the identification of the particle type:

(i) Kinematical properties are e.g. due to resonance decays superimposed on the distributions of prompt particles which are closely related to the dynamics of fragmentation (cf. section 3.2.3). Particle identification helps to overcome these distortions since promptly produced particles are made out more easily.

(ii) The relative yield of the particles with different flavours and spins provides fundamental insight as to how the conversion of quarks into hadrons depends on their quantum numbers.

(iii) As will be discussed in the following section, particle identification is an important tool for studying the space–time development of jets as well as for tagging jets of a certain flavour.

Stable particles within jets are identified by special detector components measuring the time-of-flight, Čerenkov radiation, the dE/dx loss or, in particular for photons, also the electromagnetic showering. Resonances are found by forming the appropriate particle combinations and searching for peaks in the invariant mass distribution. This search is hampered by the high multiplicity in a jet giving rise to a large combinatorial background. In particular, this affects the measurement of broad strongly decaying resonances. Long lived particles are easier to identify since their decay originates from a secondary vertex and thus the background can be strongly reduced.

These additional requirements, however, introduce experimental distortions and inefficiencies reducing the data sample available. They sometimes lead to substantial systematic errors and allow one to measure only part of the momentum spectrum. In addition some particles are very difficult to identify. The absence of a measured yield or distribution is often just due to experimental problems and not due to dynamical reasons.

4.1. The overall particle yield

Several kinds of mesons both of different spin and flavour have been identified. Mesons with $J^P = 0^+$, 0^-, 1^- and 2^+ have been found and their fragmentation function has been measured in most of these cases. The average yields per event of mesons consisting of u, d and s quarks measured at 10 and 30 GeV*) are listed in table 4.1.1 (partly taken from a compilation of Saxon [118], all values at

Table 4.1.1
Yields of identified mesons. N_s = number of strange quarks

J^P	N_s	type	$W = 10$ GeV	$W \sim 30$ GeV	ref.
0^-	0	π^0		5.9 ± 0.3	[121–124]
		$\pi^\pm$	8.3 ± 0.4	10.9 ± 0.3	[125, 126]
	1	K^0, $\bar{K}^0$	0.92 ± 0.12	1.46 ± 0.06	[127–132]
		$K^\pm$	1.3 ± 0.2	1.51 ± 0.10	[125, 126]
		η		0.64 ± 0.15	[121]
0^+		$f_0(975)$		$>0.05 \pm 0.02$	[133]
1^-	0	ρ^0	0.50 ± 0.09	0.80 ± 0.05	[134–137]
	1	K^{*0}	0.38 ± 0.09	0.54 ± 0.06	[134, 136, 138]
		$K^{*\pm}$	0.45 ± 0.08	0.87 ± 0.18	[126, 137]
	2	ϕ	0.08 ± 0.02	0.08 ± 0.01	[139, 140]
2^+	0	$f_2(1270)$	seen	0.14 ± 0.04	[133]
	1	$K_2^{*0}(1430)$		0.12 ± 0.06	[133]

---

*) The data from PETRA ($W \sim 35$ GeV) and PEP ($W \sim 29$ GeV) have been considered together. The difference expected due to the different energies is in most cases negligible compared to the statistical and systematic error.

$W = 10$ GeV were taken from ref. [119]). Charm and bottom hadrons are special and will be discussed in a separate section.

The values include decay products from resonances. The spin and flavour dependence of the primary fragmentation can only be inferred from a complicated unfolding of the contributions from prompt production and decays involving several assumptions about yields of not yet measured resonances, their fragmentation function, their exact branching ratios etc. This is most easily realized with a Monte Carlo program including primary production and decays. How strongly decays affect the measured distributions can be estimated from a simulation study using the LUND algorithm. In the case of pions the prompt production contributes only ~15% of the total finally detected pion yield. The fraction of prompt ρ^0's, however, is considerably higher (75%). The dynamical properties of jet development are reflected more closely in the spectra of heavy particles that are only rarely decay products.

Baryons are produced with a much smaller rate than mesons. Still, their yield is larger than first expected and came out as a surprise. It triggered the development of special models for their production. The rates measured so far at $W \sim 10$ and ~30 GeV are listed in table 4.1.2 (partly taken from ref. [118]). The results at 10 GeV are due to refs. [119, 120]. Assuming the same proton and neutron yields it can be seen that together about 1.3 baryons and antibaryons are produced in an average event at $W = 30$ GeV, i.e. about 7.5% of all particles in an event are baryons. As in the case of mesons the feed through from a decaying particle to its descendents has to be known for estimating the production of prompt baryons. Due to their higher mass and the conservation of baryon number the properties of final baryons resemble those of the prompt production more closely.

The final particle yield per event $(1/N)(\mathrm{d}N/\mathrm{d}m)$ measured around $W = 30$ GeV is displayed in fig. 4.1.1 as a function of the particle mass. Only one sign of charge was considered per particle type. The measurements of the various experiments for each particle species are in good agreement with one another. The yield is a steep function of the particle mass and exhibits a surprising regularity. It follows an exponentially falling distribution

$$\mathrm{d}N/\mathrm{d}m \sim a\,\mathrm{e}^{-5m} \tag{4.1.1}$$

over about three orders of magnitude. The errors for the individual measurements are rather large and hamper the interpretation. Beyond the global regularity that all particle yields are confined in a rather narrow band, another trend is visible.

There seems to be some dependence on the flavour of the quarks contained in the hadrons and the

Table 4.1.2
Yields of identified baryons. N_s = number of strange quarks

	type	N_s	$W \sim 10$ GeV	ref.	$W \sim 30$ GeV	ref.
Octet	p	0			0.64 ± 0.08	[125, 126]
	Λ	1			0.23 ± 0.01	[127, 128] [141, 142]
	Σ^0	1	$0.33^{+0.11}_{-0.09} \times N(\Lambda)$	[120]		
	Ξ	2	$0.08 \pm 0.01 \times N(\Lambda)$	[120]	0.019 ± 0.005	[143–146]
Decuplet	Δ^{++}	0	$<0.12 \times N(\mathrm{p})$		<0.09	[147]
	Σ^{*+}	1	$0.05 \pm 0.005^{+0.007}_{-0.005} \times N(\Lambda)$	[120]	0.017 ± 0.005	[146]
	Ξ^{*0}	2	$0.26 \pm 0.04^{+0.04}_{-0.02} \times N(\Xi)$	[120, 148]	$<0.35 \times N(\Xi)$	[145]
	Ω^-	3	$(5.4 \pm 1.8 \pm 1.2) \times 10^{-3} \times N(\Lambda)$	[120]	$0.014 \pm 0.006 \pm 0.004$	[149]
Dibaryon	d	0	$>1.6^{+1.0}_{-0.7} \times 10^{-5}$	[150]		

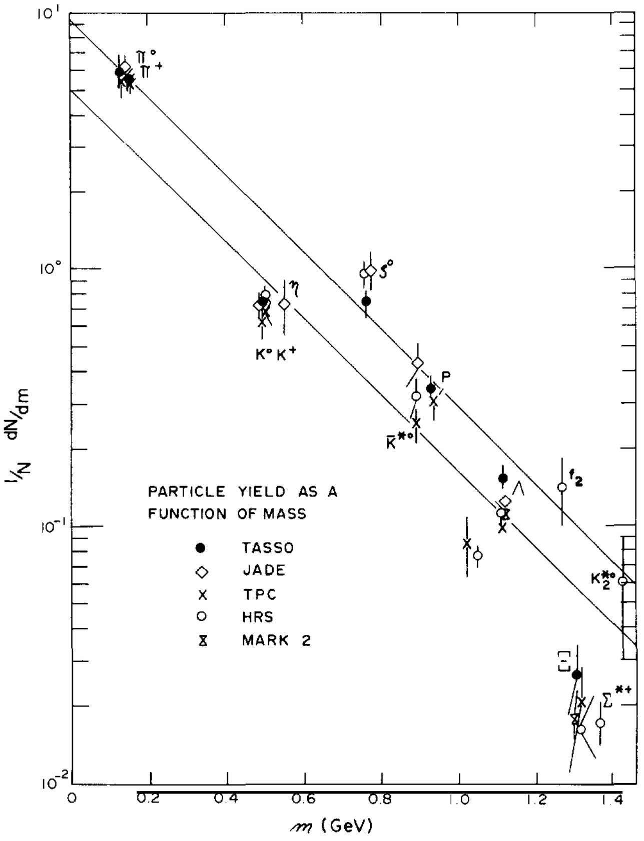

Fig. 4.1.1. Yield of final baryons and mesons as a function of the particle mass for $W \sim 30$ GeV. The measurements are taken from table 4.1.1 and 4.1.2. The two lines correspond to an exponential dependence of the yield (formula (4.1.1)). They approximate the yields of hadrons with no and with one strange quark.

baryon number of the hadrons. An example is the K^0, K^+ yield which is about the same as that of the ρ^0, though its mass is considerably less. The same is true for particles with two strange quarks: the ϕ yield lies considerably below the band of particles made out of u and d quarks, although its total strangeness is zero. This is another indication that the structure of jets is not due to longitudinal phase space. Moreover, it indicates that the particle production depends primarily on the quark content and not on the quantum numbers of the hadrons themselves. Thus hadronisation proceeds via the emission of quarks. The yield of the particles containing strange quarks is below that of only u and d quarks corresponding to values of $a_{u,d} \sim 9$ and $a_{s,(u,d)} \sim 5$. The measurements of particles with two strange quarks are still too scarce to give a reasonable value. It should be noted that this regularity is in particular surprising as the particles originate from what is generally believed to be different sources (see however ref. [50]): from the primordial fragmentation and decays[*)]. The contributions from these two sources differ for the various kinds of particles.

[*)] In fact the decay properties have to induce some breaking of this simple pattern. For example, the Σ^0 decays almost 100% electromagnetically into Λ's: ($\Sigma^0 \rightarrow \Lambda\gamma$). Since their masses are quite comparable, the exponential mass dependence would imply a ratio of 0.68 between the Σ^0 and the Λ-yield. Λ's from other sources or promptly produced Λ's would therefore contribute only about a third of the whole yield. This is difficult to conceive (I am grateful to M. Dittmar for this argument). Also the ratio of Σ^0 to Λ production at $W = 10$ GeV (see table 4.1.2) is inconsistent with such a pattern. Note, however, that the regularity observed should be due to strong interactions, some breaking due to electromagnetic and weak decays is therefore not surprising.

A compilation of the production yield in terms of

$$R_h = \frac{\sigma(e^+e^- \to h + X)}{\sigma(e^+e^- \to \mu^+\mu^-)}$$

as a function of the c.m. energy W is shown in fig. 4.1.2 (from refs. [127, 118]). Whereas for lower energies $W \leq 10$ GeV the production rate of heavy particles increases more strongly than that of light particles, the ratios of the single particle rates change only slowly for higher c.m. energies.

4.2. Fragmentation functions of identified particles

The fractions of charged stable hadrons as measured by the TASSO collaboration are displayed in fig. 4.2.1 for different c.m. energies as a function of the momentum [151, 125]. Also shown are the results from the TPC [126] and HRS collaboration [129] at $W = 29$ GeV. In general the data from the various experiments at $W \sim 30$ GeV agree with one another. TASSO finds a somewhat higher kaon yield at momenta of ~600 MeV.

Particles at low momentum (~300 MeV) are nearly exclusively pions. Their fraction decreases to about 60% for the highest momenta. The fractions of protons and kaons are steadily increasing with momentum. Protons are always produced less than kaons. At momenta above 10 GeV about 15% of the particles are protons. A comparison of the data at different energies suggests that these fractions do only depend on the momentum but hardly vary with W.

As discussed in section 2 and section 3.2, the more appropriate variable to study fragmentation is the scaled momentum $x = 2E/W$. In figs. 4.2.2a–c the fragmentation functions of different mesons are compared. In fig. 4.2.2a a selection of measurements of pseudoscalar particles is displayed, in fig. 4.2.2b that of vector particles and 4.2.2c shows yields of mesons with the same quark content but with different spin.

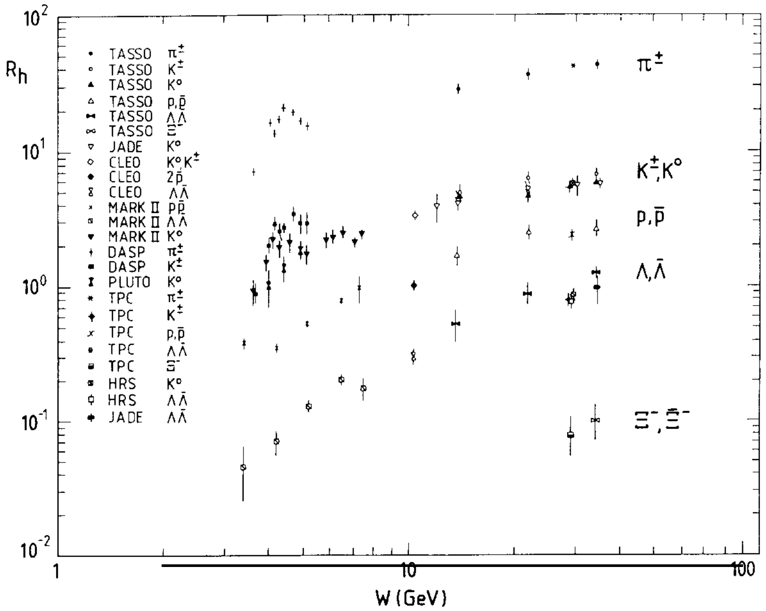

Fig. 4.1.2. Dependence of the yield of hadron h on the c.m. energy W in terms of $R = \sigma(e^+e^- \to h + X)/\sigma(e^+e^- \to \mu^+\mu^-)$ (compilation from ref. [118]).

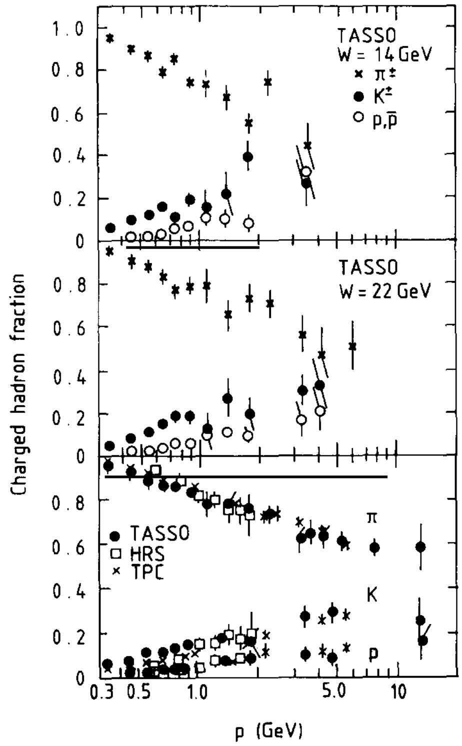

Fig. 4.2.1. Fraction of the yield of charged pions, kaons, and protons as a function of momentum for various c.m. energies $W = 14$, 22 and 30 GeV [125, 151, 126, 129].

Due to the rather substantial errors and since the various sources contribute differently to the various yields only rather qualitative conclusions can be drawn:

(i) All distributions are steeply falling over two to three decades for an increase of x from $x = 0$ to $x \sim 0.7$. This means in particular that the total particle yield discussed in section 4.1 is almost exclusively determined in the narrow region of $x \leq 0.1$.

(ii) Most of the differences between the shapes of the various fragmentation functions are in the low-x region. In particular particles like pions that are frequently decay products exhibit a steeply falling distribution here.

(iii) At high x-values the fragmentation functions have a quite similar shape. The precise dependence is, however, hidden under still considerable statistical and systematic errors.

The measurements can be well described with the standard fragmentation models. The cross sections of π^0 [123], K^0, ρ^0 and $K^*(892)$ [134] are displayed in fig. 4.2.3a together with the outcome of a simulation using the LUND Monte Carlo. In fig. 4.2.3b the inclusive cross section of the tensor mesons $f_2(1270)$ and $K_2^*(1430)$ [133] are compared to the prediction of the Webber model. In both cases the agreement is very good.

Compared to the overall yield the x-distributions allow a more reliable unfolding of the contributions from prompt production and decays and thus constrain the fragmentation parameters within a model. As discussed in section 2 in the Independent Jet Model and LUND model these parameters are in particular the softness of the fragmentation function, the relative probability for an $s\bar{s}$ pair to fluctuate out of the vacuum, and the ratio of the production rates of vector and pseudoscalar particles.

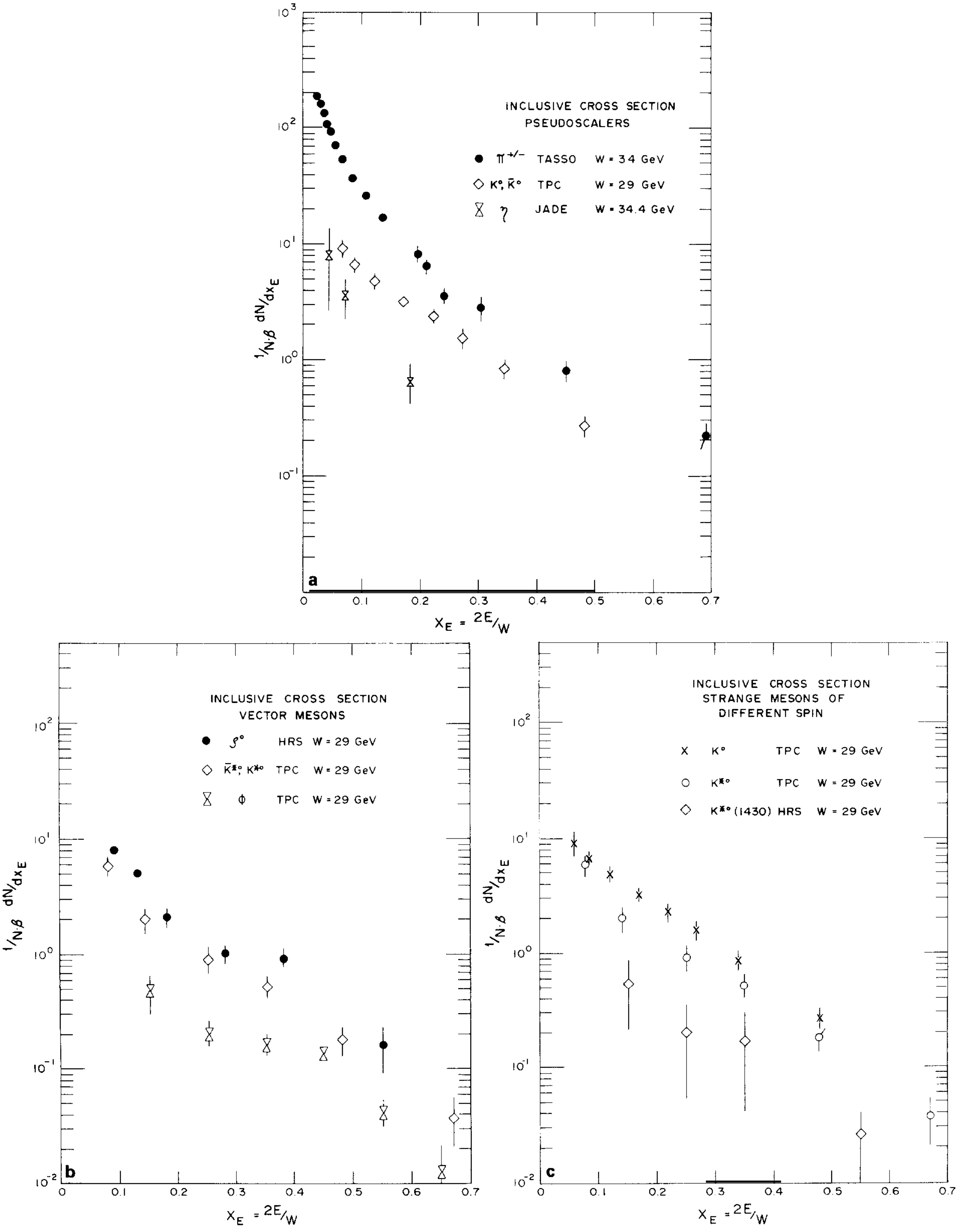

Fig. 4.2.2. Fragmentation functions of various mesons (a) pseudoscalar particles [151, 131, 121], (b) vector particles [134, 138, 139], (c) strange particles of different spin [131, 138, 133].

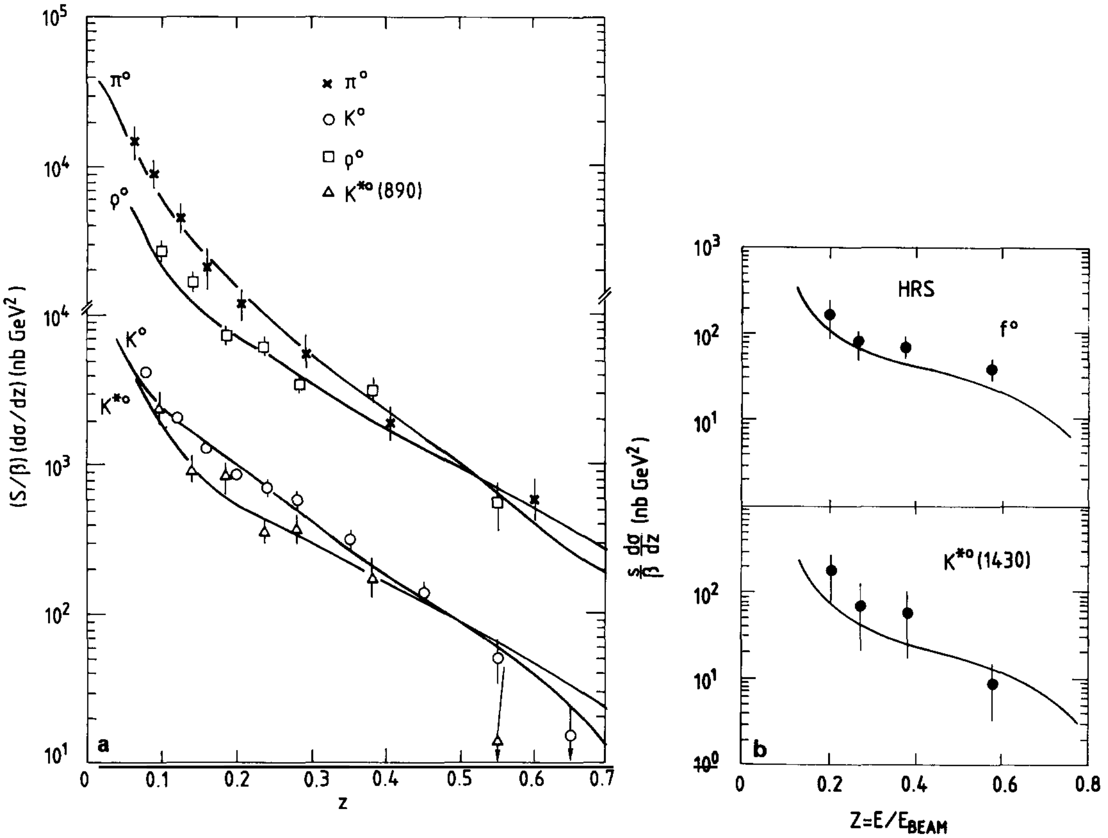

Fig. 4.2.3. Comparison of meson fragmentation functions and model predictions. (a) The LUND–Monte Carlo is compared to pseudoscalar and vector meson production (from ref. [134]). (b) The Webber–Monte Carlo is compared to tensor meson production (from ref. [133]).

The simulation programs rely on certain assumptions such as on the shape of the fragmentation functions or the production of pseudoscalar and vector particles only. A change in these assumptions will affect the outcome for the parameters within the model. The discoveries of the f_2, the $K_2^*(1420)$ and the $f_0(975)$ in jets [133] shows that these assumptions are only approximately true. In this sense the values obtained for the various parameters are only valid within a certain model. In addition the measurements have to be frequently restricted to only some part of the total x-spectrum. In particular the low x-region, which dominates the overall yield, is difficult to access experimentally (see e.g. figs. 4.2.2 and 4.2.3). One corrects for these losses by assuming some shape of the fragmentation function. It is obvious that such an extrapolation can cause substantial systematic uncertainties. Therefore it is difficult to estimate the systematic error in a reliable way and we only will quote approximate numbers for the relevant parameters. In spite of these limitations, these parameters provide useful guidelines and are necessary to proceed towards a consistent simulation of fragmentation.

In general the fragmentation parameters are assumed to be independent of the flavour and spin of the hadrons, with the notable exception of charm and bottom hadrons (see section 4.5).

The probability p_s to pick an s-quark out of the sea has been determined from the ratio of K^0/π, ϕ/K^{*0}, and K^*/ρ^0 production. A compilation of the various measurements is given in ref. [118]. The fit results are consistent with one another and give

$$p_u = p_d \sim 0.425\,, \qquad p_s \sim 0.15\,.$$

The ratio between pseudoscalar (P) and vector (V) particle production has been obtained by comparing π/ρ, K/K* and D^0/D^* production. No correction has been made for the feed-through from tensor particles or other excited states. For example, the feed-through from the direct decays $K_2^*(1420) \to K^*$ or K^0 contributes about 10% of the total K*(892) and 8% of the K^0 yield. The data are compatible with

$$V/(P+V) \sim 0.6 .$$

No value has been given for the production of tensor particles, the results from the HRS collaboration suggest that they are produced about five times less than vector particles.

In alternative schemes the parameters are proposed to depend on the spin and flavour of the particles produced. Mass dependent terms occur in the left–right symmetric fragmentation function (see eq. 2.2.5), which, however, predicts noticable variations only for particles with heavy quarks (charm, bottom, etc.). Similarly the production ratio of vector and pseudoscalar particles is suggested to depend on the masses [60, 152]. Measurements of the $V/(P+V)$ ratio are shown in fig. 4.2.4 as a function of the ratio of their masses (M_V/M_P) (compiled in ref. [134]). As can be seen the relative yield can be described by a constant as well as by some mass dependence like

$$\frac{P}{V} = \frac{1}{3}\left(\frac{M_V}{M_P}\right)^{\alpha} . \tag{4.2.1}$$

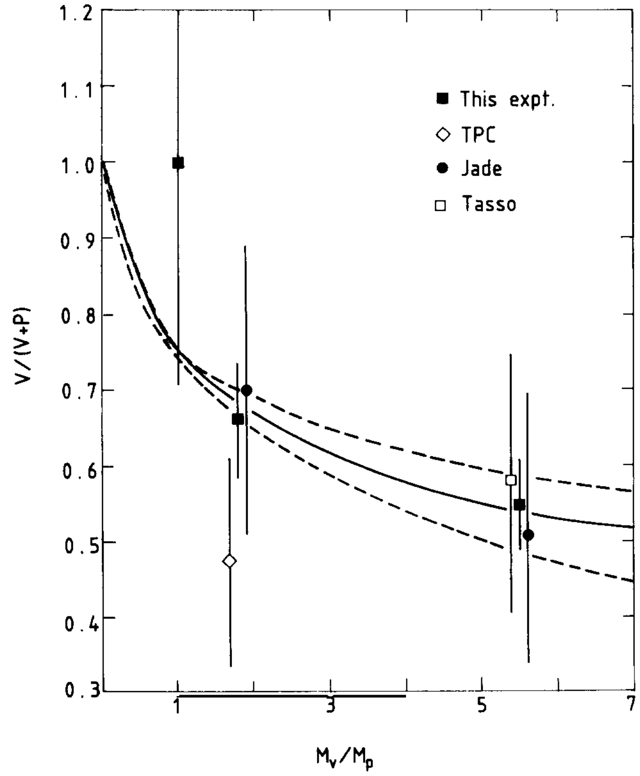

Fig. 4.2.4. Relative production yield of vector over pseudoscalar mesons as a function of the ratio M_V/M_P (from ref. [134]).

Both the JADE [137] and the HRS collaboration [134] have fitted the data to this form and find $\alpha \sim 0.5$. Note that the value of α depends heavily on the D*/D ratio which is still only marginally known (see section 4.5.7).

Since the simulation algorithms describe the particle distributions quite well, they can be used for estimating the contributions of certain kinds of particles to the production. Figures 4.2.5a,b show the contributions to the total charged pion cross section and the ρ^0 cross section. As already pointed out in the previous section, most of the pions are decay products. In particular in the low-x region the fraction of prompt pions is tiny. The ρ^0 spectrum reflects the primary fragmentation function quite well (note, however, that contributions from tensor particles are not included).

Using the simulation program one finds that although an average event contains ~13.5 charged and ~14 neutral final particles at $W = 35$ GeV, in total only 10 neutral and charged particles are produced directly.

4.3. Baryon production

The same questions raised for mesons are also valid for baryon production in a jet. The extra dimension in modelling baryon production is to find how a quark manages to pick up two instead of one parton to form a hadron. The first measurements of baryon production in jets at PETRA showed a rather high abundance of baryons and were followed by a variety of models describing their production mechanism. These models can be classified according to their basic ideas as follows.

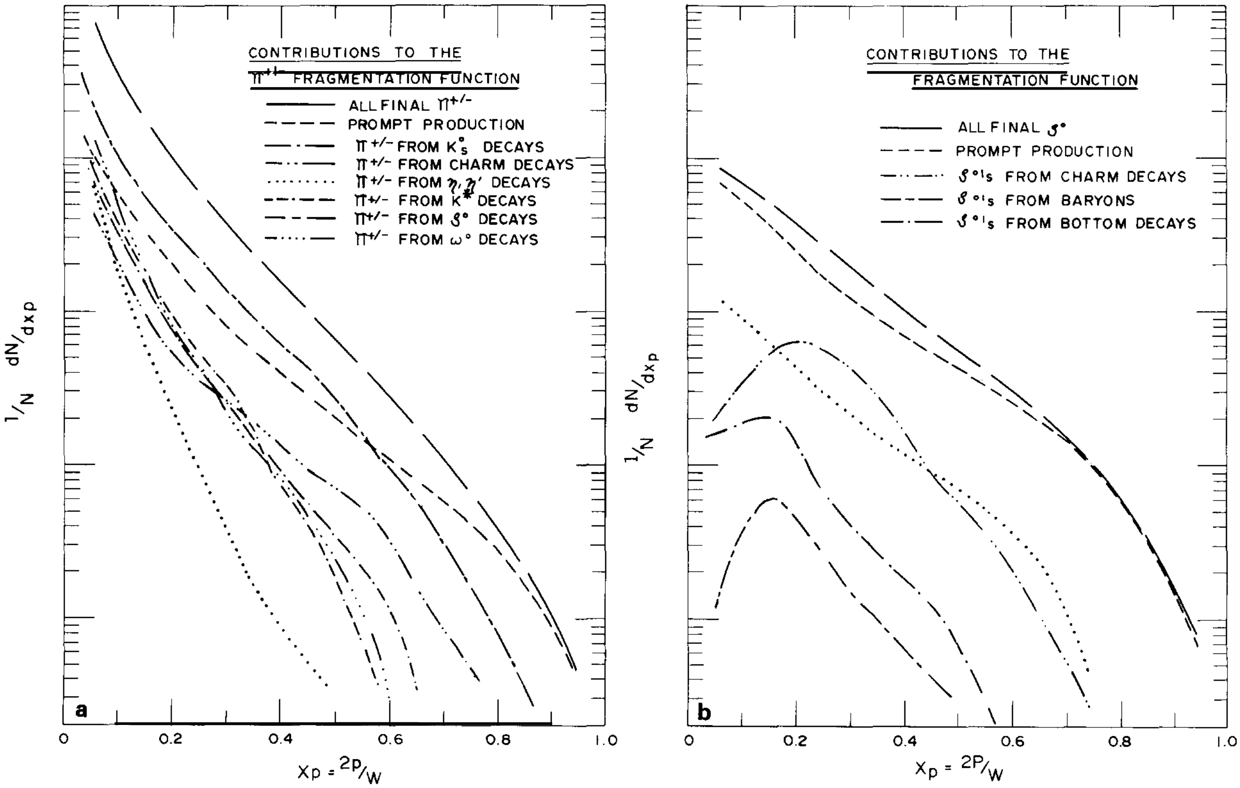

Fig. 4.2.5. Monte Carlo calculation of the contribution of various sources to the yield of final particles as a function of x_p (a) for pions, (b) for ρ^0's.

(a) *Stochastic parton production.* The model of Černy et al. [153] is one example. In this approach partons are produced according to a limited p_T phase space. Within this model mesons are formed if a quark and an antiquark are adjacent in rapidity, a baryon (antibaryon) if there exists a local accumulation of three quarks (antiquarks). The baryon number in such a model is therefore only globally conserved. A baryon and an antibaryon can be kinematically quite far apart. The ratio of mesons and baryons is fixed by combinatorics. The ratio of the various kinds of baryons is related to the product of the probabilities to pick each quark contained in a baryon individually out of the sea. In practice both the ratio of meson to baryon yield and the various production rates of baryon types can be changed by hand. However, it would invalidate the basic idea of the model.

(b) *Diquark model.* To incorporate baryon production into the mechanism of hadronisation, a variety of models introduced the concept of diquark loops (fig. 4.3.1). Several different ways to realize this have been suggested.

(b1) Diquarks couple directly to the virtual γ or the Z^0. Such a mechanism has been perceived by the Stockholm group [16] and Meyer [154] as a way to describe the baryon production at high x-values. Such a scheme would result in a pair of leading baryons in opposite jets.

(b2) Instead of picking a $q\bar{q}$-pair out of the sea, a quark combines with a diquark leaving an anti-diquark to form an antibaryon in the subsequent step of fragmentation (fig. 4.3.1a). The most frequently applied models are due to Meyer [154] and in particular due to the LUND group [155], a similar mechanism has been suggested in ref. [156]. Within these models the baryon number is conserved locally, the baryon–antibaryon pair is supposed to be produced with similar rapidities. To incorporate this idea into the standard fragmentation models requires additional free parameters. Again

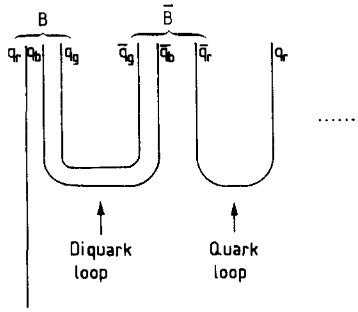

a) Simple diquark model

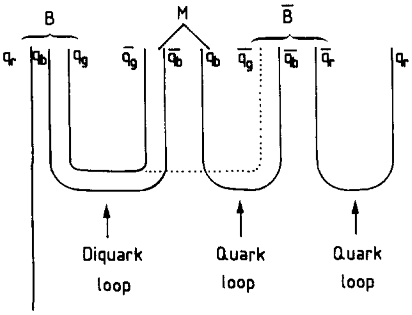

b) Popcorn model

Fig. 4.3.1. Models of baryon production. (a) Via a "pointlike" diquark/antiquark pair; (b) Popcorn model. The quark indices refer its colour.

they have to be adjusted by comparing the model to the data. Each kind of diquark has in general a different probability to fluctuate out of the vacuum. Meyer correlates the probability of producing a diquark with its flavour content: sd-diquarks are reduced by a factor $p(\mathrm{s})/p(\mathrm{u})$ compared to ud-diquarks, ss-diquarks by a factor $(p(\mathrm{s})/p(\mathrm{u}))^2$. He thus introduced elements of a stochastic production of diquark flavours into his model. Within the LUND program the diquark is treated as an entity and its probability is determined by the mass of the diquark according to eq. 2.2.8. However, since these masses are not known*⁾, the probability can be adjusted to agree with the data. Strange diquarks are suppressed since they are assumed to be more heavy. Out of the same reason decuplet baryons which are formed by spin-1 diquarks are supposed to be produced less frequently.

Diquark scattering has been observed in pp-collisions [158] with a strong Q^2 dependence as anticipated from a diquark form factor. Other measurements, too, contradict the concept of pointlike diquarks such as the total hadronic cross section in e^+e^- annihilation at high Q^2 which leaves no room for a (large) contribution in addition to gluon radiation (see however [16]). Therefore models of extended diquarks have been introduced.

(b3) One way to introduce extended diquarks is to assume that a quark–antiquark pair $\mathrm{q}^{n+1}\bar{\mathrm{q}}^{n+1}$ not matching the colour of an unsaturated diquark D_n fluctuates out of the vacuum. The squark content is reshuffled such that a meson is produced leaving a modified diquark e.g. (lower indices denote the colour, upper indices its rank) (see fig. 4.3.1b)

$$(\mathrm{q}_b^{n-1}\mathrm{q}_r^{n}) + (\bar{\mathrm{q}}_r^{n+1}\mathrm{q}_r^{n+1}) \rightarrow (\mathrm{q}_r^{n}\bar{\mathrm{q}}_r^{n+1}) + (\mathrm{q}_b^{n-1}\mathrm{q}_r^{n+1}) \cdots . \qquad (4.3.1)$$

It takes the production of at least one other $\mathrm{q}\bar{\mathrm{q}}$-pair to form a colour neutral baryon ("Popcorn model") [159–161]. As a result the production sequence baryon–antibaryon–meson is replaced by baryon–meson–antibaryon. Other schemes just convolute the probabilities for picking out two instead of one quark. In all cases the extended diquark picture predicts a fragmentation function that is softer than that of a pointlike diquark.

(c) *Cluster decay.* Within the cluster decays frequently used in QCD shower algorithms, colour neutral clusters are formed that decay isotropically into two particles. In its most simple version the kinds of particles produced are determined by conservation of quantum numbers and phase space. Depending on the mass of the cluster they can decay into baryons. Since the cluster masses are typically 1–2 GeV and fall off rapidly towards higher masses, baryon production is suppressed. The low q-value in a decay of a cluster into a baryon–antibaryon pair leads to a short range baryon number compensation. The approach can be modified by introducing special probabilities to include diquark production.

These models can be tested experimentally by measuring the overall baryon yield, the relative abundance of the different kinds of baryons, the x-distributions and in particular the way the baryon number is compensated. The latter issue is related to the dynamics of jet evolution in a more general way, its discussion will be deferred to section 8. Still, the first three points already introduce substantial constraints on the various models.

For example the prediction of the stochastic model (a) for the overall baryon yield is twice as high as the measurement [162]. These discrepancies can be cured by supplementing the model with additional free parameters. These ad hoc corrections, however, sometimes weaken the basic ideas of the models.

---

*⁾ Estimates exist e.g. within the potential model [157].

More challenging is the correct prediction of the relative yields of the various types of baryons. Within the LUND model the various particle yields can be described with a few basic parameters that have to be inferred from the data:

(i) The probability to pick out a diquark instead of a quark is found to be $P_{qq} \sim 0.07$–0.1 [143, 127].

(ii) A value of $d = (\mathrm{us}/\mathrm{ud})/(\mathrm{s}/\mathrm{d}) = 0.2$–$0.35$ for the extra suppression of strange diquarks has been obtained by the TASSO [127], TPC [142] and MARK2 [145] collaborations by comparing their Ξ and Λ cross sections. The HRS collaboration [163] digresses from this value and obtains $d = 0.89 \pm 0.10^{+0.56}_{-0.16}$ by varying the branching ratio $B(\Lambda_c \to \Lambda + X)$ and the number of charmed baryons produced and by comparing the Λ fragmentation function and the production rate of $\Lambda\bar{\Lambda}$-pairs to the LUND model. For B a value of 0.23 ± 0.10 [164] was assumed.

(iii) The relative suppression of spin-1 diquarks compared to spin-0 diquarks is $P_1 = (\mathrm{ud})_1/(\mathrm{ud})_0 \leq 0.08$ with 95% CL [147]. This value is in agreement with the result on Σ^* production in ref. [146] which can be described by $P_1 \sim 0.05$. The ARGUS collaboration [120] finds some indication that the ratio of spin-1 to spin-0 diquarks depends on the strangeness content of the diquarks. For example they find $N(\Xi^*)/N(\Xi) \sim 1/4$. In comparing the prompt production one should notice that the Ξ^* decays with 100% into Ξ, thus the ratio of prompt production is about 1/2. On the other hand $N(\Sigma^*)/N(\Lambda) \sim 0.05$ corresponding to a ratio of prompt production of about ~0.2.

As already discussed in the case of mesons, these numbers have to be used with caution and should be interpreted as general guidelines, but not as precise measurements.

With the appropriate parametrisation both the size and spectrum of baryon production can be well described in the LUND model. This can be seen from fig. 4.3.2, where the fragmentation functions for various octet baryons are reproduced together with curves obtained with the LUND simulation program. For the model calculation the same fragmentation function for baryons and mesons has been assumed. The feed through of Ξ's into Λ's and Λ's into protons has been included.

These results are already in contradiction to some concepts of baryon production. For example, the straightforward assumption that the ratio of decuplet to octet production equals that of vector to pseudoscalar production (see ref. [153]) is ruled out. Also the expectation of $d = 1$ for stochastic qqq accumulation without diquarks is in contradiction to most experiments. However, this result is still disputed. The most simple cluster model in the Webber–Monte Carlo has difficulties in describing the suppression of Ξ's and decuplet baryons. Some of these deficiencies can be cured by introducing additional parameters, by, for example, introducing a splitting $g \to D + \bar{D}$ where D denotes a diquark.

The measurement of a surprising large yield of Ω-production by MARK2 [149][*] digresses from the simple prediction of the LUND group. Note that the much lower yield determined by ARGUS [120] at $W = 10\,\mathrm{GeV}$ is affected by phase space. The remarkable result is that the Ω yield $(0.014 \pm 0.006 \pm 0.004)$ is larger than the upper limit of the Ξ^{*-} (<0.008). Since the quark content of the Ω is $(\mathrm{s} + \mathrm{ss}_1)$, but of the Ξ^{*-} $(\mathrm{s} + \mathrm{ds}_1, \mathrm{d} + \mathrm{ss}_1)$, where the lower index 1 indicates spin-1 diquarks, one would expect at least one additional suppression due to the strange instead of the d-quark contained in the Ω. The LUND prediction for Ω-production is

$$p_\Omega \propto d^2 (p_s/p_u)^2 p_s p_1 p_{\mathrm{diq}} \sim 2 \times 10^{-5} \tag{4.3.2}$$

or about 0.0002 Ω's per event in gross disagreement with the data. It seems difficult to accommodate all

---

[*] Measurements of Ω-production from other experiments (TASSO, TPC) at $W \sim 30\,\mathrm{GeV}$ are contained in an internal report [165] and a conference contribution [166], they are quoted in ref. [167] but never made it to a publication.

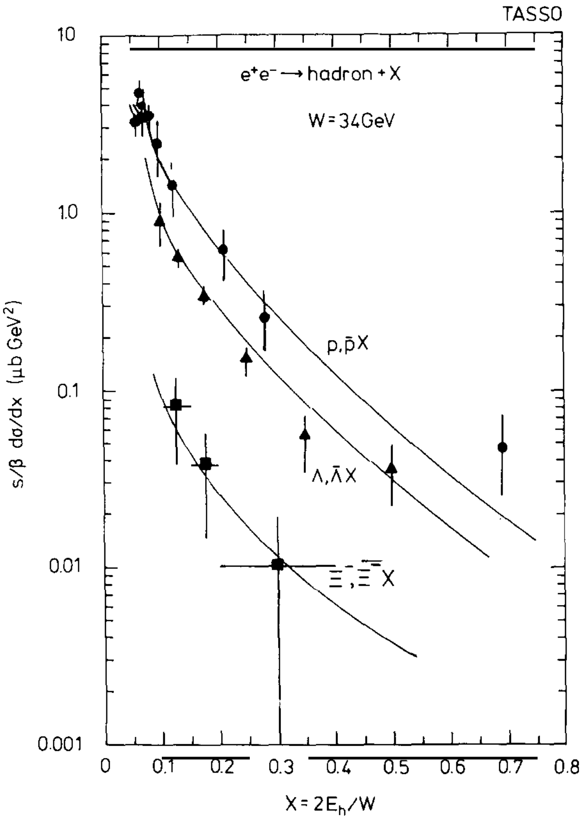

Fig. 4.3.2. Fragmentation function of various baryons at $W = 34$ GeV [144]. The curves are obtained with the LUND Monte Carlo.

measurements of the baryon sector with the simple parametrisation of the LUND group. Of course it would be interesting having more reliable calculations of the diquark masses to estimate the production yields in jets. Final conclusions require more precise data on the decuplet baryons.

All the data are in very good agreement with the idea of diquarks. In particular the reduced yield of $\frac{3}{2}^+$-baryons can be naturally explained in these models. Not much information is available for a discrimination between the different versions of the diquark model. The ARGUS collaboration [120] compared their measurements of ratios of baryon yields to the popcorn and the pointlike diquark model. The decuplet baryons are less suppressed in the popcorn model since in that case the diquark and antidiquark are not both required to be in a spin-1 state. However, the measurements are not conclusive enough to discriminate between these two approaches.

It is remarkable that the fragmentation function assuming pointlike diquarks can describe the baryon yield even at high x. A comparison of the proton fraction as a function of x_p [125, 126] with a possible parametrisation for extended diquarks

$$f(\eta) \propto \frac{1-\eta}{\eta} \exp\left(-\frac{b \cdot m^2}{\eta}\right), \tag{4.3.3}$$

where η is the light cone variable defined in eq. (2.2.1), shows that in the decisive region of high x the data are not accurate enough to discriminate between pointlike and extended diquarks (fig. 4.3.3 taken from ref. [168]).

In addition to the fragmentation function several experiments determined the transverse momentum spectrum of the final hadrons. As an example the Λ yield as a function of p_T^2 is displayed in fig. 4.3.4 together with that of all charged particles [141]. The Λ's have a considerably wider distribution. The MARK2 collaboration parametrised the yield by the sum of two exponentials

$$\frac{d\sigma}{dp_T^2} = c_1 \exp\left(-\frac{p_T^2}{2d_1^2}\right) + c_2 \exp\left(-\frac{p_T^2}{2d_2^2}\right) \tag{4.3.4}$$

and found consistent results of the d's for the two data sets

$$d_1^\Lambda = 0.350 \pm 0.035 \text{ GeV}/c\,, \qquad d_2^\Lambda = 0.655 \pm 0.055 \text{ GeV}/c\,,$$

$$d_1^\pm = 0.310 \pm 0.005 \text{ GeV}/c\,, \qquad d_2^\pm = 0.627 \pm 0.014 \text{ GeV}/c\,.$$

The relative contributions of those two components, however, is different. This can be explained by the different importance of the various contributions to the p_T-spectrum. According to the standard ideas about hadronisation, those are (i) the primordial p_T of the hadrons (cf. section 2.2) of ~440 MeV; (ii) the transverse momentum due to decays of ~300 MeV; (iii) in a fraction of events the transverse momentum due to hard gluon emission which leads to particles of high transverse momentum ~1 GeV.

Since the large majority of the charged particles are decay products from heavier resonances, but a high fraction of Λ's is directly produced, those are expected to have a wider spectrum extending to larger values of p_T.

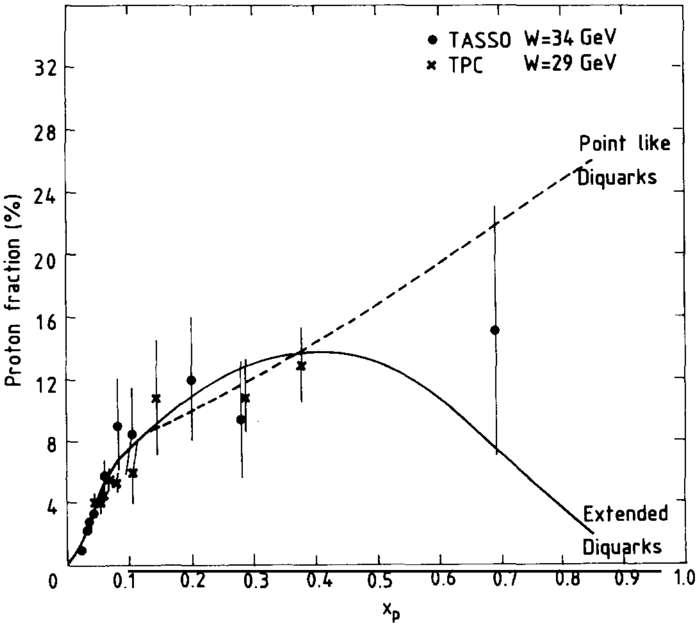

Fig. 4.3.3. Proton fraction as a function of x_p measured at $W = 29$ and 34 GeV together with model predictions assuming pointlike (dashed curve) and extended diquarks (solid line) [168].

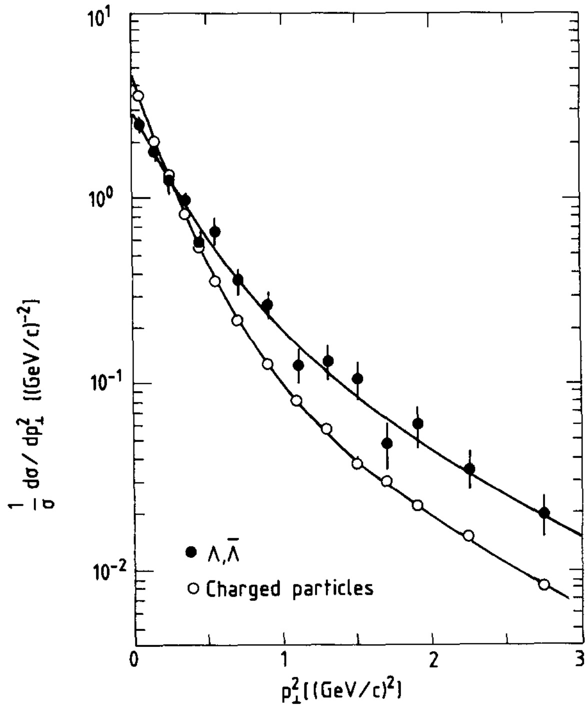

Fig. 4.3.4. p_T^2 spectrum of Λ production (full circles). Also shown is the spectrum of all charged particles. Both distributions are normalised [141]. The curves represent fits to the sum of two exponentials (see text).

In table 4.3.1 we list other measurements. The measurements are difficult to compare since they refer to different jet axes and have been determined in different x and even p_T intervals. Due to the different weight of the various contributions to the transverse spectrum and the different conventions applied one cannot meaningfully determine an average value. For those particles that are not frequently decay products the measurements indicate an average $\langle p_T^2 \rangle$ of about 0.5 GeV^2. The values for σ*) tend to be smaller than the corresponding value of $\sigma \sim 0.5$ GeV. This can be explained by the special parametrization and cuts applied. It should be noted that the p_T spectrum of all particles is well described in the standard fragmentation models assuming the same primordial p_T (e.g. the LUND group sets $\sigma_q \sim 320$ MeV, see eq. (2.2.6)) for all quark/diquark species.

Other results on baryon production will be discussed in sections 4.5, 5.2, and in particular in sections 8.3 and 8.4 where results on the local compensation of quantum numbers are presented. These are more sensitive to basic assumptions of the various models.

4.4. QCD effects in the particle spectra

The QCD effects in the fragmentation have been discussed in sections 3.2.2 and 3. As was pointed out mass effects wash the QCD properties out both for the predicted dip in the rapidity and the scale breaking observed for x_p-values >0.2. The use of identified particles should increase the sensitivity to the dynamics of jet evolution.

---

*) Assuming an exponential fall-off with p_T^2 it follows $\sigma = (\langle p_T^2 \rangle / 2)^{1/2}$.

Table 4.3.1
Average squared transverse momentum of various particle species

particle	$\langle p_T^2 \rangle$ [GeV^2]	σ [Gev]	ref.
all charged	0.53 ± 0.05		[181]
	0.311 ± 0.02		[3]
		0.31 ± 0.005	[141][a)]
$\pi^\pm$	$0.30 \pm 0.01 \pm 0.02$		[131]
K^0	$0.51 \pm 0.10 \pm 0.18$		[131]
		0.31 ± 0.01	[127]
K^{*0}	$0.57 \pm 0.07 \pm 0.13$		[131]
ϕ	1.00 ± 0.40		[139]
Λ^0	0.56 ± 0.07		[181]
		0.38 ± 0.04	[127]
		0.350 ± 0.035	[141][a)]
D^*	0.62 ± 0.08		[181]
		$0.36 \pm 0.02 \pm 0.04$	[192]

[a)] only first exponent of 4.3.2 taken.

The scaled cross section $(s/\beta)(\mathrm{d}\sigma/\mathrm{d}x_E)$ for pions and kaons, respectively, measured at c.m. energies betwen 5.2 GeV [169] and 34 GeV [151] is shown in fig. 4.4.1a and b. No clear interpretation is possible due to the high statistical and systematic errors. Whereas for $x \geq 0.15$ the particle yield is significantly higher at $W = 5.2$ GeV than at the PETRA energies, very little variation is visible in the PETRA range only.

The use of a specific type of particle allows also a more reliable check of the prediction for a drop in the particle yield due to coherent gluon emission discussed in section 3.2.2. The particle yield is shown in terms of $\mathrm{d}N/\mathrm{d}\ln(x_E)$ in fig. 4.4.2 (the data are taken from ref. [126]). Here the scaled energy instead of the scaled momentum has been used. In the case of the pions there is some indication of a decrease for $x_E < 0.03$ below the plateau values with a significance of $\sim 7\sigma$–8σ. Between $0.03 < x_E < 0.06$ the yield is about constant and then drops for higher x-values. No depletion at low x-values is observed for kaons and protons. It seems to be premature to interpret these results as evidence for the coherence effect predicted, in particular since also phase space effects would qualitatively lead to such a decrease.

4.5. Heavy quarks

The identification of charmed and bottom hadrons in jets provides new methods to tackle new questions of jet development. The special flavour of these measurements is that hadrons of known rank can be examined. The results obtained about jets of tagged flavour will be discussed in sections 5 and 7. In this section the properties of the charmed and bottom hadrons themselves will be discussed.

4.5.1. Phenomenology of the fragmentation function of heavy quarks

Following kinematical ideas of Suzuki [170] and Bjorken [171], Peterson et al. [108] suggested a parametrisation of the heavy quark fragmentation function which is widely used by experiments. The energy transfer ΔE in the hadronisation of a heavy quark $Q \to H + q$ is

$$\Delta E = E_H + E_q - E_Q . \qquad (4.5.1)$$

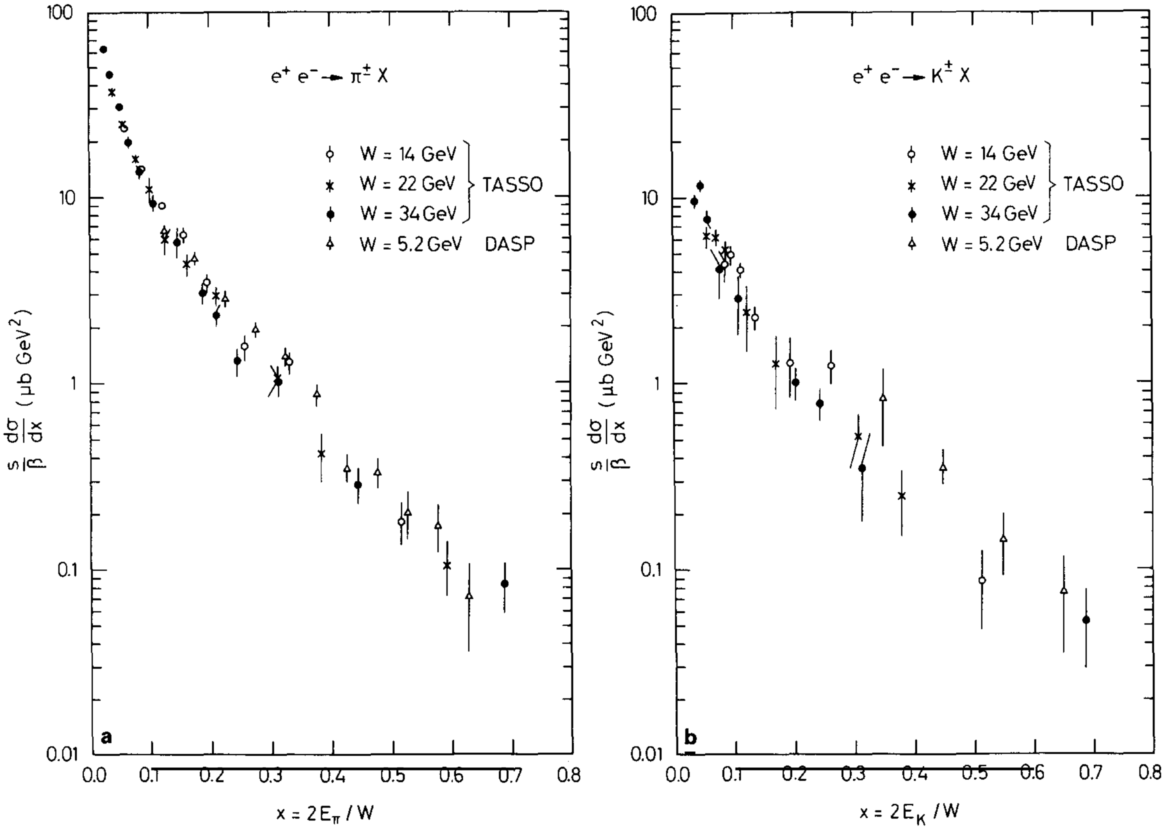

Fig. 4.4.1. Fragmentation functions of mesons at c.m. energies between $W = 5.2$ and 34 GeV [151, 169] for (a) pions and (b) kaons.

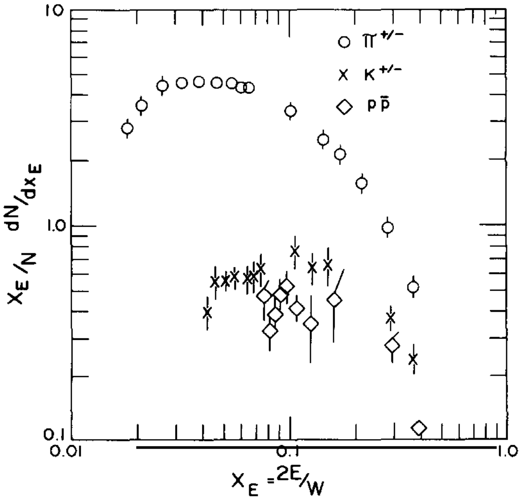

Fig. 4.4.2. Distribution of $(x_E/N)(dN/dx_E)$ as a function of x_E for various types of particles (data taken from ref. [126]).

With P being the momentum of Q and x the momentum fraction retained by the hadron H, this can be rewritten as

$$\Delta E = \sqrt{m_Q^2 + x^2P^2} + \sqrt{m_q^2 + (1-x)^2P^2} - \sqrt{m_Q^2 + P^2}\,, \tag{4.5.2}$$

where $m_H \sim m_Q$ was assumed in the first term. For $P \gg m_Q$ this can be expanded to give

$$\Delta E = 1 - \frac{1}{x} - \frac{\varepsilon_Q}{1-x} \tag{4.5.3}$$

with $\varepsilon_Q = (m_q/m_Q)^2$. Since the transition amplitude is proportional to $(\Delta E)^{-1}$ the energy spectrum of the hadrons containing heavy quarks is

$$D_Q^H(z) \propto \frac{1}{x[1 - 1/x - \varepsilon_Q/(1-x)]^2} \tag{4.5.4}$$

where the $1/x$ term takes into account the longitudinal phase space.

This equation has just one free parameter ε_Q. Although derived under rather simple assumptions without any dynamical considerations, it describes the data remarkably well and is used as a guideline for analysing the data. The essential idea behind it is that the hadrons containing the heavy quark retain most of the energy of the heavy quark. In contrast to u, d and s-quarks, heavy quarks are therefore supposed to have a hard fragmentation function. The average value of x as a function of ε is displayed in fig. 4.5.1 (from [172]).

Other authors proposed different shapes for the fragmentation function of heavy quarks:

(i) A continuation from the Kuti–Weisskopf model [173] for deep inelastic lepton nucleon scattering to e^+e^- annihilation into charmed hadrons leads to

$$D(x) = \frac{\Gamma(3-\alpha_c)}{\cancel{\Gamma(1-}\,\alpha_c)}\,\frac{(1-x)}{x^{\alpha_c}}\,, \tag{4.5.5}$$

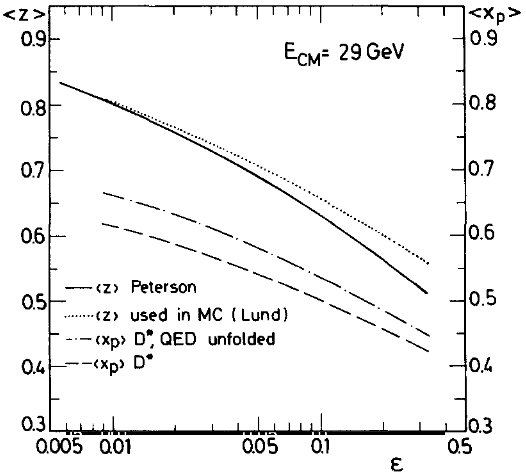

Fig. 4.5.1. Average value of $\langle x_p \rangle$ of the Peterson fragmentation function of charmed quarks as a function of ε (from ref. [172]). The z-variable is $z = (E + P_\parallel)_H/(E + P_\parallel)_Q$ (see 2.2.1), whereas $x_p = 2p_H/W$. The various lines correspond to various options in the simulation and the expected outcome of a direct measurement.

where α_c is the Regge intercept with a value between -2 and -4 [174]. When this formula is compared to the data, α_c is left as a free parameter*).

(ii) Assuming heavy quark kinematics in an Artru–Mennessier string Bowler [175] finds

$$D(x) \propto \frac{1-x}{x} \exp\left\{-bm_Q^2\left(\frac{m_M^2}{m_Q^2}\frac{1}{x} - 1 - \ln\frac{m_M^2}{m_Q^2 x}\right)\right\} \tag{4.5.6}$$

with one free parameter b, and m_M the meson mass.

(iii) The left–right symmetric fragmentation function of ref. [57] (see section 2.2) leads to

$$D(x) \propto (1/x)(1-x)^a \exp\{-b \cdot m_T^2/x\}\,, \tag{4.5.7}$$

where a and b are free parameters, $m_T = \sqrt{m^2 + p_T^2}$. For large values of m_T the maximum of $D(x)$ is shifted to higher x-values. Note that since $m_M \sim m_Q$ and $m_T^2 \sim m_M^2$ this equation is quite similar to that of Bowler.

In all these parametrisations the kinematic effect due to the high mass of these quarks is implicitly included. The different formulations reflect the different dynamical assumptions used.

The properties of heavy quarks inside a jet have been measured with two methods:

(1) The direct reconstruction of the hadrons containing heavy quarks. In the high energy continuum only charmed hadrons have been successfully reconstructed. The large decay multiplicity of bottom hadrons implying a substantial amount of π^0's makes their identification very difficult. The reconstruction of the few bottom hadrons at their threshold takes advantage of a momentum constraint [176, 177].

(2) The identification of semileptonic decays of c- and b-hadrons. To tag charm and bottom particles events with electrons and muons of high transverse momentum relative to the jet axis have been selected. This method works due to the high q-value of heavy quark decays and since charm and bottom quarks are nearly the only source of prompt leptons in a jet. Up to now this is the only way to extract information about the fragmentation of bottom quarks. It involves, however, in addition to an excellent electron and muon detection system, a complicated unfolding of decay branching ratios, decay properties, and relative yields.

4.5.2. *Experimental results on the charm system*

The cleanest signal for studying the fragmentation properties of heavy quarks is provided by the decay $D^{*\pm} \to \pi^\pm D^0$. It has a very small q-value, the mass difference is $\Delta m = m_{D^*} - m_{D^0} \sim m_\pi$. This transition can therefore be identified with only a very small background. Other reconstructed charmed particles are D^0, $D^\pm$, D^{*0}, $D^{**0}(2420)$, D_s, D_s^*, and Λ_c (see e.g. the compilation in ref. [118]). In fig. 4.5.2 (taken from ref. [178]) the fragmentation function of a $D^{*\pm}$ is displayed as measured by various experiments around $W = 30$ GeV [178–181]. Their results agree with one another in the region $x \geq 0.5$. Some discrepancies exist for the low-x region $x < 0.5$. There the background to the D* signal becomes considerable. Compared to the fragmentation function of the light quarks, that of the D* is found to be significantly harder, only very few D* can be found at low x. Note that the D* from B-decays should predominantly populate the region $0.2 < x_E < 0.4$.

In fig. 4.5.3 the measurements at $W \sim 10$ GeV [182–184] based on a much larger data sample than those of fig. 4.5.2 are compared to various models. Threshold effects may still be important at these energies since $\beta_{D^*} \sim 0.9$. The different parametrisations lead to similar results and describe the data

---

*) For application to the data the equation is simplified to $x^\alpha(1-x)$ with α a free parameter.

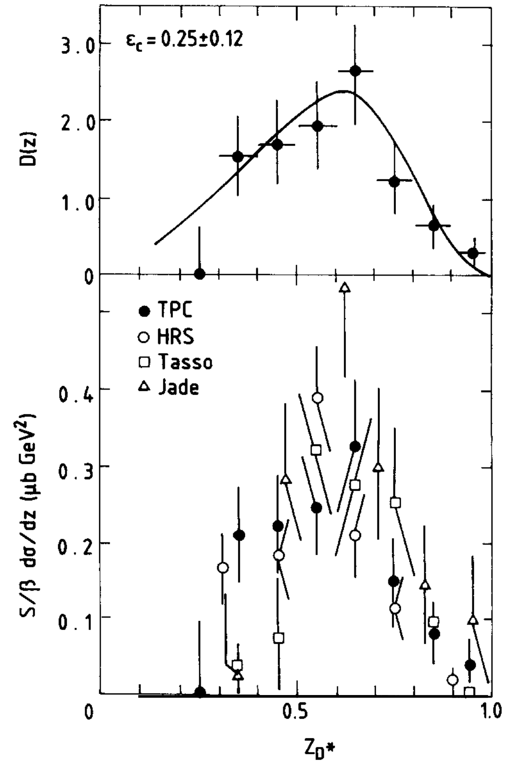

Fig. 4.5.2. D* fragmentation function from various experiments at $W \sim 30$ GeV compiled in ref. [178] together with the result of a fit to the data of ref. [178] using eq. (4.5.4).

quite well. This suggests that the kinematical effects dominate the distribution such that it is not possible to discriminate between the various dynamical concepts at the moment. It is therefore justified to keep the relatively simple parametrization of eq. (4.5.4) as the basic guideline.

In applying this equation to the data, one has to carefully discriminate between various possible definitions of x, as well as to take into account QCD and QED effects properly. How the shape of the effective fragmentation function (4.5.4) is changed by various dynamical effects is displayed for $W = 34$ GeV in fig. 4.5.4 (from ref. [172]). As can be seen both QCD bremsstrahlung and initial photon radiation shift the D*'s to smaller values of x and change the shape of the distribution. In analysing their data, the various experiments used different variables and quote therefore results of quite large variations. Bethke [172] has analysed the published data on D* production at energies around $W = 30$ GeV and corrected them consistently for QED and QCD effects on the basis of the fragmentation function (4.5.4). He then determined

$$\langle z_c \rangle = \left\langle \frac{(E + p_\parallel)_{D^*}}{(E + p_\parallel)_c} \right\rangle$$

and finds a high consistency of the various measurements yielding

$$\langle z_c \rangle = 0.71 \pm 0.01 \pm 0.03$$

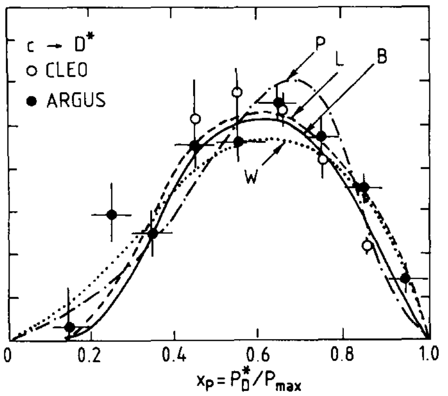

Fig. 4.5.3. D* fragmentation function at $W \sim 10$ GeV together with model predictions of Peterson et al. (P), the LUND group (L), Webber (W) and Bowler (B) (compiled in ref. [167]).

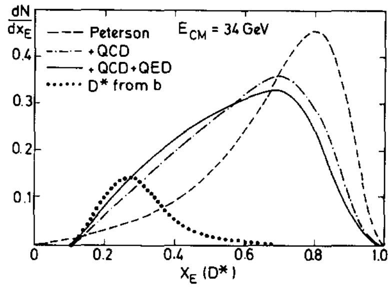

Fig. 4.5.4. Monte Carlo simulation of the Peterson fragmentation function at $W = 34$ GeV and distortions due to QCD and QED bremsstrahlung. Also shown is the expected contribution from decays $B \to D^* + X$ [172].

which corresponds to $\varepsilon_c \sim 0.04$ and to a directly measurable average scaled energy of charmed particles $\langle x_c \rangle \sim 0.6$.

The fragmentation functions for other charmed hadrons have also been analysed in terms of the parametrisation (4.5.4):

(i) For the D^{*0} [185, 186] the data are consistent with the parametrisation obtained for the $D^{*\pm}$ fragmentation function.

(ii) For the D** [187] the ARGUS collaboration finds $\varepsilon_c = 0.12 \pm 0.05$ (uncorrected for QED or QCD effects).

(iii) For the D_s [188, 140], the two experiments obtain larger values for ε_c with substantial errors.

(iv) The Λ_c fragmentation function [189] (see below) can well be described by the fragmentation function for charmed mesons ($\varepsilon = 0.21 \pm 0.08$ for the Λ_c, $\varepsilon = 0.14$ for mesons).

The same is true for the value of ε_c obtained through the lepton spectrum. A compilation of these measurements can be found in ref. [190]. A precise determination of the fragmentation functions from the various types of charmed particles is interesting in view of testing the various functions suggested. As an example consider the difference of D_s and D^0. Whereas the Peterson function predicts D_s to be softer ($\varepsilon_{D_s}/\varepsilon_D \sim m_s/m_d$), it should be harder for the symmetric LUND fragmentation since $m_{D_s} > m_D$. However, the data are still too imprecise to be sensitive to these subtle effects. In addition the feedthrough from D**, D_s^{**}, etc. has to be known for a reliable answer.

A result of particular interest in view of the various models of baryon production is the fragmentation function of the Λ_c spectrum measured by CLEO [189] (see also ref. [184]). The observed distribution (fig. 4.5.5) is compared to the shape given in fig. 4.5.4 with a value of $\varepsilon = 0.14$. The application of the Peterson function is only meaningful if the two light quarks fusing with the charm quark act as one entity like a diquark. The measurement is also compared to a convolution of quark fragmentation functions [191] of the Peterson type assuming that two separate quarks u and d combine with the charm quark. This can be regarded as one type of the extended diquark models. Figure 4.5.5 shows that it fails to reproduce the data. This result supports the assumption of (nearly) pointlike diquarks, however, the data are not sensitive enough for detailed conclusions about a possible diquark form factor.

In addition to the measurement of its longitudinal fragmentation function, the D*'s provide a

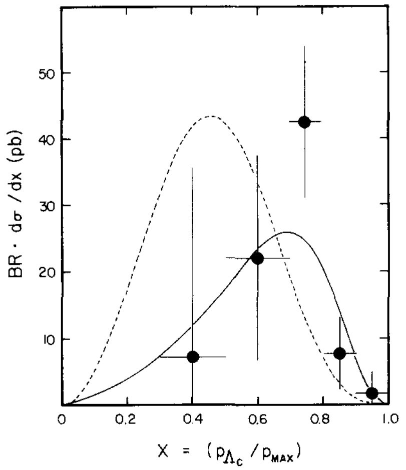

Fig. 4.5.5. Fragmentation function of the Λ_c [189]. The measurement is compared to fragmentation functions predicted by Peterson et al. (full curve) and de Grand (dashed curve).

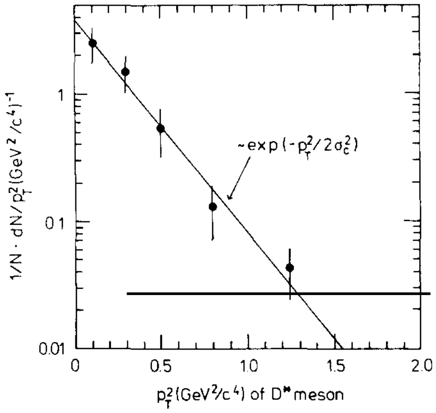

Fig. 4.5.6. Spectrum of the transverse momentum of D*'s with respect to the quark axis [192]. The measurement is compared to the fit result assuming an exponential fall-off.

relatively clean way to determine the p_T spectrum of particles with respect to the parton axis. The D* is known to be produced directly (leaving aside possible decays like D**→D*) and the original quark axis coincides with the jet axis. Its p_T spectrum is therefore a direct measure of the p_T spectrum of hadrons with respect to the original quark[*]. The p_T^2 spectrum is displayed in fig. 4.5.6 as measured by the TASSO collaboration [192]. Also shown is a fit result assuming

$$(d\sigma/dp_T^2) \propto \exp(-p_T^2/2\sigma_c^2)\,,$$

As can be seen, the shape agrees very well with an exponential distribution, with $\sigma_c = (0.36 \pm 0.02 \pm 0.04)$ GeV/c. A similar result has been obtained by JADE [181]. This result is in agreement with that obtained for other particle species (cf. section 4.3).

The D*-measurement has also been used to determine the ratio of the production of vector mesons to the sum of vector and pseudoscalar mesons (cf. section 2.2) $r = V/(P + V)$ by comparing the D* and D cross sections. The measurements are still subject to considerable statistical and systematic errors, the latter largely due to uncertainties in the D and D* branching ratios. Assuming that the charmed quark has the same chance as the light ones of picking up quarks from the sea, r can be estimated from the D* cross section alone. We denote by $R(x)$ the cross section for inclusive production of particle x in terms of the pointlike QED muon pair cross section and by p_{qq}, p_s the probabilities for picking a diquark or s-quark out of the vacuum (see sections 4.2, 4.3). It follows

$$R(\mathrm{D}) = 2(1 - p_{qq})(1 - p_s)R(c\bar{c}) - R(\mathrm{D}^*)\,, \qquad (4.5.8)$$

$$R(c\bar{c}) = \tfrac{4}{3}(1 + \alpha_s/\pi)\,. \qquad (4.5.9)$$

---

[*] Note that possible distortions due to gluon bremsstrahlung are reduced since in most cases only D*'s with a large x are selected for such an analysis. These events therefore have only a limited phase space for a third jet.

Then

$$R(\mathrm{D}) \sim 2.21 - R(\mathrm{D}^*) \Rightarrow \left(\frac{V}{P+V}\right)_{\mathrm{c}} = \frac{R(\mathrm{D}^*)}{2.21}\,. \tag{4.5.10}$$

No attempt has been made to correct for contributions from charmed mesons of higher excitation like the D** since the information about them is too scarce. Since most experiments are sensitive to the high x-region only, the contributions from B-decays can be neglected. To obtain $R(\mathrm{D}^*)$, its cross section has to be extrapolated to lower x-values using one of the parametrisations given above. The results from the various experiments are listed in table 4.5.1. Here all results have been consistently modified according to the by now best known values of the branching ratios $\mathrm{BR}(\mathrm{D}^0 \to \mathrm{K}^-\pi^+) = 0.042 \pm 0.004 \pm 0.004$ [193] and $\mathrm{BR}(\mathrm{D}^{*+} \to \mathrm{D}^0\pi^+) = 0.49 \pm 0.08$ [2]*).

As can be seen, the measurements agree reasonably well with one another, however their errors are still large. Assuming $R(\mathrm{D}^{*\pm}) = R(\mathrm{D}^{*0} + \bar{\mathrm{D}}^{*0})$ as well as uncorrelated errors and adding statistical and systematic errors in quadrature as well, one finds $R(\mathrm{D}^*)$ from charm events to be ~2.08 ± 0.23 and therefore $r_{\mathrm{c}} = (V/(P+V))_{\mathrm{c}} \sim 0.94 \pm 0.10$. One should be aware that this value is inversely proportional to the $\mathrm{BR}(\mathrm{D}^{*+} \to \mathrm{D}^0\pi^+) \times \mathrm{BR}(\mathrm{D}^0 \to \mathrm{K}^-\pi^+)$ which has changed considerably in the course of the various measurements quoted above. The various experiments assumed values that differed by ~40% depending on the time of publication. It is not obvious that the number will not change in future time.

The result indicates a very high inclusive cross section of D*'s: nearly all charmed, non-strange, primarily produced mesons seem to be vector particles. The HRS collaboration has measured both D* and D^0-production and determined r_{c} as $1.0^{+0.3}_{-0.2}$ [134], consistent with the measurements discussed above. These values are larger than the ratio for light quarks (see discussion above), however, a definite conclusion about a possible mass dependence requires more precise data.

4.5.3. Experimental results on bottom hadrons

The fragmentation function of the b-quark can only be measured indirectly through the longitudinal and transverse momentum spectra of prompt leptons. To extract it one has to unfold the fragmentation and decay properties of bottom (and charm) hadrons. The MARKJ collaboration [196] fitted their μ-spectrum leaving the muonic branching ratios for charm and bottom quarks as well as ε_{c} and ε_{b} as

Table 4.5.1
Measurements of the cross section of D* and D^0-production in terms of the pointlike QED muon cross section

Experiment	$R(\mathrm{D}^{*\pm})$	$R(\mathrm{D}^{*0})$	$R(\mathrm{D}^*)$
MARK2 [194]	2.00 ± 0.99		
CLEO [189]	0.97 ± 0.11 ± 0.31		
TASSO [180]	0.80 ± 0.20 ± 0.28		
JADE[b] [185]	1.23 ± 0.36	1.44 ± 0.48	
HRS [179]	0.96 ± 0.31	0.63 ± 0.22	1.92 ± 0.46[a]
DELCO [195]	1.27 ± 0.20 ± 0.28		
TPC/2γ [178]	1.01 ± 0.16		

[a] b-decay products included.
[b] only $x > 0.4$.

---

*) Since most experiments do not discriminate between the various contributions to the systematic error, it was not attempted to appropriately scale down the error according to the by now more accurate determination of the branching ratio.

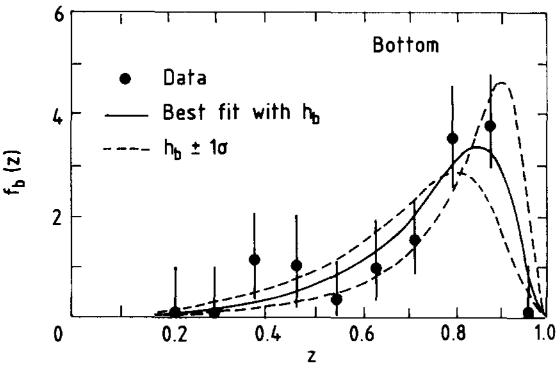

Fig. 4.5.7. Bottom fragmentation function unfolded from the μ-spectrum by ref. [196]. Also shown (full line) is the fit using eq. (4.5.4). Here $h_b = \sqrt{\varepsilon_b}$, the dashed lines represent the curves allowing for a 1σ deviation of h_b.

free parameters. For the charm fragmentation function they obtain $\langle z_c \rangle = 0.46 \pm 0.02 \pm 0.05$, a value less than what has been determined by the more direct analysis of the D* fragmentation function. The bottom fragmentation function extracted is shown in fig. 4.5.7 and is seen to be even harder than that for charm. This is expected from the arguments given in section 4.5.1. A compilation of the measurements of the b-fragmentation function is given in ref. [197]. The average value is $\langle z_b \rangle = 0.83 \pm 0.01 \pm 0.02$ or $\varepsilon_b \sim 0.006 \pm 0.001 \pm 0.002$ and thus

$$\frac{\varepsilon_b}{\varepsilon_c} = \frac{0.006}{0.04} \sim \left(\frac{m_c}{m_b}\right)^2$$

in rough agreement with eq. (4.5.3).

4.6. *Energy fractions of the different components in a jet*

Now that all measurements on the fragmentation into specific kinds of particles are discussed, they can be summarized with respect to their response in the various components of a typical e^+e^- detector. Such measurements are interesting e.g. for searches for possible yet unknown non- or weakly interacting particles inside a jet. In particular, such a compilation is relevant for designing experiments aiming to measure the total energy of jets. In fig. 4.6.1 the contributions of charged particles, neutral electromagnetic particles, neutral hadrons (K_L^0, n) to the total energy are displayed as a function of the c.m. energy W [124, 198, 199, 3, 96, 127, 151].

The fraction of neutral and charged energy in hadronic events has been measured directly using the drift chambers and the electromagnetic calorimeters. The contribution from K_L^0's and neutrons was estimated from the cross sections for K_s^0 and p assuming $\sigma(K_L^0) = \sigma(K_s^0)$ and $\sigma(n) = \sigma(p)$*⁾.

As can be seen from fig. 4.6.1 the energy fractions show no significant energy variation. The charged hadron component amounts to 60%, the neutral electromagnetic component to 25%, 6% can be attributed to K_L^0's [127], about another 7% to neutrons [151]. The remaining energy can be explained as being due to electrons, muons and neutrinos leaving essentially nothing for any unknown, non- or

---

*⁾ Note that this is presumably an overestimation of the neutron yield. The LUND simulation predicts 10–15% less neutrons than protons due to decay properties.

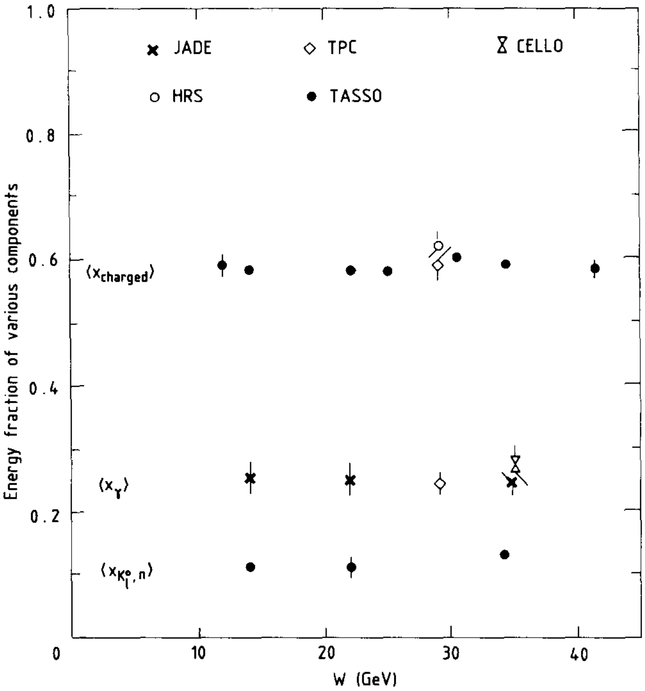

Fig. 4.6.1. Components of the energy of a jet with respect to their response to different parts of the detector [3, 96, 124, 127, 151, 198, 199].

weakly interacting particle. These results are also important in view of the experimentation with jets at future accelerators. They will be reiterated in section 11.1.

4.7. Conclusions

Although there are about 13.4 charged and 14 neutral final particles (mostly photons) in a jet at $W = 34$ GeV, only ~10 particles are produced directly during the evolution of jets according to simulation studies. A large fraction of particles originates from decays.

The data can be well described with a single primordial fragmentation function for all hadrons from u, d or s-quarks. The function is relatively soft, leading to an average value $\langle x \rangle \sim 0.10$. In contrast the heavy quarks charm and bottom have a hard fragmentation function with $\langle x_E^c \rangle \sim 0.6$ and $\langle x_E^b \rangle \sim 0.75$. The data are in very good agreement with the parametrisation of the eq. (4.5.4) which is derived from kinematic considerations only.

The mass dependence of the production yield of the various hadrons exhibits a remarkably regular behaviour. It is steeply falling according to an exponential mass dependence. Particles of different quark content have a different yield even though their mass may be similar. The yield decreases with the mass of the partons. This is consistent with the conjecture that the probability of picking a quark q out of the sea is suppressed with increasing mass of q. Up and down quarks are each produced about three times as frequently as strange quarks. There exists no indication for charm and bottom production in the sea.

The production of baryons can be well described assuming the existence of diquarks in the sea. Both the fragmentation functions and the relative particle yields agree with the assumption of pointlike diquarks. Strange and decuplet baryons are suppressed compared to (u, d) or octet baryons, as expected due to the higher masses of diquarks containing strangeness or having spin 1.

The best estimates for the relevant parameters used in simulation programs like that of the LUND group are $p_s \sim 0.15$ (probability to pick an s-quark out of the vacuum), $p_{qq} \sim 0.08$ (diquark production) and $V/(P+V) \sim 0.6$ at least for u, d, and s-quarks (fraction of vector mesons produced).

The results reveal that the production of particles is predominantly depending on the parton content. Even particles of similar mass and same quantum numbers are produced with a different frequency if their quark content differs. This excludes any phase-space-like models, but shows that a jet develops via the emission of individual quarks.

5. Jets of known flavour

The hadronic events produced in e^+e^- collisions evolve from various kinds of primary partons: quarks (u, d, s, c and b) and to a lesser extent from gluons. The identification of a certain primary parton and the examination of its impact on the general jet properties supplies ways of extracting the dynamical properties of jet evolution. One example is the contribution of charmed events to the scale breaking of the fragmentation function discussed in section 3.2. Moreover new questions can be addressed e.g. as to what extent does the original parton affect the subsequent fragmentation. In addition it may provide means for tagging jets of a certain flavour. The first aspect will be discussed more thoroughly in section 7, the possibility of kinematic flavour tagging in section 11.

In this section we will summarize the inclusive distribution of particles in quark and gluon jets.

5.1. Quark jets

Once a more detailed insight into the general properties of fragmentation had been obtained and a high number of events accumulated, it became possible to study the properties of jets originating from a special kind of quarks. The first results were published by the TASSO collaboration [192] on the properties of charm jets. The method developed there (see fig. 5.1.1) was subsequently applied to other kinds of partons and by other experiments. It consists of two steps. In the first one events with a property specific to a certain flavour are selected, e.g. in the case of the charmed events those where a D* has been detected. An event is then divided into two hemispheres. One of these hemispheres bears the marks from the special selection applied and is thus biased, e.g. not all x-values or decay modes of the D* have been considered. The opposite hemisphere, however, is free of special requirements and

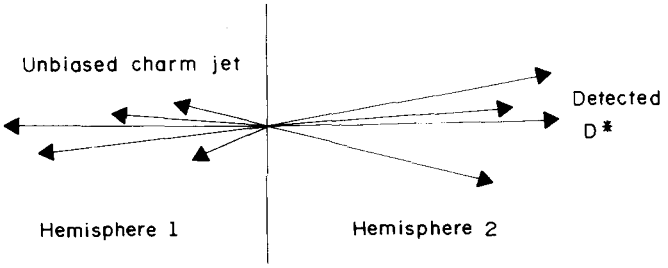

Fig. 5.1.1. Schematic picture of the method for tagging an unbiased jet of known flavour.

therefore gives a representative, unbiased picture of a jet originating from the kind of quark tagged in the other jet. This unbiased jet is analysed. In most cases it is compared to an average jet.

Results have been obtained for jets originating from both bottom and charm quarks. In the case of the light quarks no discrimination between u, d, or s jets has been achieved. Instead a mixture of light quark jets could be isolated from the total event sample.

5.1.1. Bottom jets

The properties of jets originating from bottom quarks have been measured by the DELCO [200], MARK2 [201], and TPC collaborations [202] at $W = 29$ GeV. For their tag they required electrons and muons with a high transverse momentum p_T with respect to the jet axis. The size of the samples*) as well as their estimated purity and the tagging efficiency ε are listed in table 5.1.1. It should be noted that the lower efficiency in the sample of the DELCO collaboration is due to their more stringent requirements on the purity.

The average multiplicity in b-jets compared to those in average jets are listed in table 5.1.2**). The measurements indicate a significantly higher multiplicity in bottom jets

$$\langle n_{CH} \rangle_b - \langle n_{CH} \rangle_{av} \sim 1.6 .$$

The TPC collaboration determined the fraction of particle types in bottom jets. The results suffer from still considerable errors. It seems that the higher yield is due to pions which contribute 6.9 ± 0.5 (b-jets) compared to 5.45 ± 0.25 (average jets) and possibly to a smaller part due to kaons: 0.85 ± 0.30 compared to 0.70 ± 0.05. Within the large errors no difference is seen in the proton yield: 0.35 ± 0.30 for b-jets and 0.30 ± 0.05 in average jets.

Characteristic distributions of the unbiased bottom jet are displayed in fig. 5.1.2 where they are compared to the average jet. Whereas the p_T^2 distribution for bottom jets resembles that of average jets, their fragmentation function $(1/N_{jet})(dN/dx_p)$ is softer, which is reflected in the significantly higher mean charged multiplicity already discussed. The most spectacular differences occur in the rapidity and sphericity distribution. The rapidity distribution is not flat as for the average jets but has an enhancement around $y \sim 1.4$. In addition the particle yield $(1/N_{jet})(dN/dy)$ decreases more rapidly in bottom jets: it drops below 1 at a rapidity of $y \sim 2.20$ for bottom jets but at $y \sim 2.65$ for average jets. Since the p_T^2 distributions are similar but the x_p-distribution is softer in bottom jets, it follows that the sphericity $S = 3/2(\Sigma\ p_T^2/\Sigma\ p^2)$ of bottom jets should be broader. As can be seen from fig. 5.1.2d, this is indeed the case.

Table 5.1.1
Characteristics of samples of tagged bottom events

Experiment	lepton	number events	b [%]	c [%]	uds [%]	ε [%]
DELCO	e	146	83 ± 6	11 ± 4	6 ± 2	2.4
MARK2	$e + \mu$	688	64 ± 8	16 ± 8	20 ± 8	12.8
TPC	e	83	69 ± 6	20 ± 3	11 ± 3	3.6
TPC	μ	193	64 ± 6	17 ± 4	19 ± 2	8.6

---

*) The TPC collaboration used b-enriched as well as c-enriched samples for the analysis. Their results were obtained by unfolding the two samples. The values quoted here and in the following section about charm jets refer to the appropriately enriched sample.

**) The value determined by the TPC collaboration includes only hadrons, the additional contribution from leptons can be estimated from the semileptonic branching ratios of the b and c-quarks to be ~0.4.

Table 5.1.2
Multiplicity in b-jets

Experiment	E_{jet} [GeV]	$\langle n_{CH} \rangle_b$	$\langle n_{CH} \rangle_{av}$
MARK2	14.5	$8.05 \pm 0.25 \pm 0.5$	$6.45 \pm 0.05 \pm 0.3$
TPC	14.5	7.95 ± 0.50	6.4 ± 0.3
DELCO	14.5	7.61 ± 0.46	6.16 ± 0.01

The values for some representative average parameters are listed in table 5.1.4 together with results from jets originating from charm and from light quarks.

As already becomes clear from the multiplicity, the properties of bottom events are dominated by the properties of the bottom hadrons at the c.m. energies discussed. The CLEO collaboration [203] has measured an average charged multiplicity from b-decays of $\langle n_{CH} \rangle = 5.5$ and thus only ~2.4 particles in the b-jets at $W \sim 30$ GeV originate from the subsequent fragmentation. In addition the rapidity interval for the fragmentation of the residual system is limited. Using the measured b-fragmentation function

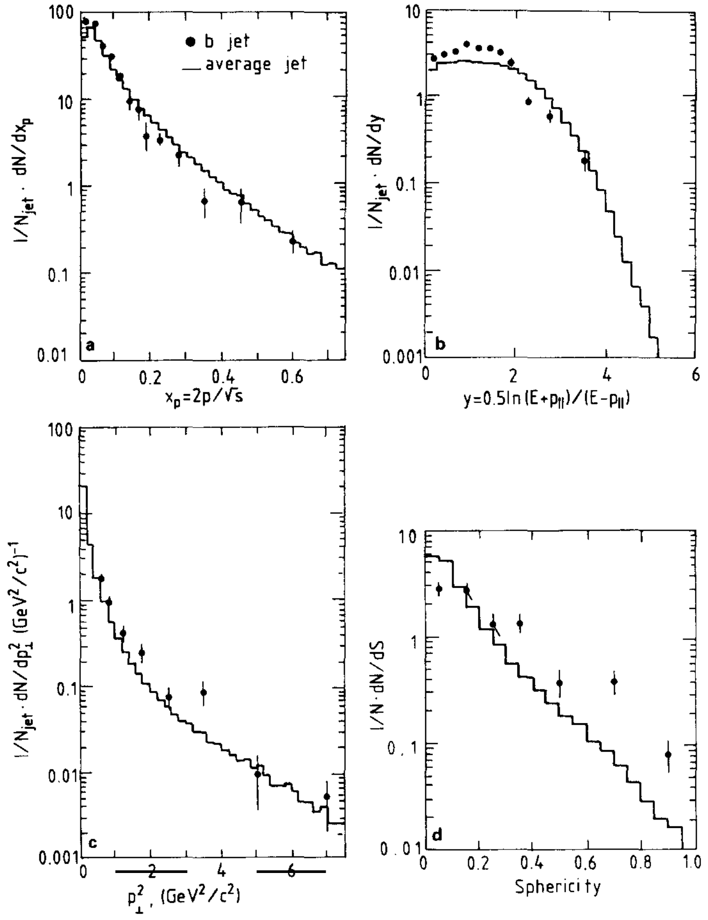

Fig. 5.1.2. Characteristic jet properties of average (histogram) and bottom jets (full circles) [200]: (a) $x_p = 2p/W$, (b) rapidity, (c) $(1/N_j)(\mathrm{d}N/\mathrm{d}p_T^2)$, (d) sphericity.

(cf. section 3.5) yielding $\langle x_b \rangle \sim 0.75$, the typical energy of the residual system is found to be

$$\langle E_{\rm res} \rangle = (1 - \langle x_b \rangle)(W/2) \sim 3.6\,\mathrm{GeV}$$

and the corresponding maximum rapidity is therefore

$$y_{\max} \sim \ln \frac{2\langle E_{\rm res} \rangle}{m_\pi} = 3.9 \,.$$

Since most particles are found within a rapidity range $y < y_{\max} - 2.5$ (cf. section 3.3.3), the majority of particles from the subsequent fragmentation are expected to be in a small range of $y \le 1$.

A more thorough evaluation of the various contributions to bottom jets can be obtained by convoluting the b-fragmentation function, the decay distributions of bottom hadrons (which have been inclusively determined at DORIS and CESR), and a model of the subsequent fragmentation. This has been done by the DELCO group in the case of the rapidity distribution. The different components as calculated with the LUND Monte Carlo are shown in fig. 5.1.3. The overall distributions of the data and the result of the simulations agree very well. The simulation reveals the enhancement around $y \sim 1.4$ as being due to the decay products of the bottom particle. The high decay multiplicity reflects itself in a high particle density around $y \sim 1.4$. The position and width of the enhancement can be estimated from the properties of bottom hadrons and their fragmentation function [204].

The particle yield at low rapidity values is least influenced by the bottom decay and most sensitive to the subsequent fragmentation.

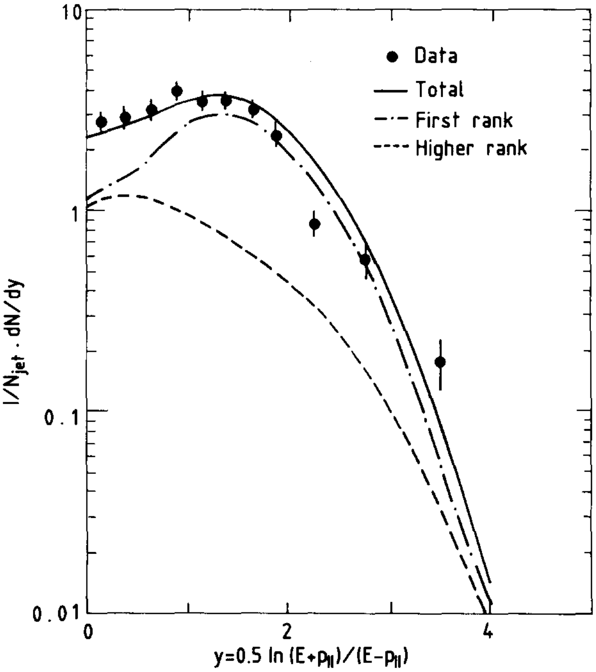

Fig. 5.1.3. The measured rapidity distribution of bottom jets compared to a Monte Carlo simulation (full line) [200]. Contributions of the first rank (dashed–dotted line) and higher rank (dashed line) mesons as predicted in the Monte Carlo calculation are displayed.

5.1.2. Charm jets

Results on the properties of charm jets have been published by the TASSO [192], the HRS [205], the MARK2 [201], and the TPC [202] collaborations. The first two used the reconstruction of a D* as a tag, the other two high p_T leptons.

The D* selection resulted into ~100 events or about 1% of the total charmed events collected. The purity is ~85%. With the high p_T-lepton tag a much larger sample of ~1000–2000 events or 10% of the charmed sample has been selected. However, the purity is only 35 ± 8% (MARK2) and ~50% (TPC) hardly exceeding the fraction of charmed events in the overall sample.

The multiplicities in charm jets and those in average jets can be read from table 5.1.3. In contrast to bottom jets, the multiplicity of charm jets does not differ significantly from the average ones, although all measurements indicate somewhat more charged particles. Considering just the statistical error of the measurements (the systematic ones are presumably strongly correlated), one finds

$$\langle n_{CH}\rangle_c - \langle n_{CH}\rangle_{av} \sim 0.3 .$$

The TPC collaboration has studied the particle content of charm jets and measured 5.40 ± 0.45 pions in charm jets compared to 5.35 ± 0.25 in average jets and 0.30 ± 0.05 protons. Some indication exists for an increased kaon yield in charm jets, although the errors are too large for any definite conclusion: 1.0 ± 0.25 in charm jets, the average jet contains only 0.70 ± 0.05. Since the TPC collaboration considered the bottom and charm enriched sample together, the errors quoted for the two samples are correlated. Combining the heavy quark sample they find a higher kaon yield than in the average jet of a significance of 3σ–4σ. They are unable to determine if the difference is due to charm or bottom jets.

The results on the particle distributions and the topological properties as measured by the TASSO experiment are displayed in fig. 5.1.4. Shown are the measurements of the fragmentation function, the rapidity, the p_T^2-distribution, the sphericity and the thrust for both the charm and the average jets. None of these distributions exhibits significant differences between the two samples. For example, the height of the rapidity plateau is 2.3 ± 0.2 for the charm jet and 2.32 ± 0.02 for the average jet.

Thus in contrast to the bottom jets, charm jets are not significantly different from average jets. This is of course only true within the still quite large systematic and statistical errors. For example, the simulation programs predict that the fragmentation function of the final particles in charm jets falls off more steeply at high x than that for light quarks. This has been mentioned in section 3.2 and exploited by the HRS collaboration to tag light quarks (see next section). As can be seen from fig. 5.1.4a the data are consistent with such a behaviour, but the statistical significance is too small for any definite conclusion.

It is suggestive to relate the similarity of the two kinds of jets to the fact that the properties of charm jets are dominated by the subsequent fragmentation. Repeating the arguments given above for the bottom jets one estimates that ~5.2 charged particles are produced in the subsequent fragmentation, compared to the average multiplicity from charm decays of ~2.3 [206]. With $\langle x_c\rangle \sim 0.6$ the charmed

Table 5.1.3
Multiplicity of c-jets

Experiment	E_{jet} [GeV]	$\langle n_{CH}\rangle_c$	$\langle n_{CH}\rangle_{av}$
TASSO	17.0	7.5 ± 0.5 ± 0.3	6.70 ± 0.02 ± 0.3
MARK2	14.5	6.6 ± 0.25 ± 0.49	6.45 ± 0.05 ± 0.3
TPC	14.5	6.6 ± 0.9	6.40 ± 0.30

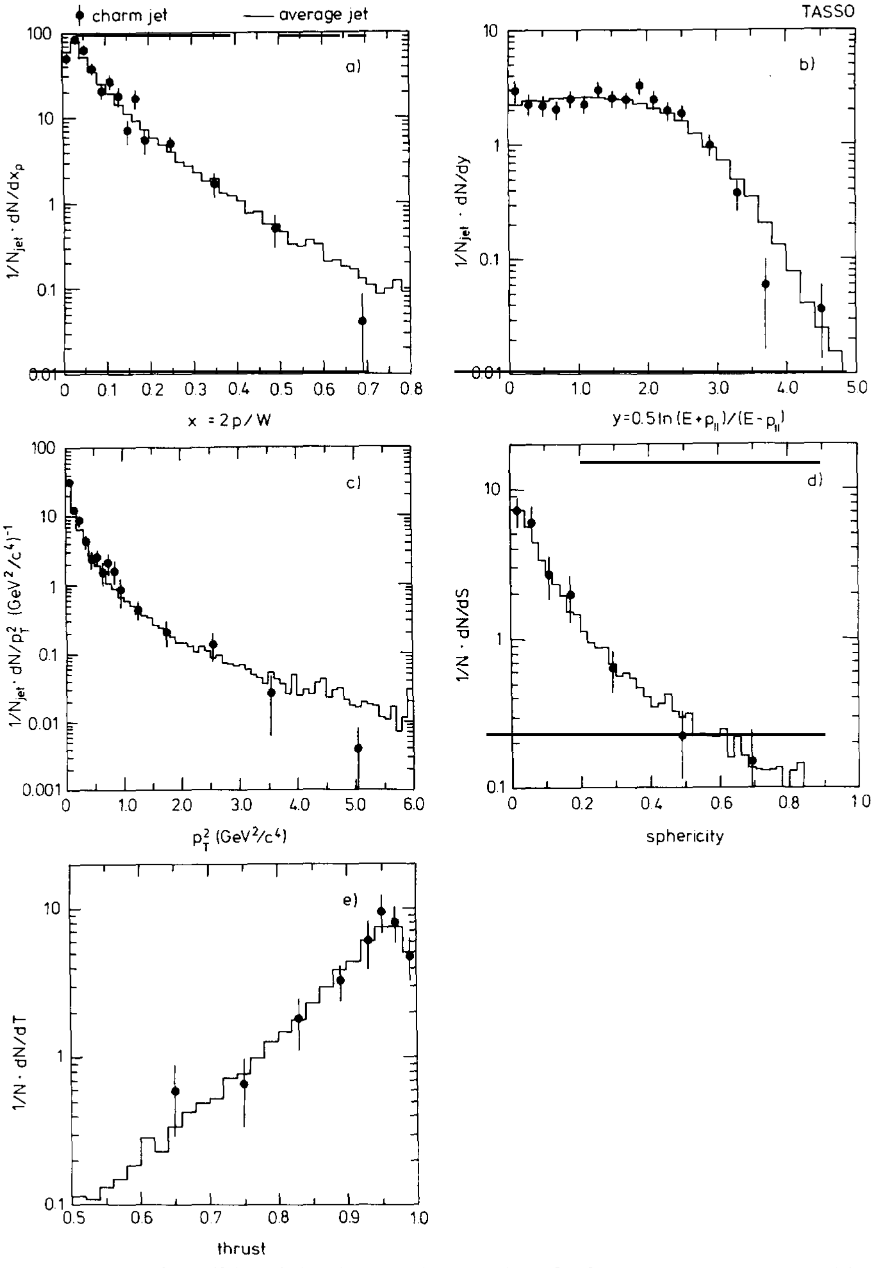

Fig. 5.1.4. Characteristic properties of charm (full circles) and average (histogram) jets [192]. Shown are (a) $x = 2 \cdot p/W$; (b) rapidity; (c) transverse momentum squared; (d) sphericity; (e) thrust.

hadrons cluster around $y \sim 2.3$ leaving a maximum rapidity interval for the subsequent fragmentation of typically $y_{\max} \sim 5.0$.

No enhancement in the rapidity distribution like that for bottom quarks can be seen for charm jets. The reason for this property is threefold: (i) The multiplicity from charm decays does not strongly exceed the density in average jets of ~2.2; (ii) the rapidity distribution of charmed hadrons is much wider than that from bottom hadrons and therefore the final particles are spread out more; (iii) the position of the charm rapidity is centered around $y \sim 2.3$ where the particle yield from the subsequent fragmentation starts to decrease ($y_{\max} - 2.5 \sim 2.5$). This apparently broadens the plateau.

The contributions from the charm system and from the subsequent fragmentation to the rapidity spectrum are displayed in fig. 5.1.6.

5.1.3. Light (uds) quarks

The HRS collaboration [205] has selected a sample of 314 events originating from uds quarks (~1.4% of all uds events collected) with a purity of ~89%. The events have been obtained by requiring that they contain at least one charged stable particle with $x_p > 0.7$ ("trigger particle"). They were compared to a sample of charm jets. The number of events observed is displayed in fig. 5.1.5a as a function of the momentum of the trigger particle p_{trig} together with the momentum distribution of the reconstructed D*'s. Although the D* has a considerably harder fragmentation function than the hadrons from light quarks, their decay products are found at low x-values and therefore heavy quarks do not contribute significantly to events with a high p_{trig}. Their contribution to the background is estimated from a Monte Carlo study and shown in fig. 5.1.5b as a function of p_{trig}. The HRS collaboration required a momentum of the trigger particle of $x_p > 0.7$ or $p > 10.15$ GeV. To reduce the impact of gluon radiation which should wash out possible differences between charm and (uds)-jets, they applied a cut in both samples to select only two jet events.

The values of the mean jet variables are listed in table 5.1.4 together with those from bottom and average jets. Note that due to the special cut applied against three-jet events, these values cannot be directly compared to those obtained in other experiments and discussed in the previous sections. The average values of the two data samples for charm and light quark jets differ only in their average multiplicity (~3.5σ), the charm jets contain ~15% more particles than the uds jets. Correspondingly the average momentum of particles in charm jets is somewhat lower. The average p_{T} and the jet variables sphericity and thrust are very similar.

The rapidity distributions of charm and light quark jets are displayed in fig. 5.1.6. Also shown are the predictions from a Monte Carlo calculation. As can be seen the data are well reproduced (full curve). The simulation program allows one to disentangle particles from the primary produced hadron (either directly produced or in decays) and those from the subsequent fragmentation. The overall distributions are very similar for both samples although the two sources contribute in a different way to both cases. The plateau is ~10% higher for charm jets and its width*) is 2.8 ± 0.1 compared to 3.0 ± 0.1 for light quark jets. The similarity between charm and average jets found by the HRS collaboration is consistent with the result of the TASSO collaboration discussed in section 5.1.2.

5.1.4. Conclusion

The comparison of jets originating from quarks of different flavour revealed some dependence of their properties on the flavour. All these differences, however, can be attributed to the properties of the particles containing the first produced quark.

For uds and charm jets the differences are too small to use them for topological flavour tagging. The jets from bottom quarks are significantly broader and exhibit an enhancement in the rapidity. These features allow one to select b-enriched event samples at PETRA and PEP energies. Methods developed for topological bottom tagging will be discussed in section 11.

---

*) The width is defined as the rapidity value where $(1/N_{\mathrm{ev}})(\mathrm{d}N/\mathrm{d}y) = 1$. Note that the width is larger than that for the average jet discussed in section 5.1.1. This discrepancy is presumably due to the cut applied against three jets.

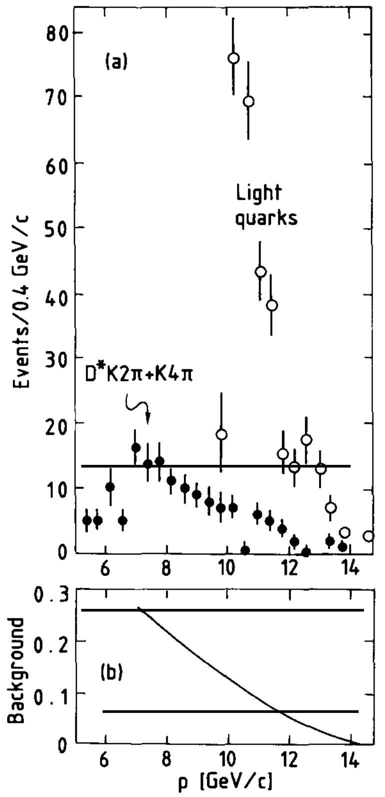

Fig. 5.1.5. Light quark tagging by selecting a high x trigger particle [205]. (a) Particle spectrum of light quarks and of $D^* \to K2\pi$, $K4\pi$; (b) background of b and c-events to a light quark sample as a function of the momentum of the trigger particle.

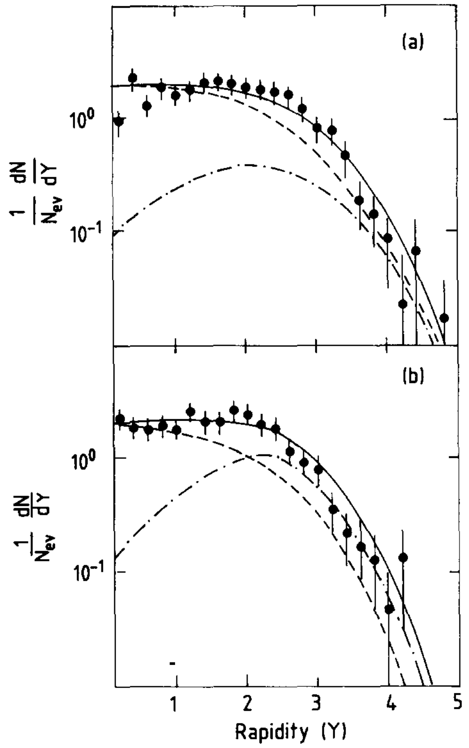

Fig. 5.1.6. Rapidity distribution of the events originating from light (a) and from charmed (b) quarks [205] together with results from a Monte Carlo simulation (full curve). Also shown are the contributions from first rank particles (dashed–dotted) and subsequent ranks (dashed).

A compilation of the average values of some representative distributions for jets of different flavours is listed in table 5.1.4.

The data can be well described by the fragmentation models which include both the decay properties of bottom and charm particles and a fragmentation of the subsequent system independent of the first rank hadron. This will be discussed in more detail in section 7.

Table 5.1.4
Average values of some variables for jets of different flavour

Parameter	b-jet	c-jet[a]	uds-jet[a]	average
n_{CH}	7.84 ± 0.3	6.6 ± 0.5	6.1 ± 0.2 ± 0.65	6.16 ± 0.01
p	1.06 ± 0.04	1.38 ± 0.06	1.52 ± 0.04	1.29 ± 0.01
p_T			0.39 ± 0.01	0.40 ± 0.01
p_T^2	0.31 ± 0.03	0.274 ± 0.001		
S	0.26 ± 0.02	0.094 ± 0.010	0.087 ± 0.007	0.141 ± 0.001
$1 - T$	0.149 ± 0.009	0.082 ± 0.005	0.092 ± 0.004	0.106 ± 0.003

[a] Additional cuts applied with the exception of the multiplicity.

5.2. Gluon jets

5.2.1. Global distributions

The discovery of events with hard gluon emission immediately raised the question if gluon jets differ from quark jets. Experimental information on the gluon fragmentation from the e^+e^- continuum events is, however, still rather scarce since the jets at $W \sim 35$ GeV are not well enough separated to simultaneously allow an unambigous association of particles to jets and to extract a high purity of gluon jets. Gluon jets from other processes like $\Upsilon(1S) \rightarrow ggg$ or the gluon scattering at high energy $p\bar{p}$ collisions are more easily accessible and have contributed important information.

Results have been obtained on the fragmentation function and the particle content within a gluon jet.

Since the three-gluon coupling determining the properties of a gluon jet is stronger than the qqg-coupling relevant for a quark jet, the multiplicity in gluon jets is supposed to be higher and correspondingly the fragmentation function softer than in quark jets. In the limit $s \rightarrow \infty$ lowest order QCD calculations lead to a multiplicity in the gluon jet of

$$\langle n \rangle_{\text{gluon}} = \tfrac{9}{4} \langle n \rangle_{\text{quark}} \tag{5.2.1}$$

and a larger width [207, 208]. The ratio $\frac{9}{4}$ reflects the ratio of the colour charge of the gluon C_g to that of the quark C_q. Higher order calculations modify the results to [209]

$$\frac{\langle n \rangle_{\text{gluon}}}{\langle n \rangle_{\text{quark}}} = \tfrac{9}{4}[1 - 0.27\sqrt{\alpha_s} - 0.07\alpha_s] , \tag{5.2.2}$$

where five flavours are assumed. The expression in the square brackets reduces the ratio by ~10% at $W = 34$ GeV.

Within the QCD shower models the higher gluon multiplicity is naturally taken into account since the higher ggg-coupling is explicitly included in the parton evolution. This is not true for models with a high Q^2 cutoff like that of the LUND group and the independent fragmentation scheme. Within the LUND model the gluon is not treated as a single entity but is split into a quark/antiquark pair and thus contributes to two incoherently fragmenting strings. Still, this model predicts a higher multiplicity in the direction of the emitted hard gluon since two strings contribute to the particle yield in the direction of the gluon and the multiplicity in each of the strings is proportional to $\ln(W)$, W being the mass of the string. Within the Independent Jet Model the properties of the gluon jet can be adjusted by an ad hoc parametrisation.

To determine the fragmentation function [210] and the multiplicity [211] of a gluon jet in e^+e^- annihilations, the MARK2 and HRS collaborations selected symmetric three-jet events, i.e. events where all jets are emitted under a relative angle of 120 degrees. In such a configuration each jet has the same energy $E_{\text{jet}} = W/3$ and thus the same probability of originating from a gluon. The properties of gluon jets can then be unfolded using the knowledge about the properties of quark jets.

The HRS collaboration selected 276 symmetric three-jet events. From Monte Carlo simulations they estimate that a quark jet produced at $W' = 2E_{\text{jet}}$ contains ~5.2 charged particles. To find the ratio of average multiplicities of gluon and quark jets, they compare the multiplicity distributions of the jets within the selected events to a model assuming a Poissonian multiplicity distribution in each of the three jets. The same average multiplicity $\langle n_1 \rangle = \langle n_2 \rangle$ was attributed to two of the jets, the "quark jets". The average multiplicity of the third jet, the "gluon jet", $\langle n_3 \rangle$ was left free. The model reproduces the measurement for $\langle n_3 \rangle = \langle n_g \rangle = 6.7^{+1.1}_{-2.1} \pm 1.0$ which has to be compared to $\langle n_1 \rangle = \langle n_2 \rangle = 5.2$ thus giving a ratio

$$\frac{\langle n_3 \rangle}{\langle n_1 \rangle} = \frac{\langle n_g \rangle}{\langle n_q \rangle} = 1.29^{+0.21}_{-0.41} \pm 0.20 . \qquad (5.2.3)$$

The large errors do not allow detailed conclusions. This result is consistent with an equal average multiplicity of gluon and quark jets and is ~2.5σ below the theoretical expectation (5.2.2). The discrepancy with the QCD prediction may be attributed to the relevance of phase space effects at the low jet energies considered. The observed distributions agree with predictions of the LUND model. A higher multiplicity within gluon jets has been observed at the p$\bar{\text{p}}$-collider [212].

The fragmentation function of the gluon was determined by the MARK2 collaboration also using symmetric three-jet events. They unfolded contributions from quarks and gluons to the average jet which has a fragmentation function given by

$$\frac{1}{\sigma_{\text{tot}}} \frac{1}{3} \frac{\mathrm{d}\sigma}{\mathrm{d}x}$$

with $x = 3p/W$. The quark fragmentation function at $W' \sim 19.3$ GeV was obtained by interpolating the data of fig. 3.2.5. At this energy the fraction of events with hard gluon bremsstrahlung is very small and it is safe to assume that all the particles originate from quarks. The fragmentation function of the gluon can therefore be written as the difference

$$\left(\frac{1}{\sigma_{\text{tot}}} \frac{\mathrm{d}\sigma}{\mathrm{d}x_p}\right)_{\text{gluon}} = 3\left(\frac{1}{\sigma_{\text{tot}}} \frac{1}{3} \frac{\mathrm{d}\sigma}{\mathrm{d}x_p}\right)^{\text{symm}}_{29} - 2\left(\frac{1}{\sigma_{\text{tot}}} \frac{1}{2} \frac{\mathrm{d}\sigma}{\mathrm{d}x_p}\right)_{19.3} . \qquad (5.2.4)$$

The average fragmentation function (full circles), the unfolded fragmentation function (open circles) and the interpolated quark fragmentation function at $W = 19.3$ GeV (dashed lines) are compared with one another in fig. 5.2.1. The gluon jet tends to have a softer fragmentation function than the quark jet.

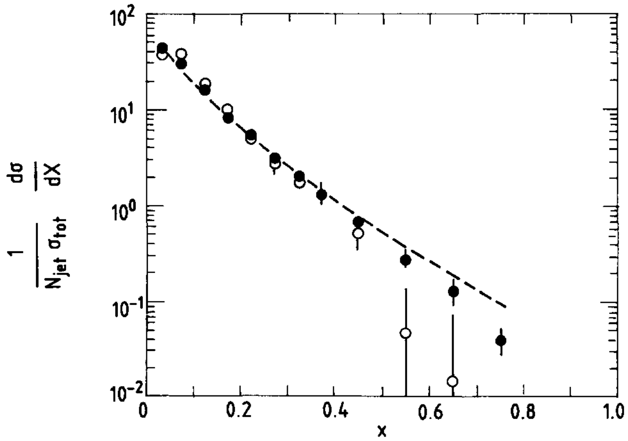

Fig. 5.2.1. Fragmentation function in symmetric three-jet events at $W = 29$ GeV [210]. Shown are the measured average function (full circles), the expected quark function (dashed line), the unfolded gluon function (open circles).

As mentioned before this behaviour is expected theoretically and is consistent with the indication for a larger multiplicity discussed before. It is also supported by results in p$\bar{\text{p}}$ collisions [213].

The distribution of the transverse momentum of particles within quark and gluon jets has been analysed by the JADE collaboration [214]. For this measurement a sample of events with three clearly separated jets was selected.

Since the radiated gluon is predominantly low energetic the gluon jet was identified with the lowest energetic jet found (see appendix A.5). The JADE group estimates that this is correct for about 50% of the events. To unfold the distributions of the gluon jet, one has to take care of possible uncertainties in determining jet energies, errors of the reconstructed directions and ambiguities in associating particles to jets. It therefore requires a careful comparison with simulation studies.

The JADE collaboration determined the average p_T's of each of the three jets as a function of the jet energy. Their measurements are displayed in fig. 5.2.2a. The $\langle p_T \rangle$ of jet 3 which has the highest fraction of gluons is larger than that of jets 1 and 2 for all jet energies considered. Figures 5.2.2b and c are obtained from simulation studies using the independent fragmentation scheme. For fig. b it was assumed that the fragmentation in a gluon jet and in a quark jet is the same. As can be seen, the data cannot be reproduced assuming an equal transverse momentum distribution. The Independent Jet Model can describe the data with a broader p_T-distribution of the gluon jet. For a Gaussian p_T distribution with respect to the jet axis (cf. eq. (2.2.6)) the data require

$$\sigma_q^{\text{quark}} = 330\,\text{MeV}\,; \qquad \sigma_q^{\text{gluon}} = 500\,\text{MeV}\,.$$

As mentioned before, the gluon is not fragmented individually in the LUND model but is split to form parts of two q$\bar{\text{q}}$ strings. Its prediction is in good agreement with the data without introducing new

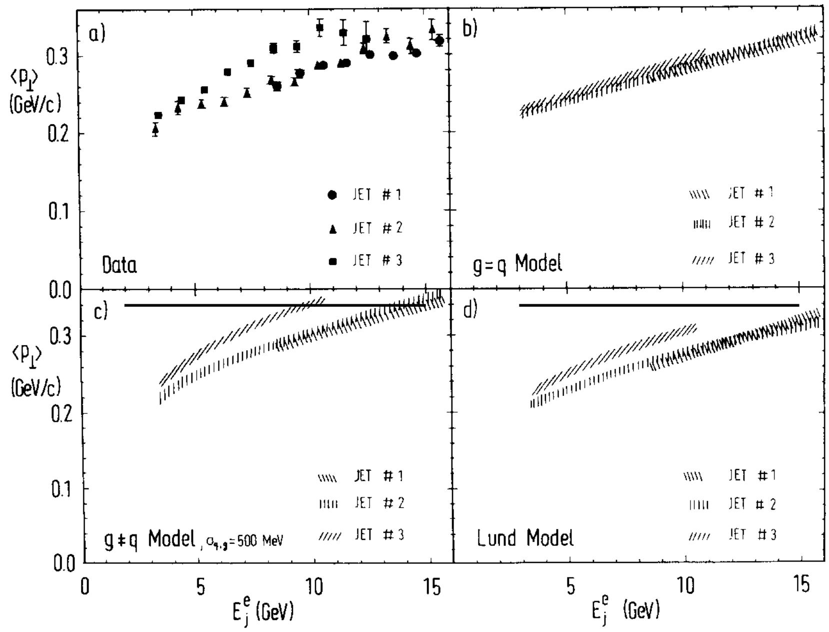

Fig. 5.2.2. Average p_T with respect to the jet axis as a function of the energy of the jets in three-jet events [214]. Data (a) and model predictions (b–d). The Independent Jet Model is used for (b) and (c) assuming the same p_T distribution for gluon and quark jets, respectively a higher p_T of the gluon jet. The result for (d) was determined using the LUND model.

parameters (see fig. 5.2.2d). The TASSO collaboration [215] finds a result consistent with that of the JADE group. However, their data do not exclude an equal transverse component in the quark and gluon jet.

5.2.2. Particle content in the gluon jet

The main information about the quantum number content of gluon jets has been obtained through data on the $\Upsilon(1S)$ which is assumed to decay predominantly into three gluons. Data collected in the continuum at $W \geq 30$ GeV are still not conclusive.

Evidence for a more abundant baryon production on the resonance ($\Upsilon(1S)$) than in the continuum around it ("off resonance") has been found by DASP2 [216], CLEO [217], and ARGUS [120]. In the case of protons the significance is only marginal as can be seen from table 5.2.1 where the yield of protons, kaons and pions is listed for both data "on" and "off" the resonance. The DASP2*) data indicate a higher proton yield with a significance of $\sim 2.7\sigma$, the CLEO data [119] of $\sim 2\sigma$. Both experiments find no increase of the kaon and pion yield on the resonance.

The data on hyperon production exhibit a more significant difference between the two data samples. The ratio of particle yields on and off the resonance found by CLEO and ARGUS are the following: (i) For Λ production: the CLEO group has determined the yield relative to the K^0 production. They find $N(\Lambda)/N(K^0)$ to be in the continuum $0.07 \pm 0.01 \pm 0.01$ and on the $\Upsilon(1S)$ resonance $0.21 \pm 0.01 \pm 0.03$. The ARGUS collaboration determined the ratio of Λ production on and off the resonance: $\Lambda_{\mathrm{on}}/\Lambda_{\mathrm{off}} = 2.9 \pm 0.4$. That is, both experiments find about a 5σ increase of the Λ-yield in gluon jets. (ii) For the Ξ production: both experiments determine the ratio $N(\Xi)/N(\Lambda)$ and obtain in the continuum $0.07 \pm 0.01 \pm 0.01$ (CLEO) and 0.09 ± 0.02 (ARGUS), and on the resonance $0.10 \pm 0.01 \pm 0.02$ (CLEO) and 0.08 ± 0.01 (ARGUS), respectively. The results of the two experiments are consistent with each other and indicate that the ratio is the same on and off the resonance. Thus also the Ξ's are produced more copiously on the resonance.

These results suggest that baryons or at least hyperons are more abundant in gluon than in quark jets.

No other significant difference in the quantum number content has been found. The numbers of different particle species as measured by CLEO [119] are listed in table 5.2.2. It should be noted that the total multiplicity differs by only $\sim 25\%$.

The production rate for a particle containing a quark of flavour f is assumed to be

$$N_f \propto p_f \cdot n(q \to H + q'),$$

Table 5.2.1
Proton, kaon and pion yield on and off the $\Upsilon(1S)$

Particle	on/off	DASP2	CLEO
protons	on	0.081 ± 0.021	0.60 ± 0.09
	off	0.015 ± 0.011	0.40 ± 0.06
$K^\pm$	on	0.154 ± 0.027	1.3 ± 0.2
	off	0.183 ± 0.039	1.4 ± 0.2
$\pi^\pm$	on	0.765 ± 0.048	8.3 ± 0.4
	off	0.802 ± 0.059	8.7 ± 0.4

Table 5.2.2
Yield of various particle species on and off the $\Upsilon(1S)$

	continuum	$\Upsilon(1S)$
all	13.4 ± 0.8	16.5 ± 1.9
charged	10.0 ± 0.5	10.7 ± 0.5
vector	2.9 ± 0.4	3.6 ± 0.7
strange	2.3 ± 0.3	2.8 ± 0.4
baryon	0.80 ± 0.12	1.20 ± 0.18

*) Data were only considered in the momentum range $0.3 < p < 1.5$ GeV.

where p_f is the probability to pick out a parton with flavour f from the sea and n the number of steps in the fragmentation chain. Therefore two reasons for an increased N_f can be envisaged. It could be just due to a larger number of steps $n(q \to H + q')$ in the fragmentation chain or a larger effective p_f. The increase of the average multiplicity is too small to explain the higher hyperon yield, instead it indicates that p_f may be different in gluon jets.

The corresponding studies in the high energy continuum are hampered by the problems of associating particles to jets already discussed before.

The TASSO collaboration [127] has selected three-jet candidates and reconstructed their energy and direction along the lines explained in appendix A.5. The yield of K_s^0 and Λ per jet is displayed in fig. 5.2.3 as a function of the jet energy. It is compared to the yield per jet in all events produced at $W = 14$, 22 and 34 GeV. Since the fraction of distinct three-jet events for this reference sample is small, the corresponding jet energy was assumed to be $W/2$. The data show some tendency for both a higher K^0 and Λ yield in the three-jet events than for two-jets. The significance is marginal. Also shown is a simulation study assuming the K^0 respectively Λ-yield within the gluon jet to be f times that in the quark jet. The lines correspond to $f = 0$, 1, 2 and 3. No clear conclusion can be drawn from this measurement.

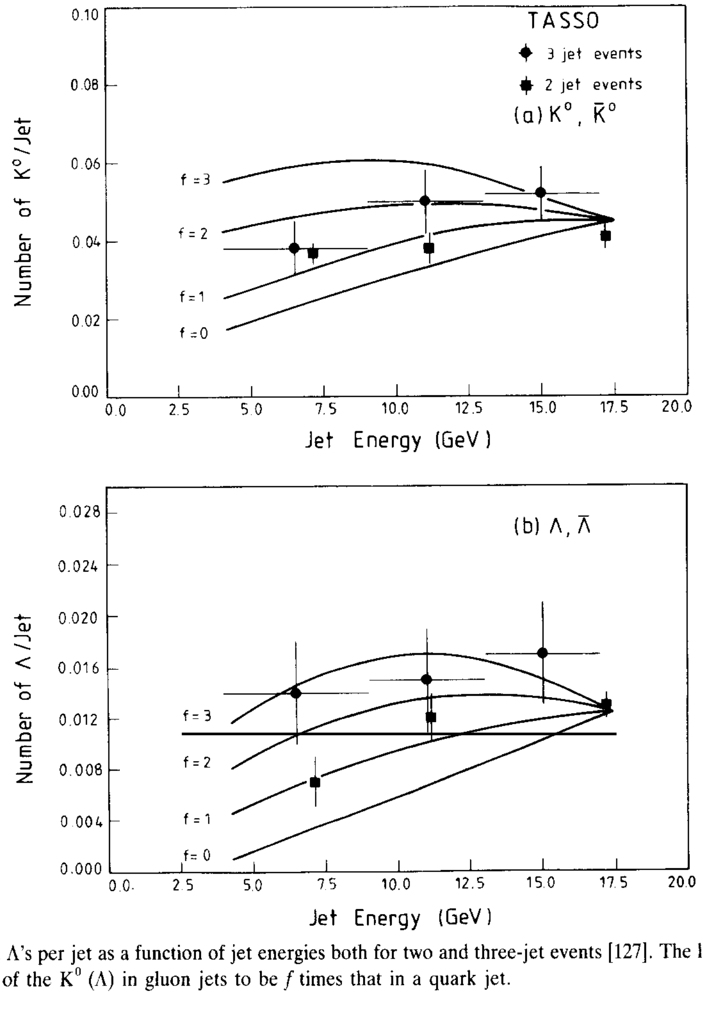

Fig. 5.2.3. Number of K^0's and Λ's per jet as a function of jet energies both for two and three-jet events [127]. The lines are results of Monte Carlo simulations assuming the yield of the K^0 (Λ) in gluon jets to be f times that in a quark jet.

The MARK2 collaboration [141] has compared the thrust distribution of events with at least one Λ detected to that for all events. As can be seen from fig. 5.2.4, the fraction of events containing a Λ increases with decreasing thrust, i.e. broader events. The interpretation, however, is not clear, since low thrust events have a higher multiplicity. Thus the increase may just reflect that more steps are taken in the fragmentation process (see discussion above).

A similar analysis has been pursued by the JADE collaboration [218] using their η-sample. In fig. 5.2.5 the ratio of η to π^0 yield is plotted as a function of the event sphericity. Within the statistical and systematic errors the data are compatible with a constant ratio, although some trend exists towards a higher yield with sphericity.

No final explanation for the increased baryon yield in the Υ(1S) decays has been found although it can be accommodated in some models. The LUND-group [219] argues that it is because diquarks cannot be primarily produced in continuum events. There the virtual photon only couples to quarks and not to diquarks. Such suppression is not true in the three-gluon decay. Field [220] relates the high abundance of baryons to the occurrence of higher cluster masses in the context of QCD shower models on the resonance. To resolve this puzzle, more precise data in particular for the different types of baryons would be helpful. Also measurements from the decay of toponium into three gluons (if it could be identified) may indicate the solution.

A larger η yield in gluon jets is perceived in ref. [221] where it is assumed that the chromo-electric flux tube developing through a gluon predominantly breaks up into an SU(3) singlet.

Results have also been obtained on the charge flow in gluon jets. In contrast to quark jets, those

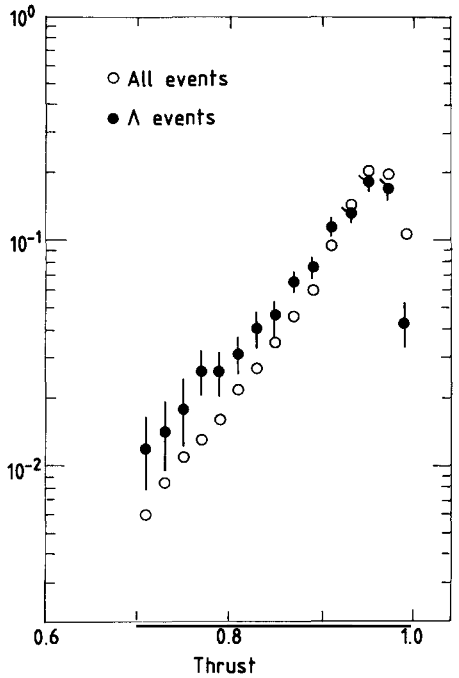

Fig. 5.2.4. Normalized thrust distribution of all events and those containing a Λ [141].

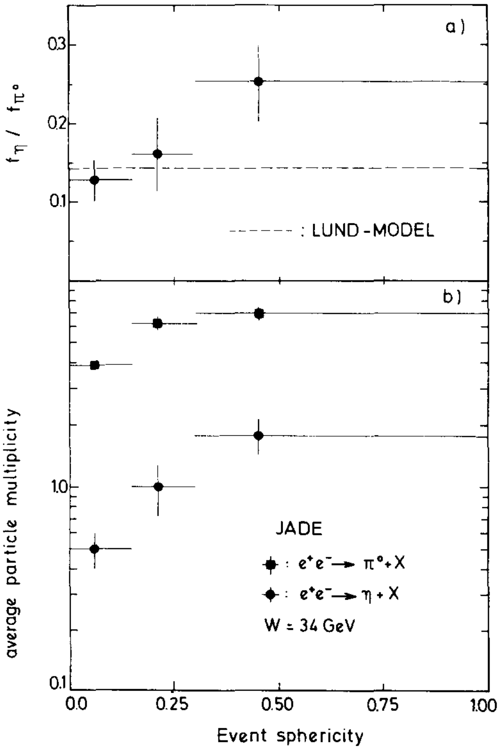

Fig. 5.2.5. η-yield as a function of the event sphericity [218]. Shown are (a) ratio of η to π^0 production; (b) η and π^0 multiplicity.

from gluons do not exhibit long range charge correlations, indicating that they have a zero charge [119], see also ref. [213]. We will come back to this measurement in section 8.1.

5.3. Conclusions

In general only little difference has been found between jets originating from different kinds of partons. This result is valid for the overall properties of jets as well as for the types of particles within a jet. It holds true both for jets from the various types of quarks and from gluons.

These results indicate that the mixture of all flavours gives a representative picture of the jet and event properties. Only small biases are introduced by not considering a specific type of jet.

There exist two notable exceptions.

The jets from bottom quarks at $W = 29\,\mathrm{GeV}$ are broader than the average jets. The particle distribution exhibits a significant enhancement in the rapidity around

$$y \sim \ln \frac{2\langle x_\mathrm{b}\rangle E_\mathrm{beam}}{m_\mathrm{b}} \, .$$

This accumulation as well as all the other specific properties of bottom jets can be attributed to the decay properties of bottom hadrons alone.

Hyperons are significantly more abundant in gluon jets than in quark jets. Indications have also been found for a softer fragmentation function, a higher value of the average transverse momentum and a higher multiplicity. However, all these results require confirmation from higher statistics samples and probably higher energies.

PART II. LOOKING INSIDE JETS

Whereas the first part covered single particle distributions and event measures, this second part is devoted to correlations inside jets as well as to comparisons with fragmentation models. In some sense the first part outlined only a static picture of jets in their final configuration. In this part the experimental information as to how a jet develops and about the structure of the hadronisation region will be presented. To this end we will discuss correlations between various parts of the event and between individual particles. Its aim is to identify substructures in the hadronisation region, to explore the shape and size of the sources, and to study the sequence of particle emission. In addition, the information about the border line between perturbative and non-perturbative effects will be summarized in section 9.

Various methods have been applied to serve as a microscope for the region between 10^{-2} and 1 fm. We will enter this part by summarizing some of the most frequently used.

II.A. How quantum numbers are compensated inside a jet. The evolution of a jet is reflected in how the particles succeed one another. Quantum number compensation is one of the most powerful tools for studying the sequence of parton production during jet development.

The methods used and their general ideas can be visualized by the schematic event of fig. II.1 which exhibits the typical features conceived for fragmentation. A primary pair of quark and antiquark is produced that rapidly flies apart forming a string between them. The string breaks up at some point giving rise to another $\mathrm{q\bar{q}}$ pair. These combine with the primary pair to form a hadron and another

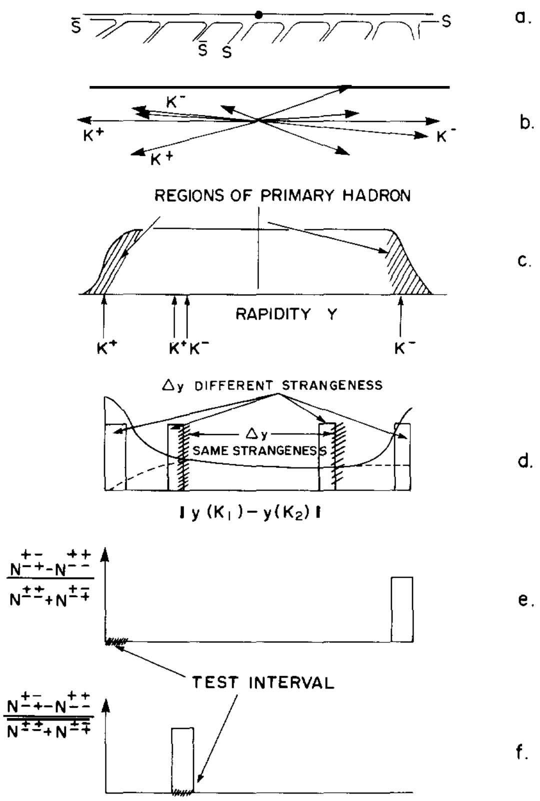

Fig. II.1. Schematic view of mechanisms and methods for detecting quantum number compensation. (a) Fragmentation chain with two s$\bar{\text{s}}$-pairs. (b) Resulting particle momenta with four charged kaons. (c) Rapidity distribution. (d) Distribution of rapidity differences for pairs of particles with the same and opposite strangeness. The full and dashed lines represent smoothed distributions. (e, f) Charge compensation function for two different reference intervals.

string. The process continues until all energy is absorbed into hadrons. Since hadronisation occurs stepwise the quark and antiquark are absorbed in subsequently produced hadrons. The small space–time interval in which the q$\bar{\text{q}}$ pair fluctuates out of the vacuum translates into a small distance in space–time between the production vertices for the hadrons. As a result those have very similar rapidities. These features suggest to study the compensation of quantum numbers as a function of their distance in rapidity.

The difference in rapidity Δy is related to the invariant mass M of system of two particles of mass m_i as (see appendix A.1)

$$\langle \Delta M^2 \rangle = \langle M^2 - m_1^2 - m_2^2 \rangle \sim \langle m_{\mathrm{T1}} m_{\mathrm{T2}} [\mathrm{e}^{\Delta y} + \mathrm{e}^{-\Delta y}] \rangle \, . \tag{II.1}$$

Here $m_{\mathrm{T}} = \sqrt{m^2 + p_{\mathrm{T}}^2}$ and we assumed that the difference of the azimuthal angles

$$\langle \Delta\phi = \phi_1 - \phi_2 \rangle = \pi/2$$

and therefore $\langle \cos \Delta\phi \rangle = 0$. The rapidity difference gives an expanded view of the mass of the particle pair and allows conclusions about the mass scale at which two hadrons are generated out of the vacuum.

Particles with several kinds of quantum numbers have been tested for the compensation mechanism. The most straightforward is the charge, studying the compensation of strangeness or baryon number requires particle identification and is thus more difficult. However, as will be discussed below it is also more rewarding.

The schematic event of fig. II.1 indicates two kinds of compensation mechanisms:

(a) The compensation due to the first partons. These are produced at a common point in space coupling to the virtual photon (or Z^0). Their (relative) Q^2 is very high and the hadrons containing them are normally in different event hemispheres and quite far apart in rapidity space. Evidence for this long range correlation would be extremely important. Firstly it constitutes a direct proof of the relation between the rapidity and the rank of a particle and secondly it opens a way for determining the quantum numbers of the first produced parton.

(b) The compensation due to the partons picked out of the sea. These are due to the emission of a flavour neutral entity like a $q\bar{q}$ pair or a gluon splitting into a quark and an antiquark. They are expected within a small range of rapidity and reveal more about the low Q^2 scenario.

The methods applied for studying the compensation mechanism depend on the size of the available data sample and the experimental acceptance. They can be illustrated using the event of fig. II.1:

(i) If only a few pairs of particles in a wide region of rapidity have been collected, the events can be divided into two hemispheres with respect to the event axis and analysed in terms of how many pairs can be found in the same, respectively, opposite hemisphere.

(ii) A data sample in a limited range of rapidity can be analysed in terms of the distance in rapidity between two particles (see fig. II.1d).

(iii) If both a large rapidity interval and a large data sample are available, compensation can be studied in the most detailed way. Each particle i with a rapidity value y_i' acts as a test particle and the compensation of its quantum numbers at some position y can be studied. Several kinds of two-dimensional functions $f(y, y')$ have been defined. They are in general of the form

$$A(y, y') = \frac{N^{+-,-+}(y, y') - N^{++,--}(y, y')}{N^{+-,-+}(y, y') + N^{++,--}(y, y')} . \tag{II.2}$$

Here + and − denote a positive or negative quantum number like the electric charge or strangeness of the particle considered and e.g. $N^{++}(y, y')$ is the number of pairs of positively charged particles with one particle at rapidity y, the other one at y' (see figs. II.1e and f).

In all of these cases both the pairs of opposite and equal quantum numbers are considered. The main physics interest is concentrated on the pairs of opposite quantum numbers, since they reveal the kinematical and space–time relation of a parton and its conjugate partner. The equal sign pairs constitute a very convenient way for determining the background in an event*). This background can be either due to experimental problems (e.g. misidentification of the particle type) or to trivial correlations (e.g. between different pairs of strange/antistrange quarks, which are produced at different points in space–time).

II.B. Dividing an event into larger parts. In addition to the compensation of specific quantum numbers of partons within two particles, several experiments searched for long-range correlations of topological properties. Examples of such correlations have been found in pp collision. They provide an

---

*) See however sections 8.3 and 10 where interesting applications of particles with the same sign are considered.

important check on the iterative jet development perceived in the standard models of jet evolution. These assume that at each stage of jet development the residual system hadronises according to the general rules that hold true for the total system. By separating some part of an event and studying its property as a function of the residual part, this assumption can be experimentally tested. One special application is to separate the particle containing the primary parton and to study the impact of the primary flavour on the subsequent fragmentation.

II.C. Comparing data and models. In the absence of a complete theoretical calculation of jet properties, phenomenological models and their realization in computer programs to simulate fragmentation have turned out to be an essential tool for studying jet properties. As discussed in section 2, several models of hadronisation exist.

An understanding of how a quark converts into hadrons is therefore related to finding the model based on the adequate concept. However, these concepts are buried beneath a variety of kinematical constraints and uncertainties about the kinds of hadrons produced. These are reflected in the ad hoc parameters needed in all approaches. A certain choice of those is unrelated to the basic concept of these models but influences their predictions considerably. As an example the variation of the fragmentation functions is displayed in fig. II.2 for different values of the probability to produce vector mesons in the jet ($V/(P+V)$ ratio, cf. section 2.2). For the calculation with the LUND simulation all other parameters were fixed. Shown is the fractional change of the fragmentation function of final particles by changing $P/(P+V)$ from 0.5 to 0.25 and 0.75, respectively. As can be seen the results differ by more than 25% in some regions of x. In principle the fraction of vector particles within jets can be measured, in practice the experimental results constraining these parameters are not very precise (cf. section 4.2) and their values cannot be reliably predicted by theoretical calculations.

These models include in addition ad hoc solutions to overcome technical problems in generating the

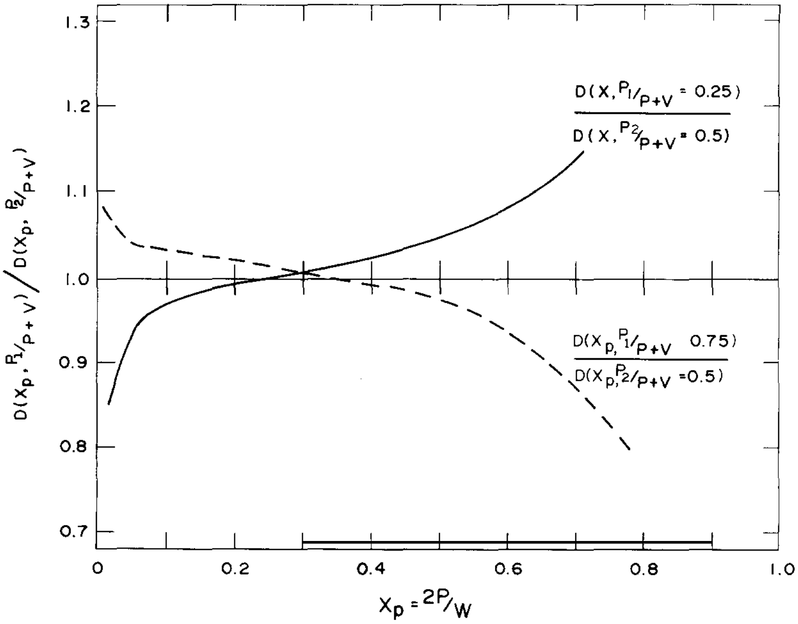

Fig. II.2. Relative variation of the fragmentation function with the $P/(P+V)$ ratio (Monte Carlo simulation).

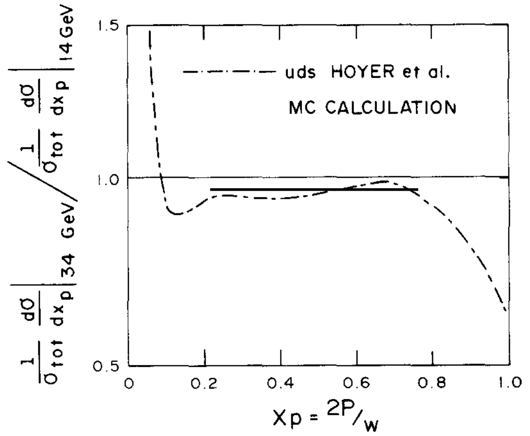

Fig. II.3. The ratio of the fragmentation functions at $W = 34$ GeV and $W = 14$ GeV as a function of $x_p = 2p/W$ determined with the Independent Jet Model. QCD corrections were neglected.

events. For example, in the Independent Jet Model the energy and momentum have to be reshuffled among the particles after the fragmentation of each parton has come to an end (cf. section 2.2.2). How this is done influences the particle distribution. In fig. II.3 its effect on the scale breaking of the fragmentation function is displayed. In particular the fall-off at high values of x_p is purely a result of the way energy and momentum are conserved in the particular model considered.

Thus, the following two criteria have to be fulfilled for a discrimination between the various approaches and a selection of the model representing the underlying dynamics of jet development: (1) Some discriminative distribution has to be found that is closely related to the basic ideas of the models; (2) It has to be established that a possible failure of one model is not due to an inappropriate parametrisation.

6. The space–time structure of the hadronisation region

As already stated in the introduction, jet development can be divided into three space–time regions. In a small region up to ~0.05 fm away from the production point of the primary quarks, partons exist asymptotically free. Outside of this region these partons convert into hadrons. This source of hadrons is in the focus of fragmentation studies. In a third region of order one fermi away from the interaction point, the jet consists entirely of hadrons which then decay and/or interact in the detector.

The global structure of the hadronisation region has to be inferred from the relation among the observed particles which are detected at a distance of about 10^{15} times the radius of the region of interest. In the following sections we will present results from an interferometric method, first applied in astronomy to measure the diameter of distant stars [222, 223]. It has the potential of providing information about the local space–time structure between the emission of two particles. More related to the global structure of the hadronisation region is the particle and energy flow in the events that will be discussed in 6.2.

6.1. *Bose–Einstein correlations*

As was first discovered by ref. [224] pion pairs π_1 and π_2 produced in pp-collisions behave differently at small differences in momentum

$$\Delta p = |p_1 - p_2| \tag{6.1.1}$$

depending on whether they are of equal or different charge. Soon after the experimental findings this behaviour was attributed to the symmetry properties of pions [225]: elementary quantum mechanics requires the wave function for two indistinguishable bosons to be symmetric.

This effect can be understood (see refs. [226, 227]) by considering two indistinguishable pions with momenta $\boldsymbol{k}_1$, $\boldsymbol{k}_2$ emitted from two discrete sources A and B (see fig. 6.1.1). In addition we assume the particle emission from these two sources to be completely incoherent. The conditional wave function at the point C of the observer is then given by

$$A_{12} = \exp(\mathrm{i}\boldsymbol{k}_1 \cdot \boldsymbol{x}_\mathrm{A} + \phi_\mathrm{A}) \exp(\mathrm{i}\boldsymbol{k}_2 \cdot \boldsymbol{x}_\mathrm{B} + \phi_\mathrm{B}) . \tag{6.1.2}$$

Here π_1 with momentum $\boldsymbol{k}_1$ is emitted from $\boldsymbol{x}_\mathrm{A}$ and π_2 with momentum $\boldsymbol{k}_2$ from $\boldsymbol{x}_\mathrm{B}$. Since pions obey Bose–Einstein symmetry, the total wave function must be symmetric under the exchange of π_1 and π_2, i.e.

$$\begin{aligned} A &= (1/\sqrt{2})[A_{12} + A_{21}] \\ &= \frac{1}{\sqrt{2}} [\exp(\mathrm{i}\boldsymbol{k}_1 \cdot \boldsymbol{x}_\mathrm{A} + \phi_\mathrm{A}) \exp(\mathrm{i}\boldsymbol{k}_2 \cdot \boldsymbol{x}_\mathrm{B} + \phi_\mathrm{B}) + \exp(\mathrm{i}\boldsymbol{k}_2 \cdot \boldsymbol{x}_\mathrm{A} + \phi_\mathrm{A}) \exp(\mathrm{i}\boldsymbol{k}_1 \cdot \boldsymbol{x}_\mathrm{B} + \phi_\mathrm{B})] . \end{aligned} \tag{6.1.3}$$

The rate of observing two pions of equal charge is therefore

$$P = 1 + \cos \Delta\boldsymbol{k} \cdot \Delta\boldsymbol{x} \tag{6.1.4}$$

which is proportional to the ratio of the production yields of equally and oppositely charged pairs,

$$R = \frac{N^{++} + N^{--}}{N^{+-} + N^{-+}} \propto 1 + \cos \Delta\boldsymbol{k} \cdot \Delta\boldsymbol{x} .$$

The number of pairs of equally charged pions should be enhanced if they have similar momenta.

This argumentation can be generalized to sources of a density distribution $\rho(x)$ which modifies the probability function to be

$$R \propto 1 + [\rho'(\Delta k)]^2 , \tag{6.1.5}$$

$\rho'(\Delta k)$ being the Fourier transform of $\rho(x)$. To be subject to the symmetrisation property, two hadrons have to be produced at very close points $\Delta x \cdot \Delta p < 1$. The shape and size of the source is therefore reflected in the energy and momentum distributions of the particles exhibiting this effect.

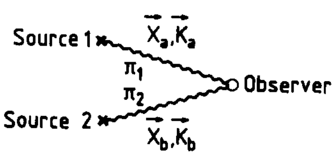

Fig. 6.1.1. Schematic picture of the contributions to the Bose–Einstein effect from two distinct sources.

In the argumentation given above, it was assumed that the two particles are emitted incoherently. The effect of a coherent contribution is to reduce R [228] which is accounted for by introducing a parameter α

$$R \propto 1 + \alpha |\rho'(\Delta k)|^2 . \tag{6.1.6}$$

The value of α has to lie between zero and one. For a totally chaotic source α takes on the maximum possible value of 1, if the pions are emitted completely coherently $\alpha = 0$*).

The Bose–Einstein effect therefore is a probe of the local space–time structure of the emitting source and is sensitive to both its size and shape as well as its coherence.

Some proposed shapes of the particle source or equivalently its Fourier transform ρ', that have been considered in experiments are given by the following.

(i) A spherically symmetric source in the rest system of the two particles considered can be parametrized by a Gaussian shape

$$R(Q^2) = 1 + \alpha\, \mathrm{e}^{-\beta Q^2} , \tag{6.1.7}$$

where $Q^2 = M^2 - 4m^2$, M being the invariant mass of the two-particle system, m the mass of the individual particles. This parametrisation has the advantage of being rather simple and of having a Lorentz invariant argument. No axis in space is distinct, α and β are free parameters.

(ii) For a source without spherical symmetry, Q^2 can be split into a longitudinal and transverse component

$$R \sim 1 + \alpha \exp[-\beta q_{\mathrm{T}}^2 - \gamma(q_{\mathrm{L}}^2 - q_0^2)] . \tag{6.1.8}$$

Here $q_{\mathrm{L}} = q_{\mathrm{L}1} - q_{\mathrm{L}2}$ is the component in the direction of the pair momentum. For high energies $q_0 \sim |q_{\mathrm{L}}|$ and $Q^2 \sim q_{\mathrm{T}}^2$ thus this equation approaches eq. (6.1.7).

(iii) Parametrisations have also been derived within the string picture. Bowler [227] suggests a form

$$R = 1 + \alpha \rho_{\mathrm{L}}'^2 \rho_{\mathrm{T}}'^2 \tag{6.1.9}$$

with $\rho_{\mathrm{T}}'^2 = \exp[-\beta_{\mathrm{T}} Q_{\mathrm{T}}^2]$ and

$$\rho_{\mathrm{L}}'^2 = A \cdot \frac{1}{1 - [\beta_{\mathrm{L}} Q_{\mathrm{L}}^2]^2 \ln \sqrt{1/\beta_{\mathrm{L}} |Q_{\mathrm{L}}^2|}} .$$

Note that for low momentum particles the factorization of the longitudinal and transverse density can only be an approximation.

(iv) Also the parametrisation of ref. [229] has been developed on the basis of the string picture. Considering the sequence 1–I–2 (2–I–1) of the particle production, where 1, 2 are identical particles and I an intermediate state, they find

---

*) The formalism can be extended to more than two particles. However, it is not obvious if anything can be learned about the parameter α which is not already known from the two-particle effect. Although measurements of three- and four-particle correlations have been published, they will not be discussed here.

$$R \sim 1 + \left\langle \frac{\cos(\kappa \cdot \Delta A)}{\cosh(b \cdot \Delta A/2)} \right\rangle . \tag{6.1.10}$$

Here κ is the string constant ($\sim 0.2\,\mathrm{GeV}^2$), b is related to the correlation length in rapidity, cf. eq. (2.2.5), and

$$\Delta A = p_1 E_2 - p_2 E_1 + (p_1 - p_2)E_1 - (E_1 - E_2)p_1 \kappa^2 . \tag{6.1.11}$$

This formula has been implemented in the LUND simulation program (see fig. 6.1.2). As has been shown in ref. [230] this shape is similar to the eq. (6.1.9).

(v) The Kopylov–Podgoretsky parametrisation [231]

$$R(q_\mathrm{T}, q_0) = 1 + \lambda \left[\frac{2J_1(q_\mathrm{T}, \xi)}{q_\mathrm{T}\xi} \right]^2 \frac{1}{1 + q_0 \tau^2} \tag{6.1.12}$$

follows from a model of thermally excited oscillators on the surfce of a sphere. Here $q_\mathrm{T} = q_{\mathrm{T}1} - q_{\mathrm{T}2}$, where $q_{\mathrm{T}i}$ is the momentum of particle i transverse to the pair momentum and $q_0 = |E_1 - E_2|$. J_1 is the Bessel function of the first kind, ξ, λ and τ are free parameters. This parametrisation is not Lorentz invariant.

The Bose–Einstein symmetry has been studied in hadron–hadron, lepton–hadron and e^+e^- collisions (see review in ref. [232]), in the latter case by the MARK2 [233, 234], TASSO [235–237], CLEO [238], and the TPC [239] groups.

The main experimental difficulty is, besides particle identification, how to normalize the field of equally charged pions. In addition to kinematical problems, that partly cancel in the ratio of equally to oppositely charged particle pairs, dynamical differences between equal and unequal charge combinations exist. They are due to the short range quantum number correlations addressed before as well as to decays of neutral resonances into oppositely charged particles ($\omega^0 \rightarrow \pi^0\pi^+\pi^-$). Both effects change the shape of the measurement but are completely unrelated to the Bose–Einstein symmetrisation. The distortions are corrected for by mixing particles from different events, by comparing the observed R to that obtained from a Monte Carlo simulation (without the symmetrisation property), or by parametrising the ratio in a region not affected by the Bose–Einstein correlations.

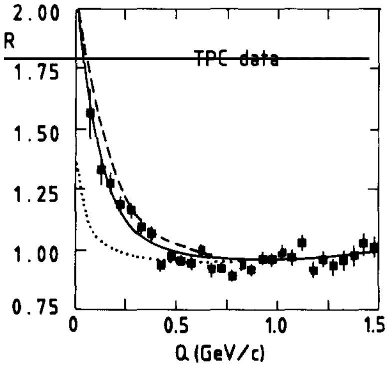

Fig. 6.1.2. Measured ratio R of the number of particles of the same charge over the number of opposite charge as a function of $Q = \sqrt{M^2 - 4m_\pi^2}$ [239]. The lines are results from calculations of the model of ref. [229] assuming different parametrisations of κ and b (see text). The dotted curve takes into account effects from resonance decays.

Most e^+e^- experiments prefer to parametrise the measured effect by eq. (6.1.7). A compilation of their results using this formula is listed in table 6.1.1. Here β is interpreted as the radius r of the source. It should be noted that the results for α and β are correlated.

As can be seen, all experiments observe the Bose–Einstein effect with high significance (as an example the measurement of ref. [239] is displayed in fig. 6.1.2). The quantitative results, however, show a considerable variation.

The size of the source is measured as ~0.8 fm. Since the Bose–Einstein effect is sensitive to hadrons and not to quarks and gluons this result sets a bound to the region where quarks and gluons exist before hadronisation. Quarks can be apart at most 0.8 fm before converting into a hadron. Such a limit is consistent with the radii of hadrons.

The uncorrected values of the coherence factor as listed in the table spread considerably around an average value of ~0.5. For interpreting the results in terms of incoherence one has to consider that the value of α is reduced by particles that cannot exhibit the symmetrisation properties. Firstly background from misidentified particles decreases the observed enhancement, secondly decay products from long-lived particles like K_s^0, Λ, charm and bottom hadrons are included in the total sample. Those are, however, not subject to the symmetrisation property since they originate from points in space that are too far away from the source. The fraction of fake combinations due to these effects can be large, for example the TASSO group estimates that only about 50% of all pairs considered are capable of exhibiting the Bose–Einstein enhancement. The corrections for these combinations affect its size only, the radius remains unchanged. As can be seen from table 6.1.1, α approaches its maximum allowed value after the corrections have been applied. This indicates an almost completely incoherent emission. Note that the correction procedures of each experiment are different thereby complicating a common interpretation.

Measurements of the size, shape and magnitude of the coherence exist also as a function of several event and particle properties. However, no significant dependence on either of these parameters has been found. Data have been analysed (i) for different energies, (ii) for on and off a resonance [238], (iii) for different multiplicities [239], (iv) for different angles of the particle pair with respect to the event axis [236].

Within the systematic and statistical uncertainties no dependence on any of these special selections has been found.

Several experiments attempted a determination of the shape of the source comparing the various parametrisations (6.1.7–6.1.12) to the data. The measurements are not sensitive enough to discriminate between the various models. They are consistent with the simplest parametrisation of eq. (6.1.7) assuming a spherically symmetric emission in the rest system of two particles.

Table 6.1.1
Results for the Bose–Einstein effect

Experiment	W [GeV]	α (uncorrected)	α (corrected)	r [fm]
CLEO	10.4	0.41 ± 0.04	1.20 ± 0.23	0.86 ± 0.08
	$\Upsilon(1S)$	0.50 ± 0.09	1.45 ± 0.25	0.99 ± 0.14
TPC	29	$0.61 \pm 0.05 \pm 0.06$		$0.65 \pm 0.04 \pm 0.05$
TASSO	34	0.35 ± 0.05	$0.70 \pm 0.06 \pm 0.09$	0.81 ± 0.06

6.2. The string effect

It is already evident from the existence of jets, i.e. narrow bundles of particles, that the hadronisation region is not isotropic. Rather the hadrons are emitted along one distinct axis in space coinciding with the direction of the emanating primary quarks. However, do two subsystems exist each of which is centered around one of the quarks as suggested by the Independent Jet Model? Or is there only one system as proposed by the String Model? And how is the region of hadronisation shaped in the case of gluon bremsstrahlung?

Whereas the Bose–Einstein effect has the potential of exploring how the structure of the hadronisation region is shaped locally around the emission point of two particles, the energy and particle flow probes its global structure. Following a proposal of ref. [240] the JADE group was the first to compare the measured energy and particle flow in three-jet events to the predictions of simulation models and thereby to discriminate between the until then frequently used Independent Jet Model and the String Model. Their analysis and the subsequent theoretical and experimental developments contributed largely to the picture of the hadronisation region.

6.2.1. The high cut-off models

Although based on different concepts, the String and the Independent Jet Model can describe two-jet events very well by suitably adjusting the fragmentation parameters. However, the treatment of gluon bremsstrahlung leads to different event topologies such that the conceptual differences cannot be concealed. The crucial point is that in two-jet events the axis of fragmentation coincides in both models with the axis of the primary quark/antiquark pairs (fig. 6.2.1). This ceases to be true in the string approach to gluon bremsstrahlung.

In the Independent Jet Model the individual partons fragment and as a consequence the fragmentation proceeds in three subsystems along the direction of the three partons. In the string approach a

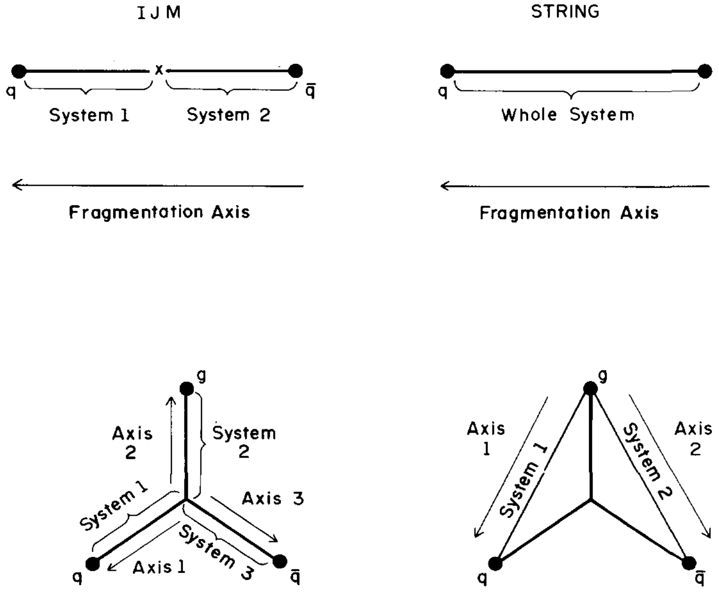

Fig. 6.2.1. Schematic diagram of Independent Jet and String fragmentation.

colour neutral system, the string, fragments and therefore the axis of fragmentation coincides with the axis of the string. Since these strings are formed by the quark and one part of the gluon, the antiquark and the other part of the gluon, respectively, their directions are not identical to those of the partons but move in the overall c.m. system of the event.

As suggested [240] this different treatment of fragmentation in three-jet events can be used to discriminate between the two different concepts. In the LUND model the momenta of the particles produced (neglecting decays and momentum components transverse to the string) are distributed along a hyperbola. Defining as x the direction into which the whole string is moving and as y the axis perpendicular to the direction of motion in the three parton plane, the hyperbola is given by

$$p_x^2 - p_y^2\beta^2\gamma^2 = \beta^2\gamma^2 m^2 , \tag{6.2.1}$$

where β and γ are the Lorentz factors of the string in the laboratory system, $\beta = \cos \frac{1}{2}\theta_{\mathrm{qg}}$, and m is the mass of the particle considered. Within the Independent Jet Model, however, the particles are distributed along the asymptotes

$$p_x^2 - p_y^2\beta^2\gamma^2 = 0 . \tag{6.2.2}$$

The main difference between the two models should therefore be visible for low-momentum particles in the region between the quark and the gluon. It should be more prominent for heavy particles. Although the basic features remain, contributions from the transverse momenta in the event plane smear the difference somewhat out.

The JADE collaboration [241–243] was the first to use the particle and energy flow of three-jet events to compare the Independent Jet and the LUND model. The data could very well be described by the string model, whereas the Independent Jet Model failed.

The energy and particle flow measured by JADE together with the model predictions of the LUND group and of the Independent Jet Model as realized by Hoyer et al. is shown in fig. 6.2.2. The procedure for reconstructing angles and energies is discussed in appendix A.5.

The data shown in fig. 6.2.2 exhibit accumulations of particles at $\theta = 0°$, ~155° and ~230°. According to the discussion in appendix A.5, the first two are mainly due to quarks or antiquarks, the third peak to gluons. The discrepancies between the String Model and the Independent Jet Model show up in the regions between the peaks. Whereas the String Model reproduces the data nicely, the Hoyer et al. model, the most frequently applied version of the Independent Jet Model predicts too large a yield between the quark and antiquark and a too low one between the quark (antiquark) and the gluon. This effect is visible for the particle and energy flow and even more pronounced for the flow of particles with a high $p_{\mathrm{T,out}}$. The latter increase is due to the larger effect of the Lorentz boost on these particles.

The conclusions of the JADE collaboration have meanwhile been confirmed by the TPC [244, 245] and the TASSO [215] collaborations. Both of them show that the effect also holds true if the second order QCD matrix element is used.

As discussed in the beginning of this part, the models considered require a set of parameters that influence the detailed predictions. To establish that the observed difference is fundamental, one has to relate it to the basic concepts of these models as well as to show that it is not due to some inappropriate parametrisation. The first criterion has been discussed before. In the string model the hadronisation proceeds along the strings which are moving out of the region between the two quarks. In the Independent Jet Model particles are distributed symmetrically around each of the jet axes. Therefore

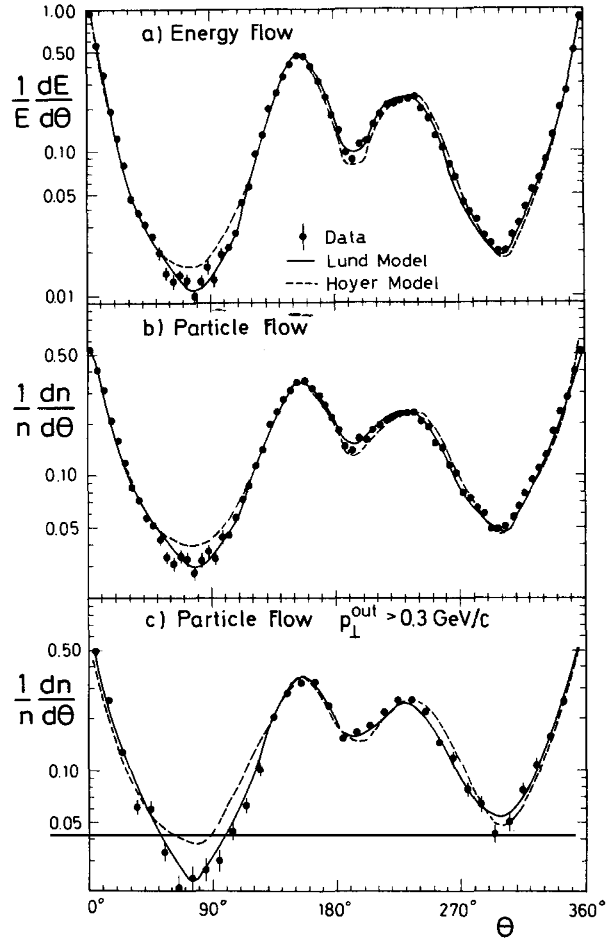

Fig. 6.2.2. Energy and particle flow in three-jet events. The data are compared to the LUND (solid line) and the Independent Jet Model (dashed line) [241].

the lower particle yield in the region between the two quarks in the LUND model is indeed related to its basic concepts.

Both the JADE and the TASSO collaboration have varied the fragmentation parameters over a wide range. In particular the treatment of the gluon is uncertain in the Independent Jet Model and several different options were tried to describe the observed behaviour. Although the particle yield changes slightly in the Independent Jet Model depending on whether the gluon is treated as a single quark or split into two quarks according to eq. (2.1.11), or the fragmentation function of the gluon is made softer, or the energy–momentum conservation is not imposed, no reasonable parametrisation could be found within the Independent Jet Model to reproduce the data. Note that since the gluon fragmentation is replaced by a fragmentation of two $q\bar{q}$ strings in the string model, the particle flow along the gluon direction is fixed and cannot be adjusted using special parameters.

This effect (named "string effect") reveals a major failure in the concept of Independent Jet fragmentation and strongly supports the string approach. It should, however, be noted that only a very small fraction of the particles exhibit the different structure. Typically 10% of all events are used for the analysis and only a small part of the particles populate the regions where the difference between the models is most prominent. In total only about 0.5% of the particles behave differently in both models.

It is already obvious from the collimation of jets that the particles are created within a narrow tube. The string effect sheds light on the relation between these tubes and the hard partons. In events with one hard gluon the hadrons originate from two sources and since these move within the overall c.m. system, the hadrons are produced along a hyperbola in space and time. Although in principle only shown for three-jet events, it is naturally generalized to the existence of strings in $q\bar{q}$ events.

The TASSO collaboration proceeded one step further. They analysed the string effect as a function of the momentum of particles. In fig. 6.2.3 the ratio $N(2)/N(3)$ is plotted depending on $x_{\text{in}} = p_{\text{in}}/E_{\text{beam}}$. Here $N(2)$ and $N(3)$ denote the particle yields in the region between jets 1 and 3 (the quark/antiquark and gluon) and jets 1 and 2 (quark and antiquark) and p_{in} is the momentum component in the event plane. Also shown are the predictions from the LUND and the Independent Jet Model. The shaded areas indicate the uncertainties of the model calculations. Most of the particles are at low x_{in} and here the data agree with the expectation of the LUND model, however, for $x_{\text{in}} \geq 0.04$ the data are lower than the model prediction and tend to agree more with the Independent Jet fragmentation.

6.2.2. Shower models

The comparison of QCD shower models to the measurement of the particle and energy flow lead to a surprising result. As can be seen from fig. 6.2.4 not only the string model can describe the data. Again the energy and particle flow measured by JADE is displayed. This time their results are compared to the predictions of the QCD shower models of Gottschalk [38] and Webber and Marchesini [39, 40]. The two models differ essentially in that the latter does and the former does not embody the coherent gluon emission in the matrix element for the QCD branchings [41–44] (cf. eqs. (2.1b and 3.2c)) whereas both apply a relatively similar cluster mechanism for hadronisation. The comparison indicates that the shower algorithm can reproduce the data only if this coherence is included at least for this hadronisation scheme.

The Webber model can also describe the dependence of the string effect on the particle momentum x_{in} [52]. As was discussed above, the string model fails to reproduce it.

The agreement of the QCD shower model prediction with data for a distribution that has been shown to be sensitive to details of jet models, caused a major breakthrough for QCD shower models and in particular for that of Webber and Marchesini.

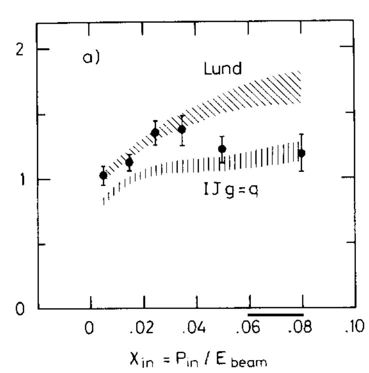

Fig. 6.2.3. Ratio of the particle yield in the region between quark (antiquark) and gluon to that between quark and antiquark as a function of the scaled momentum in the event plane [215].

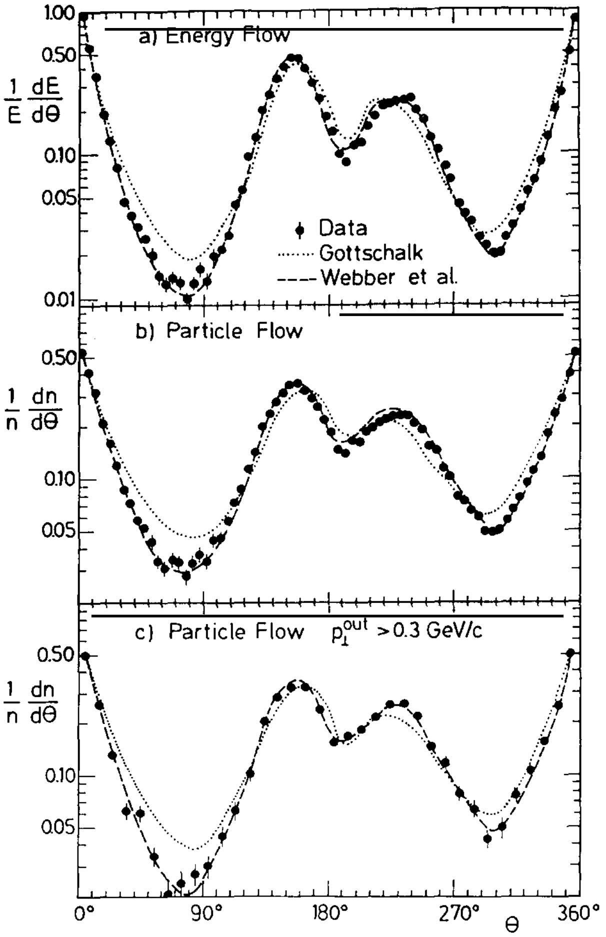

Fig. 6.2.4. Same as fig. 6.2.2. The methods compared to the data are here the QCD shower algorithms of Gottschalk (dotted line) and Webber (dashed curve) [243].

It is very striking that the predictions from two basically different concepts like the classical string and the QCD showering coincide for the sensitive energy and particle flow. Azimov et al. [50] showed that this is not accidental. Analysing the angular distribution of a secondary gluon g_2 in $q\bar{q}g_1$ events, they find that coherent gluon emission causes g_2 to be lined up in the region between quark (antiquark) and g_1. However, a negative interference causes a depletion of the g_2 yield in the region between the quark and the antiquark. Thus not only do the additional contributions in the direction of g_1 determine the larger yield of g_2 in the direction of g_1, but the interference effects cause an effective drag of low energetic particles by g_1. As a result the coherence induces an angular distribution that can be expressed as being due to an incoherent sum of two $q\bar{q}$ systems. This result is true up to $O(1/N_c)$ where N_c is the number of colours and agrees exactly with the basic assumption for the treatment of gluons in the LUND scheme.

As already discussed in the context of the other fundamental consequence of the coherence, the dip in the $x\,d\sigma/dx$ distribution (cf. 3.2.3), there exists a remarkable agreement between the calculations based on the Leading Log Approximation (LLA) with coherence and the string model. In that sense the energy- and particle flow cannot be considered as a proof for either of these approaches. Even more so as conventional (non-coherent) branchings in a shower algorithm can accommodate the string effect if the cluster decay is replaced by the string fragmentation [48].

Both approaches interpret the string effect as being due to a Lorentz boost of a colour neutral system that moves in the overall hadronic system in directions different from those of the partons. This is the consensus of the LUND approach and the theoretical evaluation of the coherence phenomenon discussed before. The string effect therefore sheds light on the global structure of the fragmentation region.

6.2.3. Additional tests of the string effect

As was also pointed out in ref. [50] there exists a qualitative difference between the particle flow between quarks in three-jet events and those of the type $q\bar{q}\gamma$, where the γ originates from either initial or final QED bremsstrahlung. Both the TPC [246] and the MARK2 collaboration [247] find the predicted difference. In fig. 6.2.5 the results obtained by MARK2 are displayed together with various model predictions. The data from $q\bar{q}$ events with photon emission exhibit the structure of boosted $q\bar{q}$ events. The particle yield between the two quarks coincides with the prediction from the LUND model with photon emission and the Independent Jet Model with gluon emission [59]. These results support the assumption that the string effect is due to the gluon emission and the different interplay between quarks/gluons and quark/antiquark. They provide a model independent test of the string effect.

There exist several other distributions for studying the string effect all showing that the string

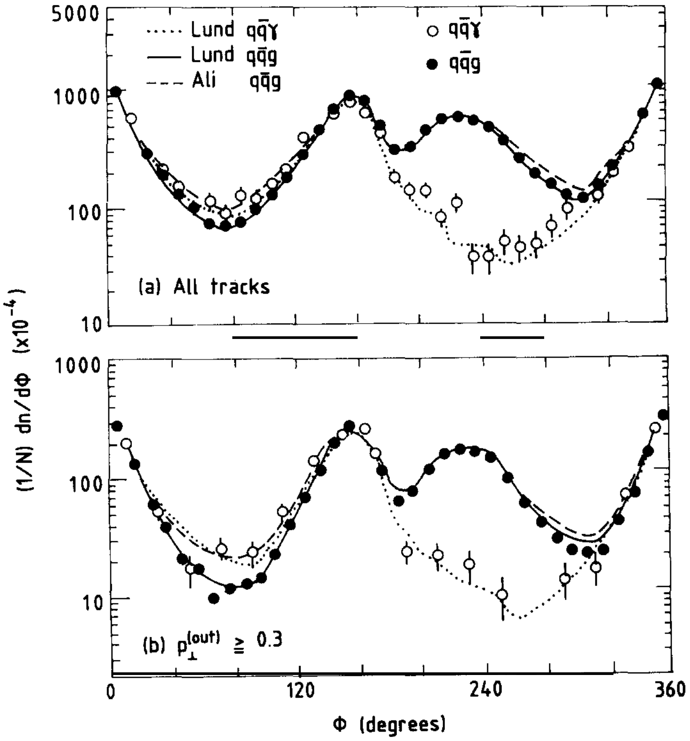

Fig. 6.2.5. Energy and particle flow in three-jet events $q\bar{q}g$ (full circles) and two-jet events with a hard photon $q\bar{q}\gamma$ (open circles) [247]. The data are compared to the LUND and the Independent Jet Model.

approach is superior to the Independent Jet Model. These tests are not independent of the results discussed before. Due to the difference between the parton direction and the fragmentation axis, the jet axes reconstructed from the final hadrons do not coincide with the parton directions. Instead those representing the quark directions are pulled towards the direction of the emitted gluon. As a result the distribution of the transverse momentum with respect to the jet axis of the particles in a jet exhibits a systematic orientation in the event plane. This orientation has been measured and compared with the Independent Jet Model and the String Model by the JADE collaboration [243]. For this analysis the transverse momenta are orientated as indicated in the insert of fig. 6.2.6. Since the directions of the high momentum particles coincide with the parton directions (see eq. (6.2.1)), they exhibit a bias into one direction and thus their $\langle p_{\mathrm{T}}^{\mathrm{in}} \rangle$ is different from zero, being directed away from the region of the gluon. Figure 6.2.6 displays the measurement from JADE. The data exhibit the features expected from string fragmentation. Again the Independent Jet Model fails to reproduce the data. A similar result has been obtained by the TASSO collaboration [215], who weighted the particles by some power of their momentum for the definition of the jet axis.

6.3. Conclusions

This section was devoted to the experimental results on the space–time structure of the hadronisation region. Information has been obtained both from the Bose–Einstein effect which is sensitive to the local structure around the point of a correlated emission of two particles, and the string effect, exhibiting the existence of global subsystems in which the hadronisation occurs.

The collimation of hadrons in jets already shows that the particle source is not isotropically distributed, but confined to a tube. In models like the Independent Jet Model fragmentation was

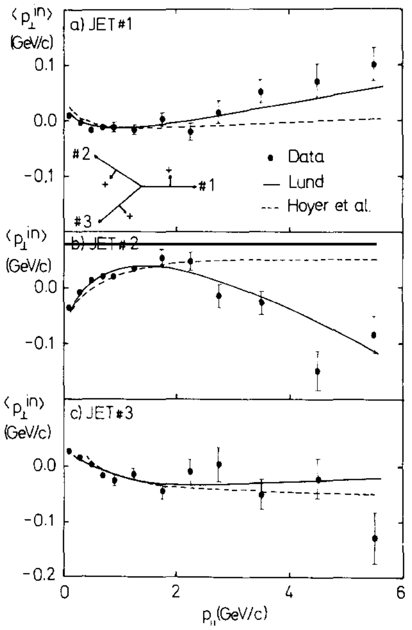

Fig. 6.2.6. Orientation of the transverse momentum in the event plane with respect to the reconstructed jet axes as a function of the parallel momentum [243].

assumed to occur within subsystems with properties determined by the energy, direction and flavour of the individual partons. The string effect reveals that this is not true. Instead hadronisation proceeds in larger, colour neutral systems: "strings". The particle and energy flow observed in events containing hard gluons indicate that the particles originate from two systems made out of the quark and one part of the gluon and of the antiquark and the other part of the gluon which are moving in the overall c.m. system. The existence of two incoherent sources of particle production is an essential feature of the string Monte Carlo's and follows also from QCD–LLA calculations if coherent gluon emission is included.

Besides offering an idea of the global structure of the hadronisation region, the discovery of the string effect had another aspect of more technical nature, but which was of no minor significance in the process of the experimental evaluation of the jet development. The string effect was the only sensitive method for discriminating between basic concepts of simulation algorithms for fragmentation. It not only proved that the Independent Jet Model includes a fundamental flaw, but in addition gave a major push to QCD shower models, once they were shown as being capable of reproducing this measurement. The important step forward within these approaches was the inclusion of coherent gluon emission. This feature, and not the dip in the rapidity discussed in the previous sections, is considered the strongest support for these QCD calculations.

It would be extremely interesting to know more about the local space–time structure at the emission point of a hadron. In theory this could be achieved by studying the Bose–Einstein effect since its shape is the Fourier transform of the space–time distribution of the source. However, the data collected are not sensitive enough to discriminate between various models of its shape. Four experiments in e^+e^- collisions have observed the Bose–Einstein effect. Their results are in agreement with a spherically symmetric two particle emission in their rest-system. Its size is $\sim$0.8 fm and the results indicate that the particles are emitted almost chaotically (incoherently).

7. How does the jet evolution depend on its prehistory?

As discussed in section 2 and visualized by the typical event displayed in the introduction to this part, the standard ideas on fragmentation assume that the quantum numbers of a hadron in a jet are correlated only to the hadrons produced immediately before and after. The pair of subsequently produced hadrons is supposed to be of similar flavour, transverse momentum, and rapidity. These short range correlations will be examined in section 8.

Otherwise every left-over parton (or pair of partons) is treated as though it forgot the history of how its jet has developed so far and acts as a source of a new jet at the residual energy. Its only relation to the particles produced before is therefore the global conservation of energy, momentum and flavour. This assumption forms the basis of the iterative scheme adopted in all simulation programs discussed. It is a relatively simple approach and has its theoretical motivation in the short distance behaviour of strong interactions. Still, the size of possible correlations cannot be calculated. In fact the prediction of the coherent gluon emission discussed several times before, digresses from these simple considerations in that it implies an angular ordering of the gluons with progressive jet evolution. Its effect on larger topological properties, however, is small.

The iterative scheme can be tested experimentally by searching for long-range correlations between different parts of an event. For the measurements discussed in this section, each event was divided into

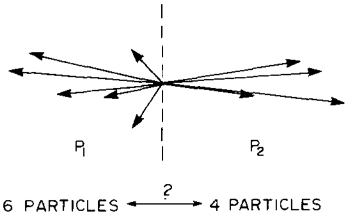

Fig. 7.1. Schematic event visualizing the measurements of correlations between larger parts of events.

two parts P_1 and P_2. The properties of one part ("P_2") were then studied as a function of those of P_1 (see fig. 7.1). In particular, what has been considered as P_1 are an event hemisphere and a single primary particle.

7.1. Forward–backward correlations

Topological correlations in events have been observed in soft pp collisions. Dividing the event into two hemispheres[*)] with respect to the beam direction and counting the particles in each of them ("forward" and "backward" hemisphere) one finds that [248] the average multiplicity n_F within one hemisphere depends linearly on the multiplicity n_B in the opposite hemisphere

$$\langle n_F \rangle = a + b n_B \tag{7.1.1}$$

with $b \sim 0.5$ at a $p\bar{p}$ c.m. energy of $\sqrt{s} = 540$ GeV and rising logarithmically with energy. One way to explain this behaviour is to assume that, since the protons are extended objects, they interact with a different impact parameter in each individual collision. In e^+e^- annihilations this impact parameter is always zero and therefore multiplicity correlations are not supposed to exist.

The forward–backward multiplicity correlation in e^+e^- annihilation has been measured by the TASSO group at a c.m. energy of $W = 34$ GeV [235, 236] (see also results of the HRS and TPC collaborations discussed in ref. [249]). For this analysis all events surviving their standard hadronic selection criteria were divided into two hemispheres with respect to the event axis (sphericity axis). One arbitrarily selected hemisphere, "backward hemisphere", was chosen as reference and the average multiplicity of the opposite "forward" hemisphere determined as a function of n_B. The measurement is displayed in fig. 7.1.1, the results are not corrected for detector effects and acceptance cuts. An uncorrelated production in the two hemispheres would imply a constant value of $\langle n_F \rangle$. The data (fig. 7.1.1a) exhibit a strong negative correlation for $n_B < 4$ and some positive correlation for $n_B \geq 4$. As will be discussed below, these correlations are largely due to experimental distortions.

The curve in fig. 7.1.1a is the prediction of the LUND model folded with a simulation of the TASSO detector and the cuts applied. It reproduces the data very well and can be taken as a guideline to understand the observed correlations.

(i) The most relevant cut for this analysis refers to the total multiplicity $n_F + n_B$: to exclude background, only events with at least five charged particles were accepted. How the distribution changes if all multiplicities could have been detected, is displayed in fig. 7.1.1b. Here the result of the simulation is shown with and without applying the cut on the multiplicity. Without it there is a positive correlation for all multiplicities n_B.

[*)] These measurements have not to be restricted to such a partition. Every cut in rapidity, x-distribution, etc., should be equally valid.

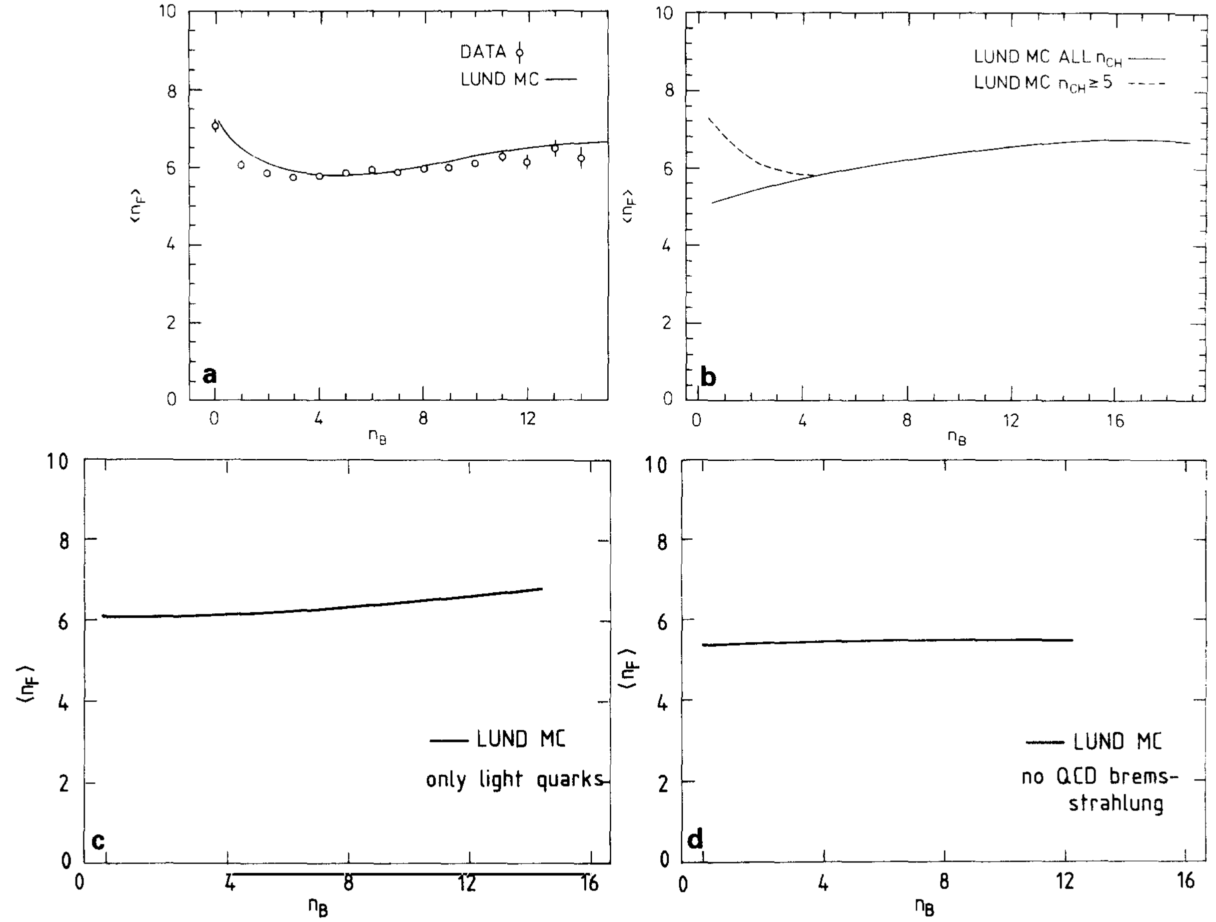

Fig. 7.1.1. Forward–backward multiplicity correlations. (a) Measured average multiplicity $\langle n_F \rangle$ as a function of the multiplicity in the backward hemisphere n_B [236]. The full curve represents the result of a Monte Carlo calculation. (b) Monte Carlo result with and without the cut on at least five charged particles. (c) Monte Carlo result for u, d and s-quark jets without initial QED bremsstrahlung. (d) Monte Carlo result of u, d and s-events omitting QCD bremsstrahlung.

(ii) As discussed in section 5.1, jets from charm and bottom quarks have larger multiplicities than those originating from u, d or s-quarks. Since the events considered are a mixture of all flavours, these different multiplicities induce positive correlations. Restricting the simulation to just u, d and s quarks and in addition eliminating initial QED bremsstrahlung leads to fig. 7.1.1c. The positive correlation persists, although it is significantly smaller.

(iii) These residual correlations can be explained by QCD bremsstrahlung. A gluon affects the multiplicity strongly if it is emitted under a fairly large angle. Therefore the additional spray of particles contributes to both hemispheres. Generating just two-jet events originating from u, d and s-quarks in the Monte Carlo leads to fig. 7.1.1d. No significant forward–backward multiplicity correlation is visible.

Thus, apart from trivial correlations due to experimental effects, the jets in e^+e^- collisions exhibit forward–backward correlations due to the mixing of events from different flavours and QCD bremsstrahlung. They are, however, much smaller than those observed in pp collisions and their origin is already found on the level of hard partons. If the models are restricted to jets of specific flavour and two quark-configurations, no forward–backward correlation exists. In that sense the conversion of partons into hadrons is independent of its position in space–time and therefore the fragmentation in one hemisphere is independent of that in the other. These features can be described by both the Independent Jet Model and the String Model. For the first one this is expected from its basic concept. In terms of the String Model the data indicate that the string breaks up uniformly along its axis.

The study of multiplicity correlations can be generalized to higher moments of the x-distribution. By replacing the exponent of x

$$n_{\mathrm{CH}} = \sum_{1}^{n} x^{0} \quad \rightarrow \quad N_{\alpha} = \sum_{1}^{n} x^{\alpha} \tag{7.1.2}$$

particular regions in x contribute dominantly to the moments depending on α. Here the sum goes over all particles in a hemisphere. Thus a variation of α is similar to scanning over the x-distribution and allows one to search for correlations between different regions in x.

The result for $\langle N_\alpha^{\mathrm{F}} \rangle$ is displayed as a function of N_α^{B} for $\alpha = 0.2$ (fig. 7.1.2a) and 0.75 (7.1.2b), F and B again refer to the two hemispheres in an event. The uncorrected data from the TASSO group (crosses) are compared with results from a simulation study using the LUND Monte Carlo in combination with a parametrisation of the TASSO detector (full line) and with the various options discussed for the case of multiplicity correlations (dashed and dashed–dotted line). The results are essentially the same as those for the multiplicity correlations and support the conjecture of an uncorrelated fragmentation.

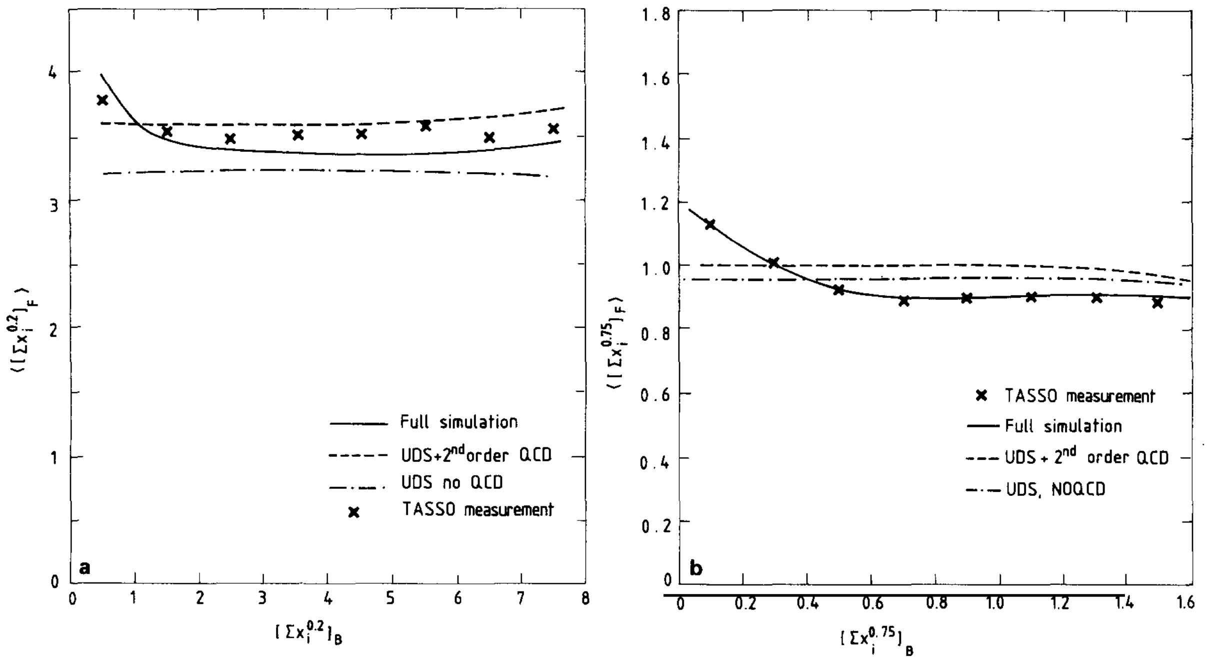

Fig. 7.1.2. The same as for fig. 7.1.1. Here higher moments of the fragmentation function are used. (a) $M = \Sigma x^{0.2}$, (b) $M = \Sigma x^{0.75}$. The results of the model calculations for the various conditions outlined above are compressed into one plot.

7.2. The non-leading system

The assumption of an iterative scheme of fragmentation can best be tested with events originating from heavy quarks. As already discussed in section 5.1, the structure of these events is both due to the fragmentation and decay properties of the charmed and bottom hadrons themselves and the fragmentation of the residual system. Since the multiplicity and momentum distributions of the decay products of the hadrons containing the primary quarks as well as their fragmentation function are well known, their contribution can be subtracted either directly or statistically. The residual system has a c.m. energy W' which is substantially below the total c.m. energy W due to the hard fragmentation function of charm and bottom. It allows a meaningful comparison to events produced directly at these W'.

In figs. 5.1.3 and 5.1.6 the rapidity distributions for bottom and charmed jets is compared to the results from simulation studies. For these Monte Carlo calculations the subsequent fragmentation was assumed to proceed like the standard fragmentation at reduced energy which is only a small fraction of the total energy (~50% for charm-, ~20% for bottom-events). Since the results from the simulation coincide with the data, this is a first indirect evidence that a jet indeed develops in discrete steps, each of them determined by the energy of the residual system.

The MARK2 [201] and the TPC collaboration [202] determined the multiplicity and energy of the residual system by

$$\langle W_{\mathrm{res}}^{\mathrm{Q\bar{Q}}} \rangle = E_{\mathrm{cm}}(1 - 2\langle x_{\mathrm{Q}} \rangle)\,, \tag{7.2.1}$$

$$\langle n_{\mathrm{res}}^{\mathrm{Q\bar{Q}}} \rangle = \langle n_{\mathrm{CH}} \rangle - 2\langle n_{\mathrm{CH}}^{\mathrm{Q}} \rangle\,. \tag{7.2.2}$$

Here $\langle n_{\mathrm{CH}}^{\mathrm{Q}} \rangle$ is the average charged decay multiplicity of hadrons containing the heavy quark Q, x_{Q} their fractional energy. Their results are listed in table 7.2.1. Here the multiplicity of the average jet is taken from measurements at a total energy close to the residual energy, its error corresponds to a linear interpolation in the energy range of the residual jet. Within the considerable errors there is a good agreement between the residual and the average jet. The results are displayed in fig. 7.2.1 and compared to the average multiplicities found in events of all flavours at various c.m. energies. With average values of $W_{\mathrm{res}}^{\mathrm{c\bar{c}}} = 12.2 \pm 0.5$ and $n_{\mathrm{res}}^{\mathrm{c\bar{c}}} = 8.4 \pm 0.6$, $W_{\mathrm{res}}^{\mathrm{b\bar{b}}} = 6.1^{+0.78}_{-0.86}$ and $n_{\mathrm{res}}^{\mathrm{b\bar{b}}} = 5.4 \pm 0.8$, the multiplicities of the subsequent fragmentation fit nicely into those of the average jet.

Since the residual system is due to u, d and s-quarks only (in a different ratio than in the direct production), a precise comparison requires to subtract the contributions from charm and bottom events from the charged multiplicity of the averge events. According to table 5.1.2 there is an additional contribution of ~1.6 particles in bottom jets and ~0.3 particles in charm jets. Thus they add

$$\Delta_{\mathrm{c,b}} = 2[f_{\mathrm{c}} \cdot 0.3 + f_{\mathrm{b}} \cdot 1.6]$$

Table 7.2.1

Energy and multiplicity of the residual jet

Experiment	flavour	$W_{\mathrm{res}}^{\mathrm{Q\bar{Q}}}$	$\langle n_{\mathrm{res}}^{\mathrm{Q\bar{Q}}} \rangle$	$\langle n_{\mathrm{CH}} \rangle_{\mathrm{av}}$
TASSO*	c	12.4 ± 0.8	$8.8 \pm 1.2 \pm 0.8$	8.5 ± 0.5
MARK2	c	$11.6^{+2.1}_{-2.6}$	$8.1 \pm 0.5 \pm 0.9$	8.3 ± 0.7
TPC	c	12.2 ± 0.6	8.4 ± 0.9	8.5 ± 0.4
MARK2	b	$6.1^{+1.5}_{-3.0}$	$5.2 \pm 0.5 \pm 0.9$	5.0 ± 0.6
TPC	b	6.1 ± 0.9	5.7 ± 1.1	5.0 ± 0.6

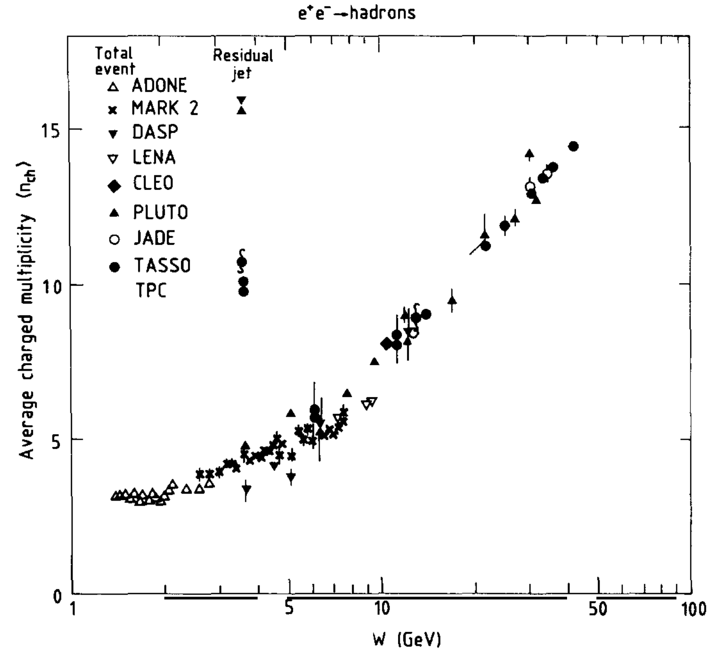

Fig. 7.2.1. Charged multiplicity in the residual jet as a function of its energy compared to the results of the total system. The measurements already displayed in fig. 3.1.1 are supplemented by the results from refs. [188, 201, 202].

particles to the average multiplicity. Here f_c and f_b are the fractions of c and b-quarks, respectively. For an uncorrelated fragmentation one therefore expects that the residual jets have a multiplicity lower by $\Delta_{c,b}$ than the average jet. The corresponding values of $\Delta_{c,b}$ below and above the bottom threshold are 0.24 and 0.53. These contributions are smaller than the errors of the measurements of the residual jet multiplicity, although not negligible*). These corrections lead to a somewhat higher multiplicity of the residual jet, however, within the large uncertainties there is a general agreement between the two data samples.

The non-leading system has been most directly compared to the properties of an average jet produced at the residual energy by the TASSO collaboration [188]. For their analysis they used charm events with a tagged D* collected at $W = 34$ GeV. As for the study discussed in section 5.1.2 the charm events were divided into two hemispheres. However, in this case the hemisphere containing the D* was analysed (see fig. 7.2.2). In particular they studied the properties of the residual jet consisting of the particles in this hemisphere excluding the D*.

The energy of the residual system is

$$E_{res} = W/2 - E_{D^*} \tag{7.2.4}$$

corresponding to $\langle E_{res} \rangle = 6.2 \pm 0.4$ GeV in their data sample. The properties of the residual jet were then compared to those of average jets produced at two different c.m. energies, firstly with a jet produced at the same total c.m. energy $W = 34.4$ GeV ($E_{jet} = 17.2$ GeV), secondly with events collected at $W = 14$ GeV ($E_{jet} = 7$ GeV), an energy very close to $\langle E_{res} \rangle$.

---

*) For this calculation it was assumed that the additional contribution is independent of W. This is true if the fragmentation functions of charmed and bottom quarks scale. Then (cf. 5.1) $\langle E_{res} \rangle = (1 - \langle x_Q \rangle) E_{beam}$ and $y^{res}_{max} \propto \ln W$. If one is far enough away from the threshold this assumption is reasonable, though not strictly true (cf. discussion in section 3.2.2).

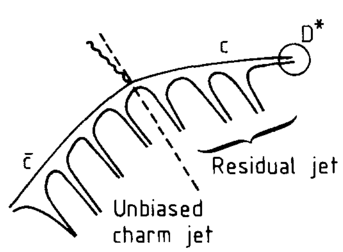

Fig. 7.2.2. Sketch of the analysis of the residual jet.

The results are displayed in fig. 7.2.3. Shown are distributions in $x_p = 2p/W$, $x_p^r = p/E_{res}$ (the momentum scaled with the energy of the residual jet), the rapidity and the p_T^2 distribution. For all distributions the residual jet exhibits the same behaviour as a jet produced at $W \sim 2E_{res}$.

The discrepancy with the high energy data for the overall x-distribution is trivial. The agreement at low x_p^r of the residual jet with the data collected at $W = 14$ GeV, or its disagreement with the high

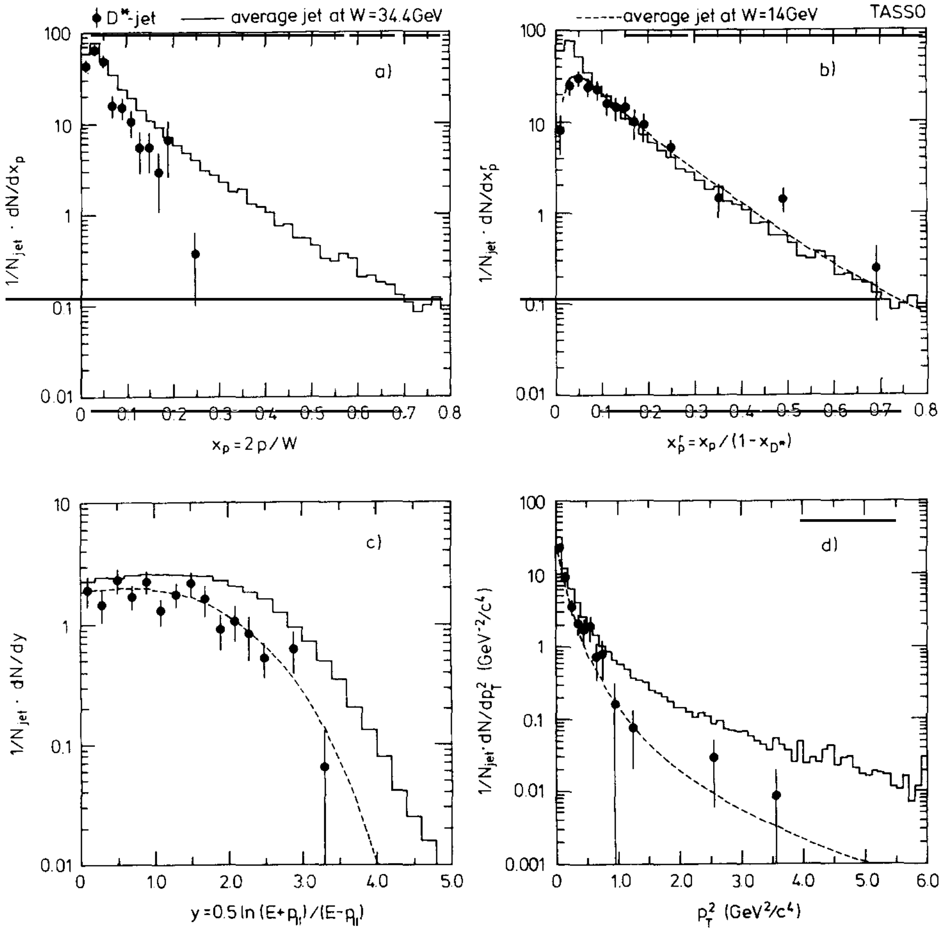

Fig. 7.2.3. Particle distributions of the residual jet. They are compared to average jets of approximately the same energy (dashed curve) as well as to those at the total c.m. energy (histogram) [188]. (a) Scaled momentum $x_p = 2p/W$; (b) reduced scaled momentum $x_p^r = p/E_{res}$; (c) rapidity; (d) p_T^2.

energy jets, can be explained by phase space (cf. eq. 3.2.3b). However, both the rapidity and the p_T^2 distribution indicate dynamical differences between jets at $W = 34$ GeV and those at $W = 14$ GeV.

The height of the plateau in the rapidity distribution agrees for the residual jet and the jets at $W = 14$ GeV: $\langle dN/dy \rangle = 1.9 \pm 0.2$, respectively $\langle dN/dy \rangle = 2.0 \pm 0.03$, but is smaller than for the jets produced at $W = 34$ GeV: $\langle dN/dy \rangle = 2.32 \pm 0.01$. The difference cannot be explained by the contribution from heavy quarks to the average events which is absent for the residual jet. The comparison of the rapidity from u, d, s-jets and c-jets (see eq. (5.1.6)) shows that the height of the plateau is the same in both cases. The DELCO data [200] exhibit a difference between the rapidity in bottom jets and average jets. The particle density for $y < 1$ in bottom jets is ~3.3 and thus about one unit higher than the average particle density. However, since bottom events contribute only 1/11 to the average sample, $\langle dN/dy \rangle_{\mathrm{uds}}$ at $W = 34$ GeV is estimated to be 2.2, still exceeding the particle density of residual jets.

The p_T^2 distribution is much broader in events produced at $W = 34$ GeV than in those at $W = 14$ GeV due to QCD bremsstrahlung. The residual jet coincides with the data at $W = 14$ GeV also in this distribution and suggests that fragmentation effects still dominate the transverse momentum. A thorough interpretation, however, has to take into account the effects of possible biases in the determination of the jet axes which may be different for the three cases considered.

The results obtained by the TASSO collaboration show in a more detailed way what has also been seen in the other measurements discussed above. Together they indicate that the residual system develops like a standard jet produced at the residual energy. A detailed evaluation of this fundamental issue of fragmentation, however, still suffers from statistical and systematic uncertainties.

7.3. Conclusions

The data discussed in this section indicate a remarkable uniformity of the jets. They all show that the fragmentation properties of a subsystem depends only on the properties of this subsystem, but not on those of the total system. No substantial topological long range correlations between larger parts of the e^+e^- events have been found.

The most straightforward explanation is that a jet develops in discrete steps. Each of these steps is largely independent of what has happened "before", the energy scale of the fragmentation is set by the energy of the remaining system.

This property is in agreement with ideas embodied in the standard fragmentation models (cf. section 2.1). Within the LUND and the Independent Jet Model the process $q \rightarrow H + q'$ is repeated and in each step the probability for $x_H \approx E_H/E_q$ is given by a function $f(x_H)$ which is almost independent of E_q. A similar behaviour holds true for the QCD shower approaches where gluons are emitted with an energy determined by the splitting functions (2.1.11) and the Q^2 of the left-over partons. In both cases the left-over parton acts as a source of a separate jet.

The data support these basic conjectures of the fragmentation models; they are, however, still too scarce and imprecise for a detailed study and a sensitivity to possible small differences.

8. How quantum numbers are compensated

In the last section we discussed the topological correlations between larger subsets within an event. This section is devoted to the correlations of individual particles. In particular we will consider how a particular flavour is compensated.

Quantum number compensation is sensitive to the sequence of hadron formation. The methods applied are those outlined in section II.A. As discussed there, one expects the existence of two different kinds of quantum number correlations in the standard hadronisation models related to different processes at different Q^2 and with different bearings on the insight into jet development. The first one is due to the emission and absorption of flavour neutral entities. Quantum numbers should be compensated at a relatively low Q^2 and thus be found within a narrow kinematical region. For the second one the primary quarks produced at high Q^2 fly apart and leave their footprints in kinematically well-separated particles.

8.1. The trace of the primary parton

The way the electric charge is neutralized within an e^+e^- event has been analysed by four experiments [6, 5, 119, 140, 236] with consistent results. In particular all these experiments find evidence for long range charge correlations and thus a trace of the primary parton.

The data shown in fig. 8.1.1 have been collected by the CLEO collaboration. They have measured

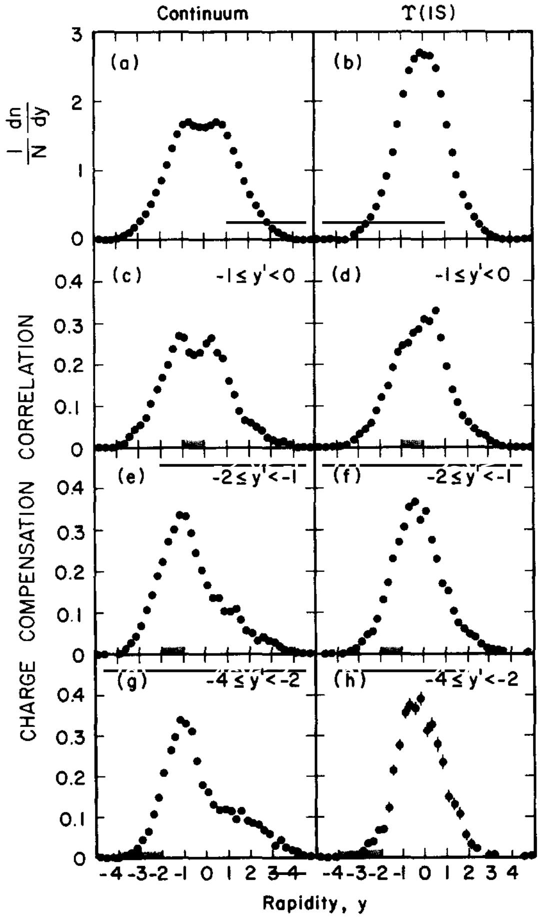

Fig. 8.1.1. Charge compensation probability in the continuum and on the Υ(1S) [119]. Shown are (a, b) total rapidity distributions; (c–h) correlation functions for different reference intervals: $-1 < y' < 0$ (c, d), $-2 < y' < -1$ (e, f), $-4 < y' < -2$ (g, h). The reference interval is indicated by the shaded bars.

the charge compensation at the lowest c.m. energy of all these experiments (~10.5 GeV) and therefore span the smallest region in rapidity. However, the particular beauty of their data is that they allow one to compare the charge correlation on the Υ(1S), resonance decaying predominantly into three gluons to those in the e^+e^- continuum, i.e. $e^+e^- \to q\bar{q}$. Due to the different charge content of the primary partons involved, the two data samples are expected to exhibit different long-range properties without strongly affecting the short range compensation.

Plotted in figs. 8.1.1a and b are the rapidity distributions for the continuum and Υ(1S), respectively. Figures c–h display the charge compensation function*) for the different reference intervals $-1 < y' < 0$, $-2 < y' < -1$ and $-4 < y' < -2$.

Both the continuum events and the data from the resonance show a high probability of a charge compensation close to the test charge. This behaviour is consistent with what is expected due to the short range mechanism discussed before. It is, however, to a large part due to the decay of neutral resonances such as $\rho^0 \to \pi^+\pi^-$.

The relative probability of two charged pions being promptly and subsequently produced during the fragmentation and that of originating from ρ^0 decays can be estimated using the parameters discussed in section 2.2. Assume a u-quark as a source of the subsequent chain. It takes the production of a $(d\bar{d})$ pair and another $(u\bar{u})$ pair to produce a $\pi^+\pi^-$ pair. In addition the final hadrons have to be pseudoscalar. Therefore the probability for the subsequent production of a π^+ and a π^- is

$$p_{\text{prompt}} \propto p_d p_u \left(\frac{P}{P+V}\right)^2 \sim 0.03$$

To produce a ρ^0 requires only one other $(u\bar{u})$ pair and that a vector particle instead of a pseudoscalar is produced

$$p_{\rho^0 \to \pi^+\pi^-} \propto p_u \frac{1-P}{P+V} \sim 0.25$$

Here p_f is the probability of picking a quark of flavour f out of the sea, P is the fraction of pseudoscalar, V that of vector particles produced in the hadronisation (see section 2.2 and section 4). Thus the interesting dynamics of quantum number compensation is buried under the well-known properties of ρ^0-decays. In addition a production chain like $\pi^+\pi^0\pi^-$ can occur quite frequently in the jet and will distort the charge compensation function. Therefore short range charge correlations are an inconclusive indicator of local quantum number compensations. There are superior ones that will be addressed in the next sections.

The data on the Υ(1S) and in the continuum behave differently for the reference interval of largest rapidity $-4 < y < -2$. For $y \to y_{\max}$ in the opposite hemisphere, the compensation function drops rapidly to zero in the case of resonance decays, but exhibits a long shoulder for the continuum events: a high fraction of charge at large y' is compensated at large distances $\Delta y = y - y'$. This feature can be naturally explained by the long range charge correlation induced by primarily produced quarks of opposite charge which reflects itself in the charge of the hadrons at high rapidity values. No long range charge correlations are expected in the three-gluon decay, since gluons are neutral. The findings of the CLEO collaboration are in good agreement with what has been seen by the other experiments quoted above.

---

*) The function is defined in a slightly different way than in section II.1. The CLEO collaboration used $[N^{+-,-+}(y, y') - N^{++,--}(y, y')]/N(y')$, i.e., they normalize the charge asymmetry to the number of reference particles and not to the number of combinations.

This evidence provides basic insight into the physics of fragmentation as well as a tool for determining the primary charge of a jet. Firstly it proves that the primary partons in the continuum events are charged and those in the 1S-decay are neutral. It secondly bears important information about the fragmentation process: the fraction of particles containing the first produced particle is especially high at high y-values. More generally: the rapidity of a particle is correlated with its rank. This correlation, however, is not at its maximum. As can be seen from fig. 8.1.1g the rapidity interval in which the compensating charge can be found is quite wide, indicating that the ordering in rapidity is only true on the average. This can be attributed to the softness of the fragmentation function for u, d and s-quarks as well as to the frequent decays that tend to mix the ranks of the produced hadrons.

Another method of studying this leading particle effect is to use jet charges instead of correlating individual particles. The charge distribution within a jet J can be condensed into a single quantity, the weighted jet charge Q_J [56]. It is obtained by summing over all particles within a jet and weighting their charge with their momentum fraction x_i.

$$Q_J(\alpha) = \sum q_i \cdot x_i^\alpha . \tag{8.1.1}$$

Here α is a free parameter that can be used to steer the relative weights of the particles depending on their scaled momentum.

For $\alpha = 0$ the weighted charge is just the sum of all charges in a jet. Its modulus is related to the charge of the primary quark and provides one of the basic measurements to show that hadron production is mediated by primary quarks (see introduction). Neglecting experimental losses and diffusion of particles from a primary hadron from one jet into the other one, the jet charge Q^f from a quark of a given flavour f equals the sum of all quarks produced in a jet:

$$Q^f = (q_f + \bar{q}_2) + (q_2 + \bar{q}_3) + \cdots + (q_{n-1} + \bar{q}_n) . \tag{8.1.2}$$

Since only quark loops of neutral charge are subsequently produced in the fragmentation chain,

$$Q^f = q_f + \bar{q}_n \quad \Rightarrow \quad \langle Q_f \rangle = q_f + \langle \bar{q}_{sea} \rangle , \tag{8.1.3}$$

where $\langle \bar{q}_{sea} \rangle$ indicates the average charge of antiquarks in the sea. The modulus of an average jet charge in events from a primary pair of f-quarks is therefore

$$\langle |Q_J^f| \rangle = |q_f + p_u \cdot (-\tfrac{2}{3}) + p_d \cdot (+\tfrac{1}{3}) + p_s \cdot (+\tfrac{1}{3})| = |q_f + \bar{q}_{sea}| , \tag{8.1.4}$$

where p_u, p_d and p_s are the probabilities for picking an u, d or s-quark out of the sea. Considering only the quark jet (not that from the antiquark) and using the values from section 4.2 $\bar{q}_{sea} \sim -0.09$. Since for hadron production in e^+e^- annihilations via a virtual photon the primary quarks are produced in proportion to the square of their charge, one obtains

$$\langle |Q_J| \rangle = \left(1 \Big/ \sum q_f^2\right) \sum q_f^2 \cdot |q_f + \bar{q}_{sea}| \sim 0.3 . \tag{8.1.5}$$

This value is much smaller than what is expected for randomly distributed charges within an event. Also the charge per hemisphere should grow with energy. Therefore the determination of $|\Sigma\, q_i|$ per hemisphere provides a test of the quark–parton model and the absorption of flavour neutral $q\bar{q}$ pairs from the sea during the fragmentation process. The PLUTO collaboration [5] measured $\langle |Q_J| \rangle = 0.55 \pm 0.25$, smaller than expected from a statistical charge distribution but in agreement with the quark–parton model.

For an increasing exponent α the high momentum particles contribute stronger to the weighted charge and in the light of the discussion above, the sign of Q_J should coincide with the sign of the primary parton inducing the jet considered. The weighted charge has been applied in ref. [6] to study long-range charge correlations. Results from the TASSO collaboration using much higher statistics are displayed in fig. 8.1.2. Some charge correlation is expected just due to the overall charge conservation. To discriminate against this trivial effect, the average product $-\langle Q_A Q_B \rangle^{*)}$ is compared to the jet charge obtained by randomising the charge among the particles of a jet but keeping the overall unweighted charge $\Sigma\, q_i$ per jet fixed. For the measurements shown it was in addition required that at least one particle in each hemisphere has a scaled momentum x exceeding some predefined value x_{cut}. For fig. 8.1.2a x_{cut} was set to 0.15, for fig. 8.1.2b to 0.35.

As can be seen from the figure, the average charge product observed coincides with that from the randomisation for α close to 0. However, for larger values of α the measured value exceeds the expectation from a random distribution significantly. This shows that the charge correlation observed is

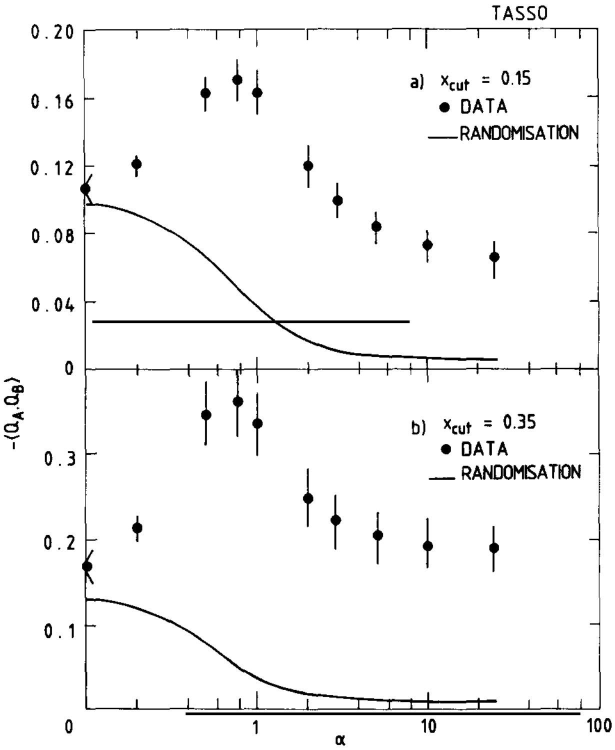

Fig. 8.1.2. Product of the weighted jet charges as a function of the exponent α. The full curve represents the expectation from a randomisation of particles within a jet (a) requiring at least one particle with $x_p > 0.15$ per jet; (b) requiring at least one particle with $x_p > 0.35$ per jet.

---

*) Since $x < 1$, x^α decreases with increasing α. For the analysis this is compensated by weighing each $Q_J(\alpha)$ with $(\Sigma\, x^\alpha / \Sigma\, x^{2\alpha})$. This is just a scale factor which has no impact on any of the qualitative conclusions discussed.

not just due to charge conservation but reflects the dynamical distribution of the particles. In this case the jet charge is dominated by the particles with the highest momentum. This is the behaviour expected from the long-range charge correlations.

It is also interesting to study the dependence of the data on α. The correlation is not at its maximum as $\alpha \to \infty$ which is expected if always the particle with the highest momentum carries the information about the charge of the primary parton. Instead $-\langle Q_A Q_B \rangle$ is largest for $\alpha \sim 0.5$–0.7 indicating that the primary hadron has a high, but not necessarily the largest momentum. This coincides with what has been discussed before: the correlation between rank and rapidity is only true in a statistical sense. The data reveal that an optimal value for determining the sign of the jet charge is around $\alpha \sim 0.5$. We will return to this problem in section 11.

One can use the results for $\alpha \to \infty$ and different values of x_{cut} to determine the integral probability that the particle of highest momentum and $x > x_{\mathrm{cut}}$ has the sign of the charge of the primary parton. Note that the weight factor mentioned in the footnote prevents Q_J from vanishing to 0, but instead it follows that $Q_J(\alpha \to \infty)$ is equal to the charge of the fastest particle. Let p_r be the probability of a correct charge sign and p_f of a wrong assignment. Then

$$-\langle Q_A Q_B \rangle (\alpha \to \infty) = (p_r - p_f)^2 = (2p_r - 1)^2 \tag{8.1.6}$$

and therefore

$$(2p_r - 1) = \sqrt{-\langle Q_A Q_B \rangle}\,. \tag{8.1.7}$$

The dependence of $(2p_r - 1)$ is displayed in fig. 8.1.3. As can be seen it is a rapidly increasing function of x_{cut}. At $x > 0.5$ one has a probability of 75% of finding the correct assignment. Note that this probability depends on the flavour of the original parton.

8.2. Pion and kaon compensation

The method discussed in the previous section was applied by the TPC group [250] to charged pions

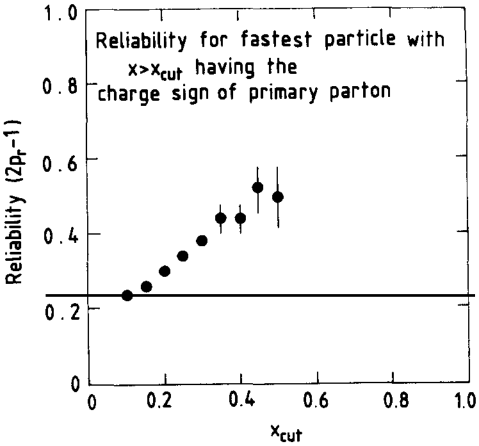

Fig. 8.1.3. Reliability that the fastest particle has the same sign of charge as the primary parton. Plotted as a function of the minimum allowed x-value of that particle.

and kaons. Due to the limited statistics available, only two reference intervals in $0 < y' < 1.5$ and $1.5 < y' < 4$ had been selected.

Their measurement of

$$q_i(y) = \rho_i^{+-,-+}(y) - \rho_i^{++,--}(y)$$

with the normalisation condition $\int q_i(y)\,\mathrm{d}y = 1$ is displayed in fig. 8.2.1. Here i denotes either pions or kaons.

Since most of the particles are pions, $\rho_\pi(y)$ (figs. 8.2.1a and b) has a shape very similar to the charge correlation discussed in the previous section. A pion with opposite charge can be found with the highest probability close to the reference particle for both intervals selected. As stated before, this behaviour is consistent with the short range mechanism, but its contribution is small compared to those from resonance decays. For the reference interval $1.5 < y' < 4$, a shoulder develops at $-4 < y < 1.5$ indicating the long range compensation due to primary partons discussed above. The data are in general agreement with both the LUND and the Webber model. The dashed curve shows in addition the LUND prediction without events from heavy quarks. Whereas for the short range part only small differences can be seen between the two LUND model calculations (and the data), the simulation of u, d and s fragmentation alone exhibits significantly less long range correlations than the simulation of all flavours.

Both long and short range compensation are visible in the kaon correlation function (figs. c and d). However, their relative importance is strongly changed. The reduction of the short range effect reflects that only few resonances with a sizable branching fraction into K^+K^- are produced: only the ϕ has been found within a jet; some contribution is due to the heavy quark decays. Therefore the amount of short

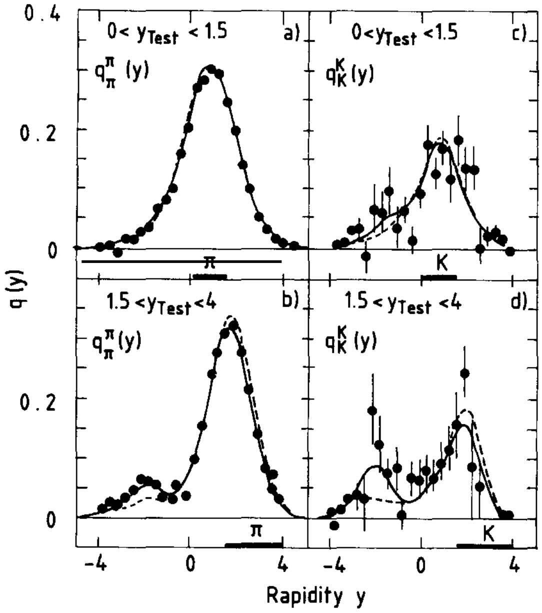

Fig. 8.2.1. Pion (a, b) and kaon (c, d) compensation function [251]. The reference intervals have been chosen as $0 < y_{\mathrm{Test}} < 1.5$ (a, c) and $1.5 < y_{\mathrm{Test}} < 4$ (b, d) and indicated by the strong black bars. Also shown are Monte Carlo predictions from Webber (dotted line) and the LUND simulation with (solid line) and without (dashed line) heavy quarks.

range compensation in the kaon spectrum represents the dynamics of jet development more closely. The TPC group claims that only about 15% of the signal for short range correlations can be explained by resonance production.

The kaon correlation function also exhibits a high compensation probability for large Δy, an indication of long range effects. As discussed before, this result suggests that one is able to select events of strange flavour by tagging the strange particle content at high rapidity values.

Also shown are the results from the three simulation programs of Webber and the LUND group with and without the production of heavy flavours. The data can be very well reproduced by both models provided all flavours are considered. Jets from light quarks alone show a much weaker long range effect. This behaviour is in agreement with what has been previously discussed about the fragmentation functions of light and heavy quarks. The high fraction of descendants from heavy quarks in the region around $y \sim 2$ is a result of the hard fragmentation function for c- and b-quarks and has already been discussed in sections 5.1.1 and 5.1.2. Since the fragmentation function of light quarks is much softer, the rapidity distribution of their leading particles is much broader.

8.3. Baryon number compensation

Baryon production provides a probe for studying short range correlations that is even more free of background from resonance decays than kaons: baryon/antibaryon pairs do hardly originate from one resonance. In addition baryons that are descendants from a heavier baryon retain a momentum very close to that of their mother particles. In that respect baryons are ideal for studying the compensation mechanism. However, they are also rare such that the statistical significance of most measurements is only marginal. In addition they are special, since it is not yet clear, how they are produced and therefore their properties may not be representative of all hadrons. Rather, baryon number compensation provides an effective tool for discriminating between various models of baryon production.

Experimental results have been obtained by several groups for $p\bar{p}$ and $\Lambda\bar{\Lambda}$ and $\bar{p}\Lambda$ pairs. In general the measurements from each single experiment have only limited statistical value. However, if combined they provide a consistent and believable picture.

The TASSO collaboration studied $p\bar{p}$ correlations both in a narrow rapidity interval around $y = 0$ [151] and for proton momenta between 1 and 5 GeV [251]. In the first study the rapidity difference $\Delta y = |y_p - y_{\bar{p}}|$ of the p and $\bar{p}$ was compared to model calculations, for the second analysis the number of $p\bar{p}$ pairs in the same or opposite hemisphere was counted.

The low rapidity data are displayed in fig. 8.3.1 in terms of the relative production angle $\theta_{p\bar{p}}$ in the $p\bar{p}$ rest system (fig. a), and the difference in rapidity $|y_p - y_{\bar{p}}|$ (fig. b). The distributions are not corrected for acceptance. Also displayed are predictions of the models of Cerny et al. [153] assuming a stochastic parton distribution, and the two models of Meyer and the LUND group assuming pointlike diquarks [154, 155] (the models are outlined in section 4.3). The distributions are folded with detector effects and acceptance cuts.

The stochastic model fails to reproduce the $\cos\theta_{p\bar{p}}$ distribution as well as the rapidity difference. Both measurements indicate that the baryons are kinematically closer together than predicted by this model. The diquark models, however, accommodate the measurement and support the assumption of short range correlations in the fragmentation process. This result is in line with what has been learned from the overall baryon yield and their fragmentation function discussed in section 4.3 and suggests that baryons are formed by picking diquarks out of the sea.

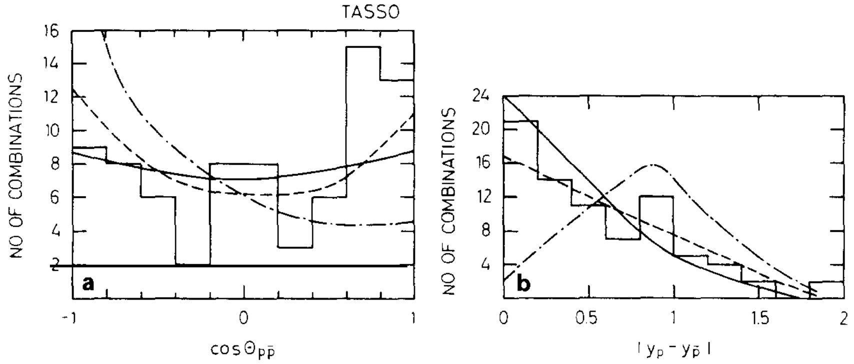

Fig. 8.3.1. Proton–antiproton correlations [151]. Shown are (a) distribution of the polar angle of the proton in the $p\bar{p}$ rest system, (b) rapidity difference of the proton and antiproton. The lines correspond to predictions of the models Černy et al. (dashed–dotted), Meyer (solid), and the LUND group (dashed).

The results from the proton–antiproton correlations measured at higher momenta are listed in table 8.3.1 [251]. The only statistically significant signal of $\sim 3.5\sigma$ originates from $p\bar{p}$ pairs in the same jet. The results are consistent with the predictions of the models of the LUND group and Meyer and constitute another facette in favour of short range baryon number compensation.

This measurement can be converted into limits on the production of a primary diquark pair (i.e. coupling directly to the γ or Z^0). Such a production is anticipated as one mode of baryon production in refs. [16, 154]. Assuming a flat fragmentation function, less than 15% of all $p\bar{p}$ pairs, corresponding to less than 0.12 $p\bar{p}$ per event, can be attributed to this mechanism.

The total number of $\Lambda\bar{\Lambda}$ ($\Lambda\Lambda$, $\bar{\Lambda}\bar{\Lambda}$) pairs measured by the TPC [142, 250], MARK2 [141], TASSO 127], and HRS [129] collaboration is 62 (21.6). This is too small a sample to allow a detailed study of the compensation mechanism. As can be seen e.g. from the TPC data (fig. 8.3.2) the prediction from the LUND Monte Carlo (dashed–dotted line), including short range correlations agrees better with the data than the dashed line for which independent production of Λ, $\bar{\Lambda}$ has been assumed. The other experiments find essentially the same result.

In summary, there exist several independent measurements supporting the short range mechanism with low significance each. Together they provide qualitative evidence for a short range mechanism of the baryon number compensation. A quantitative evaluation in terms of correlation lengths or a possible dependence on special event properties requires more precise results.

In addition to the search for short range baryon number compensation, other problems of jet development can be tackled with baryon pairs.

A more detailed study of baryon–antibaryon pair production allows one to discriminate between various models of baryon production. To this end the TPC collaboration [252] studied the angular

Table 8.3.1
Yields of pairs of equal and unequal baryon number in the same and opposite event hemisphere

Combinations	same jet	opposite jets
$pp/\bar{p}\bar{p}$	1.5 ± 2.1	3.5 ± 2.9
$p\bar{p}$	15.5 ± 4.5	1.2 ± 2.6

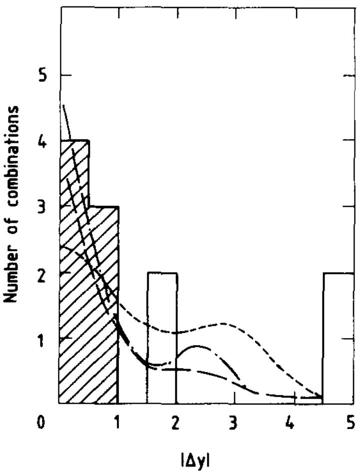

Fig. 8.3.2. Absolute value of the rapidity difference for $\Lambda\bar{\Lambda}$ pairs. Also shown are the predictions from the LUND–Monte Carlo (dashed–dotted curve) and the expectation from the statistical expectation (dotted) [242]. The dashed line corresponds to the $\Lambda\bar{\Lambda}$ production excluding background. The hatched area indicates the $\Lambda\bar{\Lambda}$ pairs found in the same event hemisphere.

distribution of the proton with respect to the sphericity axis in the $p\bar{p}$ rest frame. Their results are displayed in fig. 8.3.3 together with the predictions of the cluster decay implemented in the Webber model and of the diquark production of the LUND model (see section 4.3). Since the cluster is assumed to decay isotropically (see section 2.2) the cos θ^* distribution is flat in this model. Within the diquark model the transverse momentum of particles with respect to the event axis is assumed to be much smaller than its longitudinal component. This leads to a strong forward peak in the angular distribution. The detector acceptance distorts the theoretical expectation into the curves shown in fig. 8.3.3b. The data agree with the diquark model. To accommodate this measurement Webber introduced a coupling $g \to D\bar{D}$ (D for diquark) [253].

A further step can be made by studying the production of two baryon–antibaryon pairs. Since the identification of all baryons is difficult, the TPC collaboration [254] has used their sample of pairs of particles of the same baryon number for this. Some indication for a minimum of the correlation function in the vicinity of the reference particle can be seen from fig. 8.3.4. Within the standard

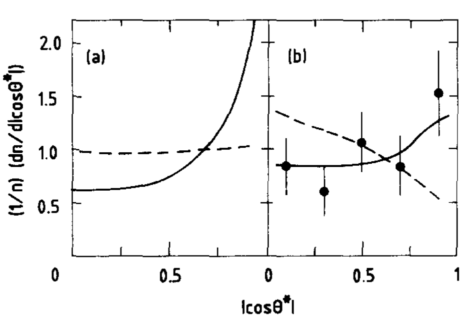

Fig. 8.3.3. Distribution of the polar angle of the proton (antiproton) in the $p\bar{p}$ rest system with (b) and without (a) detector effects [253]. Also shown are the predictions from the cluster decay embodied in the Webber–Monte Carlo (dashed line) and the diquark picture of the LUND program (solid line).

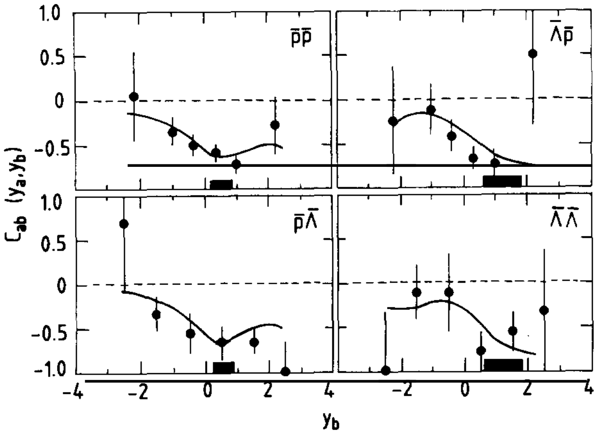

Fig. 8.3.4. Rapidity difference for pairs of two antibaryons [234]. The reference interval selected is indicated by the strong black bars. The full lines are the predictions from the LUND–Monte Carlo.

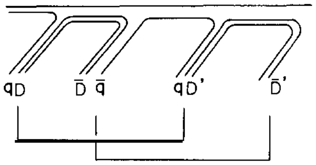

Fig. 8.3.5. Schematic diagram for the production of two baryon/antibaryon pairs.

chainlike fragmentation models these anti-correlations arise naturally since baryons can only be produced alternating with an antibaryon and possibly mesons (see fig. 8.3.5). By comparing their results to various fragmentation functions, the TPC group finds the data can be reproduced more closely with the symmetric fragmentation function of the LUND model (2.2.5) than with the parametrisations (2.2.3) and (2.2.4).

8.4. Local p_T conservation

As mentioned before, the transverse momentum in a chainlike model is assumed to be compensated locally (cf. eq. (2.2.7)). The quark and antiquark picked out of the sea have transverse momenta

$$p_T^q = -p_T^{\bar{q}} .$$

This correlation does not strictly persist in the final hadrons. The quark and antiquark combine with partons from two different pairs each having a random transverse momentum. Therefore the correlation is smeared out for subsequently produced hadrons.

Due to the reasons discussed before, baryons are an ideal place to search for local p_T conservation. However, as also mentioned, the signature for local p_T conservation may be hidden by effects due to their special production mechanism.

Several experiments used their baryon–antibaryon pairs to search for local p_T conservation. As an indicator they looked if the subsequent particles have predominantly opposite azimuthal angles with respect to the event axis. The results published so far are conflicting. The JADE collaboration [255] found a clustering of $\Lambda\bar{\Lambda}$ pairs around $\Delta\phi = 180°$. This result is supported by measurements from MARK2 [141] (see fig. 8.4.1b). On the other hand the distributions from TASSO [127], HRS [129] (see fig. 8.4.1a) and the TPC [250] group show a flat $\Delta\phi$ distribution.

The lack of convincing experimental evidence for a local p_T conservation in baryon pairs can be turned around and attributed to the special mechanism of baryon production (provided local p_T

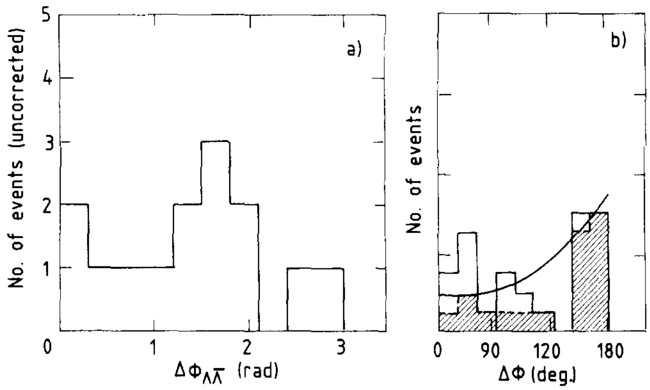

Fig. 8.4.1. Difference of azimuthal angles of a Λ and a $\bar{\Lambda}$ measured by (a) HRS [129], (b) MARK2 [141]. The shaded area corresponds to Λ, $\bar{\Lambda}$'s in the same event hemisphere. The full curve is a result from the Monte Carlo simulation assuming local p_T-conservation.

conservation holds on the parton level). The TPC collaboration [252] compared their data with the popcorn model of diquarks (see section 4.3) assuming a production chain baryon–meson–antibaryon instead of baryon–antibaryon. This model is an example of loosely bound (extended) diquarks where one of the quarks within a diquark breaks out to join a $q\bar{q}$ pair from the sea and to form a meson with some probability f.

This model was tested in terms of

$$\alpha_{\text{out}} = \frac{\langle p_{\text{Tp}}^{\text{out}} \cdot p_{\text{T}\bar{\text{p}}}^{\text{out}} \rangle}{\langle (p_{\text{T}}^{\text{out}})^2 \rangle}\,, \tag{8.4.1}$$

where $p_{\text{T}}^{\text{out}}$ is the momentum component out of the event plane. Also the equivalent parameter α_{in} was used as an indicator. It is obtained by replacing p_{out} by p_{in}, the transverse momentum component in the event plane. Ideal local p_{T} conservation for diquark pairs would yield $\alpha = -\frac{1}{2}$. In case the baryon–antibaryon pairs are always produced with an intermediate emission of a meson, α would be positive. From their measurement of α_{out} (fig. 8.4.2a) and α_{in} (fig. 8.4.2b) the TPC collaboration determines f to be

$$f > 0.45 \quad \text{at} \quad 90\% \text{ CL.}$$

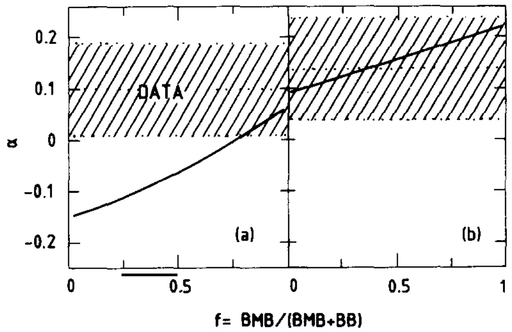

Fig. 8.4.2. Correlation coefficient of the transverse momenta of $p\bar{p}$ pairs out (a) and in (b) the event plane [252]. The shaded area indicates the measurement with its one σ error. The solid lines are the model prediction as a function of the probability f for two baryons being interspersed by a meson.

This suggests that diquarks are loosely bound objects. Note, however, that the results are based on the assumption of local p_T conservation for which no evidence has been found yet.

8.5. Conclusions

Quantum number compensation provides an effective microscope of the hadronisation region. The measurements revealed two distinct ways of how quantum numbers are neutralized within a jet:

(i) The charge and strangeness correlation function provided evidence for a quantum number compensation in effect over long ranges of rapidity $\Delta y \geq 3$–6 for test particles at high rapidities. Everything is consistent with this being the trace of the primary quarks flying rapidly apart and combining with other partons to form hadrons at relatively high x-values. The fraction of particles containing the first quark is particularly large at high rapidity and x-values. This feature allows one to obtain fundamental insight into the way the primary quark converts into hadrons and indicates a technique to trace the quantum numbers of the primary quarks.

(ii) In addition there is a high probability that two hadrons with compensating quantum numbers are produced within a narrow rapidity interval of $\Delta y \sim 1$–2. Using the equation given in the appendix A.1 expressing the relation between the rapidity difference and the invariant mass and assuming $p_T = 300\,\text{MeV}$, pion masses and the difference $\Delta\phi$ of the azimuthal angle to be $\pi/2$, this corresponds to the "virtuality" of the system $\sqrt{M^2 - m_1^2 - m_2^2}$ of 0.8–1.2 GeV. Evidence for short range compensation has been found for the charge (which is mostly due to resonance decays, however), for strangeness, and for the baryon number. The data are inconsistent with the assumption of a stochastic production of hadrons or partons. In the special case of baryon production they support the concept of diquarks.

The measurements on the topological correlations of larger subsets, discussed in section 6, suggested that the primary $q\bar{q}$ pair hadronises in an iterative way, i.e. in discrete steps. The results of this section revealed that these steps are related to the emission of a flavour neutral entity like a gluon or some other source of a $q\bar{q}$ pair. This is in line with the conclusions about the yield of identified particles (see section 4) excluding any phase spacelike model of jet development. The data are still too scarce to be more quantitative about the correlation length. They are consistent with the predictions of the standard simulation programs for fragmentation.

9. When do non-perturbative effects become important?

It is a common belief that jets are shaped by the strong interactions as described by QCD. However, as was already discussed in the first section, in its framework perturbative methods for calculating the parton distribution can only be applied up to a certain cut-off mass Q_0. Whereas for high Q^2, i.e. in narrow space and time regions, quasi-free hard partons exist, there is bound to be a cloud of gluons and partons at low Q^2 confined within a flux tube. What happens in the first region can be calculated using perturbative QCD, for the multigluon case these techniques fail. Instead ad hoc recipes have to be applied for converting the (hard) partons into hadrons.

At what value of Q^2 these effects from multipartons become dominant, is uncertain and cannot be inferred from theory. In the early stages of the development of the various fragmentation models two rather extreme views had been adopted: the QCD-shower simulation algorithms followed the partons to a low Q_0, the models based on the exact matrix element to a high Q_0. Once the partons are generated they are transformed in both cases into hadron distributions depending on the mass of the remaining parton system. The number of hadrons produced per parton is quite different in the two approaches. In the cluster decays, which often constitute the hadronisation phase in shower models, about one hadron is produced for each parton. For the high-cut-off algorithms the number is in principle unlimited. At the PETRA and PEP energies, about four to five hadrons per parton are generated. Thus in the simulation schemes two different energy scales are introduced. Their dependence on the total c.m. energy W is different.

A change of Q_0 leads to strong variations of quantities like the three-jet cross section, the particle content in an event, or the average multiplicity. Still, to obtain an estimate of Q_0 from these distributions is difficult since they are correlated with other only marginally known parameters in particular due to non-perturbative effects.

Finding the boundary between these two energy scales can only be accomplished by comparing Monte Carlo simulations with different values of Q_0 to the data. This can be achieved by either changing Q_0 within a specific simulation program or by comparing the QCD shower approach to the high Q_0 approach.

Such an analysis can only be meaningful for distributions which are rather insensitive to fragmentation effects. The results presented in this section are based on (i) asymmetries in the energy–energy correlations, (ii) the gluon fragmentation function, (iii) scaling violations of the fragmentation function, (iv) energy dependence of measures of the event topology.

Whereas the first two use a sensitive distribution at a fixed energy, the latter two exploit the variation of jet properties with energy. In addition, the information carried by prompt photon emission can reveal the mass scale of non-perturbative effects. Although essentially no experimental information is available, its potential will be addressed in section 9.5.

9.1. Asymmetry in energy–energy correlations

As proposed by Basham et al. [256] the energy–energy correlations provide a good measure of QCD effects. They are defined as

$$\frac{\mathrm{d}\Sigma}{\mathrm{d}\theta} = \frac{1}{\sigma_0} \int \frac{\mathrm{d}\sigma}{\mathrm{d}x_i\,\mathrm{d}x_j\,\mathrm{d}\cos\theta}\, x_i x_j\,\mathrm{d}x_i\,\mathrm{d}x_j\,, \tag{9.1.1}$$

where x_i and x_j are the scaled energies of particles i and j and θ the angle between them. For two-jet events $\mathrm{d}\Sigma/\mathrm{d}\theta$ exhibits peaks at $\theta = 0$ and 180° due to particles within the same and the opposite jet. Their exact shape is determined by fragmentation effects (see fig. 9.1.1d) and therefore theoretically uncertain. To overcome those one considers the asymmetry of the energy–energy correlation.

$$A(\theta) = \frac{\mathrm{d}\Sigma}{\mathrm{d}\theta}(\pi - \theta) - \frac{\mathrm{d}\Sigma}{\mathrm{d}\theta}(\theta)\,. \tag{9.1.2}$$

Since the fragmentation should be symmetric on both sides of an event, fragmentation effects tend to cancel. Schematically the distribution of this asymmetry is displayed in fig. 9.1.1e. The asymmetry should be a good measure for hard and soft gluon emission. Its tail at large angles has frequently been used to determine α_s (see review in ref. [257]). The asymmetry at small angles provides some sensitivity as to how close to the jet axis QCD effects are important.

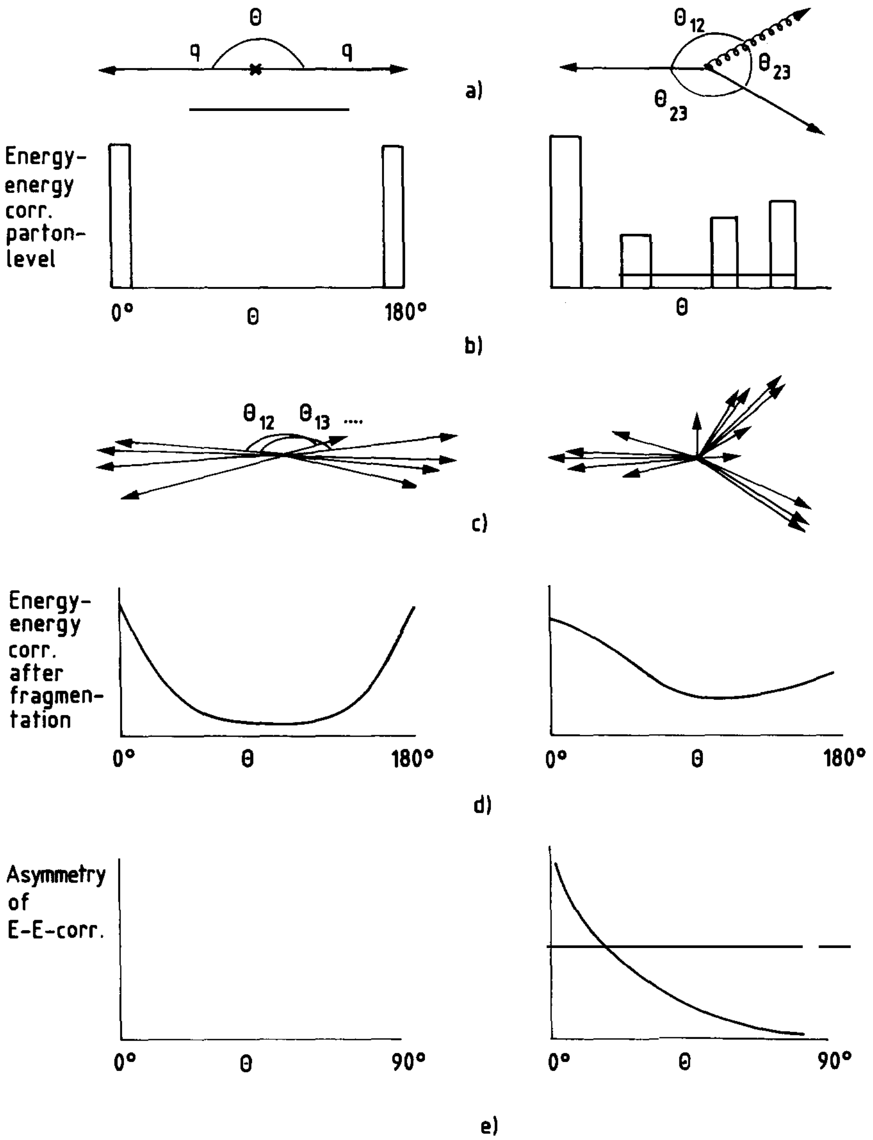

Fig. 9.1.1. Schematic view of the asymmetry in energy–energy correlations. Energy–energy correlations on the parton level (b), after fragmentation (d) and its asymmetry (e) both for two-jet and three-jet events.

The JADE collaboration [258] compared their data at $W = 34$ GeV to the predictions of the LUND simulation for various values of $y_{\min}$

$$y_{\min} = M_{kl}^2/s$$

Here M_{kl} is the minimum allowed invariant mass of two partons k and l (cf. 2.1.3).

As can be seen from the results displayed in fig. 9.1.2 the distribution at small angles θ obtained from the simulation study is very sensitive to the choice of the cut-off mass. Whereas the model predictions

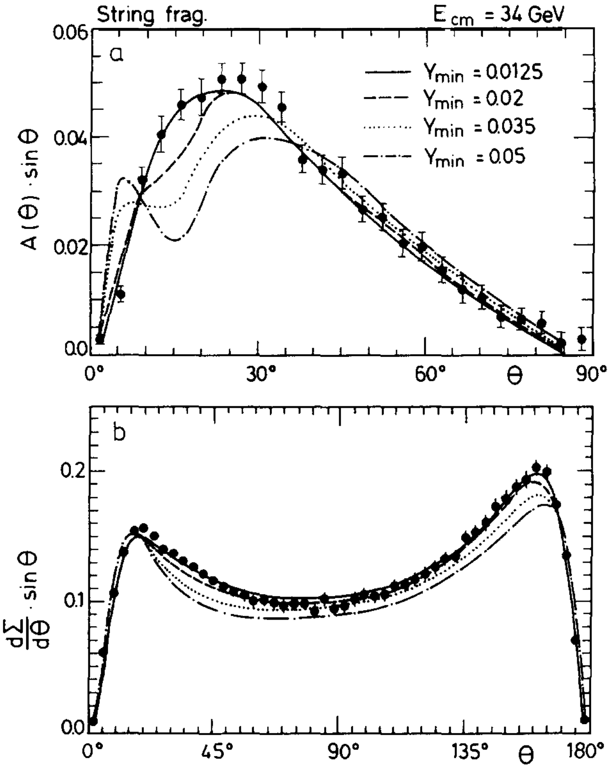

Fig. 9.1.2. The energy–energy correlation (b) and its asymmetry (a) at $W = 34$ GeV [258]. Also shown are the predictions from the $O(\alpha_s^2)$ LUND simulation assuming various values of the scaled cut-off mass $y_{\min} = M_c^2/s$.

for $\theta > 30°$ are rather independent of the values of y considered, a large value of $y = 0.05$ leads to a dip around $\theta \sim 15°$ indicating that two-jet and multi-jet events do not join smoothly. Lowering y washes the dip out and leads to a better agreement with the data. A good description can be obtained for $y_{\min} = 0.0125$, corresponding to a cut-off mass of $M_{kl} = 3.8$ GeV. This value leads to fractions of 8%, 82%, and 10% for two-, three- and four-jet events, respectively. As discussed in section 2.1 and seen in fig. 2.1.2b the high fraction of four-jet event indicates that the $O(\alpha_s^2)$ exact matrix element is not appropriate and that higher than second orders become important at these energies. Thus an even lower cut-off mass seems to be more probable.

9.2. Model predictions for the gluon fragmentation function

The different treatment of the gluon allowed one to discriminate between the approaches of the String and the Independent Jet fragmentation. The Leading Log Approximation treats the gluon fragmentation still differently. Within the context of string fragmentation the particles emitted into the direction of the gluon are due to two strings which fragment as a $q\bar{q}$ system. In the showering process the gluon splits mostly into $g \rightarrow gg$ due to its higher colour charge. This leads to an increased branching probability and therefore to a higher particle multiplicity and a softer fragmentation function compared to a quark jet (see section 5.2).

As discussed above, the MARK2 collaboration [210] has determined the gluon fragmentation function in symmetric three-jet events at $W = 29$ GeV. They also compared their measurements with model calculations. The results are displayed in fig. 9.2.1. Here the ratio of the particle yield in symmetric three-jet events over that obtained in all events at a c.m. energy $W = \frac{2}{3} \times 29\,\text{GeV} = 19.3\,\text{GeV}$ is displayed together with the predictions of the model of Ali et al., the LUND model, and the Webber model (LLA approach). Note that in the version of the Independent Jet Model used, the gluon is split into a $q\bar{q}$ pair according to the Altarelli–Parisi equation (see section 2.2.1). As already discussed, the gluon fragmentation is softer than the quark fragmentation. Both the LUND Model and the Independent Jet Model cannot accommodate this softness. The shower model of Webber, on the other hand, gives a good representation of the data. This result suggests a more frequent branching along the gluon jet and therefore a smaller cut-off mass than used in the LUND and Independent Jet Model. Note, however, that the multiplicity in a gluon jet as determined by the HRS collaboration [211] agrees with the expectation of the LUND model.

9.3. Scaling violations as a measure of the cut-off mass

The evidence for scaling violations in the fragmentation function has been discussed in section 3.2.2, where they were shown to originate from QCD bremsstrahlung and to a minor extent from kinematical effects. It is suggestive (cf. ref. [29]) to use the scaling violations as a measure of the cut-off mass.

The use of the energy variation to extract M_c seems possible since the two regions of hadronisation and parton emission respond differently to a variation of the c.m. energy. An advantage of such an analysis is its low sensitivity to the exact values of the fragmentation parameters used in the simulation. Since one considers only variations in W, a possible inappropriate assignment of these values cancels to first order. On the other hand one has to assume how M_c varies with energy. Since the strength of the gluon field should be uniquely given by the mass of a colour neutral system, the most straightforward assumption is an energy independent M_c. Other variations have been conceived, Walsh and Zerwas, e.g., suggest that confinement effects become important if a parton travels further than a distance $O(m_p^{-1})$ and therefore

$$M_c^2 \sim E_{\text{beam}} m_p \quad \Rightarrow \quad M_c \propto \sqrt{E_{\text{beam}}} \tag{9.3.1}$$

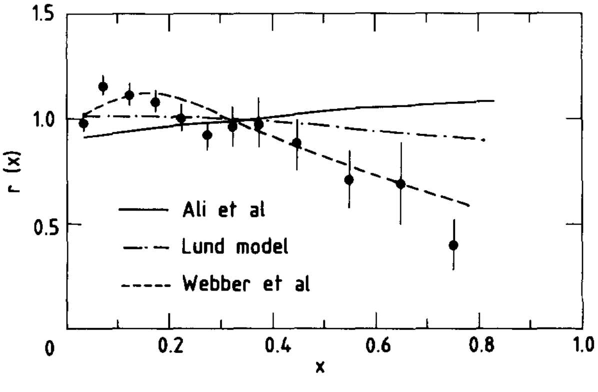

Fig. 9.2.1. Ratio of the average fragmentation function per jet in symmetric three-jet events at $E_{\text{cm}} = 29$ GeV to that of two-jet events at $W = \frac{2}{3} \times 29$ GeV [210]. The data (full circles) are compared to the Independent Jet Model (dotted line), the string model (dashed–dotted), and the shower algorithm (dashed).

In the following analysis (see also ref. [109]) the prediction of the LUND Monte Carlo is compared to the data assuming a certain cut-off mass and value of the second order QCD scale parameter $\Lambda_{\overline{\mathrm{MS}}}$. This is done in terms of the ratio of the fragmentation function at two different c.m. energies. In fig. 9.3.1 the ratios between $W = 14$ and 44 GeV, respectively 14 and 34 GeV are plotted together with results from the LUND Monte Carlo assuming $M_c = 2$, 4 and 6 GeV and $\Lambda_{\overline{\mathrm{MS}}} = 0.5$ GeV (fig. a). The variation of the simulation result on the QCD parameter Λ is shown in fig. 9.3.2. Here M_c was set to $M_c = 4$ GeV and $\Lambda_{\overline{\mathrm{MS}}} = 0.1$ and 1.5 GeV was assumed.

As already discussed in section 3.2.2 the LUND simulation on the basis of the exact second order QCD matrix element gives a poor description of the size and x-dependence of the measurements. The observed scale breaking is stronger than predicted by the model in the region $0.2 < x_p < 0.5$ for all values of M_c. The variation of the scale breaking with a change in M_c exhibits a peculiar behaviour. The ratio between $W = 14$ and $W = 35$ GeV increases when changing M_c from 6 to 4 GeV. This is expected since the fraction of three- and four-jet events should increase (cf. eq. (2.1.2)). However, this trend is reversed for the even lower value of $M_c = 2$ GeV. As discussed in section 2.1 the α_s^2 model runs into problems with unitarity at very low cut-off masses. These are reflected in the small scale breaking for

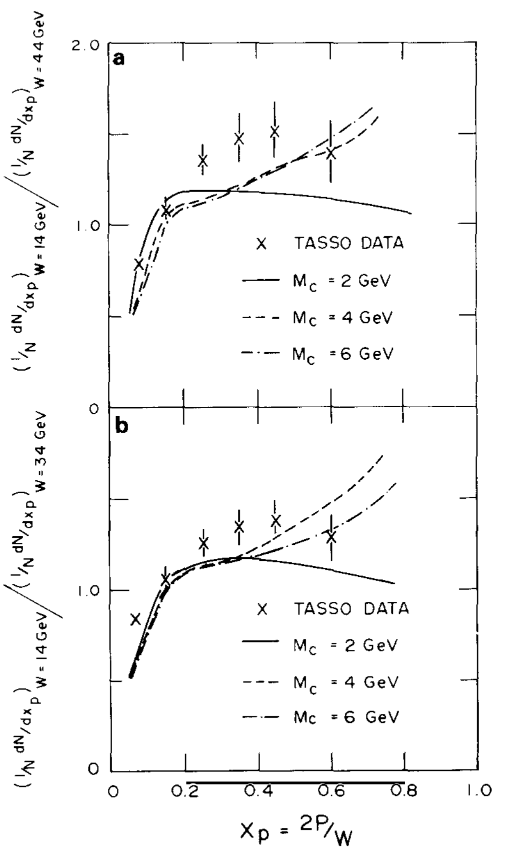

Fig. 9.3.1. Ratio of the fragmentation functions at $W = 14$ and 44 GeV (a) and 14 and 34 GeV (b) as a function of x_p. The data (crosses) are compared to the prediction of the LUND model using second order QCD corrections assuming various values of the cut-off mass M_c.

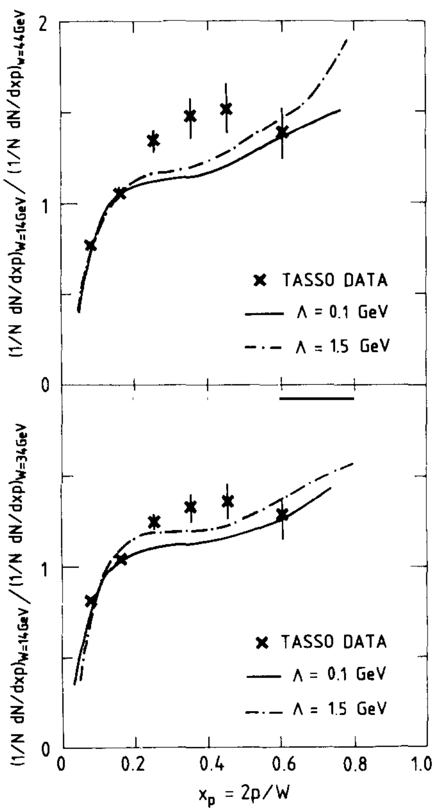

Fig. 9.3.2. The same as fig. 9.3.1. For the model calculation the QCD parameter Λ_{QCD} was varied, M_c was set to 4 GeV.

$M_c = 2$ GeV*). The strength of the scale breaking observed indicates that already at $W = 34$ GeV higher orders become necessary (although the statistical significance is marginal). The discrepancies between model and data become even more prominent for the ratio $W = 44/W = 14$ GeV. In this case the model predictions for $M_c = 4$ and 6 GeV are about the same and fall significantly short of describing the strength of the scale breaking observed.

As can be seen from fig. 9.3.2 the discrepancy persists also when the value of $\Lambda_{\overline{MS}}$ is changed. The ratio predicted by the O(α_s) model changes only marginally when increasing $\Lambda_{\overline{MS}}$ from 0.1 to 1.5 GeV. Note that from the topology of events at a fixed c.m. energy $\Lambda_{\overline{MS}}$ is determined as ~0.5 GeV.

The QCD shower algorithms provide a much better description of the scaling violations observed. In fig. 9.3.3 the measurements are compared to the LUND shower algorithm combining the parton distribution as given by the LLA down to some cut-off mass M_c with string hadronisation. The hadronic events were simulated with three different values of M_c: 0.88, 2 and 4 GeV. As can be seen, the highest cut-off mass falls short of describing the size of the scale breaking, whereas $M_c = 2$ and 0.88 GeV are in quite good agreement with the data. The value of $M_c = 2$ GeV tends to underestimate, the value 0.88 GeV to overestimate the scale breaking**). Thus within the limited accuracy of the data a cut-off

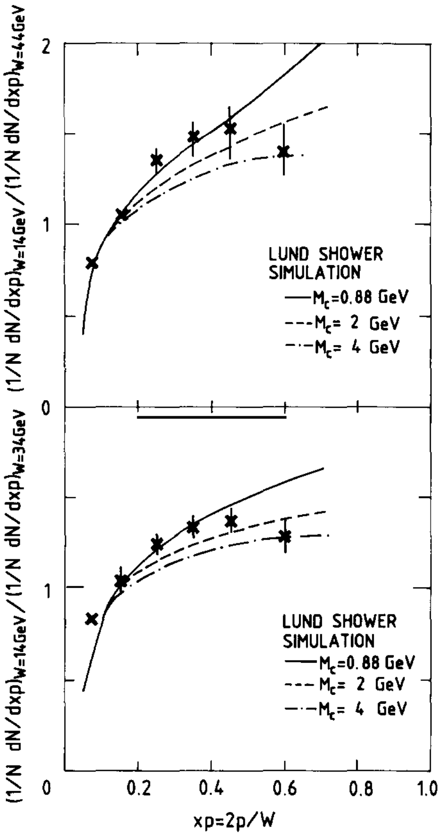

Fig. 9.3.3. Same as fig. 9.3.1. The data are compared to the LUND shower algorithm for various values of the cut-off mass.

---

*) Technically such a small cut-off is not realized in the LUND Monte Carlo at $W = 34$ and 44 GeV. Instead M_c is reset in the computer program to $M_c \sim 4$ GeV to accommodate unitarity.

**) A value of $\Lambda_{QCD} = 0.4$ GeV as used for these simulations. This limits the value of M_c since a cut-off $M_c > 2.2\Lambda$ is incorporated in the program.

mass around 1 GeV seems appropriate. Such a small value leads to an average parton multiplicity of ~10 at $W = 44$ GeV and is therefore consistent with the break-down of the $O(\alpha_s^2)$-calculations discussed before.

9.4. Topological studies

The JADE collaboration used event topologies to discriminate between the matrix element and the QCD shower approach [115]. They analysed both the data at a fixed energy of $W = 34$ GeV, where the majority of their events has been collected, and those measured at the different c.m. energies obtained at PETRA.

The topology of an event was studied in terms of the cluster multiplicity and the acoplanarity (see appendix A.2)

$$A = 4 \min\left(\sum |p_{i,\mathrm{T}}| \Big/ \sum |p_i|\right)^2$$

where $p_{i,\mathrm{T}}$ is the momentum component of particle i transverse to the event plane.

To examine the influence of the cut-off mass, they developed a cluster algorithm similar to the cut-off used in the QCD models (cf. section 2.1). The particles in an event are combined into subsamples k, l which have to fulfill

$$M_{kl}^2 / E_{\mathrm{vis}}^2 < y_{\mathrm{cut}}$$

Here E_{vis} is the total visible energy in the event, M_{kl} a quantity related to the invariant mass of two clusters, and y_{cut} is a free parameter that was varied in the analysis.

The fraction of cluster multiplicities found with this algorithm in the data and the two kinds of models of Webber and the LUND group ("$O(\alpha_s^2)$") are displayed in fig. 9.4.1 as a function of y_{cut} at

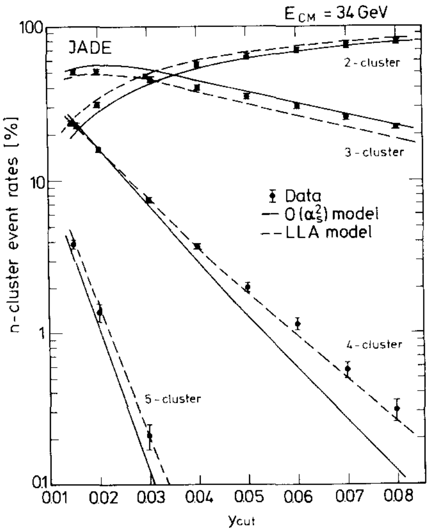

Fig. 9.4.1. Dependence of the observed n-cluster rate on the cut $y_{\mathrm{cut}} = M^2/E_{\mathrm{vis}}^2$ in the cluster algorithm [115]. The data (full circles) are compared to the LUND $O(\alpha_s^2)$ (full line) and the Webber (LLA) Monte Carlo (dashed line).

$W = 34$ GeV. For this analysis the value of Λ_{QCD} was fixed according to the results from the asymmetry of the energy–energy correlations (cf. section 9.1). Since more particles are absorbed into one cluster, the two-cluster rate increases with y_{cut}, whereas the fraction of higher multiplicites decreases. Both models exhibit discrepancies at fixed values of y_{min}. Whereas the approach based on the Leading Logarithm Approximation (LLA) underestimates the fraction of events with three clusters but agrees in the four-cluster rate, the $O(\alpha_s^2)$ model gives a better description of the three- but underestimates the four-cluster rate. Qualitatively this difference is independent of a change of the fragmentation parameters. Note, however, that at least for the four clusters the difference between model and data is less than a percent.

The energy dependence of the cluster multiplicity was studied for a fixed M_{kl} of 6.8 GeV, which corresponds to $y_{\mathrm{cut}} = 0.04$ at $W = 34$ GeV. The different fractions of cluster multiplicities are shown in fig. 9.4.2. The fractions of three and in particular of four clusters increase considerably with energy. The discrepancies found at $W = 34$ GeV persist at all energies.

A related result is obtained from the energy variation of the acoplanarity distribution (fig. 3.4.3). Since the acoplanarity is sensitive to components outside the event plane, it is particularly suited for studying the contribution from events with more than three jets. Whereas the $O(\alpha_s^2)$ model does reproduce the data at $W = 22$ GeV it falls short of describing the tail of high acoplanarity events observed at higher energies $W = 34$ GeV and $W = 44$ GeV. The LLA model, however, reproduces the data at all c.m. energies. By mixing five-jet events from the LLA approach with the result from the matrix element calculation a better agreement is observed. The JADE collaboration interprets these results as indications for events with a jet multiplicity larger than four. These cannot be generated within the $O(\alpha_s^2)$ calculations, but arise within the shower approaches.

A similar conclusion emerges from the analysis of ref. [65]. The MARK2 collaboration compared their measurements at $W = 29$ GeV as well as measurements from other collaborations at different energies to various models [48, 259, 39]. For this analysis 3–5 free parameters for each model, determining essentially the QCD evolution, were optimized.

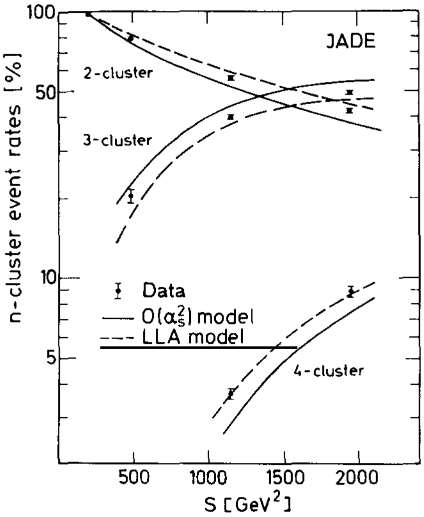

Fig. 9.4.2. Dependence of the observed n-cluster rate on the square of the c.m. energy [115]. The data (full circles) are compared to the Monte Carlo results of the LUND $O(\alpha_s^2)$-program (solid line) and the LLA model of Webber (dashed line).

The best agreement has been obtained for the LUND $O(\alpha_s^2)$ calculation and the LUND shower algorithm with some preference for the latter. The $O(\alpha_s^2)$ model has deficiencies in distributions that are sensitive to higher than second order corrections: the aplanarity, the minor-variable and the p_T^{out}-distributions (which are of course all correlated). This is in agreement with the observation of the JADE group. Within the shower models the MARK2 data could best be described with a cut-off parameter of 1 GeV, which is consistent with the analysis of scaling violations presented in section 9.3.

9.5. Direct photon production in jets

Another method to study the development of jets [29] is the use of prompt photon production in jets. The photon is an ideal tool for probing the hadronisation region since it is colourless and can break undisturbed through the gluon cloud formed between the hard partons. It therefore carries direct information about the state of the quarks. In sharp contrast to this, quarks are supposed to scatter strongly in this cloud and the outcoming hadron is deprived from carrying the direct information.

This theoretical interest has to be confronted with the huge experimental problems of identifying direct photon production in jets. Firstly photon radiation from quarks is suppressed compared to gluon radiation by the electromagnetic coupling α over the strong coupling α_s. Secondly, in addition to photon bremsstrahlung from the initial e^+ and e^-, there is a considerable amount of photons in jets due to π^0 (and η) decays. From table 4.1.1 it follows that at $W \sim 30$ GeV about 10–12 photons per event originate from meson decays.

The structure function for photons in the Born approximation has been calculated by Walsh and Zerwas [260] as being

$$\frac{1}{\sigma_0}\,\frac{d\sigma}{dx\,d\cos\theta} = \tfrac{8}{3}(1+\cos^2\theta)F_T(x, Q^2) + \tfrac{4}{3}(1+\sin^2\theta)F_L(x, Q^2)\,, \qquad (9.5.1)$$

with

$$F_T(x, Q^2) = \frac{1}{\sum R_q}\sum e_q^2\cdot R_q\,\frac{\alpha}{\pi}\,\frac{1+(1-x)^2}{x}\,\log\frac{Q^2(1-x)}{\Lambda^2}\,, \qquad (9.5.2a)$$

$$F_L(x, Q^2) = \frac{1}{\sum R_q}\sum e_q^2\cdot R_q\,\frac{\alpha}{\pi}\,4\cdot\frac{(1-x)}{x}\,, \qquad (9.5.2b)$$

where x is the fractional energy of the photon $x = 2E_\gamma/W$ and θ its polar angle, R_q is the cross section for the production of a quark q in terms of the pointlike QED cross section $e^+e^- \to \mu^+\mu^-$. The corrections due to higher order QCD effects have been calculated in refs. [261, 262].

These formulas predict the prompt photon yield to increase with energy and to have a hard fragmentation function. Both features are different for mesons which are found to fragment according to

$$d\sigma/dx \propto (1-x)^2/x\,,$$

(cf. section 3.2.1) and whose yield is found to become smaller at high x with increasing Q^2. These two properties suggest an experimental strategy for searching for prompt photon production: one should select photons with high x-values at a large angle to the beam axis. High c.m. energies should increase the purity of prompt photons.

The uncertainties about the mass scale of the hadronisation region are within the range $M_c \sim$ 1–5 GeV. Photons carrying information about this region will therefore have a $p_T \leq 2.5$ GeV. Depending on the state of quarks in this region they will exhibit a different dependence on x and p_T. For two extreme assumptions one would have the following expectations [262]:

(i) If only very little perturbative evolution exists in that region, radiation from hadrons becomes relevant. Thus the photon spectrum should reflect the fragmentation function of hadrons and vanish with $x \to 1$.

(ii) If perturbative evolution is valid down to much lower masses, the x-spectrum of photons is expected to be hard also for low p_T's.

The two scenarios are sketched in fig. 9.5.1.

As yet experiments have little to say about these predictions. Two measurements giving evidence for direct photon production have been published. The MAC collaboration [263] has found a charge asymmetry

$$A = (-12.3 \pm 3.5)\%$$

in events with a hard photon. This asymmetry is due to the interference of photon emission in the initial and final state. The JADE collaboration [121] has observed an excess of 56 ± 22 photons over the expectation from QED in a region where the contribution of photons from fragmentation is negligible.

These results do not add new information to the discussion about the non-perturbative mass scales. However, they should be seen as a first step to analyse direct photon production in a jet. The higher energies and larger data samples obtained in the near future will provide a more fertile ground for such an analysis.

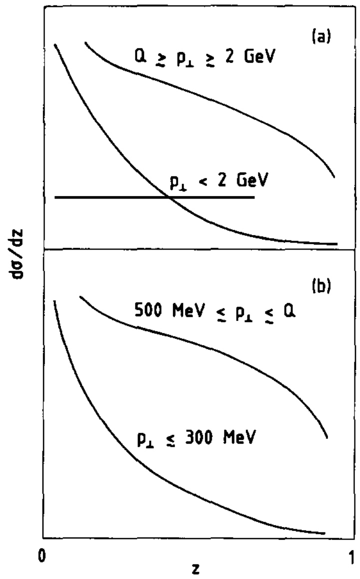

Fig. 9.5.1. Schematic view of the x (denoted by z) dependence of prompt photons of some transverse momentum to the quark direction [262]. (a) Perturbative parton evolution gets superseded by non-perturbative effects at an invariant parton mass of the order 5 GeV. (b) Perturbative parton evolution continues down to invariant masses of the order of the ρ-mass.

9.6. Conclusions

In this section the mass scale of the transition from a perturbative to a non-perturbative treatment of the development of jets has been discussed. Such a mass scale is at least a technical prescription used in all QCD inspired approaches to jet development. It indicates at which stage the mathematical power of predicting parton distributions dies out and ad hoc prescriptions have to be used for converting the partons to the finally visible hadrons.

Basically two ways have been proposed to obtain indications of the mass scale. In the first one data and simulation programs were compared at a fixed energy using different cut-offs. In the second one the energy variation of distributions sensitive to QCD effects were examined.

There is a consistent trend in all of these results towards a lower cut-off mass than traditionally used, indicating that higher than second order QCD corrections are necessary at c.m. energies around $W = 40$ GeV. The experimental indications are a low y_{cut} to describe the asymmetries of the energy–energy correlations, the better reproduction of the gluon fragmentation function by shower models, the breakdown of the $O(\alpha_s^2)$ prediction of the scale breaking of the fragmentation function and the relatively strong component of transverse momenta out of the event plane.

These results suggest that the trend to higher jet multiplicities persists with increasing energy: at $W < 20$ GeV the data could well be described as being just two-jet events, evidence for three-jet events was found at $W \sim 30$ GeV, four jets are essential to describe the data at $W \sim 44$ GeV*⁾.

Higher jet multiplicities can only be accomplished through shower approaches which are based on theoretical approximations. Whereas, as discussed in the previous sections, the shower model combined with the cluster decay for hadronisation has problems in describing several features of the data, its combination with strings leads to results that are largely consistent with all known data. Within this scheme cut-off masses of 1–2 GeV lead to a good description of both the distributions at a fixed energy as well as of their energy variations. This implies that about 10 or 15 individual string-pieces fragment respectively at $W = 44$ or 100 GeV.

PART III. JETS OF THE FUTURE

As was discussed in the introduction, the interest in jet physics is at least twofold. Firstly jet properties have to be explained on the basis of a fundamental theory which is generally believed to be QCD. Secondly jets are the only experimental signature of quarks and gluons and the penetration into smaller and smaller regions of space–time requires a reconstruction of the fundamental partons in the high Q^2-interactions. In both respects there still exist many unsolved problems.

Although the general topology of hadronic events is well understood within the standard model, the connection of the details of the jet structure to a theoretical framework is only marginally developed. Our insight today is mainly due to comparisons of data with QCD motivated models that still have quite a lot of freedom in their parametrisation. The difficulties are not only due to theoretical limitations. A lot of measurements require a considerable improvement both in systematic and statistical accuracy before one can step from a qualitative comparison to a quantitative analysis.

The use of jets as manifestations of the fundamental partons has only recently emerged with the new energy scales reached in particular at the Sp$\bar{\text{p}}$S collider at CERN. The new generation of particle

---

*⁾ Indications for four-jet events have already been observed at $W = 35$ GeV [264].

accelerators of the 90's probing higher energies and at least in part producing higher event rates will open new chances for improved measurements on the structure of jets as well as make it more urgent to proceed to parton instead of hadron dynamics.

In this last part we will attempt an extrapolation from today's knowledge of jets to the chances and challenges provided by this new generation of machines.

10. Fragmentation tests at future colliders

10.1. General remarks

The agreement between models and data discussed in the previous sections is remarkable for single particle, two particle as well as event distributions.

However, much of our ignorance is hidden in some ad hoc parameters and the sometimes considerable systematic and statistical uncertainties. In many cases the agreement indicates only some qualitative feature of the jet dynamics but still lacks a precise quantitative evaluation. It can be hoped that with increasing precision of the data and larger ranges of Q^2 covered, basic questions can be addressed in a more quantitative way.

The main issues of experimental and theoretical interest at the moment are as follows:

- How does the trend towards higher jet multiplicities continue with increasing energy and what is their differential cross-section?
- How and when do non-perturbative effects become relevant and what is the relation between hadron and parton dynamics?
- How are quantum numbers precisely compensated? Today's data give a first impression of short range correlations but they are much too coarse for a detailed examination of the sequence of particle production.
- Is there any Q^2 and x-dependence in the sea content? Related to this are possible effects from a diquark form-factor.
- How much and in what respect do gluon jets differ from quark jets?

In view of the measurements of the near future, it can be hoped that some of these questions can be addressed in a more profound way.

All future machines measuring at high Q^2 can contribute essential and sometimes complementary insight into the problems of fragmentation as the various kinds of reactions have already done in the past. Data from the Sp$\bar{\text{p}}$S collider on the structure of jets are emerging and give access to W's of up to 200 GeV and in particular to gluon jets. The higher energies at the Tevatron and even more at the LHC and SSC [265–267] will extend this scope*⁾. At the ep-collider HERA it will be possible to probe jets of known flavour (u or d) up to W's of 200 GeV [268].

A big step forward can be expected from the new e^+e^- colliders. The results discussed in this article are based on c.m. energies $10 < W < 45$ GeV and event yields of ~250 000 around $W = 10$ GeV and ~40 000 at $W \sim 30$ GeV for each experiment. Soon both the c.m. energy and the event samples will be increased considerably. With the SLC and LEP producing data, millions of events at energies of $W = 100$ GeV will be waiting to be analysed.

---

*⁾ They may, however, require special detectors to do that.

It is obvious that this plethora of information will increase our insight into jet development substantially. The high energies will allow one to separate effects from fragmentation and from hard parton dynamics in a much cleaner way and to study the Q^2 dependence of various distributions with a longer lever arm. The topology of multiple jet production will show up much more pronounced. The larger data samples will lead to an increased accuracy of the properties of single particle production, two particle distributions to analyse the mechanism of quantum number compensation, and the separation of jets originating from different flavours.

As a consequence many uncertainties still plaguing today's results will be decreased. For example, the accuracy of the particle yields currently measured is mostly limited by systematic errors, a large part of those is due to uncertainties in the fragmentation. The future high statistics measurements will help in an iterative way to gain insight into the fragmentation properties as a whole and as a consequence lead to a reduction of the systematic errors. It is obvious that this higher accuracy will improve our understanding of the dynamics of jet evolution, and probably only then it will be possible to go from something like an art of choosing the correct parametrisations to a search for systematic properties and trends even if a complete calculation from the first principles of QCD is not possible.

In the following some possible qualitatively new measurements will be addressed. Partly they are illustrated by results from simulation studies. For these studies we have used parametrisations that are appropriate at the e^+e^- energies of $W = 30$–40 GeV being accessible now. It is not obvious if these pertain to the tripling of the energy. Therefore the quantitative power of the predictions is limited, however, the qualitative trends should be reliable. In addition, the effects and limitations due to detectors are neglected. These pictures should be therefore regarded as mere indications of what we might face in jet-physics in the next decade.

10.2. Some possible fragmentation studies of the future

10.2.1. Jet multiplicities

The first indications for events with more than four jets have been found at $W \sim 40$ GeV [115] and were discussed in section 9.4. At energies around $W = 100$ GeV the difference in jet topologies between the second order string formalism and the QCD shower algorithms will be much more pronounced. Figure 10.2.1 displays the fraction of cluster multiplicities as predicted by the Webber and the $O(\alpha_s^2)$ LUND programs at $W = 34$ and 100 GeV. For $W = 34$ GeV the multiplicity distributions of the two algorithms are quite similar. At the higher energy, however, they are substantially different. Whereas the majority of events remains at cluster multiplicities of ~3, the shower program predicts that about 20% of all events have more than four clusters. It will therefore lead to events with higher sphericity and aplanarity than expected from $O(\alpha_s^2)$ models. The implications e.g. on the sensitivity to top production at the Z^0 energies has been discussed in ref. [269].

It should be noted that a complete and exact QCD calculation will not be available for the higher energies and that the shower agorithms used are only approximately correct. A study of the differential distributions at the high energies should improve the understanding of how partons decay to form new sources of distinct jets.

10.2.2. Scaling violations

As discussed in section 3.2 the scaling violations observed for energies between $W = 14$ and 44 GeV are due to p_T and mass as well as to QCD effects, the latter one being of prime interest. These two features can be disentangled by their different Q^2 dependence (cf. section 9.3), in particular the first

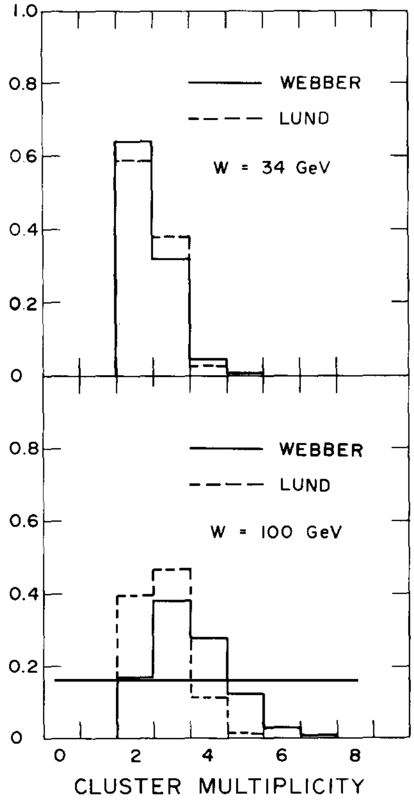

Fig. 10.2.1. Cluster multiplicity predicted by the LUND $O(\alpha_s^2)$ and Webber–Monte Carlo for c.m. energies of 34 and 100 GeV.

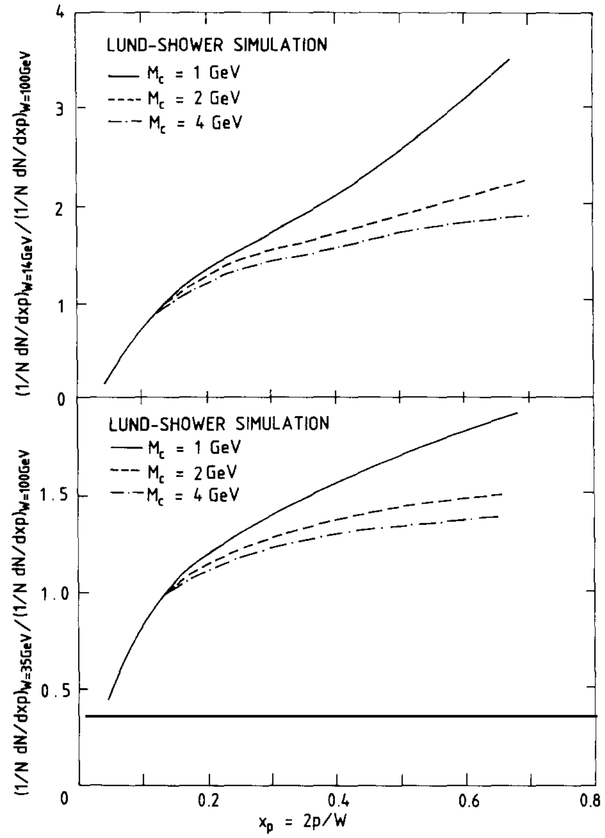

Fig. 10.2.2. Scaling violations of the fragmentation function at $W = 100$ GeV. Shown is the Monte Carlo prediction for the ratio of the fragmentation functions at (a) $W = 14$ and (b) 35 GeV to that at $W = 100$ GeV. The LUND shower algorithm was used assuming various values of the cut-off mass M_c.

effect is expected to become less important with higher energies and a comparison of the fragmentation function at $W = 14$ and 35 GeV with 100 GeV should be essentially free of kinematic distortions. Note that the flavour composition at the Z^0 is different from that in the continuum around 40 GeV. However, since the overall fragmentation properties are independent of the flavour (cf. section 5) or at least reasonably known this should impose no problem for the interpretation of scale breaking. The results of a simulation study using the LUND shower algorithm are shown in fig. 10.2.2 in terms of

$$R(x_p) = \frac{(1/\sigma_{\mathrm{tot}} \cdot \mathrm{d}\sigma/\mathrm{d}x_p)_{W=14,\ 35\ \mathrm{GeV}}}{(1/\sigma_{\mathrm{tot}} \cdot \mathrm{d}\sigma/\mathrm{d}x_p)_{W=100\ \mathrm{GeV}}}\ .$$

The results are plotted for various values of the cut-off mass M_c (cf. discussion in section 9.3). The simulation studies predict a large scale breaking effect which goes approximately like $\ln(W_1/W_2)$. Thus the ratio of the fragmentation functions for $x_p > 0.2$ is about

$$\frac{f(x_p)_{W=14\,\mathrm{GeV}}}{f(x_p)_{W=100\,\mathrm{GeV}}} \sim 2\,\frac{f(x_p)_{W=14\,\mathrm{GeV}}}{f(x_p)_{W=35\,\mathrm{GeV}}} \sim 2\,\frac{f(x_p)_{W=35\,\mathrm{GeV}}}{f(x_p)_{W=100\,\mathrm{GeV}}}\,.$$

Although the ratio for $W=35/W=100$ is not expected to be larger than what has been analysed up to now, the statistical and systematic uncertainties are much smaller here than at the lower energies. Both the longer level arm and the higher accuracy will provide a larger sensitivity to details of the predictions and parameters like the cut-off mass.

In particular, scaling violations can be studied for special kinds of particles and in the case of D*'s even for particles of known rank. The ratio of the fragmentation function of D*'s in the Webber–Monte Carlo is displayed in fig. 10.2.3. It is substantial and should be known quite precisely at least for high x_E. At low $x_E < 0.5$ the measurements at $W=34$ GeV are not very accurate and at $W=100$ GeV could be distorted by D^*'s from bottom decays or from the branching of a virtual gluon of high mass (cf. section 10.2.4). Calculations based on the leading log approach predict the average energy fraction of heavy quarks to decrease with

$$\langle x_Q \rangle^{\mathrm{LLA}} = (\alpha_s(M^2)/\alpha_s(W^2))^{-32/9 \cdot b}\,.$$

With $b = \frac{11}{3}N_c - \frac{2}{3}n_f = 7.66$ and M the mass of the heavy quark [270], this leads to a ~10% decrease between $W=34$ and 100 GeV. It seems therefore possible to test QCD predictions in a more profound way.

10.2.3. Prompt photon production

As discussed in section 9.4 the measurement of prompt photons produced in jets with a small p_T with respect to the jet axis may allow one to test the hadronisation region directly. No such measurements exist up to now at energies $W < 40$ GeV. The future chances are more promising:

- The increased statistics will be favourable to the strongly suppressed direct photon yield.

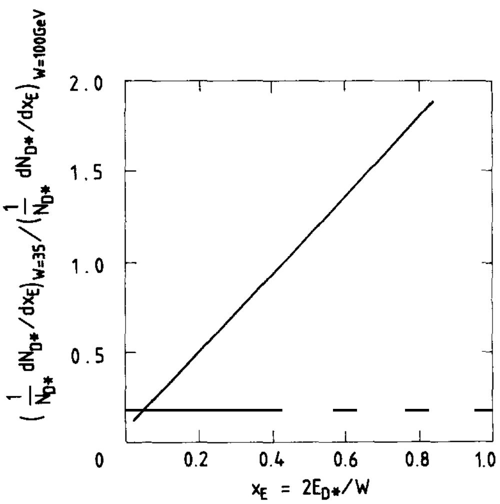

Fig. 10.2.3. Ratio of the D* fragmentation function in charmed jets at $W=35$ and 100 GeV as predicted by the Webber shower Monte Carlo.

– It will also allow one to determine the background from π^0 and η production much more reliably.
– The ratio of prompt photons to π^0's will increase with higher energies.

Still, this will be a rather difficult experiment.

10.2.4. Heavy quark production in light quark events

As discussed in section 4.5, charm and bottom quarks can only be produced as primary partons in jets around $W \sim 30$–40 GeV. In the standard string approach the probability of a fluctuation out of the vacuum is exceedingly small due to their high mass. At higher energies, however, another source of charm and bottom quarks opens up: the phase space for massive virtual partons increases. Their masses will exceed the threshold for $Q\bar{Q}$ production more frequently and a gluon can decay into a pair of charm or even bottom particles. The predictions from the Webber (shower) Monte Carlo are reproduced in fig. 10.2.4 as an example. Here a simple phase space decay of the clusters was assumed with no additional suppression factor. Only events originating from primary u, d and s-quarks are considered. Both the predictions for the number of D*'s as a function of the c.m. energy W (fig. a) and the fragmentation function (fig. b) are displayed. The number of D*'s per event is seen to rise rapidly with energy. At the Z^0 mass about 4% of all u, d and s-events are expected to contain a D*. In contrast to the hard fragmentation function of primary charm and bottom quarks, that from the $g \rightarrow Q\bar{Q}$ is softer

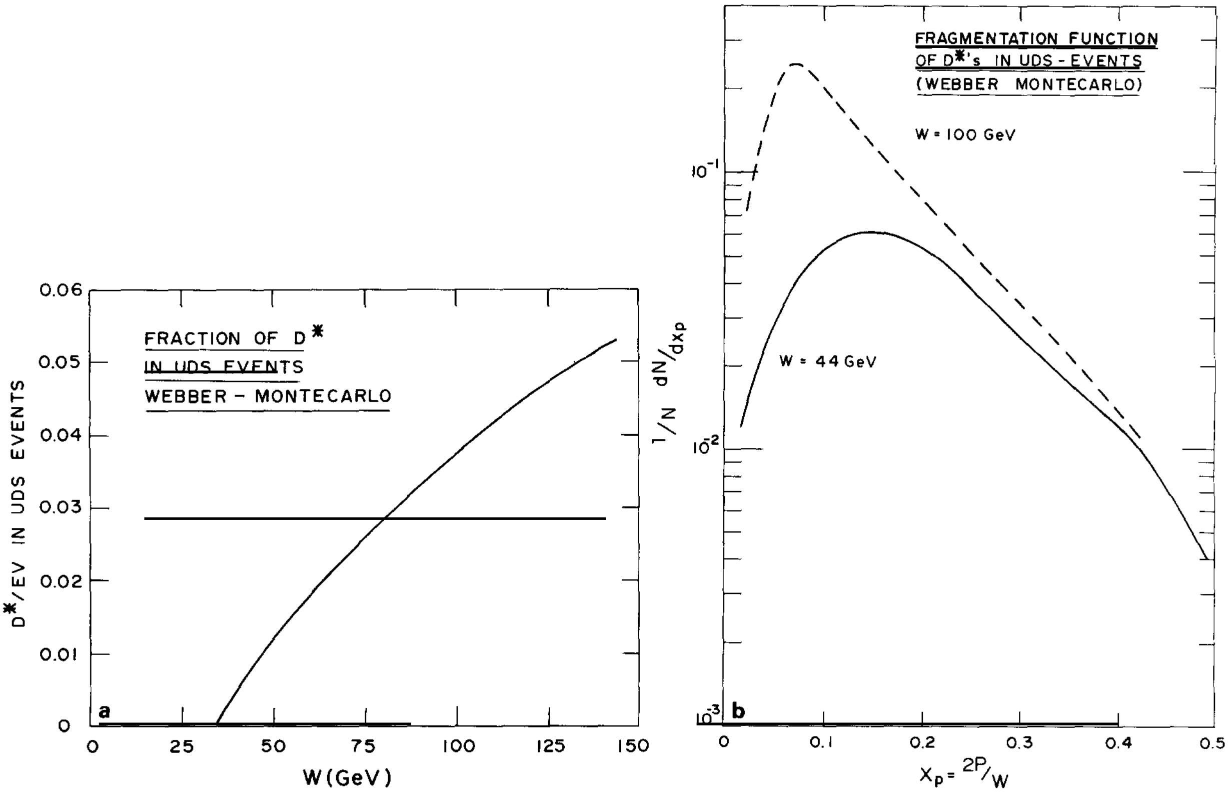

Fig. 10.2.4. D*'s in light quark events. (a) Fraction of D*'s in events from light quarks u, d and s as a function of the c.m. energy W (Webber–Monte Carlo). (b) Fragmentation function of D*'s at $W = 44$ and 100 GeV.

with an average value of x decreasing from 0.196 to 0.123 between $W = 44$ and $W = 100$ GeV. It may require considerable experimental effort to firstly identify the D*'s at those low values of x and secondly show that they are indeed coming from u, d and s-events. One signature is that two charmed particles are produced closely together in rapidity.

In addition to this source of heavy quark production, others may be conceived: motivated by a publication of the UA1-collaboration presenting a surprisingly large yield of D*'s in jets from hard $p\bar{p}$ collisions with a soft fragmentation function [271], Ali and Ingelman [272] suggested some non-perturbative mechanism for charm production. They assume that virtual quarks with a mass larger than the threshold for the production of flavour f can hadronise in particles containing f-quarks. The discussion indicates that charm production from the non-leading system may serve as a tool for exploring the masses involved during the development of jets.

10.2.5. Short range compensation scheme

The increased statistics and the progress in experimental techniques of identifying particle types will allow one to study the compensation mechanism with considerably higher accuracy. In addition to the correlations of two particles larger sequences of particle production will be accessible through three or even more subsequently produced particles $(q_1\bar{q}_2) + (q_2\bar{q}_3) + (q_3\bar{q}_4)$ $(\cdots + (q_4\bar{q}_5))$. The new scope of such an analysis is that the time structure of their production is much better defined than for two particle correlations. The ordering of two particles defines the order of the third (and fourth) one. Assume a unique relation between rank and rapidity and three particles with the same type of flavour f: $f_1, \bar{f}_2, f_3$ at rapidity values y_1, y_2, y_3. Here the quantum numbers of particles one and three are supposed to be positive and of two negative. If these three particles are subsequently produced and $y_1 > y_2$ then $y_2 > y_3$. In the standard fragmentation chain (e.g. string model) $y_3 > y_1$ is not allowed. In reality these relations are washed out since the relation between rank and rapidity is not strict.

An analysis of the production of two pairs with related quantum numbers therefore allows one to examine how such an ordering of hadron production persists with increasing distance. Distortions of such an order could be cluster decays in which the orientation is lost, the existence of subsystems (e.g. several strings) that are close together in phase space, etc.

Even if particles are not subsequently produced (which will anyhow be extremely difficult to establish experimentally in most cases), the analysis of two pairs with the same type of compensating quantum numbers is rewarding. For such an analysis, however, it is important to make sure that one does not mix hadrons from different pairs which may destroy the ordering. Rather the particles considered should belong to the same pairs. To achieve this it is preferable to analyse particles of quantum numbers that are rarely produced. A first glimpse of $BB/\bar{B}\bar{B}$ pairs has been presented by the TPC group [254] (see section 8.3).

As was pointed out before, if two baryon/antibaryon pairs are produced within one string, the baryon and antibaryon can only be produced if their difference in rank is odd, between a baryon and another baryon only if it is even. This indicator offers in principle a tool for investigating models of particle production as the popcorn model (cf. section 4.3) or the number of fragmenting subsystems. Simulation studies, however, suggest that the ordering of two $B\bar{B}$ pairs is rather strongly distorted. It requires a lot of statistics for sensitive tests.

Other problems that can be addressed are related to the correlated production of quark pairs. It is important for the understanding of baryon production to find which kinds of baryons are frequently produced close together and if indeed correlations of a diquark content can be found.

10.2.6. *Fragmentation function for different particle species*

As discussed in section 4 it is generally assumed that the fragmentation functions of different particle species are about the same. Other prescriptions like the symmetric LUND fragmentation function (2.2.5) or the mass dependence of the $V/(P+V)$ ratio (4.2.1) exist. The precision available at the Z^0 may allow one to check these assumptions in some detail.

10.2.7. *Gluon fragmentation*

The properties of gluon jets and their impact on the particle and energy flow in hadronic events have contributed to our knowledge about hadronisation in a very special way (sections 5.2, 6.2, 9.3). The details of gluon jets and how they differ from quark jets are, however, still uncertain.

At the high energies of the future the gluon jets will be better separated even if they are emitted under only moderate angle with respect to the quark jets. Their inclusive properties, their fragmentation function and their particle content can therefore be measured with much improved accuracy.

If it is not too massive the toponium system may be used as a source of gluon jets. Neglecting for a moment the problem of how to separate the decay $\Theta(1S)\rightarrow ggg$ from the increasing portion of competing decay modes and the reduced signal to background ratio, they will allow one to check several open problems like baryon production in gluon jets and to study the particle and energy flow between jets. The LUND group expects the relative enhancement of baryon production to decrease with the mass of onium states. This is not true in the model of Field (cf. section 5.2).

11. From jets to partons

With the new accelerators coming into operation during the 1990's, smaller regions of space–time will be explored, new symmetries and deeper levels of matter will be searched for. In this Q^2 regime partons act asymptotically free, the strength of the confining force of the colour field is negligible. These free partons are the relevant entities for the analysis. The physics aims at these Q^2 require to reverse the approach towards jets. The focus is not any more on how a parton converts into hadrons, but on how to extract the properties of the primary partons from jets. What has to be determined from the measurements of the final particles are the energy, momentum and flavour of the interacting quarks and gluons.

To clarify the aims and problems one can consider the process $e^+e^-\rightarrow W^+W^-$ (see e.g. ref. [273]). To measure the mass of the W-boson one has to reconstruct its invariant mass by combining jets. To study their production mechanism the direction of the W's has to be known. To determine the couplings of quarks to W-bosons the flavour of the primary quarks has to be tagged. Experimenters will be confronted with similar tasks for detecting the Higgs particle, studying supersymmetric particles or other expected or unexpected phenomena at high energies.

The problems involved in determining parton properties from the jet structure will be discussed in this section.

11.1. *The reconstruction of direction and energy*

The quality of reconstructing jet energies is determined by two effects. One is purely due to imperfections of the measuring devices: the response of the various detector components to the individual particles distorts the reconstruction of jets. The other one is related to the structure of jets: since these are extended objects, their particles scatter around and may mix with those from other jets. The ability to properly associate particles to jets limits the accuracy of determining their properties.

11.1.1. The detector response to jets

The detector devices for measuring the jet properties can be divided into (a) charged particle detector, (b) electromagnetic calorimetry, (c) hadronic calorimetry, (d) muon chambers.

These devices are sensitive to different, though partly overlapping types of particles in an event. The average fraction of energy in hadronic events from e^+e^- annihilations carried by these different types of particles has been given in section 4.6. More relevant for the quality of the measurement are the event to event fluctuations of these different components. In fig. 11.1.1 the results of a simulation of e^+e^- events at $W = 100$ GeV are displayed. Plotted is the total fractional energy of the charged hadronic, the electromagnetic and the neutral hadronic component. Each component is normalized.

These graphs show substantial fluctuations of the various components. In particular they underline the need for the measurement of the neutral hadronic component for a complete determination of the energy. For a reasonably accurate measurement of the jet energy it is therefore necessary to be sensitive to each component. To avoid systematic problems and degradations of the resolution one has to measure the various components in the same way. These fluctuations are one reason for the need for compensating calorimetry (i.e. to have the same calorimetric response for the electromagnetic and hadronic energy) [274] to obtain the best possible resolution. As for the average values, the width of these distributions does not change with the energy of the jet, a result due to the approximate scaling behaviour of the fragmentation function. The components differ substantially for different flavours, e.g.

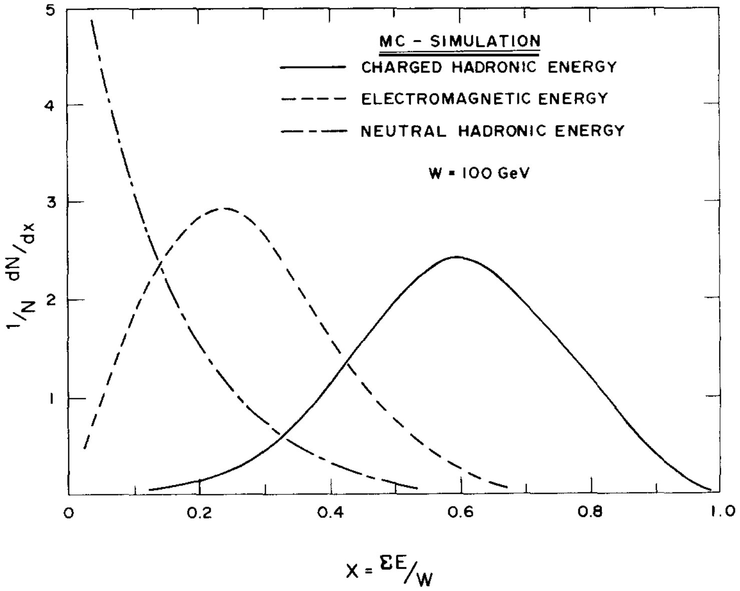

Fig. 11.1.1. Fluctuations of the various components contributing to a jet in terms of their scaled energy. Each component is normalised (Monte Carlo simulation).

the charged hadronic energy is ~15% higher for u- than for b-events. The neutral hadronic energy is in particular large for strange events.

These arguments strongly suggest the need for a full calorimetric measurement for a determination of jet energies. Its relevance for a complete reconstruction of energies, however, depends on the type of collisions analysed. The particular advantage of e^+e^- annihilations is the precise knowledge of the initial states. It allows one to reduce the fluctuations of the reconstructed energy even without full calorimetry. In this case the total energy is determined by the machine parameters to the level of 10^{-3} and the c.m. system of the event is known to coincide with the laboratory system. This allows one to apply powerful constraints for the event reconstruction (e.g., see refs. [275, 276]). At least for the charged current reactions in electron–proton collisions and for hard hadron–hadron collisions where the initial parton–parton state has to be inferred from the final products, full calorimetry becomes essential. An illustrative example has been given by Holder in a study for experimentation at the ep-collider HERA [277]. He simulated the quality of reconstructing x and Q^2, the basic parameters for describing lepton–quark interactions, with two types of detectors. The first one consisted of only a track chamber with a momentum resolution $\Delta p/p = 0.003$ and an electromagnetic calorimeter with $\Delta E/E = 0.12/\sqrt{E}$ (fig. a), the second of a hermetic calorimeter with $\Delta E/E = 0.85/\sqrt{E}$ (fig. b). The quality of the measurement in both cases is displayed in fig. 11.1.2. Clearly visible are the significant tails in fig. a which Holder attributes to the loss of K_L^0's and neutrons.

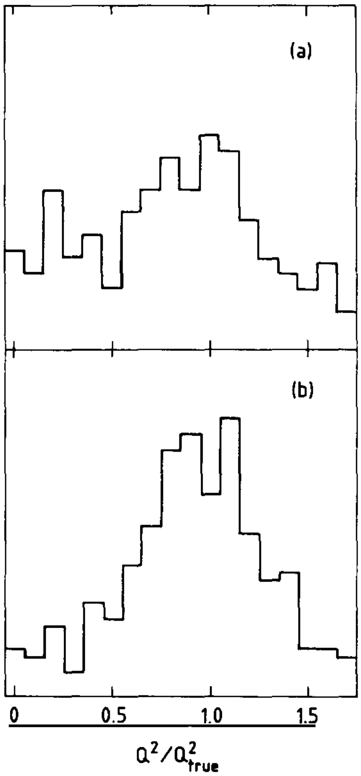

Fig. 11.1.2. Quality of reconstructing Q^2 for charged current events at the in ep-collider at HERA [277] assuming (a) a tracking device with $\Delta p/p = 0.003$ and an electromagnetic calorimeter with $\Delta E/E = 0.12/\sqrt{E}$; (b) a hermetic calorimeter with $\Delta E/E = 0.85/\sqrt{E}$.

For the design of the charged particle detector, for the estimation of possible absorptions in front of the calorimeter, and for the depth of the calorimeter it is important to know how much energy is deposited in low momentum particles. Figure 11.1.3 displays the energy fraction contained in particles of a momentum smaller than p_{cut} as a function of p_{cut}. Here only the charged component is taken into account. The curves for $W = 14$, 22, and 35 GeV are obtained from the measurements discussed in section 3.2, the curves at $W = 60$ and 100 GeV are results of Monte Carlo simulations*⁾. As expected from the approximate scaling behaviour of the fragmentation function the curves have a very similar shape shifted to higher momenta p_{cut} with c.m. energy. The momenta corresponding to the same fraction of energy increase less than linearly with W, implying still a significant energy fraction contained in particles of low momentum: more than 6% of the energy at $W = 100$ GeV is carried by particles of a momentum smaller than 1 GeV.

In contrast to the determination of the jet energy its direction is not strongly distorted by losses of particles. Since the particles are clustering within narrow bundels around the jet axis its direction is well represented by even a small fraction of the hadrons. Due to this property it is possible to reconstruct the jet axes from charged particles alone as has been frequently done at PETRA and PEP. For the reconstruction of the primary parton, say the primary quark produced in e^+e^- collisions, the situation becomes more complicated. Since a parton produced at high Q^2 can decay into several gluons and quarks at rather large angles giving rise to distinct jets, its total energy may be spread out considerably. The limited accuracy of the energy measurement then propagates into an error of the direction of the original parton.

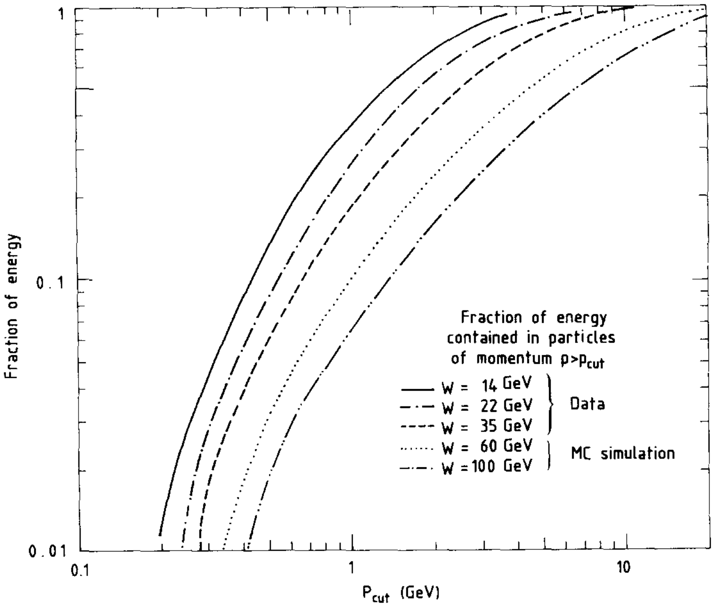

Fig. 11.1.3. Energy fraction contained in particles with $p < p_{\mathrm{cut}}$ for various c.m. energies. Data are used for $14 < W < 35$ GeV, the results for $W = 60$ and 100 GeV are due to Monte Carlo simulations.

---

*⁾ Results for $W = 2$ TeV can be found in ref. [278]. This paper contains several other interesting distributions. In particular the predictions from various different models are compared.

11.1.2. *Effects due to the broadness of jets*

The properties discussed so far are related to the particle content within jets and have to be taken into account in designing appropriate detectors. The quality of the jet measurement is also distorted due to the jet structure itself. There are two apparently contradicting trends displayed in figs. 11.1.4 and 11.1.5.

In fig. 11.1.4 the fraction of particles with at least one neighbouring particle at a relative angle less than α is displayed for various energies. This is the result from simulation studies. The plot shows a nearly linear increase of the fraction at small angles α which can be understood along the lines discussed in section 3.3.2: In the core of an event the transverse momentum distribution is nearly independent of the c.m. energy, whereas the average momentum increases linearly. Thus the opening angle at low α decreases about linearly with W. It is obvious that this trend poses a quite high challenge to the two-particle separation of tracking devices at future high energy accelerators. At large angles only a modest energy dependence can be seen.

In figure 11.1.5 it is shown which fraction of energy is lost if particles are considered only within a cone of half opening angle α around the event axis. Figure 11.1.5a is a reinterpretation of a measurement published in ref. [3]. Figure 11.1.5b is obtained from Monte Carlo simulations at $W=60$, 100 and 200 GeV. To obtain the curves each event was divided into two hemispheres and the average energy deposited in a cone around the event axis determined. This energy was normalized to the total visible energy observed in the hemisphere. These distributions reveal that the opening angle around the event axis has to be large to collect a reasonable fraction of the total energy produced. Both figs. a and b also show that the size of this cone depends only weakly on the c.m. energy W.

The reason for such a behaviour has already been discussed in section 3.3: the energy content at larger angles is dominated by hard gluon emission which varies only slowly with W. Therefore a sizeable fraction of the energy is found at large angles around the event axis.

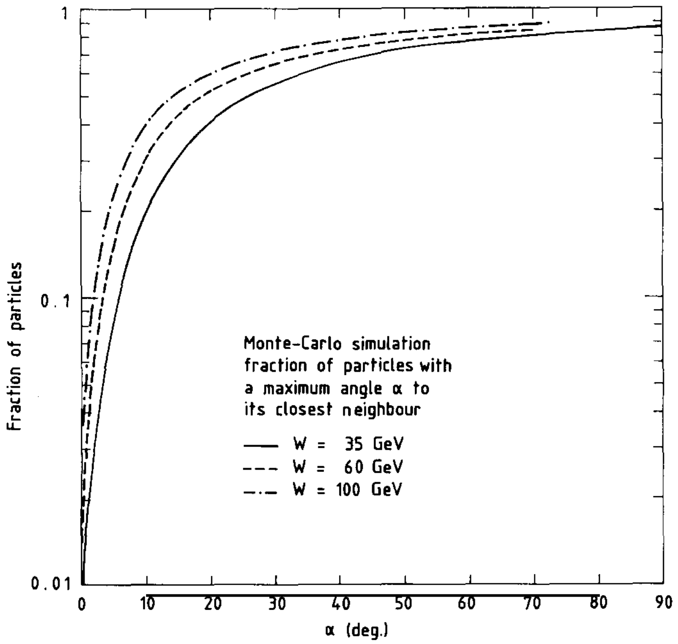

Fig. 11.1.4. Fraction of particles having an angle smaller than α to their nearest neighbour (Monte Carlo simulation).

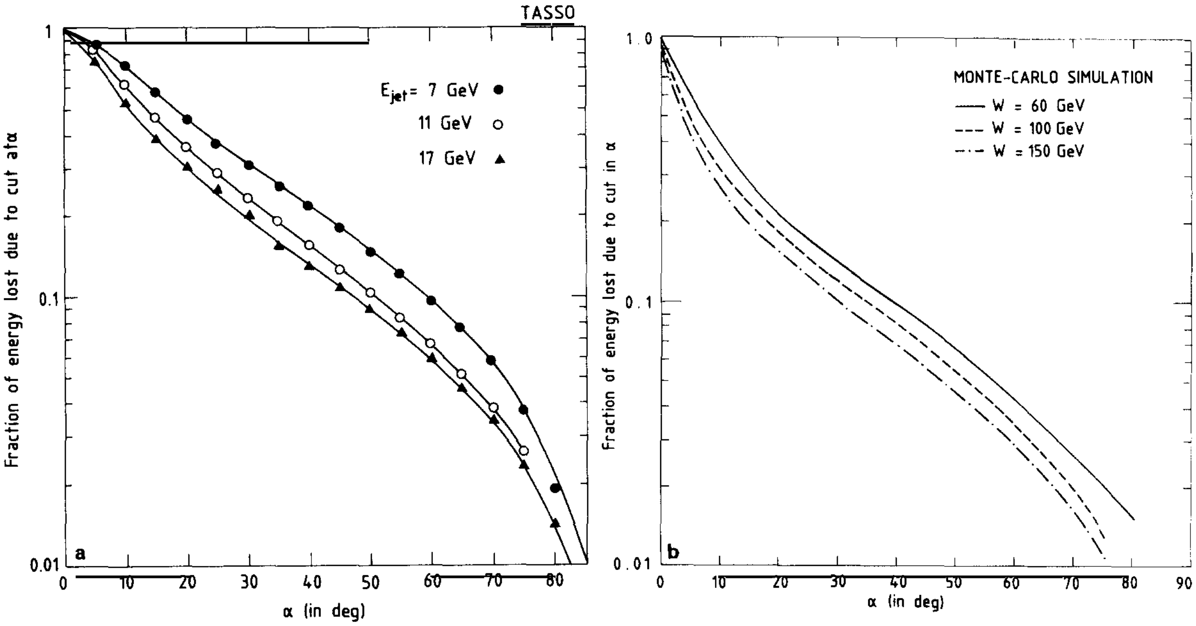

Fig. 11.1.5. Fraction of energy contained outside a cone of half opening angle α around the jet axis. Shown are (a) measurement at PETRA [3]; (b) extrapolation to higher energies using the LUND–Monte Carlo.

The broadness of an event can be expressed by the invariant mass of the particles contained in one event hemisphere. A simulation study for e^+e^--energies of $W = 2\,\mathrm{TeV}$ predicts an average mass of about 200 GeV per hemisphere [279]. The continuous spread of the energy suggested in fig. 11.1.5 is only true for a summation over all events. Since the particles in a jet line up along the direction of the hard partons, most of the energy is contained in relatively small clusters. Although on the average being smeared within a wide cone, it is clustered in decreasingly smaller regions for single events. The average multiplicity at $W = \sqrt{s}$ for jets of mass M_{jet} is given by

$$\langle n_{\mathrm{jet}}(\sqrt{s}, M_{\mathrm{jet}})\rangle \sim N(\sqrt{s})/N(M_{\mathrm{jet}}) \tag{11.1.1}$$

with $N(Q) = \exp[12\sqrt{\ln(Q/\Lambda)/33 - 2N_f)}]$, Λ is the QCD scale parameter and N_f the number of flavours [279]. Thus one expects a stronger logarithmic rise of the average jet multiplicity with energy for a fixed jet mass. It is important to note that for many problems it is the wide spread of energy due to the hard QCD components which limits the precision of an experimental analysis.

The particles (jets) originating from the decay of heavy objects will probably be distributed very similarly to what is shown in fig. 11.1.5. A reconstruction of the properties of the heavy objects requires a correct association of the particles. Potential problems have been discussed in a case study of the reaction $e^+e^- \rightarrow W^+W^- \rightarrow$ hadrons [280]. The production and hadronic decay of pairs of W-bosons was simulated for energies $\sqrt{s} = 200\,\mathrm{GeV}$. Their hadronic decay mode was implemented according to the second order QCD matrix element. The event properties were then analysed on the parton level. The energies and the polar and azimuthal angles θ and ϕ of the partons were smeared according to

$$\frac{\sigma(E)}{E} = \frac{\alpha}{\sqrt{E}}\,, \qquad \sigma(\phi) = \sigma(\theta) = 0.005\,\mathrm{rad}\,,$$

where α was varied between 0 and 1. In a second step it was attempted to reconstruct the W-bosons by combining the jets into two subsets A and B and calculating their invariant mass. The preferred combination in each event was defined by

$$d = \min[(M_A - M_W)^2 + (M_B - M_W)^2] ,$$

where M_A, M_B, and M_W are the masses of combinations A, B and the mass of the W-boson, respectively. The same procedure was applied to a model calculation where the W-bosons were only allowed to decay into two jets, an unrealistic, although frequently used assumption. The probability for misassigning at least one jet to a W is displayed in fig. 11.1.6 for the two models as a function of α. It increases strongly when hard gluon emission is included in W-decays. Its value is substantial (>25%) for realistic detector assumptions ($\alpha \geq 0.5$). It should be noted that the misassignment becomes more severe when particles instead of partons are considered since these are distributed even more isotropically. The same is true for higher jet multiplicities. This simulation study underlines that the reconstruction of events can become considerably complicated due to the broadness of parton fragmentation.

11.2. The flavour of the primary parton

In addition to the energies and momenta of the primary partons their quantum numbers are required for extracting fundamental properties of some processes. As discussed in sections 5 and 7, only the hadrons containing the first quarks reveal the original flavour, whereas the fragmentation of the residual

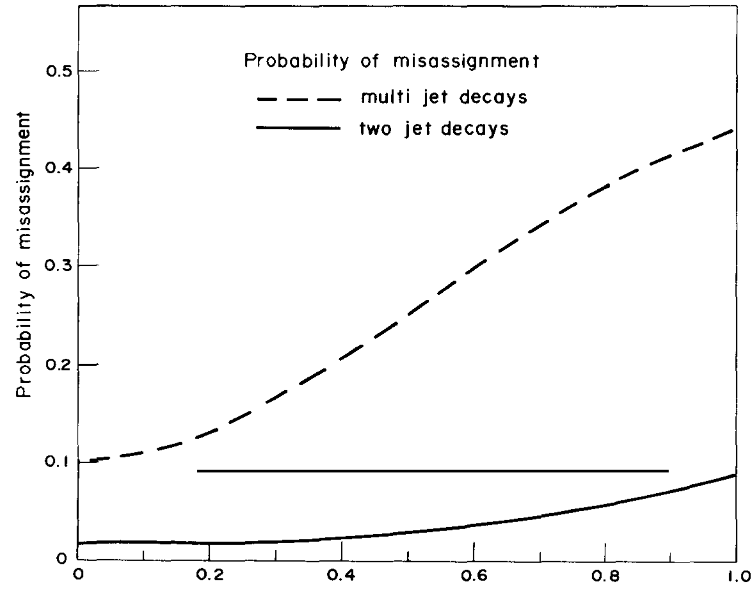

Fig. 11.1.6. Monte Carlo results for the probability of misassigning at least one jet to a W in the process $e^+e^- \rightarrow W^+W^- \rightarrow$ hadrons [280]. For the full line each W was assumed to decay into two jets, for the dashed line multijet decays were allowed. The parameter α denotes the energy resolution assumed: $\sigma(E)/E = \alpha/\sqrt{E}$.

system bears no footprints from the primary partons. The long range flavour correlation presented in section 8 indicated that the fraction of these first rank particles is especially high at large rapidity or x-values.

Before summarizing the potentials for identifying a certain flavour, the less challenging problem of determining the direction of the charge flow in an event will be discussed. The aim is to identify into which event hemisphere the negative (or positive) quark has been scattered. Such a tool is useful for problems involving charge asymmetry (e.g. [263]) and adds important information when combined with other methods, e.g. to tag light flavours (see discussion below).

In section 8 the use of the weighted jet charge [56]

$$Q_A = \sum q_i x_i^{\alpha} \tag{11.2.1}$$

was introduced as one method of finding evidence for charge correlations. Here the sum refers to all particles in a hemisphere with respect to the event axis. As was already proposed by Field and Feynman, the weighted charge can be used for determining the charge direction inside an event. A way to exploit the full information contained in both jets A and B is to calculate

$$Q = Q_A - Q_B\,. \tag{11.2.2}$$

The sign of Q should coincide with the sign of the charge of the primary quark scattered into hemisphere A.

The probability of assigning the correct charge direction to an event has to be found from simulation studies. Since the data and the results from the simulation agree, the values obtained should be believable. The highest probability of ~70% is expected for α between 0.5 and 0.75, a value at which also the maximum charge correlation has been observed in the data (cf. fig. 8.1.2). The probability can be increased to values of more than 80% by selecting events with a larger total weighted charge $|Q| > Q_{\mathrm{cut}}$ at the price of a lower efficiency. It should be noted that the distribution of Q depends significantly on the flavour of the primary particle. This implies different probabilities for the various flavours. In addition the fraction of events of a certain flavour is changed by a cut in Q. Whereas both the probability and the efficiency can be quite high for u-quarks, they are considerably less for the light charge-$\frac{1}{3}$ quarks and even more so for the heavy quarks since their original charge is smeared through the decays. Thus a reasonably efficient method for identifying the direction of the charge exists, but since its efficiencies and reliabilities are different for various flavours it is subject to substantial systematic problems limiting the applicability of the method.

Variations of these methods exist, e.g. the MAC collaboration [281] used the rapidity y instead of the scaled momentum defining the weighted jet charge

$$Q_{\mathrm{jet}} = \sum q_i y_i^{\kappa}\,. \tag{11.2.3}$$

For their analysis they only selected events with different signs of the charges of the two jets and chose $\kappa = 0.2$.

The identification of a special flavour requires that we proceed one step further and search for footprints of the first particle. As already discussed in section 5 these can be

- special topological features like a particle with a high momentum fraction x for the light quarks or a broad event for the bottom particle,

- detection of the first produced particle like a D* for charm jets,
- tagging of a special property like high p_T leptons or long lifetimes,
- or a combination of these methods.

In how far these tagging possibilities can be applied, depends on the quality of the measurement, the purity and efficiency required, the possible bias introduced by the tagging method, and the kind of parton to be selected.

One should note that these tagging methods introduce some bias. For example, the respective semileptonic decay fractions and life times of neutral and charged bottom particles may be different, similar to what has been seen for the D^0 and the D^+ [282]. These biases may be relevant for some kinds of analysis and it is always important to estimate their impact on the results.

There exist basic differences in tagging light and heavy flavours. Since charm and bottom quarks do not contribute to the sea, the detection of a heavy quark immediately indicates that the event originates from a charm or bottom quark. Light flavours, however, appear at all stages of the jet development. Thus it is much more complicated to identify which of the produced particles reflects the quantum numbers of the primary parton. In addition the fragmentation function of light quarks is soft, smearing out the correlation between rank and momentum.

The methods applied at PETRA and PEP will be summarized in the following paragraphs for each of the flavours together with some outlook towards higher energies.

11.2.1. Bottom quarks

Bottom hadrons have rather unique features which help their identification. The methods applied can be divided into separating the products of bottom decays and a search for their footprints in the total event structure. As already discussed in sections 4.5 and 5.1.1, the method most frequently applied for tagging bottom quarks is to identify a lepton of high transverse momentum. Since prompt leptons are strongly suppressed in the normal fragmentation scheme and the p_T spectrum of leptons from bottom decays extends to quite high values, leptons of a high momentum and high p_T with respect to the jet axis provide a unique signature of bottom particles. An example of a measured p_T spectrum of muons with its various contributions as estimated from a Monte Carlo study is shown in fig. 11.2.1 (from ref. [117]). The impurities in the data samples collected are either due to charm decays or to experimental imperfections like background from punch through, kaon decays, etc. In combination with QCD effects these sources contribute to particles of high p_T. The efficiency of the selection is strongly correlated to the purity required. For purities of ~80%, the typical detection efficiency achieved of this method is ~2.5% [200].

The rather long lifetime of ~1 ps (picosecond) of the bottom quark suggests the use of the advancing technology for reconstructing secondary vertices for tagging. As has been discussed in ref. [283], high precision vertex detectors can identify tracks with high probability that do not originate from the interaction point of the event. Combining this information with the special features of bottom hadrons such as their heavy mass and high decay multiplicity, efficiencies for bottom tagging are estimated to reach up to 40% with a purity of almost 100%. This method seems very promising for future experiments.

The explicit reconstruction of bottom hadrons is expected to be less efficient (however, see ref. [284]). The low branching ratios of exclusive two-body decays of the bottom hadrons and their high decay multiplicities lead to a large combinatorial background that seems to be forbidding.

The special topology of bottom jets discussed in section 5.1.1 is suggestive for applying topological

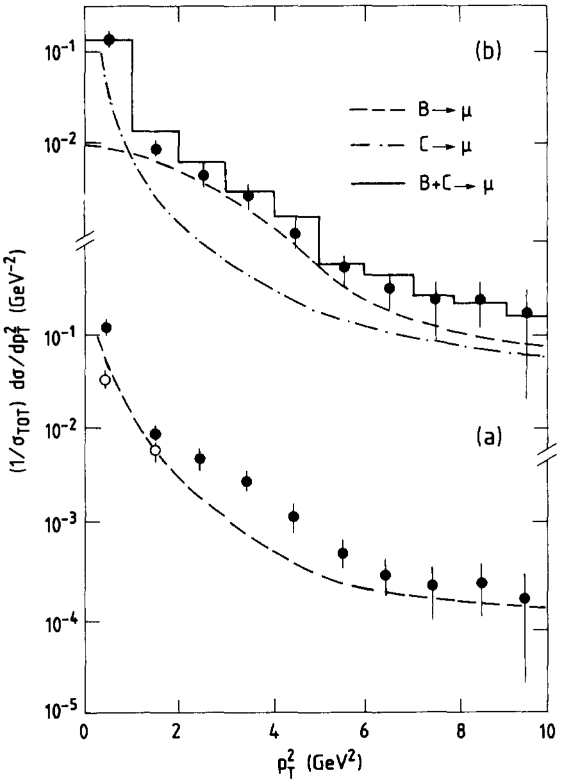

Fig. 11.2.1. Measured prompt μ-yield as a function of p_T^2 and its comparison to Monte Carlo results [117]. Total sample: solid line; contributions from bottom decays: dashed line; from charm decay products: dotted line.

methods to select bottom events. As was pointed out in section 5.1, it is in particular the high particle density from b-decays and the high p_T of its descendants that can be exploited for tagging purposes.

Marshall [285] studied the power of several variables like thrust, or M_{jet}, i.e. the invariant mass, calculated from all particles observed in one hemisphere, for tagging purposes at $W = 35$ GeV. He found that $\Sigma\, E_T^{\text{out}}$, the sum over the transverse component of particles out of the event plane, is the most discriminative one. This variable is sensitive to the high p_T's of the particle from bottom decays and in addition allows one to separate against events with hard gluon bremsstrahlung since the large p_T components of these events are confined in the event plane. The tagging efficiency can be improved by combining observables. This can be done by assigning to some event property a probability to originate from a certain flavour. The joint probability of several, if possible uncorrelated, variables then reveals a more complete picture of the kind of jet considered. This method was applied by the JADE collaboration for a determination of the forward–backward asymmetry of bottom quarks due to the electroweak interference [286]. For each event they determined the transverse mass, the transverse component of a tagged muon, and the transverse missing momentum and assigned corresponding probabilities of originating from a bottom quark. From these individual probabilities they then attributed a joint one to the event. With this rather complete exploitation of event features they succeeded in getting a result of very small statistical and systematical errors.

Another method takes advantage of the high density of particles from bottom decays in some rapidity interval and has been applied by the TASSO collaboration for determining the bottom lifetime [287]. They divided each event into two hemispheres with respect to the event axis. Then all particles were boosted with some Lorentz factor β which was optimized for $W = 34$ GeV ($\beta = 0.7$). Within each hemisphere the sphericities S_1 and S_2 were calculated and events selected by requiring

$$S_1 S_2 > S_{\mathrm{cut}} . \tag{11.2.4}$$

Here S_{cut} too is an optimized quantity. With this method the purity could be increased by a factor 3 compared to the total event mixture thereby reducing the efficiency for bottom events by only about 50%. The basic idea behind this method is to transform the laboratory system S into the rest-system S′ of the bottom quark. For light quarks this boost increases the momentum of most particles. Since the transverse momentum does not change

$$S_{\mathrm{uds}} = \frac{3}{2} \frac{\Sigma p_{\mathrm{T}}^2}{\Sigma p^2} \rightarrow S'_{\mathrm{uds}} = \frac{3}{2} \frac{\Sigma p_{\mathrm{T}}^2}{\Sigma p'^2} < S_{\mathrm{uds}} .$$

In contrast bottom decay products are transformed into their rest-system and therefore their momentum p is reduced. Thus

$$S_{\mathrm{b}} = \frac{3}{2} \frac{\Sigma p_{\mathrm{T}}^2}{\Sigma p^2} \rightarrow S'_{\mathrm{b}} = \frac{3}{2} \frac{\Sigma p_{\mathrm{T}}^2}{\Sigma p'^2} > S_{\mathrm{b}} .$$

This method is efficient because of the very sharp fragmentation function of bottom hadrons causing only a moderate spread of the γ-factor of the bottom quarks.

The chance for tagging bottom events at c.m. energies around the Z^0 mass improves due to its higher production fraction. Whereas they contribute only about 10% of all hadronic events at $W \sim 35$ GeV, this fraction rises to more than 20% at $W \sim M_{Z^0}$. In particular the ratio with respect to the strongly competing $c\bar{c}$ production becomes more favourable changing from 1 : 4 to better than 1 : 1. On the other hand many topological features making b-events unique at lower energies, are smeared out. For example, due to the higher-jet multiplicities at these energies the jet masses or the transverse component out of the plane cease to be good indicators.

How strongly the topological features of bottom events are influenced by QCD effects can be seen from fig. 11.2.2. Here the rapidity distribution of bottom events is plotted using the second order QCD Monte Carlo of the LUND group (dashed–dotted curve) and their shower formalism (full curve). As can be seen, the enhancement around

$$\langle y \rangle \sim \ln(2\langle x_{\mathrm{b}} \rangle E_{\mathrm{beam}}/m_{\mathrm{b}})$$

comes out quite differently in the two approaches. Despite being at about the same value of rapidity and having the same width, it is much more pronounced in the second order formalism, whereas hardly visible in the case of the shower algorithm. This is evidently due to a much larger fraction of rather soft hadrons in the region of $0 < y < 2$. Note the dramatic difference in the height of the plateau in the two approaches. This indicates that the efficiency and reliability of any topological method depends heavily

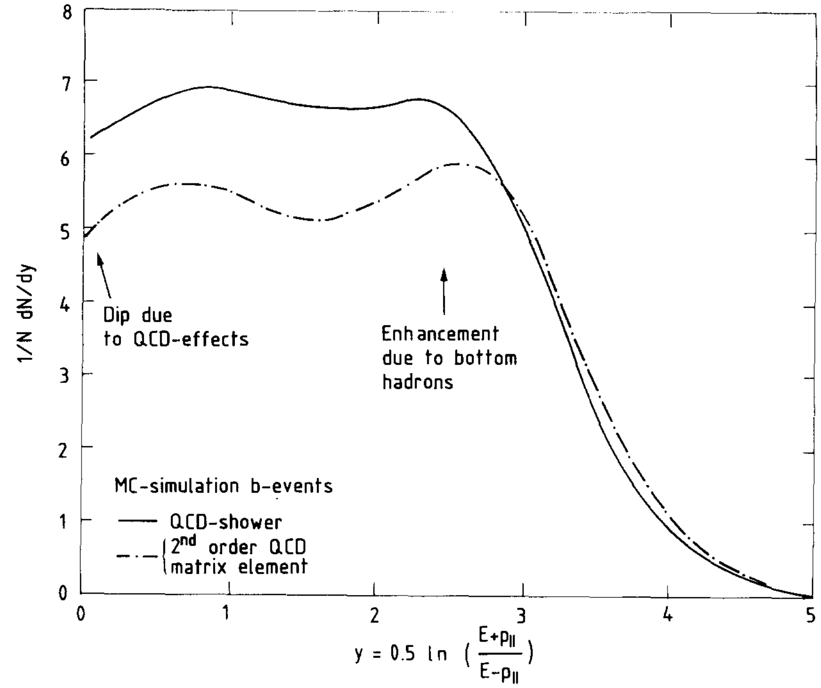

Fig. 11.2.2. Rapidity distribution in bottom events at $W = 100$ GeV as predicted by the LUND-Monte Carlo. The full line is due to a QCD showering program, the dashed-dotted line to the $O(\alpha_s)$ algorithm.

on the actual fragmentation. In view of the superior description of the hadronic data around 30–40 GeV with the shower approach (cf. section 9), it seems to be difficult to develop an effective topological tag of bottom events at $W \geq 100$ GeV. This can be expressed using a simple method for tagging bottom events. A weight

$$W = \sum w_i = \sum \exp - [(y_i - y_b)^2/(2\sigma_b^2)] \tag{11.2.5}$$

was attributed to each event. Here y_0 is the average rapidity of the b-hadrons, y_i the rapidity of each particle in the event, σ_b is the width of the rapidity distribution of the b-decay products. With $y_b = 2.6$ and $\sigma_b = 1$ a purity of ~40%, i.e., a doubling of the purity in the total sample, corresponds to an efficiency of ~50% in the second order approach. In the QCD shower algorithm the corresponding efficiency for the same purity is 2%. The high particle density in the decay of heavy quarks has also been analysed in ref. [288] for t-quark production.

11.2.2. Charm quarks

In principle many of the features that are promising for the tagging of bottom quarks like their semileptonic decay, long lifetime, or enhancement in the rapidity should also be applicable for selecting charm events. However, since these properties are less pronounced in charm decays and jets, they do not provide the most efficient tagging methods.

Breakstone et al. [283] have analysed the possibility of using the finite lifetime of charmed particles for tagging. Monte Carlo studies suggest a reliability of at most 50% for finding charm events inclusively.

The transverse momentum spectrum of prompt leptons extends up to $p_T \sim 1$ GeV. In this region particles from the standard fragmentation contribute significantly and the background e.g. from Dalitz decays, K and π-decays or experimental imperfections is much higher than that for bottom decays. In addition the leptons from the cascade transition $b \to c \to \ell$ contribute in this region. The signal from charm decays may be improved by selecting particles with higher longitudinal momentum, however, the enrichment and efficiencies obtained are marginal (cf. section 5.1.2).

Also topological methods do not seem very promising. As discussed in section 5.1.2 the properties of charm jets are very similar to those of average jets and can hardly be used to increase the purity of charm events.

Charm jets of highest purity can be selected by explicitly reconstructing charmed particles. In contrast to bottom hadrons charmed particles have only a moderate decay multiplicity and larger branching fractions for two-body decays. Combinatorial background can be reduced by requiring a hard fragmentation function. As discussed in section 4.5.2 several kinds of charmed hadrons have been identified within jets at $W \sim 30$ GeV. In particular the favourable hadronic decay $D^{*,\pm} \to \pi^\pm D^0 \sim m_\pi$ is an efficient tag for charmed events. The difference $\Delta m = m(D^*) - m(D^0)$ is small and provides a rather unique signal of charm production at least at high x-values. Potential background for charm jets is due to bottom-, and at higher energies possibly gluon jets (see section 10), charmed particles from these sources, however, have smaller momenta.

11.2.3. Light uds quarks

The relative ease of tagging heavy quarks is due to two of their special properties: the decay properties of charmed and bottom hadrons make them stand out and no heavy quarks are produced in the sea. Particles from u, d, or s-quarks are different: they can be found everywhere in the jet. In addition their fragmentation function is soft, causing the higher rank hadrons to frequently have a higher momentum than those from the first rank.

As already discussed before, the mixture of u, d and s-events exhibits features that are special compared to events from heavy quarks. This has been used by the HRS collaboration [205]. They tagged a mixture of u, d and s-quarks by requiring a high x-particle in the event and obtained a purity of 89% for an efficiency of 1.4% (see section 5.1.3). However, as already stated before, to have a mixture instead of a pure sample limits the possible applications.

Selecting events of a special type of light flavour is more troublesome. The identification of first rank hadrons requires them to be distinct from particles produced in the residual fragmentation. The probability of originating from the primary quark has to be significantly higher than its production from sea-products. This singles out diquarks and strange quarks as potential tools for flavour tagging since they are relatively suppressed in the vacuum.

One method for tagging u and s events at least at the Z^0 has been suggested by Dittmar [289]. Similarly to the HRS analysis he selects events with one particle, the "trigger particle" having a high momentum of $x > 0.6$. In addition, this particle is required to be a proton or a kaon. This enriches up and strange quark events.

Since protons are made out of two u and one d-quark, they have an increased probability or originating from u-quark jets. The enrichment becomes even stronger due to symmetry constraints of the proton wave function. A proton can be formed either by a u-quark and a spin-0 diquark (ud) or a d-quark and a spin-1 diquark (uu). Since spin-1 diquarks are suppressed and diquarks are not primary partons, a first rank proton stems with a high probability from a primary u-quark.

A similar argument is true for kaons. For the almost equal production rates of primary $\bar{s}$ and u quarks at the Z^0, the ratio of the probabilities that a charged kaon originates from a primary s-quark picking up a u-quark and that it is due to a primary u-quark picking up an $\bar{s}$-quark is given by the ratio of the quark content in the sea. Measurements indicate a ratio $p_s/p_u \sim 1/3$ (cf. section 4.2) and thus s-quark jets are enriched by tagging the first rank kaon. Note that this good signal to background ratio is closely related to the similar production rate for the different quark species at the Z^0. This ceases to be true for the QED continuum and the reliability depends therefore on the c.m. energy.

To further suppress the contribution from kaons and protons originating from higher ranks in the fragmentation chain, it was required that the weighted charge $Q_J = \Sigma\, e_i \cdot x^{0.5}$ (cf. sections 8.1, 11.2) of the opposite hemisphere has a sign opposite to the charge of the trigger particle. Simulation studies using the LUND program predict an efficiency of ~3% for s-quarks and ~1% for u-quarks for a reliability of ~80% and close to 100%, respectively. Detector efficiencies for identifying hadrons were folded into the simulation*⁾.

No other reliable method has been proposed for u-quarks. It should be noted that the equivalent method for d-quarks would require identification of neutrons in a jet, which is beyond the experimental capabilities.

Other schemes for tagging strange quarks require the identification of two high momentum strange particles in opposite hemispheres. In ref. [290] the expected high efficiency and purity of particle identification in Ring Imaging Čerenkov counters is exploited to select events in which the highest momentum kaons in the two event hemispheres have opposite charge. Strange events can also be selected by requiring a ϕ-meson at high x-values**⁾. The ϕ is a good indicator since it can only originate from s-quarks, in contrast to a charged kaon which has a considerable chance of originating from a u-quark. In addition the production rate for ϕ's in the subsequent fragmentation is only small $\propto p_s^2$, which has again to be compared with the charged kaon rate $\propto p_u p_s$, being three times as high (here p_s, p_u are the probabilities for picking an s- or u-quark out of the sea). As can be seen from fig. 11.2.3 reproducing the results of a simulation study with the LUND program, an efficiency of ~6% can be reached for a purity of 80% by selecting ϕ's with $x_\phi > 0.5$. Background or two-particle separation specific to certain detectors have not been taken into account and these numbers will deteriorate.

Thus the tagging of a special kind of light flavour is a rather involved task which requires very good hadron identification. Efficiencies of ~1% for u-quarks and more for s-quarks can be reached. The tagging of s-quarks profits from the democratic production cross sections at the Z^0. Its reduced rate for pure γ-exchange makes s-tagging even more difficult.

11.2.4. Gluon jets

Properties of gluon jets have so far been determined either from processes like $\Upsilon(1S) \rightarrow ggg$, gluon scattering in pp collisions, or rather indirectly for three-jet events in the e^+e^- continuum. In the latter a certain probability to originate from a gluon was assigned to each jet according to the QCD matrix element. It allows only a rather low purity and implies considerable systematic errors. The measurements indicate that the differences between quark and gluon jets are small. Neither the differences in the fragmentation functions nor those in the particle content seem to be prominent enough for using them as a gluon tag.

---

*⁾ For his analysis Dittmar assumed the particle identification capability of the OPAL detector coming into operation at LEP. The particle kind is obtained through the measurement of the energy loss with $\sigma(dE/dx)/(dE/dx) = 3.5\%$.

**⁾ I am grateful to A. Shapira for discussions about this point.

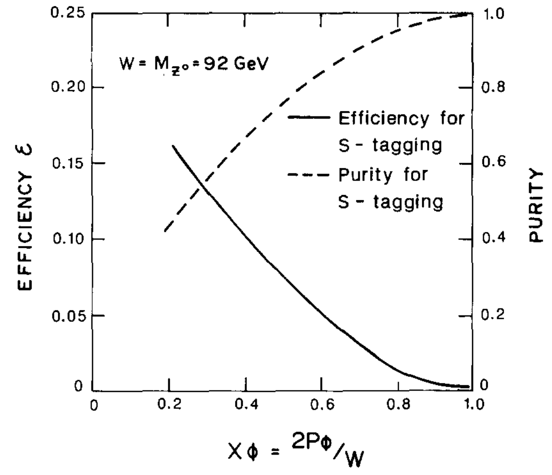

Fig. 11.2.3. Efficiency (solid line) and purity (dashed line) of strange quark tagging using ϕ's as a function of $x_\phi = 2p_\phi/W$ at the Z^0 mass.

Some improvement can be expected at higher energies since the jets will be better separated even for gluon jets of low x_g. For these energies they can be relatively safely identified from the QCD prediction. If charm production in gluon jets becomes sizeable (cf. section 10) at higher c.m. energies, the low x, high p_T charm production can be conceived as a way to identify the gluon jet. However, such a sample is experimentally difficult to select and will be presumably strongly biased.

Gluon jets may also be identified via the quark jets. If in a three-jet event the two jets originating from a quark can be identified, then the assignment of the third one is obvious. Such a procedure has been proposed by Nilles and Streng [291] for $c\bar{c}g$ events. The rate R and efficiency ε, however, are expected to be small, being

$$R = \frac{\sigma_f}{\sigma_{tot}} r\varepsilon_{f_1}\varepsilon_{f_2} \quad \text{and} \quad \varepsilon = \frac{\sigma_f}{\sigma_{tot}} \varepsilon_{f_1}\varepsilon_{f_2} . \tag{11.2.8}$$

Here σ_f is the cross section for the production of a certain flavour f, σ_{tot} the total hadronic cross section, r the fraction of events with a clear, separable third jet ($r \sim 0.1$), and ε_{f_1,f_2} is the efficiency for tagging the flavours of jets 1 and 2 allowing for different requirements for the two jets.

As a result the efficiencies of identifying gluon jets in $c\bar{c}g$ events will be of the order 10^{-3}–10^{-4} of the charm cross section assuming the tagging efficiencies obtained so far (see section 5.1). This fraction may be increased by combining the topological criteria given by the QCD matrix element for hard gluon emission with the identification of only one jet.

11.3. Conclusions

The physics goals at the energy scale of and beyond the standard model require to treat jets as condensates of the primary parton. They are the only experimentally accessible information about the quarks and gluons. Those entities are of real interest since they have been directly produced in the space–time region to be explored and therefore carry the footprints of the possible new symmetries.

Although one would wish to analyse jets just as their leptonic partners electron or muon, their reconstruction is much more complicated. This is mainly because they are extended objects with rather strongly fluctuating consistency. Still, at the high Q^2 to be explored in the next decade, the energy of the parton will be confined in rather narrow cones and experimental devices exist to measure their energy and direction with quite high precision.

The identification of the parton type is much harder. As already found in analysing the data around $W = 30$ GeV, tagging of jets from heavy quarks is possible with efficiencies of typically 2–10% and may be even higher with appropriate experimental devices. The tagging of light jets is less efficient but is possible at least for the mixture of u, d and s quarks. Methods of identifying u and s-quarks separately have been proposed (the latter at least at the Z^0 mass). Their efficiencies are of O(1–3%) with acceptable reliabilities. The tagging of gluon jets will improve compared to the PETRA and PEP energies, but it will still be difficult to obtain a clean high statistics sample. In most of these cases it is not enough to use topological methods alone. Rather it is the detailed particle structure that reveals the parton flavour putting requirements on experimental devices. Lepton identification, a good momentum resolution, vertex detection, and the identification of the hadron type are necessary assets for extracting the maximum information about the primary parton.

12. Conclusion

It is just somewhat more than ten years ago that the first evidence for jets in e^+e^- annihilations has been found. By then it required a detailed statistical analysis to be convinced of their existence. With the higher energies accessible at PETRA and PEP, a detailed picture of jets has emerged both at a fixed energy and as a function of the c.m. energy.

This data flow led to a very good qualitative understanding of jet properties materializing in rather evolved simulation algorithms. The models developed are a mixture of theoretically well founded QCD-calculations and ad hoc parametrisations. The latter reflect our ignorance how to calculate strong interaction processes in a regime where non-perturbative methods are not applicable anymore.

The models have turned out to be a big success and their development into large systems of computer code is a necessary asset for understanding the processes in the hadronisation region. For a fixed c.m. energy they are capable of describing even rather subtle effects. Once an appropriate parametrisation for the fragmentation of a single particle has been found, they reproduce the overall event topology, the relative production yield of the various particle species and the two-particle distributions very well. In doing this they provide means for disentangling the various stages of jet development and allow one to proceed from the mixture of various processes as reflected in the final particles to the immediate dynamics at the parton level.

In general, however, today's conclusions are in many cases only slightly more than qualitative, being hampered both by the uncertainties in the theoretical penetration into the small Q^2-region as well as by the systematic and statistical limitations of the data. There exist many examples of the need for more accurate measurements: the fragmentation functions of different particle species to reveal the mass and spin-dependence of fragmentation, such distribution shedding light on the jet dynamics like short range correlations or the exact structure of non-leading jets. In all these cases measurements of a limited accuracy exist. They are consistent with the most simple expectations, but have enough room for more involved models: All data indicate that particles of compensating flavour are produced at very close space–time points. However, at the moment, for example, they do not reveal if intermediate particles are produced as perceived in some models.

On the other hand only very few attempts have been made for phenomenological or even theoretical considerations of jet dynamics outside of the standard fragmentation models. Exceptions are the extensive discussions about multiplicity distributions, models for baryon production and in particular the effects of coherent gluon emission. These developments have been of great help for the improved understanding of fragmentation, in particular where it has been possible to outline the connection of the measured distributions to the basic theory.

What understanding of jet development have we reached? In the last years lots of data that sharpened our general picture of fragmentation have been contributed. The basic experimental results can be expressed along the following main lines:

(1) Hadrons in jets originate from hard primary quarks and gluons.
(2) Fragmentation proceeds within colour neutral systems and not along individual partons.
(3) Non-perturbative effects become important at virtual masses of ~1 GeV.
(4) Hadronisation proceeds in discrete steps.
(5) The system left over at each step fragments according to its retained mass. It develops like a primarily produced system of the same mass.
(6) The various steps are related by the emission of flavour neutral quanta.
(7) The production yield of hadrons is primarily determined by their parton content, not by the property of the hadron itself.

Most models for fragmentation are constructed along these lines. During the recent years considerable progress has been achieved in finding experimental evidence for these features. The measurements supporting these ideas are listed in table 12.1. No experimental finding digresses from these lines. All of this constitutes a lot of progress, but of course to each of these points further questions can be attached, some of them are mentioned in chapter 10. In general one needs a more quantitative approach to hadronisation, say, instead of finding evidence for short range correlations determine the correlation length.

In that sense the physics of jets is far from being settled. It remains an important field of research that may be able to explore the transition from a region of hard partons to that where the interactions

Table 12.1
Measurements related to basic features of jet development

Feature	experimental evidence	section
primary quarks and gluons	cross section, angular and charge distribution	Introduction
colour neutral system	string effect	6.2
non-perturbative effects	energy dependent, comparison with models	9
discrete steps	hemisphere correlations, structure of non-leading system	7
recursive fragmentation	hemisphere correlations, structure of non-leading system	7
emission of flavour neutral quanta	short range correlations	8
parton production	mass and spin dependent	3.1, 3.3

become really strong such that colour confinement determines the final properties. There exists good hope that with the larger statistics and higher energies available especially at the next generation of e^+e^- colliders, many open questions can be tackled at least from the experimental side.

The focus of the future frontier of experimental high energy physics will be in a space–time region where quarks and gluons interact asymptotically free. To explore it one requires a reconstruction of these partons from jet properties. The broadness and diversity of jets complicates such an analysis. Their particles are distributed in a relatively broad region and those of different jets frequently overlap with one another complicating the association of particles to partons. In general it is relatively straightforward to determine the energy and direction of these asymptotically freely interacting partons. To know their flavour is much more complicated and seems in general only feasible for heavy quarks. It requires not only monitoring the overall energy and particle flow but to obtain more refined informations about the jet structure.

The use of jets as entities has already begun and everything indicates that the problems can be managed with appropriate detectors and with a better knowledge of the hadronisation process.

Acknowledgements

This article grew out of my work as a member of the TASSO collaboration at DESY. I want to thank the whole collaboration for all the interesting and profitable discussions that helped me to penetrate deeper and deeper into the physics of jets. Moreover my gratitude goes to all of those who provided this exciting and fruitful atmosphere at DESY.

I enjoyed the advice and productive criticism of many people during the writing of this review. In particular I want to thank M. Bowler, M. Dittmar, W. Kittel, W. Koch, J. Raab, D. Saxon, T. Sjöstrand, R.K. Sundaresan, G. Tysarczyk and B. Webber for discussions. They did not hesitate to share their knowledge with me.

My special thanks go to E. Lohrmann whose permanent support and encouragement was essential for this endeavour.

Last but not least I profited from the kindness of S.L. Wu. She gave me the opportunity to use the TEX-system on her VAX and thus smoothed my transition from Ottawa to Geneva.

Appendix

A.1. Variables for inclusive particle production

Scaled variables

As discussed in section 3, the particle distribution within jets obeys approximate Feynman scaling, the variables used are

$$x_E = \frac{2E}{W}, \qquad x_p = \frac{2p}{W}, \qquad x_{\|} = \frac{2p_{\|}}{W},$$

where E is the energy, p the momentum and $p_{\|}$ the momentum component parallel to the event axis of some particle, W is the total c.m. energy, $\Sigma x_E = 2$.

These variables are related by

$$x_E = (1/\beta)\, x_p\,, \qquad x_{\parallel} = x_p\sqrt{1 - p_T^2/p^2}\,.$$

They coincide for $\beta \to 1$ and in case of a limited p_T for $p \to \infty$, respectively.

The Lorentz invariant cross section can be expressed in terms of these variables as

$$E\,\frac{d^3\sigma}{dp^3} = \frac{x_E}{\pi}\,\frac{d^3\sigma}{dp_T^2\, dx_{\parallel}}$$

In analogy the transverse component can be scaled as

$$x_T = 2p_T/W\,.$$

Rapidity

The shape of the particle distribution becomes especially simple in terms of the longitudinal rapidity ("rapidity")

$$y = \tfrac{1}{2}\ln\frac{E + p_{\parallel}}{E - p_{\parallel}} = \tfrac{1}{2}\ln\frac{(E + p_{\parallel})^2}{m^2 + p_T^2} = \ln\frac{(E + p_{\parallel})}{m_T}$$

with the transverse mass $m_T^2 = m^2 + p_T^2$. The maximum value of the rapidity for a particle of mass m is given by

$$y_{\max} = \ln\frac{\sqrt{m^2 + (p_{\parallel}^{\max})^2} + p_{\parallel}^{\max}}{m} \sim \ln\frac{W}{m}$$

for $p_{\parallel} \gg m$.

The rapidity has the simple property of being additive under a Lorentz transformation along the event axis

$$y \to y' = y + \tfrac{1}{2}\ln\left(\frac{1 + \beta}{1 - \beta}\right).$$

Therefore the difference between rapidities y_a, y_b of two particles a and b is invariant under a Lorentz boost.

$$\Delta y = y_a - y_b = \Delta y' = y'_a + y'_b\,.$$

Since

$$dp_{\parallel}/E = dy$$

the Lorentz-invariant cross section can be expressed as

$$E\,\frac{\mathrm{d}^3\sigma}{\mathrm{d}p^3} = \frac{\mathrm{d}^3\sigma}{\pi\,\mathrm{d}p_{\mathrm{T}}^2\,\mathrm{d}y}\,.$$

Due to insufficient particle identification the true rapidity is often approximated by the pion rapidity, attributing the pion mass to every particle. Assume a particle of certain momentum p. If the mass m_{A} is assigned to this particle the resulting rapidity is denoted by y_{A}, for a mass m_{B} it is y_{B}. Then

$$y_{\mathrm{A}} = y_{\mathrm{B}} + \ln(m_{\mathrm{B}}/m_{\mathrm{A}})$$

for $y \gg 0$ and $p_{\mathrm{T}} = 0$.

In section 8 quantum number correlations were discussed in terms of the rapidity difference. Its connection to the invariant mass M of a system of two particles of mass m_1 and m_2 is interesting [292]

$$M^2 = m_1^2 + m_2^2 + 2m_{\mathrm{T}_1}m_{\mathrm{T}_2}\cosh(y_1 - y_2) - 2p_{\mathrm{T}_1}p_{\mathrm{T}_2}\cos(\phi_1 - \phi_2)\,.$$

Here $m_{\mathrm{T}} = \sqrt{m^2 + p_{\mathrm{T}}^2}$ and p_{T} the transverse momentum to the event axis. ϕ_i denotes the azimuthal angle.

It is instructive to realize the close connection of the rapidity to the light-cone variable η used in the standard fragmentation schemes [56]. With

$$\eta = \frac{E + p_{\parallel}}{2P_{\mathrm{q}}}\,; \qquad Y_z = -\ln\eta$$

it follows

$$y = -Y_z + \ln(2P_{\mathrm{q}}/m_{\mathrm{T}})\,.$$

A.2. Two-jet variables

To obtain a measure of the jettiness of an event as well as to determine the event axis both linear and quadratic quantities are used. Depending on which momentum component they refer to they are either minimized or maximized. The most frequently used are the thrust and the sphericity variable.

Sphericity

The sphericity [293] is defined as

$$S(\hat{n}) = \min_{\hat{n}} \frac{3}{2}\,\frac{\Sigma\,p_{\mathrm{T}i}^2}{\Sigma\,p_i^2}\,,$$

where the factor $\frac{3}{2}$ scales the upper limit of S to 1. The sphericity axis minimizing the above expression can be found analytically by diagonalizing the tensor

$$I_{\alpha\beta} = \sum_{i=1}^{N} (p_i^2\delta_{\alpha\beta} - p_{i\alpha}p_{i\beta})\,.$$

The value of the sphericity is given in terms of the eigenvalues λ_i as

$$S = \frac{(3/2)\lambda_3}{\lambda_1 + \lambda_2 + \lambda_3} .$$

The convention is to order the λ's according to $\lambda_3 < \lambda_2 < \lambda_1$. The extreme values of S ($S = 0, 1$) correspond to a perfectly jetlike and an isotropic event, respectively. The eigenvector of λ_3 is the sphericity axis. The other eigenvalues and vectors have the following meaning:

(i) $\lambda_2 = \frac{3}{2}\Sigma\,(p_{\mathrm{T}}^{\mathrm{in}})^2/\Sigma\, p^2$ and $\hat{n}_2$ is the momentum component transverse to the sphericity axis in the event plane defined by $\hat{n}_3$ and $\hat{n}_2$.

(ii) $\lambda_3 = \frac{3}{2}\Sigma\,(p_{\mathrm{T}}^{\mathrm{out}})^2/\Sigma\, p^2$ and $\hat{n}_3$ parametrises the component out of the event plane, this component is the smallest of all momentum contributions. It is a measure of how far the event is restricted to a plane. It is therefore referred to as aplanarity A*). For perfectly flat events $A = 0$.

The information of the sphericity tensor can be fully exploited by correlating two of the three eigenvalues. A convenient way is to plot A versus S. The two variables are limited by $A < \frac{1}{2}S$, the particle density is therefore expressed within a triangle as shown in fig. 3.4.5. The regions characteristic for special types of events are indicated.

Since the sphericity is quadratic in p_{T} and p, its value is different if an event is considered at the level of partons, prompt particles or final particles. This complicates comparing measurements to theoretical predictions which are mostly calculated on the parton level. Since the sphericity changes with the splitting of one parton into (several) soft ones, it is considered as being not "infrared safe".

Another less frequently used variable obtained by minimizing the transverse momentum component is the spherocity [294]

$$S'(\hat{n}) = \min_{\hat{n}} \left(\frac{4U}{\pi}\right)^2 \left[\sum_{i=1}^{N} |p_{i\mathrm{T}}|\right]^2 .$$

As discussed by Brandt and Dahmen [295] the spherocity variable exhibits instabilities against the relative angles and the axis determined with S' does not always coincide with the intuitively preferred direction.

Thrust

Instead of searching for an axis along which the transverse momentum is minimized, one can also look for a maximum of the parallel component. This is the basis for the second popular jet measure, thrust [296, 297]

$$T(\hat{n}_1) = \max_{\hat{n}_1} \frac{\Sigma\, \boldsymbol{p}_i \cdot \hat{\boldsymbol{n}}_1}{\Sigma\, p_i} .$$

This quantity is linear in momentum and thus does not depend on what stage of the jet development it is determined, it is "infrared safe". This renders the thrust distribution in particular useful when comparing data to theoretical predictions.

The disadvantage is that its determination requires an iterative procedure with the number of steps increasing with particle multiplicity N as $\sim 2^N$.

---

*) Note that in section 9.4 another way of parametrising the component out of the event plane has been used (acoplanarity).

The concept of thrust can subsequently be applied to find the event plane: the vector $\hat{\boldsymbol{n}}_2$ orthogonal to $\hat{\boldsymbol{n}}_1$, spanning the plane of the event, is determined by calculating the thrust of the transverse momenta with respect to $\hat{\boldsymbol{n}}_1$. With $\hat{\boldsymbol{n}}_3 = \hat{\boldsymbol{n}}_1 \times \hat{\boldsymbol{n}}_2$ one obtains the three components analogous to those from the sphericity tensor. Note, however, that in contrast to the sphericity they have to be calculated in separate steps. The quantities corresponding to $p_{\mathrm{T}}^{\mathrm{in}}$ and $p_{\mathrm{T}}^{\mathrm{out}}$ are then

$$M_1 = \frac{\cancel{\Sigma\, \boldsymbol{p} \cdot \hat{\boldsymbol{n}}_2}}{\Sigma\, |p|}\ ; \qquad M_2 = \frac{\Sigma\, \boldsymbol{p} \cdot \hat{\boldsymbol{n}}_3}{\Sigma\, |p|}$$

and sometimes referred to as "major" and "minor". The quantity

$$O = M_1 - M_2$$

is called oblateness [298].

A.3. Three-jet measures

The sphericity and thrust concept can be generalized in a rather straightforward manner to three-jet events by defining three non-overlapping partitioned sets of particles C_1, C_2, C_3.

In the case of the generalized sphericity [299], one finds axes $\hat{\boldsymbol{m}}_1$, $\hat{\boldsymbol{m}}_2$ and $\hat{\boldsymbol{m}}_3$ and requires

$$\sum_{\mathrm{C}_1} (\boldsymbol{p}_j \times \hat{\boldsymbol{m}}_1)^2 + \sum_{\mathrm{C}_2} (\boldsymbol{p}_j \times \hat{\boldsymbol{m}}_2)^2 + \sum_{\mathrm{C}_3} (\boldsymbol{p}_j \times \hat{\boldsymbol{m}}_3)^2$$

to be at its minimum. To ease the finding of the sets C_i and axes $\hat{\boldsymbol{m}}_i$ fulfilling this requirement, the normal to the event plane determined by $\hat{\boldsymbol{m}}_1$, $\hat{\boldsymbol{m}}_2$ and $\hat{\boldsymbol{m}}_3$ is assumed to coincide with $\hat{\boldsymbol{n}}_1$ of the sphericity tensor. This reduces the task of sorting the particles since it becomes a planar problem which can be relatively easily solved. The three-jettiness is then defined as

$$J_3 = \frac{1}{N-3} \sum \left\{ \frac{\Sigma\, (\boldsymbol{p}_j \times \hat{\boldsymbol{m}}_\tau)^2}{\Delta_\tau^2} \right\}.$$

Here $\Delta_\tau^2 = \frac{1}{2} \langle p_{\mathrm{T}}^2 \rangle_\tau$ with $\langle p_{\mathrm{T}}^2 \rangle$ the average transverse momentum squared of a jet with energy E_τ. In general $\langle p_{\mathrm{T}}^2 \rangle_\tau$ is assumed as $\sim 0.1\,(\mathrm{GeV}/c)^2$ similar to the case of two-jet events.

The generalised thrust method has been defined in ref. [295]. It requires the maximization of the linear term

$$\sum_{\mathrm{C}_1} \boldsymbol{p}_j \cdot \hat{\boldsymbol{m}}_1 + \sum_{\mathrm{C}_2} \boldsymbol{p}_j \cdot \hat{\boldsymbol{m}}_2 + \sum_{\mathrm{C}_3} \boldsymbol{p}_j \cdot \hat{\boldsymbol{m}}_3 = T_3' .$$

The three-jettiness is called triplicity in this case and is defined as

$$T_3 = \max T_3' / \sum |p_i| .$$

An exact solution of this equation is an extremely time consuming procedure. Approximations have been suggested (see discussion in ref. [300]).

A.4. Multi-jet analysis

As discussed above, the extension of the concept of the sphericity or thrust to higher jet multiplicities is limited by the necessary amount of computer time. An alternative approach is to use cluster algorithms which can be applied to any number of jets. They therefore are in particular important for the higher c.m. energies where the frequent occurrence of events with more than three jets is expected. Its application to multi jet events has been first suggested by Lanius [301] and Babcock and Cutkosky [302].

A fundamental difference to the methods discussed before is that the number of clusters is in general free for each individual event. The sphericity or thrust variable determines the direction of two (collinear) jets, the triplicity or generalized sphericity assumes three jets, no particular jet multiplicity is used for the cluster method.

The basic ingredient of a cluster algorithm is some measure of similarity or distance between two particles. Various means have been suggested, e.g., (1) the angle between particles and their total energy [303], (2) the angle between particles [304], (3) the invariant mass of particles [115].

Particles which are adjacent in space are combined into clusters. This requires an optimization of the measure of similarity and leads to some arbitrariness in the resulting cluster multiplicity. However, as was pointed out before, such an arbitrariness corresponds to our present uncertainty of when to call some bundle of particles a jet. The finding of clusters can be simplified by e.g. using the minimum spanning tree algorithm, combining the nearest lying neighbours with some test particle. This avoids considering all possible combinations.

As an example of a cluster algorithm we will list the different steps for cluster finding proposed in ref. [303]. Their scheme has been applied in various experiments.

(a) Finding preclusters:

- all measured particles are used and are members of a precluster;
- two particles belong to the same precluster if $\boldsymbol{n}_i \cdot \boldsymbol{n}_k > \cos\alpha$, α is a predefined value. This defines preclusters D_i with $\boldsymbol{n}_{\mathrm{D}_i} = \Sigma\, \boldsymbol{p}_k / \Sigma\, |\boldsymbol{p}_k|$.

(b) Combining preclusters into clusters:

- each precluster is a member of exactly one cluster;
- two preclusters are combined into one cluster if $\boldsymbol{D}_i \cdot \boldsymbol{D}_j > \cos\beta$, β is predefined and $\beta \geq \alpha$.
- a cluster has to fulfill $\Sigma\, E_k > E_{\mathrm{tot}}(1-\varepsilon)$ where again ε is a predefined energy and E_{tot} is the total measured energy. The number of clusters has to be minimal.

Most other cluster algorithms avoid defining preclusters and come along with less free parameters.

A.5. Treatment of three-jet events

For studying the detailed properties of three-jet events, it is frequently necessary to explicitly reconstruct the jets (see e.g. sections 5.2 and 6.2). The general procedure of treating these events can be divided into four major steps:

(1) Only events exhibiting clear three jet structure are selected. This can be achieved e.g. by cuts in the sphericity or thrust. Typically 10% of all events are retained.

(2) The three-jets are found with one of the methods discussed before in this appendix (triplicity, generalized sphericity). From the associated particles one reconstructs the observed energy and direction given by the energy and momentum vector sum of all particles in each jet.

(3) Since in most cases the angles are quite well determined, whereas the energies are distorted by

losses and measurement errors (cf. discussion in section 11.1), the energies are reconstructed from the jet directions assuming massless parton kinematics.

$$E_j = \frac{\sin \delta_{kl}}{\sin \delta_{jk} + \sin \delta_{kl} + \sin \delta_{lj}} E_{\mathrm{cm}} . \tag{A.5.1}$$

where δ_{ab} is the angle between jets a and b. With the additional constraint $\Sigma\, \delta_{ij} = 2\pi$ the outcome can be improved by fitting energies and angles.

(4) The jets are then ordered according to their energy $E_1 > E_2 > E_3$ with corresponding angles θ_1, θ_2 and θ_3 in the plane of the event. All events are directed in an equal manner within the plane by fixing $\theta_1 = 0$ and $\theta_2 > \theta_3$ with $\theta_2 < 180°$. By ordering the jets according to their energies one enriches jet 1 with quarks and jet 3 with gluons.

The efficiency and reliability of this method depends on the quality of the detector as well as on the detailed cuts applied. For their analysis of the string effect at $W = 35$ GeV (section 6.2) the JADE group estimates in their sample jet 1 to be closest to the gluon direction in 12% of their events, the equivalent numbers for jet 2 and jet 3 are 22% and 51%. The remaining 15% are due to broad two-jet events simulating three-jet structures.

References

[1] G. Hanson et al., Phys. Rev. Lett. 35 (1977) 1609.
[2] Review of Particle Properties, Phys. Lett. B 170 (1986).
[3] TASSO Collab., M. Althoff et al., Z. Phys. C 22 (1984) 307.
[4] CELLO Collab., H.J. Behrend et al., Phys. Lett. B 183 (1987) 400.
[5] PLUTO Collab., C. Berger et al., Nucl. Phys. B 124 (1983) 189.
[6] TASSO Collab., R. Brandelik et al., Phys. Lett. B 100 (1981) 117.
[7] TASSO Collab., R. Brandelik et al., Phys. Lett. B 86 (1979) 243;
MARKJ Collab., D.P. Barber et al., Phys. Rev. Lett. 43 (1979) 830;
PLUTO Collab., C. Berger et al., Phys. Lett. B 86 (1979) 418;
JADE Collab., W. Bartel et al., Phys. Lett. B 91 (1980) 142.
[8] G. Wolf, in: Proc. of the 14th International Symposium on Multiplarticle Dynamics (Granlibakken, Lake Tahoe, California, 22–27 June 1983) ed. R. Lander.
[9] P. Söding and G. Wolf, Ann. Rev. Nucl. Part. Sci. 31 (1981) 231.
[10] P. Söding, Testing the Standard Model, in: AIP Conf. Proc. 81, Particles and Fields: (Santa Cruz, 1981) eds C.A. Heusch and W.T. Kirk.
[11] TASSO Collab., R. Brandelik et al., Phys. Lett. B 97 (1980) 453.
[12] PLUTO Collab., C. Berger et al., Phys. Lett. B 97 (1980) 459.
[13] CELLO Collab., H.J. Behrend et al., Phys. Lett. B 110 (1982) 329.
[14] S. Yamada, in: Proc. XXIInd Int. Conf. on High Energy Physics (Leipzig, GDR, 19–25 July 1984) eds A. Meyer and E. Wieczorek.
[15] W. Ochs, Z. Phys C 15 (1982) 227.
[16] S. Frederiksson, M. Jandel and T.I. Larsson, Phys. Rev. Lett. 51 (1983) 2179.
[17] G. Preparata and G. Valenti, Nucl. Phys. B 183 (1981) 53; Phys. Rev. Lett. 47 (1981) 891.
[18] Ch. Quigg, Gauge Theories of the Strong, Weak and Electromagnetic Interactions (Benjamin and Cummings, Menlo Park, 1983).
[19] P. Becher, M. Böhm and H. Joos, Eichtheorien der Starken und Elektroschwachen Wechselwirkung (Teubner, Stuttgart, 1983) (in German).
[20] G. Altarelli, Phys. Rep. 81 (1982) 1.
[21] R.K. Ellis, D.A. Ross and E.A. Terrano, Nucl. Phys. B 178 (1981) 421.
[22] K. Fabricius, G. Kramer, G. Schierholz and I. Schmitt, Z. Phys. C 11 (1982) 315.
[23] F. Gutbrod, G. Kramer and G. Schierholz, Z. Phys. C 21 (1984) 235.
[24] T. Sjöstrand, in: Proc. XXIIIrd Conf. on High Energy Physics (Berkeley, California, 16–23 July 1986) ed. C. Loken.
[25] G. Kramer, Springer Tracts Mod. Phys. 102.
[26] J. Ellis, M.K. Gaillard and G.G. Ross, Nucl. Phys. B 111 (1976) 253.
[27] G. Kramer, G. Schierholz and J. Willrodt, Z. Phys. C 4 (1980) 149.

[28] E. Laermann and P.M. Zerwas, Phys. Lett. B 89 (1980) 225.
[29] T.F. Walsh and P. Zerwas, SLAC-PUB 2939 (unpublished).
[30] J.D. Bjorken, in Proc. Symp. on Physics in Collision 2 (Stockholm, 1982) p. 343.
[31] T. Kinoshita, J. Math. Phys. 3 (1962) 650.
[32] T.D. Lee and M. Nauenberg, Phys. Rev. 133 (1964) 1594.
[33] G. Fox and S. Wolfram, Phys. Rev. Lett. 41 (1978) 1581; Nucl. Phys. B 149 (1979) 413; Phys. Lett. B 82 (1979) 134.
[34] K. Konishi, A. Ukawa and G. Veneziano, Nucl. Phys. B 157 (1979) 45; Phys. Lett. B 80 (1979) 259.
[35] R. Odorico, Nucl. Phys. B 172 (1980) 157.
[36] P. Mazzanti and R. Odorico, Phys. Lett. B 95 (1980) 133; Z. Phys. C 7 (1980) 61.
[37] R. Field and G. Fox, UFTP-82-30 (1982) Univ. of Florida preprint.
[38] T. Gottschalk, Nucl. Phys. B 214 (1983) 201.
[39] G. Marchesini and B.R. Webber, Nucl. Phys. B 238 (1984) 1.
[40] B.R. Webber, Nucl. Phys. B 238 (1984) 492.
[41] A.H. Mueller, Phys. Lett. B 104 (1981) 161.
[42] A. Bassetto et al., Nucl. Phys. B 207 (1982) 189.
[43] B.I. Ermolaev and V.S. Fadin, JETP Lett. 33 (1981) 269.
[44] Yu.L. Dokshitzer, V.S. Fadin and V.A. Khoze, Phys. Lett. B 115 (1982) 242; Z. Phys. C 15 (1982) 325; Z. Phys. C 18 (1983) 37.
[45] A. Bassetto, M. Ciafaloni and G. Marchesini, Phys. Rep. 100 (1983) 201.
[46] G. Marchesini, in: XVth Int. Symp. on Multiparticle Dynamics (Lund, Sweden, 10–16 June 1984) eds G. Gustafson and C. Peterson.
[47] G. Altarelli and G. Parisi, Nucl. Phys. B 216 (1977) 298.
[48] M. Bengtsson and T. Sjöstrand, Nucl. Phys. B 289 (1987) 810.
[49] B.R. Webber, Ann. Rev. Nucl. Part. Sci. 36 (1986) 253.
[50] Y. Azimov et al., Yad. Fiz. 43 (1986) 149; Phys. Lett. B 165 (1985) 147.
[51] B.R. Webber, in: Proc. XVIth Symp. on Multiparticle Dynamics (Kiryat Anavim, Israel, 1985) ed. J. Grunhaus.
[52] B. Klima, in: Proc. IXth Warsaw Symp. on High Energy Physics (Kazimierz, Poland, 25–31 May 1986) ed. Z. Adjuk; and DESY 86-070.
[53] M. Bengtsson and T. Sjöstrand, Phys. Lett. B 185 (1987) 435.
[54] A. Krywicki and B. Petersson, Phys. Rev. D 6 (1972) 924.
[55] J. Finkelstein and R.D. Peccei, Phys. Rev. D 6 (1972) 2606.
[56] R. Field and R.P. Feynman, Nucl. Phys. B 161 (1978) 1.
[57] B. Andersson, G. Gustafson and B. Soderberg, Z. Phys. C 20 (1983) 317.
[58] P. Hoyer et al., Nucl. Phys. B 161 (1979) 349.
[59] A. Ali, E. Pietarinen, G. Kramer and J. Willrodt, Phys. Lett. B 93 (1980) 155.
[60] B. Andersson, G. Gustafon, G. Ingelman and T. Sjöstrand, Phys. Rep. 97 (1983) 33.
[61] G. Gustafson, Z. Phys. C 15 (1982) 155.
[62] S. Wolfram, in: Proc. 15th Recontre de Moriond (1980) ed. J. Tran Thanh Van.
[63] D. Amati and G. Veneziano, Phys. Lett. B 83 (1979) 87.
[64] Ya.I. Azimov, Yu.L. Dokshitzer, V.A. Khoze and S.I. Troyan, Z. Phys. C 27 (1985) 65.
[65] MARK2 Collab., A. Petersen et al., Phys. Rev. D 37 (1988) 1.
[66] CELLO Collab., H.J. Behrend et al., Nucl. Phys. B 218 (1983) 269.
[67] J.L. Siegrist et al., Phys. Rev. D 26 (1986) 969.
[68] B.H. Wiik and G. Wolf, Springer Tracts Mod. Phys. 86 (1979).
[69] M.L. Perl, High Energy Hadron Physics (Wiley, New York, 1974).
[70] W. Thome et al., Nucl. Phys. B 129 (1977) 365.
[71] A. Bassetto, M. Ciafaloni and G. Marchesini, Phys. Lett. B 83 (1978) 207.
[72] K. Konishi, Rutherford Report RL 79-035 (1979).
[73] W. Furmanski and S. Pokorski, Nucl. Phys. B 155 (1979) 253.
[74] A.H. Mueller, Phys. Lett. B 104 (1981) 161; Nucl. Phys. B 213 (1983) 85.
[75] P. Carruthers and C.C. Shih, Int. J. Mod. Phys. 2 (1987) 1447.
[76] A. Bialas and F. Hayot, Phys. Rev. D 33 (1986) 39.
[77] HRS Collab., M. Derrick et al., Phys. Rev. D 34 (1986) 3304.
[78] Z. Koba, H.B. Nielsen and P. Oleson, Nucl. Phys. B 40 (1972) 317.
[79] UA5 Collab., G.J. Alner et al., Phys. Lett. B 138 (1984) 304.
[80] PLUTO Collab., C. Berger et al., paper in preparation.
[81] LENA Collab., B. Niczyporuk, Z. Phys. C 9 (1981) 1.
[82] JADE Collab., W. Bartel et al., Z. Phys. C 20 (1983) 187.
[83] HRS Collab., M. Derrick et al., Phys. Lett. B 168 (1986) 299.
[84] M.G. Bowler and P.N. Burrows, Z. Phys. C 31 (1986) 327.
[85] A. Giovanni, Nuovo Cimento 15A (1973) 543.

[86] W.J. Knox, Phys. Rev. D 10 (1974) 65.
[87] A. Giovanni and L. van Hove, Z. Phys. C 30 (1986) 391;
L. van Hove and A. Giovanni, Contr. paper to the XVIIth Symposium on Multiparticle Dynamics (1986), Torino preprint DFTT 11/86.
[88] UA5 Collab., G.J. Alner et al., Phys. Lett. B 160 (1985) 193.
[89] NA22 Collab., M. Adamus et al., Phys. Lett. B 160 (1986) 239.
[90] HRS Collab., M. Derrick et al., Phys. Rev. D 33 (1986) 3304.
[91] C.K. Chew and Y.K. Lim, Phys. Lett. B 163 (1985) 257.
[92] NA22 Collab., M. Adams et al., Z. Phys. C 32 (1987) 475.
[93] P. Carruthers and C.C. Shih, Phys. Lett. B 137 (1984) 425.
[94] HRS Collab., M. Derrick et al., Phys. Lett. B 165 (1986) 299.
[95] P. Mättig, in: Proc. First Int. Workshop on Local Equilibrium in Strong Interaction Physics (Bad Honnef, FRG, 3–6 September 1984) eds D.K. Scott and R.M. Weiner.
[96] HRS Collab., D. Bender et al., Phys. Rev. D 31 (1985) 1.
[97] R.P. Feynman, Phys. Rev. Lett. 23 (1969) 1415.
[98] S.D. Drell, D.J. Levy and T.M. Yan, Phys. Rev. 187 (1969) 187; Phys. Rev. D 1 (1970) 1617.
[99] R. Baier and K. Fey, Z. Phys. C 2 (1979) 339.
[100] G. Altarelli, R.K. Ellis, G. Martinelli and So-Young Pi, Nucl. Phys. B 160 (1979) 301.
[101] J.F. Patrick et al., Phys. Rev. Lett. 49 (1982) 1232.
[102] TASSO Collab., R. Brandelik et al., Phys. Lett. B 114 (1982) 65.
[103] HRS Collab., M. Derrick et al., Phys. Lett. B 164 (1985) 199.
[104] Z.F. Ezawa, Nuovo Cimento 23A (1974) 271.
[105] G. Farrar and D.R. Jackson, Phys. Rev. Lett. 35 (1975) 1416.
[106] A.I. Vainshtain and V.I. Zacharov, Phys. Lett. B 72 (1978) 368.
[107] E.L. Berger, Z. Phys. C 4 (1980) 289.
[108] C. Peterson, D. Schlatter, I. Schmitt and P.M. Zerwas, Phys. Rev. D 27 (1983) 105.
[109] P.D. Dauncy, thesis at the University of Oxford, RAL-T-034 (unpublished).
[110] Ya.I. Azimov, Yu.L. Dokshitzer and V.A. Khoze, in: Physics of Hadron Production in Annihilations into Light and Heavy Quarks, Materials from the XVIIIth Winter School at the Leningrad Inst. Nucl. Phys. (in Russian). I am grateful to Mrs. I. Schulz-Dahlen for her translation.
[111] A.E. Chudakov, Izv. Akad. Nauk. SSSR Ser. Fiz 19 (1955) 650.
[112] Yu.L. Dokshitzer, V.A. Khoze, S.I. Troyan and A.H. Mueller, Rev. Mod. Phys. 60 (1988) 377.
[113] PLUTO Collab., C. Berger et al., Z. Phys. C 22 (1984) 103.
[114] M.R. Pennington, Cornerstones of QCD, Rep. Prog. Phys. 46 (1983) 393.
[115] JADE Collab., W. Bartel et al., Z. Phys. C 33 (1986) 23.
[116] TASSO Collab., M. Althoff et al., Z. Phys. C 26 (1984) 157.
[117] MARKJ Collab., B. Adeva et al., Phys. Rep. 109 (1984) 131.
[118] D. Saxon, Quark and gluon fragmentation, in: Electron–Positron Collisions at High Energies, eds A. Ali and P. Söding, to be published.
[119] CLEO Collab., S. Berends et al., Phys. Rev. D 31 (1985) 2161.
[120] ARGUS Collab., H. Albrecht et al., Phys. Lett. B 183 (1987) 419.
[121] JADE Collab., W. Bartel et al., Z. Phys. C 28 (1985) 343.
[122] TASSO Collab., W. Braunschweig et al., Z. Phys. C 33 (1986) 13.
[123] CELLO Collab., H.J. Behrend et al., Z. Phys. C 20 (1983) 207.
[124] TPC Collab., H. Aihara et al., Z. Phys. C 27 (1985) 187.
[125] TASSO Collab., W. Braunschweig et al., DESY 88/164.
[126] TPC Collab., H. Aihara et al., Phys. Rev. Lett. 52 (1984) 577.
[127] TASSO Collab., M. Althoff et al., Z. Phys. C 27 (1985) 27.
[128] MARK2 Collab., H. Schellman, Phys. Rev. D 31 (1985) 3013.
[129] HRS Collab., M. Derrick et al., Phys. Rev. D 35 (1987) 2639.
[130] JADE Collab., W. Bartel et al., Z. Phys. C 20 (1983) 187.
[131] TPC Collab., H. Aihara et al., Phys. Rev. Lett. 53 (1984) 2378.
[132] PLUTO Collab., C. Berger et al., Phys. Lett. B 104 (1981) 79.
[133] HRS Collab., M. Derrick et al., Phys. Rev. Lett. 57 (1986) 1990.
[134] HRS Collab., M. Derrick et al., Phys. Lett. B 158 (1985) 519.
[135] TASSO Collab., R. Brandelik et al., Phys. Lett. B 117 (1982) 135; 183 (1987) 419.
[136] MARK2 Collab., H. Schellman et al., SLAC – PUB 3448.
[137] JADE Collab., W. Bartel et al., Phys. Lett. B 145 (1985) 441.
[138] TPC Collab., H. Aihara et al., Phys. Rev. Lett. 53 (1984) 2378.
[139] TPC Collab., H. Aihara et al., Phys. Rev. Lett. 52 (1984) 2201.
[140] HRS Collab., M. Derrick et al., Phys. Rev. Lett. 54 (1985) 2568.
[141] MARK2 Collab., C. de la Vaissiere et al., Phys. Rev. Lett. 54 (1985) 2071.

[142] TPC Collab., H. Aihara et al., Phys. Rev. Lett. 54 (1985) 274.
[143] TPC Collab., H. Yamamoto, in: QCD and Beyond, Proc. Hadronic Session of the 20th Recontre de Moriond, ed. J. Tran Thanh Van (1985).
[144] TASSO Collab., R. Brandelik et al., Phys. Lett. B 130 (1983) 340.
[145] MARK2 Collab., S.R. Klein et al., Phys. Rev. Lett. 58 (1987) 644.
[146] HRS Collab., S. Abachi et al., Phys. Rev. Lett. 58 (1987) 2647.
[147] TASSO Collab., M. Althoff et al., Z. Phys. C 26 (1984) 181.
[148] CLEO Collab., M.S. Alam et al., Phys. Rev. Lett. 53 (1984) 24.
[149] MARK2 Collab., S.R. Klein et al., Phys. Rev. Lett. 59 (1987) 2412.
[150] ARGUS Collab., H. Albrecht et al., Phys. Lett. B 157 (1985) 326.
[151] TASSO Collab., M. Althoff et al., Z. Phys. C 17 (1983) 5.
[152] B. Andersson and G. Gustafson, LU – TP 82-5 (unpublished).
[153] V. Cerny, P. Lichard and J. Pisut, Phys. Rev. D 16 (1977) 2822; Acta Phys. Pol. B10 (1979) 629; Phys. Rev. D 18 (1978) 2409; Czech. J. Phys. B 31 (1981) 1302.
[154] T. Meyer, Z. Phys. C 12 (1982) 77.
[155] B. Andersson, G. Gustafson and T. Sjöstrand, Nucl. Phys. B 197 (1982) 45.
[156] S. Ritter and J. Ranft, Acta Phys. Pol. B 11 (1980) 259.
[157] G. Lichtenberg et al., Z. Phys. C 19 (1983) 19.
[158] A. Breakstone et al., Z. Phys. C 28 (1985) 335.
[159] A. Casher, H. Neuberger and S. Nussinov, Phys. Rev. D 20 (1979) 179.
[160] M.G. Bowler, Oxford Nucl. Phys. Rep. 76/81 (1981) (unpublished).
[161] A. Bartl, H. Fraas and W. Majerotto, Phys. Rev. D 26 (1982) 1061.
[162] K.W. Bell et al., Rutherford Rep. RAL-82-011 (1982).
[163] HRS Collab., P. Baringer et al., Phys. Rev. Lett. 56 (1986) 1346.
[164] K. Abe et al., Phys. Rev. D 33 (1986) 1.
[165] TASSO Collab., M. Dittmar, Ph.D. Thesis, DESY-F1-85-01 (unpublished).
[166] TPC Collab., H. Aihara et al., Contribution Int. Conf. on High Energy Physics (Bari, 1985).
[167] D. Saxon, in: Proc. Int. Conf. on High Energy Physics (Bari, 1985) p. 513.
[168] K.W. Bell, Baryon Production in e^+e^--Annihilation at PETRA (thesis) (September 1985) RAL-T-015.
[169] DASP Collab., R. Brandelik et al., Nucl. Phys. B 148 (1979) 189.
[170] M. Suzuki, Phys. Lett. B 71 (1977) 139.
[171] J.D. Bjorken, Phys. Rev. D 17 (1978) 171.
[172] S. Bethke, Z. Phys. C 29 (1985) 175.
[173] J. Kuti and V. Weisskopf, Phys. Rev. D 4 (1971) 3418.
[174] V.G. Kartvelishvili, A.K. Likhoded and V.A. Petrov, Phys. Lett. B 78 (1978) 615.
[175] M.G. Bowler, Z. Phys. C 11 (1981) 169.
[176] CLEO Collab., R. Giles et al., Phys. Rev. D 30 (1984) 2279.
[177] ARGUS Collab., H. Albrecht et al., Phys. Lett. 185 (1987) 218.
[178] TPC Collab., H. Aihara et al., Phys. Rev. D 34 (1986) 1945.
[179] HRS Collab., S. Aklen et al., Phys. Rev. Lett. 51 (1983) 1147.
[180] TASSO Collab., M. Althoff et al., Phys. Lett. B 126 (1983) 493.
[181] JADE Collab., W. Bartel et al., Phys. Lett. B 146 (1984) 121.
[182] CLEO Collab., P. Avery et al., Phys. Rev. Lett. 51 (1983) 1139.
[183] R.S. Galik, in: Proc. Int. Conf. on High Energy Physics (Bari, 1985) p. 513.
[184] R. Orr, in: Proc. Int. Conf. on High Energy Physics (Bari, 1985) p. 517.
[185] JADE Collab., W. Bartel et al., Phys. Lett. B 161 (1985) 197.
[186] HRS Collab., E.H. Low, Phys. Lett. B 183 (1987) 232.
[187] ARGUS Collab., H. Albrecht et al., Phys. Rev. Lett. 56 (1986) 549.
[188] TASSO Collab., M. Althoff et al., Phys. Lett. B 136 (1984) 139.
[189] CLEO Collab., T. Bowcock et al., Phys. Rev. Lett. 55 (1985) 923.
[190] JADE Collab., W. Bartel et al., Z. Phys. C 33 (1987) 339.
[191] Th.de Grand, Phys. Rev. D 26 (1985) 3298.
[192] TASSO Collab., M. Althoff et al., Phys. Lett. B 135 (1984) 243.
[193] MARK3 Collab., J. Adler et al., Phys. Rev. Lett. 60 (1988) 89.
[194] MARK2 Collab., J.M. Yelton et al., Phys. Rev. Lett. 49 (1982) 430.
[195] DELCO Collab., H. Yamamoto et al., Phys. Rev. Lett. 54 (1985) 522.
[196] MARKJ Collab., B. Adeva et al., Phys. Rev. Lett. 51 (1983) 443.
[197] J. Chrin, Z. Phys. C 36 (1987) 163.
[198] JADE Collab., W. Bartel et al., Z. Phys. C 9 (1981) 315.
[199] CELLO Collab., H.J. Behrend et al., Z. Phys. C 14 (1982) 189.

[200] DELCO Collab., M. Sakuda et al., Phys. Lett. B 152 (1985) 399.
[201] MARK2 Collab., P.C. Rowson et al., Phys. Rev. Lett. 54 (1985) 2580.
[202] TPC 2γ Collab., H. Aihara et al., Phys. Lett. B 184 (1987) 299.
[203] CLEO Collab., M.S. Alam, Phys. Rev. Lett. 49 (1982) 357;
B. Gittelman and S. Stone, CLNS 87/81.
[204] P. Mättig, Int. J. Mod. Phys. 3 (1988) 1.
[205] HRS Collab., P. Kesten et al., Phys. Lett. B 161 (1985) 412.
[206] MARK2 Collab., R. Schindler et al., Phys. Rev. D 24 (1981) 78.
[207] M.B. Einhorn and B.G. Weeks, Nucl. Phys. B 146 (1978) 445.
[208] K. Shizuya and S.H. Tye, Phys. Rev. Lett. 41 (1978) 787.
[209] J.B. Gaffney and A.H. Mueller, Nucl. Phys. B 250 (1985) 109.
[210] MARK2 Collab., A. Petersen et al., Phys. Rev. Lett. 55 (1985) 1954.
[211] HRS Collab., M. Derrick et al., Phys. Lett. B 165 (1985) 449.
[212] UA2 Collab., P. Bagnaia et al., Z. Phys. C 20 (1983) 117.
[213] UA1 Collab., G. Arnison et al., Nucl. Phys. B 276 (1986) 253.
[214] JADE Collab., W. Bartel et al., Phys. Lett. B 123 (1983) 460.
[215] TASSO Collab., M. Althoff et al., Z. Phys. C 29 (1985) 29.
[216] DASP2 Collab., H. Albrecht et al., Phys. Lett. B 102 (1981) 291.
[217] CLEO Collab., M.S. Alam et al., Phys. Rev. Lett. 53 (1985) 24.
[218] JADE Collab., W. Bartel et al., Phys. Lett. B 130 (1983) 454.
[219] B. Andersson, G. Gustafson and T. Sjöstrand, Phys. Scr. 32 (1985) 574.
[220] R.D. Field, Phys. Lett. B 135 (1984) 203.
[221] C. Peterson and T.F. Walsh, Phys. Lett. B 91 (1980) 455.
[222] R. Hanbury and R.Q. Twiss, Philos. Mag. 45 (1954) 663; Nature 178 (1956) 1046.
[223] E.M. Purcell, Nature 178 (1956) 1449.
[224] G. Goldhaber et al., Phys. Rev. Lett. 3 (1959) 181.
[225] G. Goldhaber, S. Goldhaber, W. Lee and A. Pais, Phys. Rev. 120 (1960) 300.
[226] M. Gyulassy, Phys. Rev. C 20 (1979) 2267.
[227] M.G. Bowler, Z. Phys. C 29 (1985) 617.
[228] G.N. Fowler and R.M. Weiner, Phys. Lett. B 70 (1977) 201.
[229] B. Andersson and W. Hofmann, Phys. Lett. B 169 (1986) 364.
[230] M.G. Bowler, Phys. Lett. B 185 (1987) 205.
[231] G.I. Kopylov and M.I. Podgoretsky, Sov. J. Nucl. Phys. 15 (1972) 219; 18 (1974) 336.
[232] G. Goldhaber, in: Proc. First Int. Workshop on Local Equilibrium in Strong Interaction Physics (Bad Honnef, FRG, 3–6 September 1984) eds D.K. Scott and R.M. Weiner.
[233] G. Goldhaber, in: Proc. Int. Conf. on High Energy Physics (Lisbon, 1981) eds J. Dias de Deus and J. Soffer, p. 767.
[234] G. Goldhaber and I. Juricic, LBL-21531 (1986), Contribution to the Second Int. Workshop on Local Equilibrium in Strong Interaction Physics (Santa Fe, New Mexico, 9–12 April 1986).
[235] W. Koch, in: Proc. XIIIth Int. Symp. on Multiparticle Dynamics (Volendam, 1982) eds W. Kittel and J. Metzger.
[236] TASSO Collab., M. Althoff et al., Z. Phys. C 29 (1985) 347.
[237] TASSO Collab., M. Althoff et al., Z. Phys. C 30 (1986) 355.
[238] CLEO Collab., P. Avery et al., Phys. Rev. D 32 (1985) 2294.
[239] TPC Collab., H. Aihara et al., Phys. Rev. D 31 (1985) 996.
[240] B. Andersson, G. Gustafson and T. Sjöstrand, Phys. Lett. B 94 (1980) 211.
[241] JADE Collab., W. Bartel et al., Phys. Lett. B 101 (1981) 129.
[242] JADE Collab., W. Bartel et al., Z. Phys. C 21 (1983) 37.
[243] JADE Collab., W. Bartel et al., Phys. Lett. B 134 (1985) 31.
[244] TPC Collab., H. Aihara et al., Phys. Rev. Lett. 54 (1985) 270.
[245] TPC Collab., H. Aihara et al., Z. Phys. C 28 (1985) 31.
[246] TPC Collab., H. Aihara et al., Phys. Rev. Lett. 57 (1986) 945.
[247] MARK2 Collab., P.D. Sheldon et al., Phys. Rev. Lett. 57 (1986) 1398.
[248] UA5 Collab., K. Algard et al., Phys. Lett. B 123 (1983) 361.
[249] J. Dorfan, in: Proc. Int. Symp. on Lepton and Photon Interactions at High Energies (Cornell Univ., Ithaca, New York, 4–9 August 1983) ed. D. Cassel.
[250] TPC Collab., H. Aihara et al., Phys. Rev. Lett. 53 (1984) 2199.
[251] TASSO Collab., M. Althoff et al., Phys. Lett. B 139 (1984) 126.
[252] TPC Collab., H. Aihara et al., Phys. Rev. Lett. 55 (1985) 1047.
[253] B. Webber, EARWIG4, unpublished.
[254] TPC Collab., H. Aihara et al., Phys. Rev. Lett. 57 (1986) 3140.

[255] JADE Collab., W. Bartel et al., Phys. Lett. B 104 (1981) 325.
[256] C.L. Basham, L.S. Brown, S.D. Ellis and T. Love, Phys. Rev. Lett. 41 (1978) 1585; Phys. Rev. D 19 (1979) 2018; Phys. Rev. D 24 (1981) 2383.
[257] F. Barreiro, Fortschr. Phys. 34 (1986) 503.
[258] JADE Collab., W. Bartel et al., Z. Phys. C 25 (1984) 231.
[259] T. Gottschalk and D. Morris, Nucl. Phys. B 288 (1987) 729.
[260] T.F. Walsh and P.M. Zerwas, Phys. Lett. B 44 (1973) 195.
[261] K. Sasaki, Phys. Rev. D 24 (1981) 1177.
[262] E. Laermann et al., Nucl. Phys. B 207 (1982) 205.
[263] MAC Collab., E. Fernandez et al., Phys. Rev. Lett. 54 (1985) 95.
[264] JADE Collab., W. Bartel et al., Phys. Lett. B 115 (1982) 338.
[265] M. Derrick and T. Gottschalk, in: Proc. 1984 Summer Study on the Design and Utilization of the Superconducting Super Collider (23 June–13 July 1984, Snowmass, Colorado) eds R. Donaldson and J.G. Morfin.
[266] T. Akesson et al., in: Proc. of the ECFA – CERN Workshop Large Hadron Collider in the LEP Tunnel (Lausanne and Geneva, 21–27 March 1984) ed. M. Jacob, ECFA 84/85, CERN 84-10.
[267] Z. Kunszt et al., in: Proc. Workshop on Physics at Future Accelerators (La Thuile, Italy, and Geneva, Switzerland, 7–13 January 1987) ed. J. Mulvey, CERN 87-07.
[268] P. Mättig, in: Proc. VIIth Warsaw Symposium on Elementary Particle Physics (Kazimierz, Poland, 20–26 May 1984) ed. Z. Adjuk.
[269] G. Hanson, in: Proc. of the Second MARKII Workshop on SLC Physics (986), SLAC-306.
[270] Ya.I. Azimov, Yu.L. Dokshitzer and V.A. Khoze, Yad. Fiz. 36 (1982) 1510.
[271] UA1 Collab., G. Arnison et al., Phys. Lett. B 147 (1984) 222.
[272] A. Ali and G. Ingelman, Phys. Lett. B 156 (1985) 111.
[273] A. Böhm and W. Hoogland, eds, Proc. ECFA Workshop on LEP2 (Aachen, FRG, 29 September–1 October 1986) CERN 87 - 08, ECFA 87/108; in particular the contributions from M. Davier, E. Longo and P. Roudeau.
[274] G. Wolf, HERA: Physics, Machine and Experiments, DESY 86-089, in: Proc. of the Advanced Study 1986, St. Croix, Virgin Islands.
[275] J. Bijnens et al., in: Proc. ECFA Workshop on LEP2 (Aachen, 1986), eds A. Böhm and W. Hoogland; CERN 87-08; ECFA 87/108.
[276] J. Hilgart et al., Z. Phys. C 35 (1987) 347.
[277] M. Holder, in: Proc. Workshop Experimentation at HERA (Amsterdam, 9–11 June 1983) DESY HERA 83/20 (1983).
[278] P.N. Burrows and G. Ingelman, Z. Phys. C 34 (1987) 91.
[279] G. Marchesini and B.R. Webber, in: Proc. Workshop on Physics at Future Accelerators (La Thuile, Italy, and Geneva, Switzerland, 7–13 January 1987) Vol. II, CERN 87-07.
[280] P. Mättig and M. Dittmar, Z. Phys. C 35 (1987) 221.
[281] MAC Collab., W.W. Ash et al., Phys. Rev. Lett. 58 (1987) 1080.
[282] TPS Collab., J. Raab et al., Phys. Rev. D 37 (1988) 2391.
[283] A. Breakstone et al., Proposal for the Addition of a Silicon μ-strip Detector to the MARKII Detector at the SLC, July 1985.
[284] P. Roudeau, in: Proc. Int. Symp. on the Production and Decay of Heavy Hadrons (Heidelberg, 20–23 May 1986) eds K.R. Schubert and R. Waldi.
[285] R. Marshall, Z. Phys. C 26 (1984) 291.
[286] JADE Collab., W. Bartel et al., Phys. Lett. B 146 (1984) 121.
[287] TASSO Collab., M. Althoff et al., Phys. Lett. B 149 (1984) 259.
[288] T. Gottschalk and T. Sjöstrand, in: Proc. 1984 Summer Study on the Design and Utilization of the Superconducting Super Collider (23 June–13 July 1984, Snowmass, Colorado) eds R. Donaldon and J.G. Morfin.
[289] M. Dittmar, Internal OPAL note and private communication.
[290] K. Kleinknecht et al., in: Proc. ECFA Workshop on LEP2 (Aachen, 1986); eds A. Böhm and W. Hoogland; CERN 87-08; ECFA 87/108.
[291] P. Nilles and K.H. Streng, Phys. Rev. D 23 (1981) 1944.
[292] M. Jacob, in: Proc. 1973 CERN-JINR School of Physics (Ebeltoft, Denmark, 17–30 June 1973) ed. O. Kofoed-Hansen, CERN 73-12.
[293] J.D. Bjorken and S.J. Brodsky, Phys. Rev. D 1 (1970) 1416.
[294] H. Georgi and M. Machachek, Phys. Rev. Lett. 39 (1977) 1237.
[295] S. Brandt and H.D. Dahmen, Z. Phys. C 1 (1979) 61.
[296] S. Brandt, Ch. Peyrou, R. Sosnowski and A. Wroblewski, Phys. Lett. B 12 (1964) 57.
[297] E. Fahri, Phys. Rev. Lett. 39 (1977) 1587.
[298] D.P. Barber et al., Phys. Rev. Lett. 43 (1979) 830.
[299] S.L. Wu and G. Zobernig, Z. Phys. C 2 (1979) 107.
[300] S.L. Wu, Phys. Rep. 107 (1984) 60.
[301] K. Lanius, DESY report 80/36.
[302] J.E. Babcock and R.E. Cutkosky, Nucl. Phys. B 176 (1980) 113.
[303] H.J. Daum, H. Meyer and J. Bürger, Z. Phys. C 8 (1981) 167.
[304] T. Sjöstrand, Comp. Phys. Comm. 27 (1982) 243.